

GEOFORSCHUNGSZENTRUM POTSDAM
STIFTUNG DES ÖFFENTLICHEN RECHTS

Scientific Technical Report

ISSN 1610-0956



*Institut für Geowissenschaften
Mathematisch-Naturwissenschaftliche Fakultät
Universität Potsdam*



Neogene seismotectonics of the south-central Chile margin

Subduction-related processes over various
temporal and spatial scales

Daniel Melnick

Geboren am 25.12.1976 in Santiago, Chile

Dissertation
zur Erlangung des akademischen Grades
Doktor der Naturwissenschaften (Dr. rer. nat.)
in der Wissenschaftsdisziplin Geologie

eingereicht an der Mathematisch-Naturwissenschaftlichen Fakultät
der Universität Potsdam

Potsdam, im Januar 2007

dedicado a Amerika Manzanares, amor de mi vida...

Scientific Technical Report STR 07/01

DOI: 10.2312/GFZ.b103-07012

GeoForschungsZentrum Potsdam

Abstract

The Andean orogen is the most outstanding example of mountain building caused by the subduction of oceanic below continental lithosphere. The Andes formed by the subduction of the Nazca and Antarctic oceanic plates under the South American continent over at least ~200 million years. Tectonic and climatic conditions vary markedly along this north-south-oriented plate boundary, which thus represents an ideal natural laboratory to study tectonic and climatic segmentation processes and their possible feedbacks. Most of the seismic energy on Earth is released by earthquakes in subduction zones, like the giant 1960, M_w 9.5 event in south-central Chile. However, the segmentation mechanisms of surface deformation during and between these giant events have remained poorly understood. The Andean margin is a key area to study seismotectonic processes because of its along-strike variability under similar plate kinematic boundary conditions.

Active deformation has been widely studied in the central part of the Andes, but the south-central sector of the orogen has gathered less research efforts. This study focuses on tectonics at the Neogene and late Quaternary time scales in the Main Cordillera and coastal forearc of the south-central Andes. For both domains I document the existence of previously unrecognized active faults and present estimates of deformation rates and fault kinematics. Furthermore these data are correlated to address fundamental mountain building processes like strain partitioning and large-scale segmentation.

In the Main Cordillera domain and at the Neogene timescale, I integrate structural and stratigraphic field observations with published isotopic ages to propose four main phases of coupled styles of tectonics and distribution of volcanism and magmatism. These phases can be related to the geometry and kinematics of plate convergence. At the late Pleistocene timescale, I integrate field observations with lake seismic and bathymetric profiles from the Lago Laja region, located near the Andean drainage divide. These data reveal Holocene extensional faults, which define the Lago Laja fault system. This fault system has no significant strike-slip component, contrasting with the Liquiñe-Ofqui dextral intra-arc system to the south, where Holocene strike-slip markers are ubiquitous. This contrast in structural style along the arc is coincident with a marked change in along-strike fault geometries in the forearc, across the Arauco Peninsula. Thereon I propose that a net gradient in the degree of partitioning of oblique subduction occurs across the Arauco transition zone. To the north, the margin parallel component of oblique convergence is distributed in a wide zone of diffuse deformation, while to the south it is partitioned along an intra-arc, margin-parallel strike-slip fault zone.

In the coastal forearc domain and at the Neogene timescale, I integrate structural and stratigraphic data from field observations, industry reflection-seismic profiles and boreholes to emphasize the influence of climate-driven filling of the trench on the mechanics and kinematics of the margin. I show that forearc basins in the 34-45°S segment record Eocene to early Pliocene extension and subsidence followed by ongoing uplift and contraction since the late Pliocene. I interpret the first stage as caused by tectonic erosion due to high plate convergence rates and reduced trench fill. The subsequent stage, in turn, is related to accretion caused by low convergence rates and the rapid increase in trench fill after the onset of Patagonian glaciations and climate-driven exhumation at ~6-5 Ma. On the late Quaternary timescale, I integrate off-shore seismic profiles with the distribution of deformed marine terraces from Isla Santa María, dated by the radiocarbon method, to show that inverted reverse faulting controls the coastal geomorphology and segmentation of surface deformation. There, a cluster of microearthquakes illuminates one of these reverse faults, which presumably reaches the plate interface. Furthermore, I use accounts of coseismic uplift during the 1835 $M > 8$ earthquake made by Charles Darwin, to propose that this active reverse fault has been mechanically coupled to the megathrust. This has important implications on the assessment of seismic hazards in this, and other similar regions.

These results underscore the need to study plate-boundary deformation processes at various temporal and spatial scales and to integrate geomorphologic, structural, stratigraphic, and geophysical data sets in order to understand the present distribution and causes of tectonic segmentation.

Zusammenfassung

Die Anden sind eine einzigartige Gebirgskette entstanden aus der Subduktion von ozeanischer unter kontinentale Lithosphäre. Seit mehr als 200 Millionen Jahren bewirkt die Subduktion der ozeanischen Nazca- und Antarktisplatte unter den Südamerikanischen Kontinent eine stete Entwicklung des aktiven Plattengrenzsysteams. Entlang der Plattengrenze ändern sich die tektonischen und klimatischen Bedingungen in markanter Weise und machen dieses Orogen zu einem idealen natürlichen Laboratorium für das Studium tektonischer und klimatischer Prozesse und deren rückgekoppelte Wechselwirkungen. Der grösste Teil der seismischen Energie auf der Erde wird durch Erdbeben an Subduktionszonen freigesetzt, wie das spektakulärste Beispiel des Valdivia-Bebbens von 1960 im süd-zentral chilenischen Küstenbereich – mit M_w 9,5 das stärkste je gemessene seismische Ereignis, unterstreicht. Die Verteilungsmechanismen der Oberflächendeformation während und zwischen solchen gewaltigen Vorgängen blieben jedoch weitgehend unverstanden. Wegen seiner im Streichen veränderlichen Eigenschaften blieben bei ähnlich bleibenden plattenkinematischen Randbedingungen nimmt die Subduktionszone des Anden-Orogens eine Schlüsselstellung für das Studium seismotektonischer Segmentationsprozesse ein.

Aktive Deformationsprozesse sind im zentralen Teil der Anden in grösserem Umfang untersucht worden, während der mittlere bis südliche Abschnitt des Orogens bisher weniger Bearbeitung fand. Die vorliegende Arbeit ist auf die seismotektonischen Prozesse des Neogen und Spätquartärs in der Hauptkordillere und dem Küstenbereich der südlichen Zentralanden konzentriert. In beiden Strukturzonen kann die Existenz bisher nicht bekannter aktiver Störungen belegt werden und es werden Abschätzungen der Deformationsraten sowie der Kinematik präsentiert. Diese Daten bilden desweiteren die Basis, um Aussagen zu grundlegenden gebirgsbildenden Prozessen, der Verformungsverteilung und der gross-skaligen Segmentation zu treffen.

Für das Neogen im untersuchten Abschnitt der Hauptkordillere sind strukturelle und stratigraphische Geländebeobachtungen durch publizierte Isotopendaten ergänzt worden, so dass vier Hauptphasen mit jeweils spezifischem tektonischen Stil und Verteilungsmustern von Vulkanismus und Magmatismus unterschieden werden können. Auf der spätpleistozänen Zeitskala sind die Geländebeobachtungen mit seismischen und bathymetrischen Seeprofilen aus der Lago-Laja-Region kombiniert worden, die sich nahe der Wasserscheide der Anden befinden. Diese Daten belegen extensionale holozäne Störungen, die das Lago-Laja-Störungssystem bestimmen. Im Gegensatz zum dextralen Liquiñe-Ofqui-System im Süden, wo holozäne, dextrale Blattverschiebungen allgegenwärtig sind, besitzt dieses Störungssystem keine signifikante Blattverschiebungskomponente. Dieser Kontrast entlang der Kordillere fällt mit einer markanten Änderung der Störungsmuster im Forearc zusammen. Im Norden verteilt sich die randparallele Komponente der schrägen Subduktion auf eine breite Zone diffuser Verformung, während sie im Süden entlang einer Intra-arc- und randparallelen Blattverschiebungszone partitioniert auftritt.

Im Küstenbereich werden Struktur- und stratigraphische Daten aus Geländebeobachtungen mit reflektionsseismischen Profilen und Bohrlochmessdaten verbunden, um Information zum Einfluss einer klimatisch-gesteuerten Auffüllung des Grabens auf die Mechanismen und die Kinematik des Randes während des Neogen zu erhalten. Es zeigt sich, dass Forearc-Becken im Segment bei 34–45° S eozäne bis frühpliozäne Dehnung und Subsidenz aufzeigen, denen spätpliozäne und noch aktive Hebung und Verkürzung folgten. Das erste Stadium kann mit tektonischer Erosion infolge hoher Plattenkonvergenzraten und geringerer Grabenauffüllung erklärt werden. Das nachfolgende Stadium hingegen ist mit Akkretionsprozessen zu erklären, die durch geringe Konvergenzraten und gesteigerte Grabenauffüllung nach dem Einsetzen der Patagonischen Vereisung und klimagesteuerter Exhumierung vor etwa 6–5 Ma verursacht wurden. Auf der spätpleistozänen Zeitebene werden seismische Profile mit der Oberflächenentwicklung aus deformierten, ^{14}C -datierten, marinen Terrassen der Isla Santa María integriert und gezeigt dass die Küstenmorphologie und die Segmentation der Oberflächendeformation von Aufschiebungen kontrolliert werden. In diesem Gebiet zeichnet ein Cluster von Mikrobeben eine dieser Störungen, die vermutlich die Plattengrenzfläche erreicht, deutlich nach. Desweiteren zeigen Berechnungen der koseismischen Hebung während des Erdbebens von 1835 mit $M > 8$ nach Aufzeichnungen von Charles Darwin, dass diese aktive Verwerfung mechanisch an die Subduktionszone gekoppelt war und durch das Ereignis von 1835 aktiviert wurde. Diese Erkenntnisse haben grosse Bedeutung für die Abschätzung der seismischen Gefährdung in der Region.

Die gewonnenen Ergebnisse dieser Arbeit unterstreichen den Bedarf an integrierten Untersuchungen der Deformationsprozesse an aktiven Plattenrändern in verschiedenen Zeit- und Raumskalen, ebenso wie die Notwendigkeit, diese mit geomorphologischen, strukturellen und geophysikalischen Datensätzen zu verknüpfen, um einen Beitrag zum Verständnis der gegenwärtigen Verteilung und Ursachen der tektonischen Segmentation sowie der Gefährdungsabschätzung zu leisten.

Resumen

La cadena Andina es el ejemplo tipo de orogénesis causada por subducción de litosfera oceánica bajo continental. Los Andes han sido formados por la subducción de las placas oceánicas de Nazca y Antártica bajo el continente Sudamericano durante al menos los últimos 200 millones de años. Los ambientes tectónicos y climáticos varían marcadamente a lo largo del margen andino, el cual representa un laboratorio natural ideal para el estudio de procesos tectónicos y climáticos, y sus posibles interacciones. La mayor parte de la energía sísmica del planeta es liberada por grandes terremotos en las zonas de subducción; pero los mecanismos de segmentación de la deformación superficial durante y entre estos eventos gigantes no han sido comprendidos en su totalidad. El margen Andino es una zona clave para el estudio de procesos de segmentación sismotectónica debido a su variabilidad bajo condiciones de borde cinemáticas similares.

Este estudio se enfoca en procesos activos sismotectónicos, en las escalas de tiempo Neógeno y Pleistoceno tardío, en la Cordillera Principal y el antearco costero de los Andes del centro sur. En ambas regiones documento la existencia de fallas activas no reconocidas previamente y presento estimaciones de sus tasas de deformación y de su cinemática. Uso éstos datos para abordar procesos fundamentales en la creación de cadenas montañosas como son la partición de la deformación y la segmentación.

En el antearco costero y escala de tiempo Neógeno, integro datos estructurales y estratigráficos obtenidos mediante observaciones de terreno, perfiles sísmicos de reflexión y perforaciones de la industria petrolera para contribuir a la comprensión de la influencia del cambio climático en la mecánica y cinemática del margen. Muestro que las cuencas de antearco en el segmento entre los 34 y 45°S registran extensión y subsidencia entre el Eoceno y Plioceno Inferior seguido de alzamiento y contracción desde el Plioceno Superior hasta el presente. Interpreto el primer estadio causado por erosión tectónica debido a la alta tasa de convergencia entre las placas y ausencia de materiales lubricantes en la fosa. Interpreto el segundo estadio como debido a condiciones acrecionarias causadas por una baja en la tasa de convergencia y a un aumento drástico en el flujo de sedimentos a la fosa, causado por el comienzo de las glaciaciones Patagónicas y la rápida exhumación de éstos desde los ~6-5 Ma. En la escala de tiempo Pleistoceno tardío, integro estructuras interpretadas en perfiles sísmicos con terrazas marinas deformadas datadas mediante radiocarbono en la zona del Golfo de Arauco e Isla Santa María, respectivamente. Muestro que fallas normales invertidas controlan la geomorfología costera y la segmentación de la deformación superficial. También muestro que una agrupación de microsismos alineados iluminan una de éstas fallas inversas, la cual probablemente llega en profundidad hasta la zona interplacas. Uso las medidas de alzamiento cosísmico durante el terremoto $M > 8$ de 1835 tomadas por Charles Darwin para proponer que ésta falla inversa activa se encuentra mecánicamente acoplada con la zona de subducción y que fue gatillada por aquel evento telúrico. Estas observaciones poseen una significativa implicación para el riesgo sísmico en la ciudad de Concepción.

En la Cordillera Principal y escala de tiempo Neógeno, integro observaciones estructurales y estratigráficas de terreno con edades isotópicas publicadas para proponer cuatro fases principales de evolución conjunta en estilo tectónico y volcanismo. Relaciono éstas fases con cambios en la cinemática y geometría de la zona de subducción. En la escala Pleistoceno tardío, integro observaciones de terreno con perfiles sísmicos y batimétricos en la zona del Lago Laja, cerca de la divisoria de aguas de los Andes. Estos datos muestran estructuras extensional activas durante el Holoceno y definen el sistema de fallas Lago Laja, el cual extiende el arco lateralmente a una velocidad media mínima de 1.2 mm/a. El mencionado sistema de fallas carece de una componente significativa en el rumbo, a diferencia del sistema de fallas de Liquiñe-Ofqui, ubicado al sur de la zona. Este contraste en estilo estructural a lo largo del arco y Cordillera Principal coincide con un marcado cambio en la geometría de las estructuras en el antearco, a lo largo de la Península de Arauco. Por lo tanto propongo que a lo largo de la zona de transición de Arauco ocurre un gradiente neto en el grado de partición de la deformación causada por la subducción oblicua. Al norte de Arauco, la componente paralela al margen se distribuye en una zona amplia de deformación mientras que al sur se produce la partición en una zona de falla de rumbo paralela al margen, ubicada a lo largo del arco volcánico.

Estos resultados enfatizan la necesidad de estudiar procesos de deformación a varias escalas temporales y espaciales, además de la integración de datos geomorfológicos, estructurales, y geofísicos para contribuir al entendimiento de las causas de la segmentación tectónica.

Contents

<i>Abstract</i>	i
<i>Zusammenfassung</i>	ii
<i>Resumen</i>	iv
<i>Contents</i>	v
<i>List of figures</i>	vi
<i>List of Tables</i>	vii
<i>Acknowledgements</i>	viii
<i>1. Introduction</i>	1
<i>2. Tectonic setting</i>	2
2.1 Morphotectonic segmentation of the south-central Andes (36–42°S).....	3
2.2 Neogene tectonics and climate in the Central and Patagonian Andes.....	7
<i>3. Neogene tectonic evolution of the Neuquén Andes western flank (37–39°S)</i>	8
3.1 Introduction.....	8
3.2 Tectonic setting.....	8
3.3 Geology of the study area.....	10
3.4 Segmented tectono-stratigraphy and structural evolution.....	13
3.5 Tectonic evolution.....	27
3.6 Discussion: geodynamic implications.....	29
3.7 Conclusions.....	29
<i>4. Inversion of forearc basins in south-central Chile caused by rapid glacial age trench fill</i>	31
4.1 Introduction.....	31
4.2 Tectonic setting of forearc basins in south-central Chile.....	31
4.3 Middle Pliocene forearc basin inversion and uplift.....	32
4.4 Mountain building, glacial denudation and trench fill.....	34
4.5 Discussion.....	34
<i>5. Coastal deformation and great subduction earthquakes, Isla Santa María, Chile (37°S)</i>	37
5.1 Introduction.....	37
5.2 Methods and data sources.....	38
5.3 Regional tectonic and geologic setting.....	38
5.4 Historic earthquakes.....	43
5.5 Stratigraphy of Isla Santa María.....	44
5.6 Geomorphology of Isla Santa María.....	48
5.7 Paleogeography of the Santa María Formation.....	48
5.9 Normal faulting and syntectonic sedimentation.....	51
5.10 Late Quaternary deformation rates of isla santa María.....	51
5.11 Active shortening and basin Inversion structures.....	52
5.12 Discussion.....	56
5.13 Conclusions.....	57
<i>6. Incipient axial collapse of the Main Cordillera and strain partitioning gradient between the Central and Patagonian Andes, Lago Laja, Chile</i>	59
6.1 Introduction.....	59
6.2 Methods.....	61
6.3 Regional tectonic and geologic setting.....	61
6.4 Study area: Lago Laja.....	62
6.5 The Lago Laja fault system (LLFS).....	65
6.6 Soft-sediment deformation structures adjacent to the LLFS: paleoseismic significance.....	70

6.7 Quaternary extensional structures in the Laja region	73
6.8 Deformation rates of the Lago Laja fault system	73
6.9 Quaternary shortening along the foothills of the Main Cordillera	73
6.10 Discussion	76
6.11 Conclusions	80
7. Conclusions	81
8. Bibliography	83
Appendix A – Inversion of forearc basins (Chapter 4)	94
Appendix B – Coastal deformation and subduction earthquakes (Chapter 5)	100

List of Figures

Figure 2.1: Topography and major tectonic elements of the Central, Southern, and Austral Andes	4
Figure 2.2: Morphotectonic units and major faults of the south-central Andes	5
Figure 2.3: Compiled geologic map of the south-central Andes of Chile and Argentina (36-42°S)	5
Figure 2.4: Time-space diagram of the geologic units from the south-central Andes	6
Figure 3.1: Regional location map, morphotectonic units, and faults of the Main Cordillera	9
Figure 3.2: Generalized stratigraphic chart of the Main Cordillera	11
Figure 3.3: Simplified geologic map of the western flank of the Neuquén Andes	12
Figure 3.4: Geological cross section along the Ñuble National Park	14
Figure 3.5: View of the Huemules and Calabocillo thrusts	15
Figure 3.6: View of the Bejar normal fault and Toro graben	15
Figure 3.7: Geology of the Lago de la Laja Quaternary fault system	16
Figure 3.8: Offshore 3.5 kHz seismic-reflection profile across the Lago Laja fault system	17
Figure 3.9: View of Holocene pyroclastic deposits affected by normal faults	18
Figure 3.10: Oblique air photo of the Callaqui-Copahue-Mandolegüe lineament	19
Figure 3.11: Late Quaternary normal faulting at El Barco area	21
Figure 3.12: Geological cross section of the upper Bio-Bio River	22
Figure 3.13: View of the Pino Seco thrust	23
Figure 3.14: Syntectonic deposits of the Mitrauquén Formation	23
Figure 3.15: Quaternary deformation in the Lonquimay transtensional system	25
Figure 3.16: View of Holocene pyroclastic and alluvial deposits affected by normal faults	26
Figure 3.17: Holocene volcanism and tectonics at the Llaima volcano	26
Figure 3.18: Series of maps summarizing the Neogene evolution of the western Neuquén Andes	28
Figure 4.1: Tectonic setting of the south-central Chile margin	32
Figure 4.2: Line drawing of ENAP reflection-seismic profiles	33
Figure 4.3: Late Pliocene-Pleistocene near-shore syntectonic sequence at Coi-Coi, 38.5°S	34
Figure 4.4: Age of the Nazca plate at the trench and Neogene uplift rates along the coast of Chile	35
Figure 4.5: Climate and tectonics of the Patagonian Andes	36
Figure 5.1: Seismotectonic segments, historical earthquakes, and general section of the margin	39
Figure 5.2: Regional geology, structures, and geophysical data sets of the Arauco-Concepción region	40
Figure 5.3: Geologic and geomorphic map, and shaded-relief DEM of Isla Santa María	41
Figure 5.4: View of uplifted abrasion platforms during 1751 and 1835 earthquakes	46
Figure 5.5: Aerial view showing Tertiary and late Pleistocene units	47
Figure 5.6: Aerial view showing tilted Pleistocene surface and emerged Holocene strandlines	47
Figure 5.7: Topographic asymmetry of the upper surface of Isla Santa María	49
Figure 5.8: Contour map of the base of the Santa María Formation and N-S profile	50
Figure 5.9: Uplift rates of Isla Santa María derived from calibrated AMS ¹⁴ C ages	51
Figure 5.10: Time-migrated seismic reflection profile ENAP-017	53
Figure 5.11: Time-migrated seismic reflection profile ENAP-016	54
Figure 5.12: Time-migrated seismic reflection profile ENAP-259	55

Figure 5.13: Reprocessed, time-migrated seismic reflection profile ENAP-257.....	55
Figure 5.14: Schematic profile of Isla Santa María.....	56
Figure 6.1: Location map with main neotectonic structures and Andean segments.....	60
Figure 6.2: Regional geologic map of the Main Cordillera.....	62
Figure 6.3: Geologic map of Lago Laja, shaded DEM, seismic profiles, and Quaternary faults.....	64
Figure 6.4: Panoramic view showing the dam of Lago Laja.....	65
Figure 6.5: Reflection-seismic profile Laja 14 illustrating the central part of Lago Laja.....	65
Figure 6.6: Structures in the northern segment of the Lago Laja fault system.....	67
Figure 6.7: Structures in the central segment of the Lago Laja fault system.....	68
Figure 6.8: Extract of reflection-seismic profile Laja 04 showing a hemigraben.....	69
Figure 6.9: DEM and Map of the Antuco volcano and southern segment of the Lago Laja fault system.....	70
Figure 6.10: Soft-sediment deformation structures adjacent to the Lago Laja fault system.....	71
Figure 6.11: View of the Sierra Velluda volcano and normal fault.....	74
Figure 6.12: Map and DEM of the Huépil structure along the western foothills of the Main Cordillera.....	77
Figure 6.13: Map and cross-section of Quaternary structures and strain partitioning gradient.....	79
Figure A1: Map of forearc basins and location of seismic-reflection profiles and boreholes.....	94
Figure A2: Unconformity between lower bathyal siltstones and near-shore sandstones.....	95
Figure A3: Eocene and Miocene-early Pliocene syntectonic deposition across normal faults.....	95
Figure A4: ENAP reflection-seismic profiles 28, 17, 18, and 192.....	96
Figure B1: Grain-size distribution curves comparing present and Pleistocene marine and eolian sands.....	101
Figure B3: View of shore facies of the marine unit north of Cadenas Peninsula.....	101
Figure B2: Field view and stratigraphic sections of the Santa María Formation.....	102
Figure B4: View of the eolian unit at Cadenas Peninsula.....	103
Figure B5: View of an erosive channel incised in the Santa María Formation.....	103
Figure B6: Oblique air photo to the east showing the northern normal fault.....	104
Figure B7: Structures in the central graben system.....	105
Figure B8: Oblique air photo and interpretation of the southern normal growth fault.....	107
Figure B9: DEM showing location of profiles used to calculate tilting rates.....	108

List of Tables

Table 2.1: Description and age range of the geologic units.....	6
Table 5.1: Radiocarbon ages of the Santa María Formation.....	42
Table 6.1: Field criteria for the relation of soft-sediment structures to seismites.....	72
Table 6.2: Holocene slip rates of the Lago Laja fault system.....	75
Table B1: Field data and tilt rates calculated for three reference surfaces along eight profiles.....	106
Table B2: Average tilt rates and errors for the three reference surfaces and the entire island.....	108

Acknowledgements

Many people have contributed to this project among others from Chile, Germany, Argentina, and Belgium; It will be difficult to include them all in these lines. Helmut Echter, beside his guidance and scientific advice, became a good friend over the years. I thank him for his continuous encouragement and support and for giving me the freedom to search my own research activities. I thank Manfred Strecker first for giving me the possibility to study and live in Germany, for always supporting my parallel research lines and, when necessary, for also keeping me focused. Besides his teaching guidance, I acknowledge his friendship and positiveness. Thanks to Onno Oncken and the many colleagues and friends at GFZ who besides supporting my research shared pleasant times. Helga Kemnitz helped me continuously over the past years with the German language and many administrative formalities.

Special thanks go to my friend and project colleague Bodo Bookhagen for sharing very nice field seasons and discussions about data and interpretations. Marcos Moreno, Julius Jara, Hugo Muñoz, and Matías Sanchez helped and made fieldwork very pleasant – gracias compadres! The hospitality of Rut, Don Doro, and Señora Patricia enhanced the joyce of fieldwork at Isla Santa María. Many ideas and research aims during the early stages of this study were acquired through long discussions and fieldwork with Andrés Folguera and Matthias Rosenau, thank you.

My friends Marcelo González and Pablo Zenteno provided continuous support and data in Chile. Lisandro Rojas, Juan Pablo Radic, and Constantino Mpodozis supplied seismic data from ENAP (Empresa Nacional del Petróleo, Chile), permission to publish them as well as constructive discussion on the tectonics of the Southern Andes. Marc de Batist and François Charlet (RCMG, University of Gent, Belgium) shared their seismic lines from Lago Laja and welcomed me to work with the data in Gent. Bukhard Scharf and Olaf Buettner (UFZ Leipzig) kindly shared their bathymetry from Lago Laja. Mirjam Bohm and Günter Asch provided the ISSA seismicity. All these data sets were a major source for this thesis and I thank all of them for their help.

Financial support for this study initially came from Manfred Strecker's IQN project at Universität Potsdam, from Onno Oncken's Leibniz funds at GFZ, and finally most came from the TIPTEQ project founded by the German Ministry for Education and Research (BMBF) and the German Science Foundation (DFG). Support during fieldwork to me and to students from the Universidad de Concepción was provided as well from the Collaborative Research Center SFB-267 founded by the DFG.

The unconditional support and encouragement of María Teresa and Jorge, my parents, guided me towards this thesis and was key to complete my memoria. Finally, life in Berlin wouldn't have been and will never be the same without the company and love of Amerika.

1. Introduction

Subduction zones are probably the most dynamic environments on Earth. These convergent margins are shaped by the interaction between intense tectonic, geomorphic, and climatic processes, which develop complex interactions over various temporal and spatial scales. The understanding of these processes has recently increased due to the development of new methods for age determination, analysis of digital topography, space geodesy, and remote sensing among others. With respect to the tectonic and geomorphic evolution of convergent margins, I have studied the interplay between tectonics and surface processes at various temporal and spatial scales at the south-central Chile subduction margin. In addition, I have analyzed the response of this sector of the plate margin concerning changes in climatic and tectonic boundary conditions that are ultimately responsible for the evolution of the landscape in this tectonically active region.

Most of Earth's seismic energy is released by large megathrust earthquakes in subduction zones, like the giant 1960, M_w 9.5 event in south-central Chile (e.g., Kanamori, 1977). However, the link between subduction earthquakes and surface deformation, and particularly the processes that lead to segmentation of surface deformation during and between these earthquakes are not well understood yet (e.g., Briggs et al., 2006). A link between the occurrence of forearc basins above the seismogenic zone and peaks in slip distribution on the plate interface during megathrust earthquakes has been proposed, based on a worldwide correlation (Wells et al., 2003), numerical simulations (Fuller et al., 2006), and improvements of the critical taper theory (Wang and Hu, 2006). These authors suggested that steady sedimentation in forearc basins stabilizes the wedge, preventing internal deformation. In addition, they concluded that maximum slip during megathrust earthquakes will tend to occur where the wedge is more stable. Sedimentation in forearc basins depends on the kinematics of the wedge and on the local climate and relief of the hinterland, which control sediment availability and transport to the forearc. In this study I will show that forearc basins in south-central Chile are internally deformed by crustal-scale reverse faults, and that some of these structures appear to be mechanically coupled with the megathrust.

Recent progress in the integration of structural, stratigraphic, and geophysical data as well as results from ocean drilling have shown that erosion of the continental plate's base will lead to extension and subsidence in the forearc (e.g., von Huene and Scholl, 1991; Clift and Vannucchi, 2004; von Huene et al., 2004). In turn, similar data sets from accretionary margins—sites of continental growth—show continuous compression in the forearc basins (e.g., Barnes et al., 2002; Bruhn and Haeussler, 2006). All these observations demonstrate that in order to gain insight into earthquake-segmentation processes, the long-term tectonic history and its control on the present-day architecture of the margin has to be understood first. Based on these previous studies, I address processes of seismotectonic segmentation of the Chilean subduction margin over various temporal and spatial scales.

The size of an earthquake depends on the area of fault rupture and on the amount of slip (e.g., Kanamori, 1983). Consequently, a fundamental task for the assessment of seismic hazards in such environments entails detailed mapping of maximum fault-rupture areas, fault segmentation, determination of the kinematics, and slip rates (e.g., Wells and Coppersmith, 1994). Against the backdrop of these important issues, I document the existence of previously unrecognized faults in south-central Chile's forearc and intra-arc regions and present maps and new data on deformations rates and fault kinematics.

Chapter 2 introduces the regional tectonic setting of the Andean margin, the morphotectonic segmentation of the south-central Andes and a brief comparison between the Neogene tectonic and climatic evolution of the Central and Southern or Patagonian Andes. The following four chapters are devoted to specific themes in two regions. First, chapters 3 and 4 focus on regional-scale processes in the high Andes and coastal domain, respectively. Second, chapters 5 and 6 center on local-scale processes and detailed structure of two key areas of the forearc and Main Cordillera domains, respectively. Chapter 7 integrates the main conclusions drawn from this study and addresses the importance of this work.

Particularly, in chapter 3, I integrate new field observations with the previously available data to summarize the tectonic evolution of a segment of the high Andes during the Neogene Period. I differentiate four tectonic phases and discuss the causes for the related changes in the kinematics of the orogen. Furthermore, I present new data on active faults and discuss their relation with the architecture of the volcanic arc. Apart from the academic interest, these data

could serve as a base for exploration of geothermal resources in the region and the general understanding of mountain building processes in subduction margins.

Various recent studies have addressed feedbacks between climate change and tectonic deformation over various temporal and spatial scales (e.g., Molnar and England, 1990; England and Molnar, 1990; Raymo and Ruddiman, 1992; Molnar et al., 1993; Willett, 1999; Hilley and Strecker, 2004; Thiede et al., 2005). In Chapter 4, I explore this relation, particularly in addressing the relation between uplift of the Patagonian Andes, onset of glacial denudation and the response of the plate interface and forearc wedge to the consequent increased sediment flux to the trench. I propose that similarities in the Neogene sedimentary record and structural evolution of several forearc basins along ~1200 km of the margin are indeed linked to the climate-induced filling of the south Chile trench by glacial-derived sediments.

Chapter 5 documents the existence of crustal-scale active faults in the forearc region using field data, seismic reflection profiles, and shallow microseismicity. Furthermore, I integrate evidence from deformed marine terraces and the local coastal geomorphology with data on uplift during historic earthquakes to propose that uplift and regional warping were accommodated by these crustal-scale faults, which in turn were triggered by past subduction earthquakes. Triggering of these faults during future earthquakes would localize surface deformation and strong ground motion and may help stop further rupture propagation along the subduction interface. I present evidence supporting that these crustal faults are inverted structure, which first developed during Eocene extension and probably already before. This emphasizes the role of inherited crustal heterogeneities in guiding active plate-boundary deformation and underscores the need to study tectonic processes at various time scales in order to understand the present deformation field, its segmentation, and future behavior.

One unknown aspect of Andean geology in the Main Cordillera has been the degree and style of Quaternary tectonic fault activity. In Chapter 6, I integrate geologic and geomorphic field observations with off-shore lake seismic reflection and bathymetric profiles to document the existence of an active fault system in this region. I present a map of the fault system and of its segments, estimates of deformation rates, and discuss potential hazards. Furthermore, I combine the regional kinematics of active faults in the intra-arc and forearc regions to address plausible causes for changes in the degree of strain partitioning along obliquely convergent margins.

With the exception of the first two chapters and Chapter 7 (Conclusions), each of the chapters of this thesis has been published in peer-reviewed journals.

The maps and time-space diagram presented in Chapter 2 (Figures 2.1, 2.2, 2.3) are published in “Morphotectonic and geologic digital map compilations of the south-central Andes (36°–42°S)” by Daniel Melnick and Helmut Echtler, in “*The Andes – Active Subduction Orography*”, edited by O. Oncken, G. Chong, G. Franz, P. Giese, H.J. Götze, V.A. Ramos, M.R. Strecker, and P. Wigger”, *Frontiers in Earth Sciences*, vol. 1, p. 565–568, Springer-Verlag, Berlin-Heidelberg-New York.

Chapter 3 (“Neogene tectonic evolution of the Neuquén Andes western flank (37–39°S)”) by Daniel Melnick, Matthias Rosenau, Andrés Folguera, and Helmut Echtler has been published in “*Evolution of an Andean margin: A tectonic and magmatic view from the Andes to the Neuquén Basin (35°–39°S lat)*”, edited by S.M. Kay and V.A. Ramos”, *Geological Society of America Special Paper*, vol. 407, p. 73–95, doi:10.1130/2006.2407(04).

Chapter 4 (“Inversion of forearc basins in south-central Chile caused by rapid glacial age trench fill”) by Daniel Melnick and Helmut Echtler has been published in *Geology*, vol. 34, no. 9, p. 709–712, doi:10.1130/G22440.1.

Chapter 5 (“Coastal deformation and great subduction earthquakes, Isla Santa María, Chile (37°S)”) by Daniel Melnick, Bodo Bookhagen, Helmut Echtler, and Manfred Strecker has been published in *Geological Society of America Bulletin*, vol. 118, no. 11, p. 1463–1480, doi:10.1130/B25865.1.

Chapter 6 (“Incipient axial collapse of the Main Cordillera and strain partitioning gradient between the Central and Patagonian Andes, Lago Laja, Chile”) by Daniel Melnick, François Charlet, Helmut Echtler, and Marc De Batist has been published in *Tectonics*, vol. 25, no. 5, p. TC5004, doi:10.1029/2005TC001918.

2. Tectonic setting

The Andean margin is the type-orogen related to the subduction of oceanic under continental lithosphere. This over 8000-km-long mountain belt has resulted from subduction of the Nazca and Antarctic oceanic plates below the South American continent (Figure 2.1). Ongoing subduction over the past ~200 m.y. has generated a mountain range that reaches 7 km high and 800 km wide (e.g., Mpodozis and Ramos, 1989) (Figure 2.1). Convergence of the Nazca and South American plates occurs at a present rate of 6.6 cm/yr with an azimuth of 078° as calculated from modeling of Global Positioning System data (Angermann et al., 1999; Kendrick et al., 2003). Overall plate convergence velocity along the Andes has slowed about 80% over the past 20 m.y., as derived from oceanic magnetic anomalies (De Mets et al., 1994; Somoza, 1998).

Even though the rate and direction of plate convergence is, and has been similar along the Andes of Chile and Argentina, the orogen is strongly segmented in terms of topography, crustal thickness, width, total shortening, style of active deformation, and seismic moment release (e.g., Lomnitz, 1970, 2004; Mpodozis and Ramos, 1989; Dewey and Lamb, 1992; Kley et al., 1999; Montgomery et al., 2002; Tassara et al., 2006). The causes of this segmentation have been the subject of debate over the past decades; however, the major segments of the Andes coincide with longitudinal changes in dip, age, and presence of bathymetric anomalies of the oceanic Nazca plate (Figure 2.1), as first noticed by Jordan et al. (1983) and further developed by Yáñez and Cembrano (2004). Nevertheless, some of the first-order discontinuities of the Andean orogenic system are not correlated with lower plate anomalies but with the nature and segmentation of the pre-Andean continental basement (e.g., Mpodozis and Ramos, 1989; Ramos, 1999; Kley and Monaldi, 2002). Because subduction, and consequently deformation along the western margin of the South American plate have been ongoing over at least 200 m.y., structures have been repeatedly reactivated under changing stress fields resulting in heterogeneous fabrics (e.g., Allmendinger et al., 1983, 1997; Marrett and Strecker, 2000).

The Andes have been subdivided by various authors mainly based on: distribution and geochemistry of Quaternary volcanism (e.g., Stern, 2004); long-term tectonic evolution (e.g., Jordan et al., 1983; Mpodozis and Ramos, 1989); distribution and style of active deformation (e.g., Dewey and Lamb, 1992), configuration of the pre-Andine basement (e.g., Ramos, 1999), variations in elastic thickness (Tassara and Yáñez, 2003), and lithospheric-scale structure (Tassara et al., 2006). The major along-strike segment boundaries of the Central and Southern Andes occur at 33°S, with the southern end of the flat-slab segment, collision of the Juan Fernández hot-spot chain, and northern end of the Southern Volcanic Zone; at 38°S, between the Southern Central and the Patagonian Andes with changes in kinematics, topography, structural style of active deformation, and degree of strain partitioning; and at 46.5°S, between the Patagonian and Austral Andes with collision of the Chile spreading center and southern end of the Southern Volcanic Zone (Figure 2.1). In this study, I focus on the southern Central Andes and northern Patagonian Andes of Chile, with particular emphasis on the forearc and intra-arc regions (Figure 2.2).

2.1 *Morphotectonic segmentation of the south-central Andes (36-42°S)*

The south-central Andes of Chile and western Argentina can be subdivided into the following main six morphotectonic units, based on topography, morphology, style of active deformation, and Mesozoic-Cenozoic tectonic evolution (Melnick and Echtler, 2006b): (1) Coastal Platform; (2) Coastal Cordillera; (3) Central Depression; (4) Main Cordillera; (5) Neogene back-arc basins; (6) Neuquén Mesozoic embayment and Cenozoic foreland Basin; and (7) extra-Andine massifs (Figures 2.2). These morphotectonic units can be considered as the continental-scale subdivisions of the Andean margin, first described by naturalists like Charles Darwin and Ignacy Domeyko (Darwin 1839; Domeyko 1846) and whose tectonic significance was further developed among others by Brügger (1950), Plafker and Savage (1970), Gansser (1973), Jordan et al. (1983), and Mpodozis and Ramos (1989). I focus on the Coastal Platform, which consists of uplifted Cenozoic marine and continental sedimentary sequences, and on the Main Cordillera comprising a Meso-Cenozoic magmatic arc and Neogene intra-arc volcano-sedimentary basins (Figures 2.3 and 2.4).

2. Tectonic setting

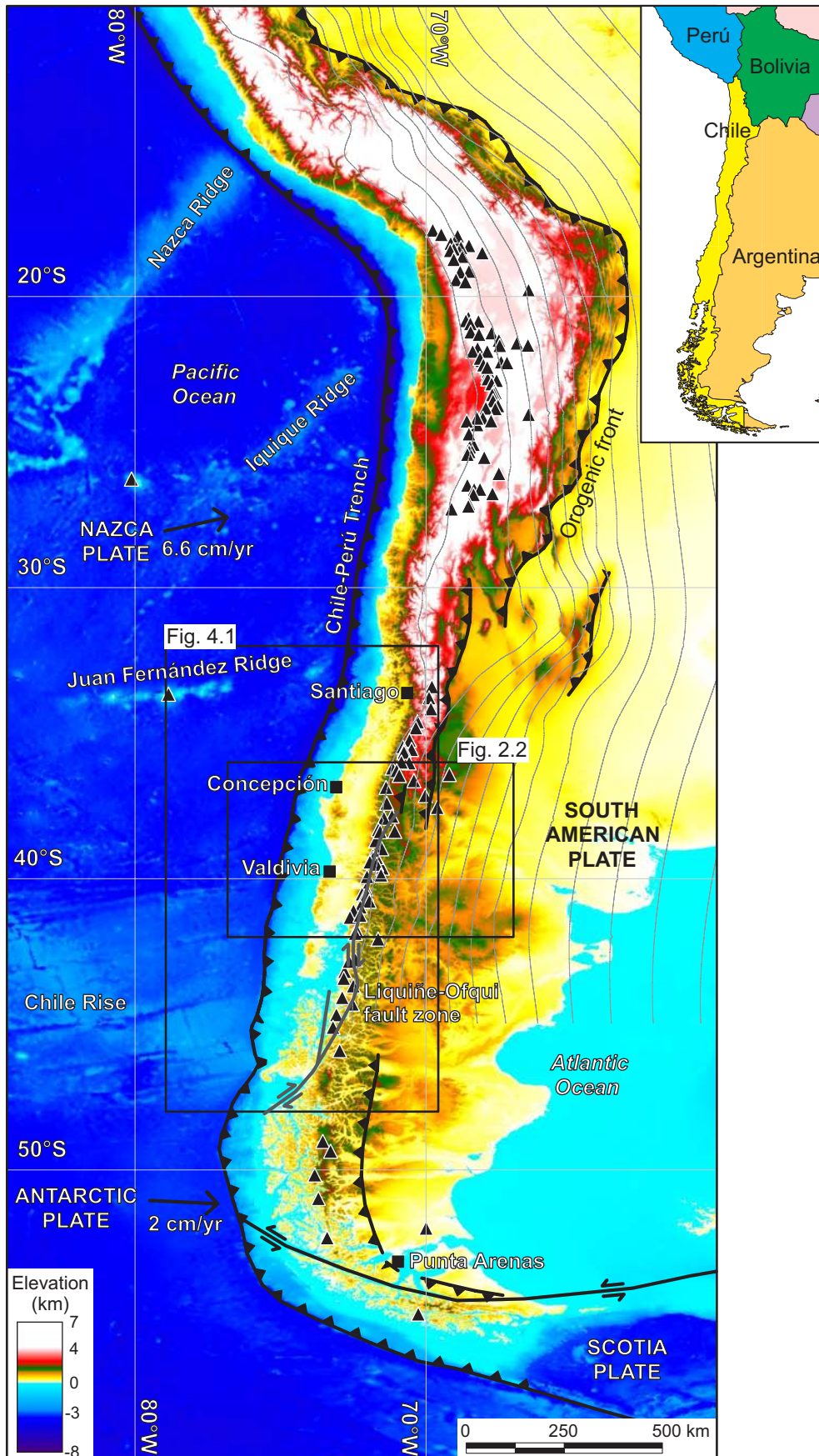


Figure 2.1: Topography and major tectonic elements of the Central, Southern, and Austral Andes. Triangles denote Holocene volcanic centers. Light grey lines are 100-km contours to the top of the subducted slab from the Nazca plate (modified after Tassara et al., 2006).

Scientific Technical Report STR 07/01

DOI: 10.2312/GFZ.b103-07012

2. Tectonic setting

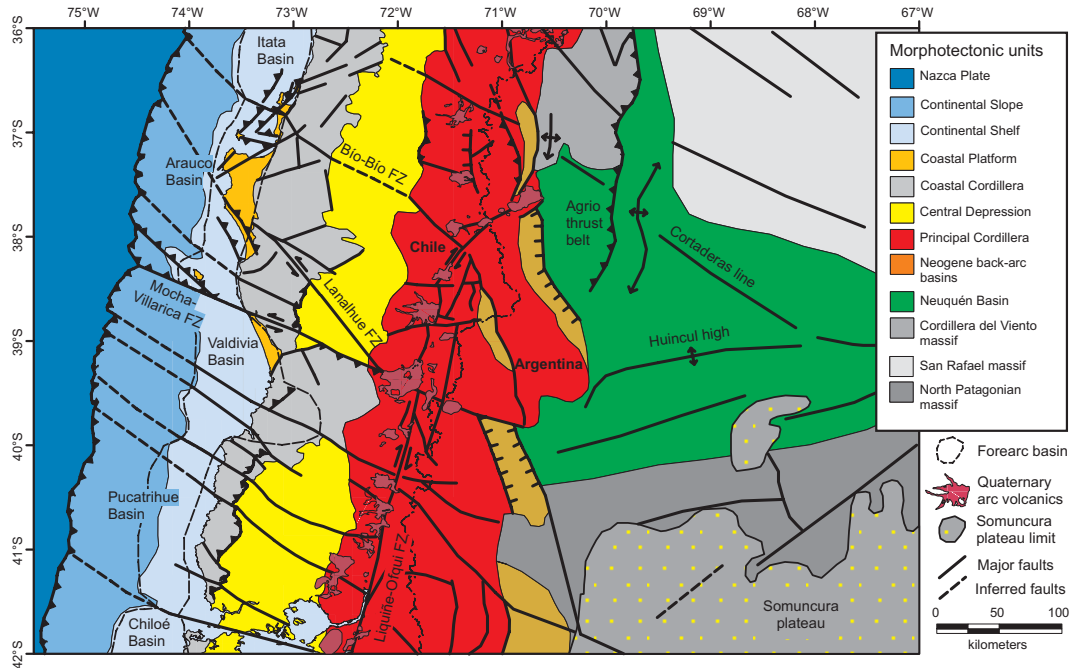


Figure 2.2: Morphotectonic units and major faults of the south-central Andes.

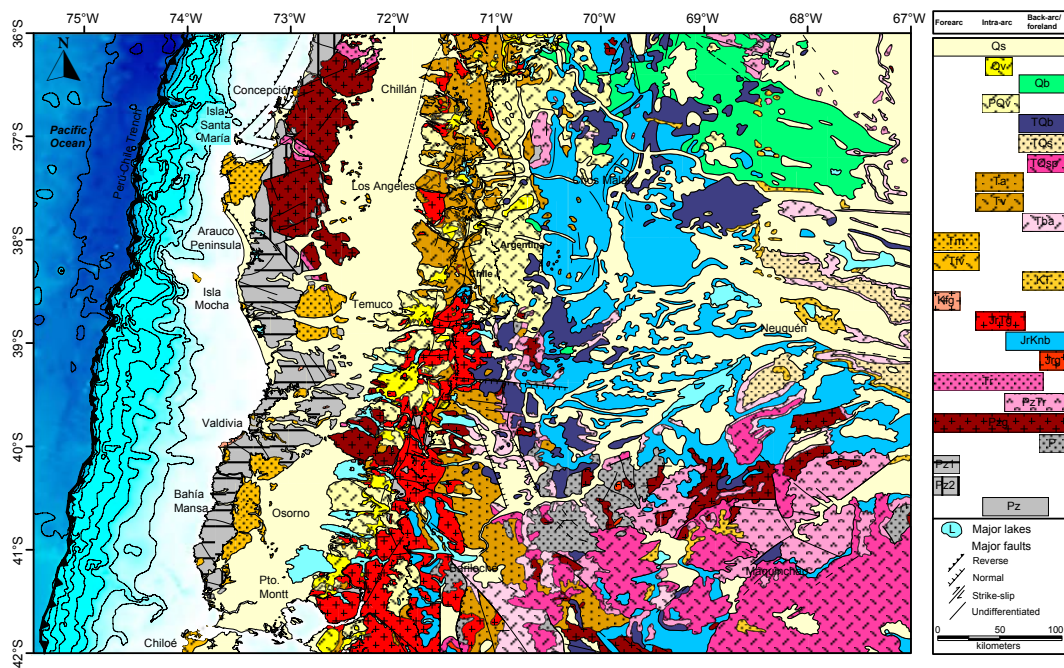


Figure 2.3: Geologic map of the south-central Andes of Chile and Argentina (36-42°S).

The major fault zones of the south-central Andes are depicted in the morphotectonic and geologic maps (Figures 2.2 and 2.3). The Main Cordillera is dominated by the Lique-Ofqui fault zone (e.g., Hervé, 1994; Lavenu and Cembrano, 1999; Rosenau et al., 2006), an arc-parallel strike-slip system, which extends along the Patagonian Andes' volcanic arc. Margin-oblique faults, like the Mocha-Villarica and Lanalhue fault zones, segment the entire margin from the Main Cordillera to the trench. These structures originated before Andean contraction (e.g., Mpodozis and Ramos, 1989; Glodny et al., 2006), and have been reactivated over the past ~200 m.y. At present, these northwest-striking faults influence the morphotectonic segmentation of the forearc region and offset the trace of the trench (Figure 2.2).

2. Tectonic setting

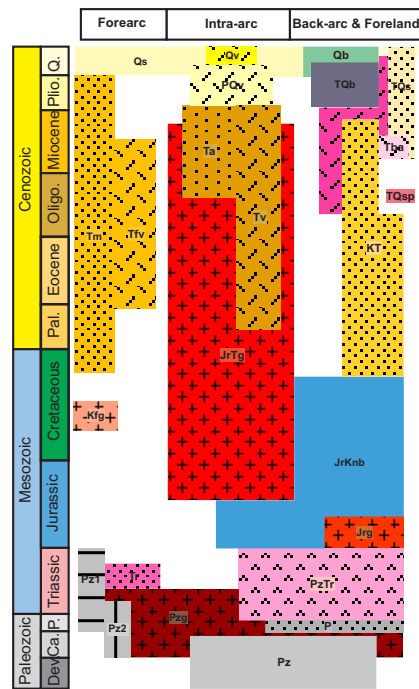


Figure 2.4: Time-space diagram of the geologic units exposed in the south-central Andes.

Code	Description	Age range
Qs	Undifferentiated sediments	Quaternary
Qv	Volcanic arc edifices	Quaternary
Qb	Back-arc plateau volcanics	Quaternary
PQv	Volcanic arc edifices and plateaus	Pliocene-Pleistocene
TQb	Back-arc volcanics	Tertiary-Quaternary
TQs	Foreland synorogenic conglomerates	Tertiary-Quaternary
TQsp	Somuncura plateau volcanics	Oligocene-Quaternary
Ta	Sedimentary intra-arc basins	Oligocene-Miocene
Tv	Volcanic intra-arc basins	Paleocene-Miocene
Tba	Back-arc volcanics	Miocene
Tm	Marine and continental forearc basins	Late Cretaceous-Pliocene
Tfv	Volcanic and continental forearc basins	Oligocene-Miocene
KT	Neuquén Basin marine and continental foreland sequences	Late Cretaceous-Tertiary
Kfg	Forearc intrusions	Middle Cretaceous
JrTg	North Patagonian Batholith magmatic arc root	Jurassic-Miocene
JrKnb	Neuquén Basin marine, continental, and volcanic sequences	Jurassic-Cretaceous
Jrg	Patagonian intrusions	Jurassic
Tr	Rift basins marine, continental, and volcanic sequences	Triassic
PzTr	Choyoi group large igneous province	Permian-Triassic
Pzg	Coastal Batholith and undifferentiated intrusions	Paleozoic-early Triassic
Pz	Metasedimentary Neuquén basement	Paleozoic
Pz1	Western Series high pressure metasediments and ultramafics	Permian-Triassic
Pz2	Eastern series high temperature metasediments	Carboniferous-Triassic
P	North Patagonian massif metasediments	Permian

Table 2.1: Description and age range of the geologic units depicted in Figures 2.3 and 2.4.

2.2 Neogene tectonics and climate in the Central and Patagonian Andes

Major tectonic, topographic, and climatic changes have occurred throughout the Neogene Period in the Andes—the past 23 m.y. Although the overall plate convergence rate has decreased ~80 % during the Neogene (Somoza, 1998; Kendrick et al., 2003), the westward drift of South America with respect to the stable hot spot reference frame has increased ~40 % over the same period (Silver et al., 1998). Paleo-elevation data and syncontractional deposits show continuous surface uplift and shortening of the Central Andean Altiplano-Puna plateau during at least the Neogene (e.g., Allmendinger et al., 1997; Elger et al., 2005; Garzzone et al., 2006; Oncken et al., 2006). In contrast, the presence of marine and continental extensional basins in the south-central Andes suggests low elevations until ~18-16 Ma south of 33°S (Jordan et al., 2001), and only syncontractional sedimentation and surface uplift between ~16 and 6 Ma (e.g., Giambiagi et al., 2003; Melnick et al., 2006a). Paleo-elevation data are consistent with >1 km of surface uplift and establishment of the present orographic barrier in the Southern Andes at ~16-14 Ma (Blisniuk et al., 2005). Thermochronological data also suggest the onset of exhumation in the Patagonian Andes at ~16 to 10 Ma, and an acceleration at ~7 Ma (Thomson, 2002; Adriasola et al., 2006). Since the latest Miocene, plate convergence obliquity has continuously increased along the Chile margin (Somoza, 1998) leading to strain partitioning and development of the Liquiñe-Ofqui strike-slip fault zone along the volcanic arc (e.g., Dewey and Lamb, 1992; Hervé, 1994; Lavenu and Cembrano, 1999). Ages of syntectonic minerals in mylonitic shear zones of the Liquiñe-Ofqui system indicate transpressional deformation at ~5-3 Ma (Cembrano et al., 2002) and neotectonic studies show ongoing dextral transpression and transtension in the southern (46-39.5°S) and northern (39.5-38°S) segments of the fault system, respectively (e.g., Rosenau et al., 2006; Melnick et al., 2006a).

Various climate proxies show significant global cooling starting at ~15 Ma (Zachos et al., 2002; Lear et al., 2001) and the onset of Patagonian glaciations between 7 and 5 Ma (Mercer and Sutter, 1982; Rabassa et al., 2005). Because topographic relief in the Patagonian Andes was high by ~7 Ma and precipitations must have been elevated due to the fact that the southern hemisphere westerlies impinged on the western flank of the orogen, glacial denudation and fluvial transport led to increased sediment flux resulting in high trench sedimentation rates of 0.3-1 mm/yr since Pliocene time and over 2 km of sediments filling the trench at present (e.g., Bangs and Cande, 1997; Molnar and Cane, 2002; Kilian and Behrmann, 2003). In contrast, the orographic shadow formed by continuous uplift of the Central Andes led to increased aridity over the past ~10 Ma and consequently low sediment flux resulting in trench fill thicknesses below 0.5 km (e.g., Yáñez et al., 2001; Hartley, 2003). This marked contrast in trench fill thicknesses between the Central and Patagonian Andes is mainly due to differences in precipitation but also enhanced by the stationary position of the Juan Fernández Ridge over the past ~10 m.y. (Figure 2.1). The Juan Fernández Ridge is a sea-mount chain, which forms a bathymetric barrier that blocks sediment transport to the north (Bangs and Cande, 1997; Yáñez et al., 2001). Lamb and Davis (2003) and Lamb (2006) proposed that elevated shear stresses caused by protracted trench-sediment starvation led to the uplift and support of the ~4-km-high Central Andean Altiplano-Puna plateau, while to the south lubrication of the plate interface by trench sediments has impeded the support of >2-km-high mountains.

3. Neogene tectonic evolution of the Neuquén Andes western flank (37–39°S)

Abstract

This paper integrates new field observations to summarize the evolution of the 37–39°S segment of the Andean margin during the Neogene period. The western Neuquén Andes represent a transitional segment between the high, broad Central Andes and the low, narrow Patagonian Andes. The Main Cordillera at this latitude was uplifted between 11 and 6 Ma. Since then, extension and transtension has dominated the area. South of 38°S, deformation concentrates along the Liquiñe-Ofqui fault zone, a crustal-scale dextral strike-slip system that accommodates part of the margin-parallel component of oblique subduction. The architecture of the volcanic arc is strongly controlled by this fault zone. We differentiate four main tectonic phases: (1) late Oligocene–middle Miocene extension and development of a segmented intra-arc continental rift basin and broad volcanic zone; (2) late Miocene shortening, resulting in uplift, exhumation, and inversion of the former basins and a volcanic gap in the Main Cordillera; (3) Pliocene–early Pleistocene extension of the orogenic structure, reestablishment of the volcanic arc, and transtension along the intra-arc zone; and (4) late Pleistocene–Holocene narrowing of the arc and localized extension-transtension along the axial intra-arc zone. In the Central Andes, shortening has been more or less continuous since the Miocene, whereas in the Neuquén Andes, shortening stopped at ca. 6 Ma, probably related to the increase of the slab angle triggering the extension of the former orogenic structure and the onset of arc-parallel strike-slip faulting. The episodic evolution and migration of volcanism are related to changes in dip of the subducting plate.

3.1 Introduction

Along-strike segmentation of convergent margin systems and associated mountain chains has been described worldwide (e.g., Fitch, 1972; Bird, 2003). The Andean convergent margin extends for ~4000 km, with a significant along-strike segmentation of its mountain belt at different scales in time and space (e.g., Gansser, 1973; Jordan et al., 1983; Mpodozis and Ramos, 1990; Dewey and Lamb, 1992; Hervé, 1994; Allmendinger et al., 1997; Jordan et al., 1997; Kley et al., 1999; Lamb and Davis, 2003). Compressional deformation, induced by the convergence between the Nazca and South American plates, is generally accepted as the main driving force that formed the actual Andean orogen, but the timing and onset of deformation remain poorly constrained in some segments of this active margin system.

The Neuquén Andes of south-central Chile and Argentina (Figure 3.1) record an episodic history of compressional, extensional, and strike-slip tectonic phases and related magmatic activity during the late Cenozoic, contrasting with the Central and Austral Andes, where compression has been more or less steady during this period.

This paper integrates new field observations with previous geochronological, stratigraphic, sedimentological, and structural data, enriched by interpretation of digital elevation models and remote-sensing images, to analyze the timing, styles, and distribution of deformation and its structural control on Pliocene-Quaternary volcanism in the western flank of the Chilean Neuquén Andes since the late Miocene.

3.2 Tectonic setting

The Neuquén Andes between 37°S and 39°S represent a transitional domain between the high (>4 km mean elevation) and broad (up to 800 km) Central Andes to the low (mean elevation <1 km) and narrow (~300 km) Patagonian Andes. The Central Andes, north of 34°S reflect differential crustal thickening of up to ~70 km, primarily due to shortening since the Miocene (e.g., Isacks, 1988; Allmendinger et al., 1997; Jordan et al., 1997; Godoy et al., 1999; Giambiagi et al., 2003) and ongoing contractional deformation along the eastern foothills (Cortés et al., 1999). South of 38°S, the Patagonian Andes have a crustal thickness of ~40 km (Bohm et al., 2002; Lüth et al., 2003), and no active foreland fold-and-thrust belt has been recognized. Pliocene to Holocene

deformation has been localized in the intra-arc zone, which is controlled by the Liquiñe-Ofqui fault zone (e.g., Hervé, 1976; Lavenu and Cembrano, 1999).

The subducting Nazca plate beneath the Neuquén Andes consists of ~25- to 35-m.y.-old oceanic crust (Tebbens and Cande, 1997). The Nazca–South American plate convergence rate is currently 66 mm/yr, as determined by modeling of global positioning system (GPS) data (Angermann et al., 1999), and ~80 mm/yr averaged over the last 5 m.y. (Somoza, 1998). Major along-strike changes in Andean morphotectonic segments and their tectonic evolution have been attributed to variations in the geometry and physical properties of the downgoing plate (e.g., Jordan et al., 1983; Yañez et al., 2002). In the Neuquén Andes segment, substantial changes in the lower plate occur across the Valdivia fracture zone system, which intersects the margin at ~40°S. Oceanic crust produced by the Chile Rise characterizes the plate to the south, whereas oceanic crust to the north formed at the East Pacific Rise. Crustal age, thickness, number of oceanic fracture zones, and plate rugosity differ markedly across the Valdivia fracture zone (Tebbens and Cande, 1997).

The western flank of the Neuquén Andes is subdivided across-strike into five morphotectonic units (Figure 3.1): (1) the Coastal Platform, which consists of uplifted Tertiary marine and coastal sequences; (2) the Coastal Ranges, which include a Permian-Triassic accretionary complex and a Paleozoic magmatic arc; (3) the Central Depression, a flat area formed by Oligocene-Miocene sedimentary and volcanic rocks, covered by Pliocene-Quaternary sediments; (4) the Main Cordillera, the focus of this paper, which consists of a long-lived Mesozoic-Cenozoic magmatic arc and intra-arc volcano-sedimentary basins; and (5) the Mesozoic Neuquén Embayment and Cretaceous-Tertiary foreland basin.

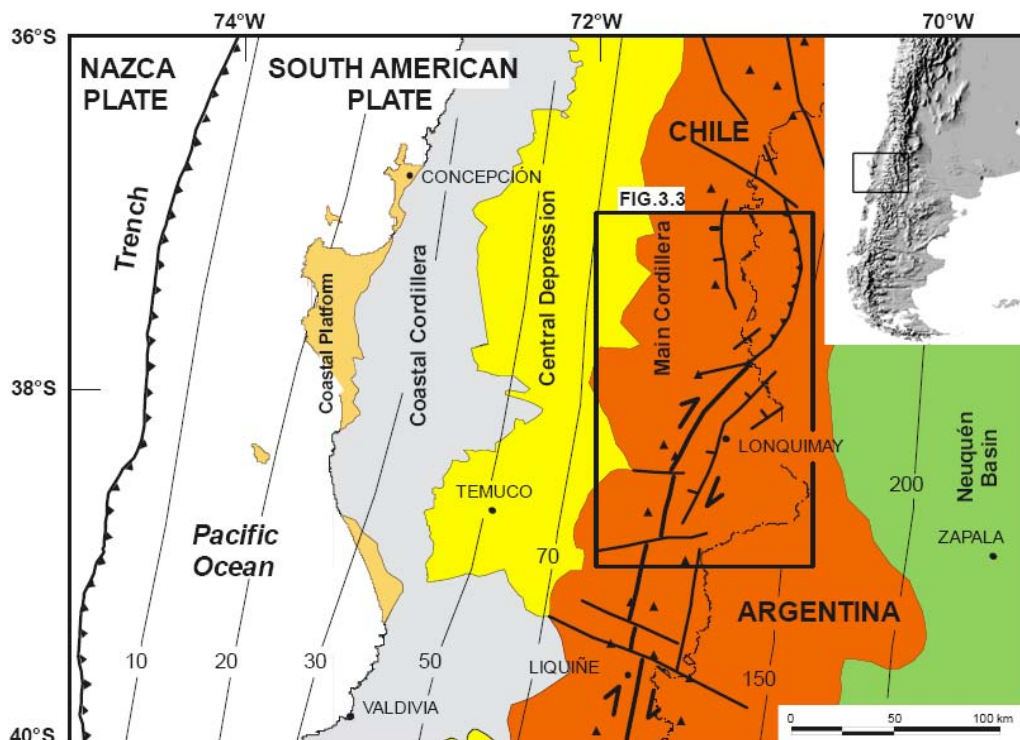


Figure 3.1: Regional location map, morphotectonic units, and Pliocene-Quaternary faults of the Main Cordillera. Contours indicate the depth to the top of the subducting Nazca plate determined using the local network seismicity from Bohm et al. (2002). Black triangles indicate Holocene volcanoes.

3.2.1 Liquiñe-Ofqui fault zone

The Liquiñe-Ofqui fault zone is the dominating structural element of the intra-arc zone of the Patagonian Andes and extends for ~1200 km from 38°S to 46.5°S. This fault zone is a dextral strike-slip system that accommodates about half of the margin-parallel component of oblique subduction (Rosenau, 2004) and deformation resulting from collision of the Chile Rise with the South American continent (Forsythe and Nelson, 1985; Cembrano et al., 2002). South of 44°S, fission-track thermochronology (Thomson, 2002), structural data, and $^{40}\text{Ar}/^{39}\text{Ar}$ ages of

syntectonic micas in mylonitic shear zones (Cembrano et al., 2002) show that the Liquiñe-Ofqui fault zone has acted since ca. 7 Ma as a transpressional zone related to the indentation and subduction of the Chile Rise. Between 39.5°S and 42°S, fault kinematic data (Lavenue and Cembrano, 1999; Rosenau, 2004) and ⁴⁰Ar/³⁹Ar ages of syntectonic micas (Cembrano et al., 2000) suggest a dominantly strike-slip regime and both transpressional as well as minor transtensional tectonics within the intra-arc zone since the Pliocene.

López-Escobar et al. (1995) noticed that most of the late Quaternary stratovolcanoes and minor eruptive centers south of 38°S are either associated with ~NNE-trending faults of the Liquiñe-Ofqui fault zone or form N50–70°E- and N50–60°W-oriented arc-oblique alignments. Following the model proposed by Nakamura (1977), they interpreted the N50–70°E alignments as indicative of the orientation of the axis of maximum horizontal stress (σ_{Hmax}), and the N50–60°W alignments as pre-existing crustal fractures that also served as channels for magma ascent. South of 38°S, NE orientations of σ_{Hmax} and strike-slip stress indicators characterize the tectonic regime of the intra-arc zone today (Reinecker et al., 2004).

South of ~39.5°S, the Liquiñe-Ofqui fault zone is a prominent fault-zone system expressed morphologically by arc-parallel and arc-oblique fiords and glacial valleys. To the north, in the area of this study, transtensional deformation characterizes the Liquiñe-Ofqui fault zone (Potent and Reuther, 2001; Melnick et al., 2002; Rosenau, 2004). The fault zone loses its morphological expression along the axis of active volcanoes, and its northern termination is formed by several splays described in this study, i.e., the Lonquimay and El Barco fault zones.

3.3 Geology of the study area

Based on the available geologic maps (Niemeyer and Muñoz, 1983; Delpino and Deza, 1995; Suárez and Emparán, 1997; SERNAGEOMIN, 2003), the stratigraphy of the western flank of the Neuquén Andes, between 37 and 39°S (Figure 3.2), can be divided into seven main sequences: (1) pre-Jurassic volcanic, intrusive, and metamorphic rocks representing the pre-Andean basement; (2) Jurassic marine and volcanic rift sequences; (3) Mesozoic and Cenozoic intrusive rocks; (4) Upper Cretaceous to Paleogene volcanic and continental sedimentary rocks; (5) late Oligocene to late Miocene volcanic complexes and continental sedimentary rocks; (6) Pliocene to early Pleistocene plateau volcanic and volcanoclastic rocks; and (7) Upper Pleistocene to Holocene stratovolcanoes and minor eruptive centers.

3.3.1 Pre-Cenozoic to Paleogene units

The basement of the Neuquén Andes is composed of metasedimentary sequences of late Paleozoic age and Permian-Triassic bimodal volcanic and intrusive rocks that form part of a large igneous province known as the Choiyoi Group (Kay et al., 1989). These rocks crop out in the Argentinean Neuquén Andes (Delpino and Deza, 1995) and along the Coastal Ranges (Hervé et al., 1988). Although this pre-Andean basement is not exposed in the Main Cordillera between 37 and 39°S, these rocks are inferred to form the basement as observed immediately to the east in the Cordillera del Viento (70.5°W, 37.2°S) and further north in the Main Cordillera at ~34°S (Giambiagi et al., 2003).

3.3.2 Mesozoic and Cenozoic intrusive rocks

The granitoids that crop out between 37 and 39°S represent the northernmost exposures of the North Patagonian Batholith (e.g., Hervé, 1994; Pankhurst et al., 1999) of Mesozoic to Miocene age. Cretaceous intrusive rocks of the Galletué Plutonic Group are exposed between 37 and 38°S as an isolated body on the western edge of the Main Cordillera and continuously south of 38.4°S (Figure 3.3). This group intrudes the Jurassic units and has a wide age range from 148 ± 8 to 80 ± 2 Ma (K-Ar, biotite, amphibole whole rock; Suárez and Emparán, 1997). Two Paleocene stocks with ages of 63 ± 2 and 58 ± 4 Ma intrude the Cretaceous-Paleogene Vizcacha-Cumilao Complex and are covered by Oligocene-Miocene rocks (Suárez and Emparán, 1997). Gräfe et al. (2002) reported apatite fission-track ages of 40.6 ± 4.5 and 33.9 ± 4.6 Ma for these small intrusive bodies.

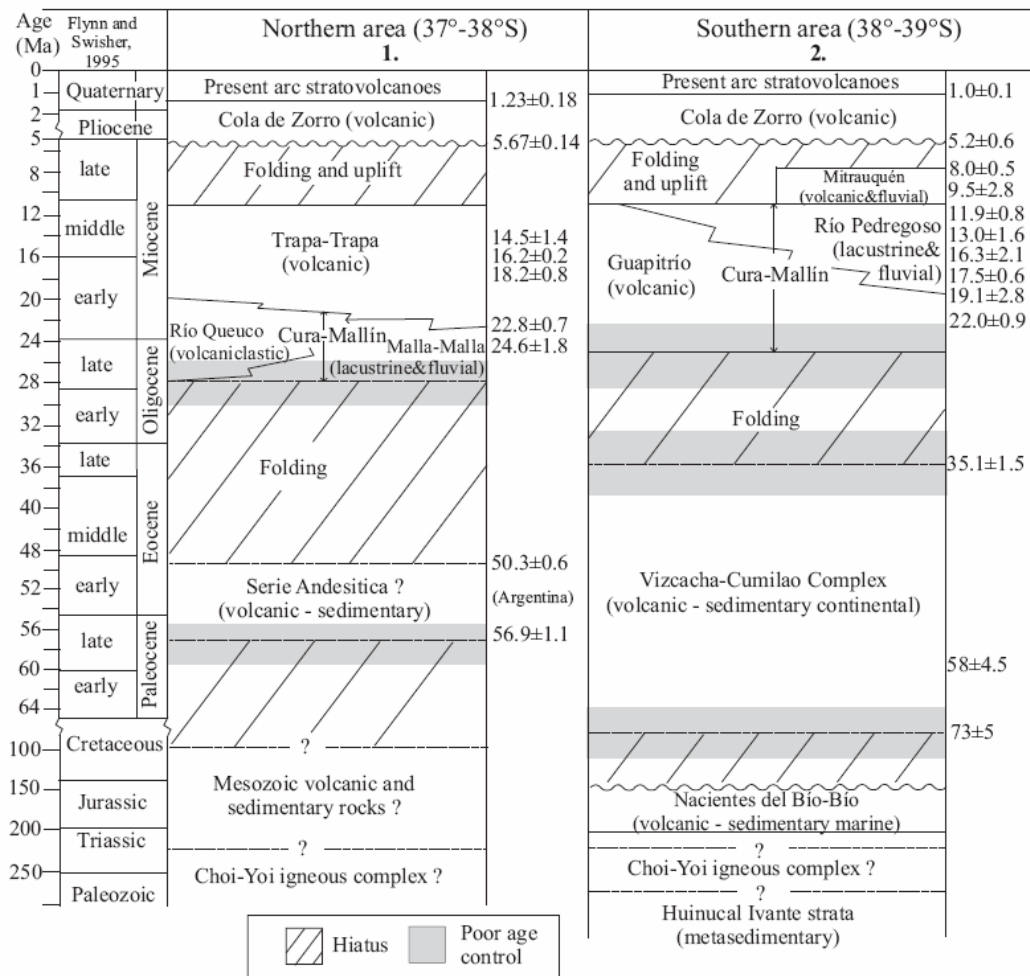


Figure 3.2: Generalized stratigraphic chart of the Main Cordillera, divided into northern (37–38°S) and southern (38–39°S) areas. Compiled from (1) Niemeyer and Muñoz (1983), Jordan et al., (2001), Linares et al. (1999); and (2) Suárez and Emparán (1995, 1997).

Miocene plutonic rocks are exposed in a N–S–trending, ~5-km-wide body between 37 and 38°S. The Melipeuco Plutonic Group (Figure 3.3) has ages ranging from 15.1 ± 1.2 to 7.2 ± 1.9 Ma, with an average value of 10.8 ± 1.8 Ma (from the seventeen K–Ar, biotite amphibole ages in Suárez and Emparán, 1997), and intrusion depths are <3 km (Seifert et al., 2005). Gräfe et al. (2002) reported an apatite fission-track age of 5.8 ± 1.0 Ma for a granite of this group. South of 38.2°S, these rocks generally form the basement of the late Quaternary stratovolcanoes. Pliocene subvolcanic intrusive rocks are exposed as irregular bodies with ages ranging from 5.2 ± 2.0 to 2.6 ± 0.4 Ma (K–Ar whole rock; Suárez and Emparán, 1997).

3.3.3 Oligocene–Miocene volcanic and sedimentary rocks

In the Chilean and Argentinean Main Cordillera between 36 and 39°S, sedimentary, volcanic, and volcanoclastic rocks of late Oligocene to middle Miocene age are described in the literature as the Cura-Mallín Formation (Niemeyer and Muñoz, 1983; Muñoz and Niemeyer, 1984; Suárez and Emparán, 1995, 1997). Between 37 and 39°S, Carpinelli (2000) and Radic et al. (2002) subdivided the Cura-Mallín basin spatially and genetically into two subbasins (Figure 3.2), which are described in detail in the respective geographic sections below. These authors, as well as Jordan et al. (2001), concluded on the basis of stratigraphic and structural data and interpretation of seismic reflection lines that the mid-Tertiary basins between 34 and 42°S, including the Cura-Mallín basin, were deposited in a continental intra-arc rift during an extensional tectonic regime.

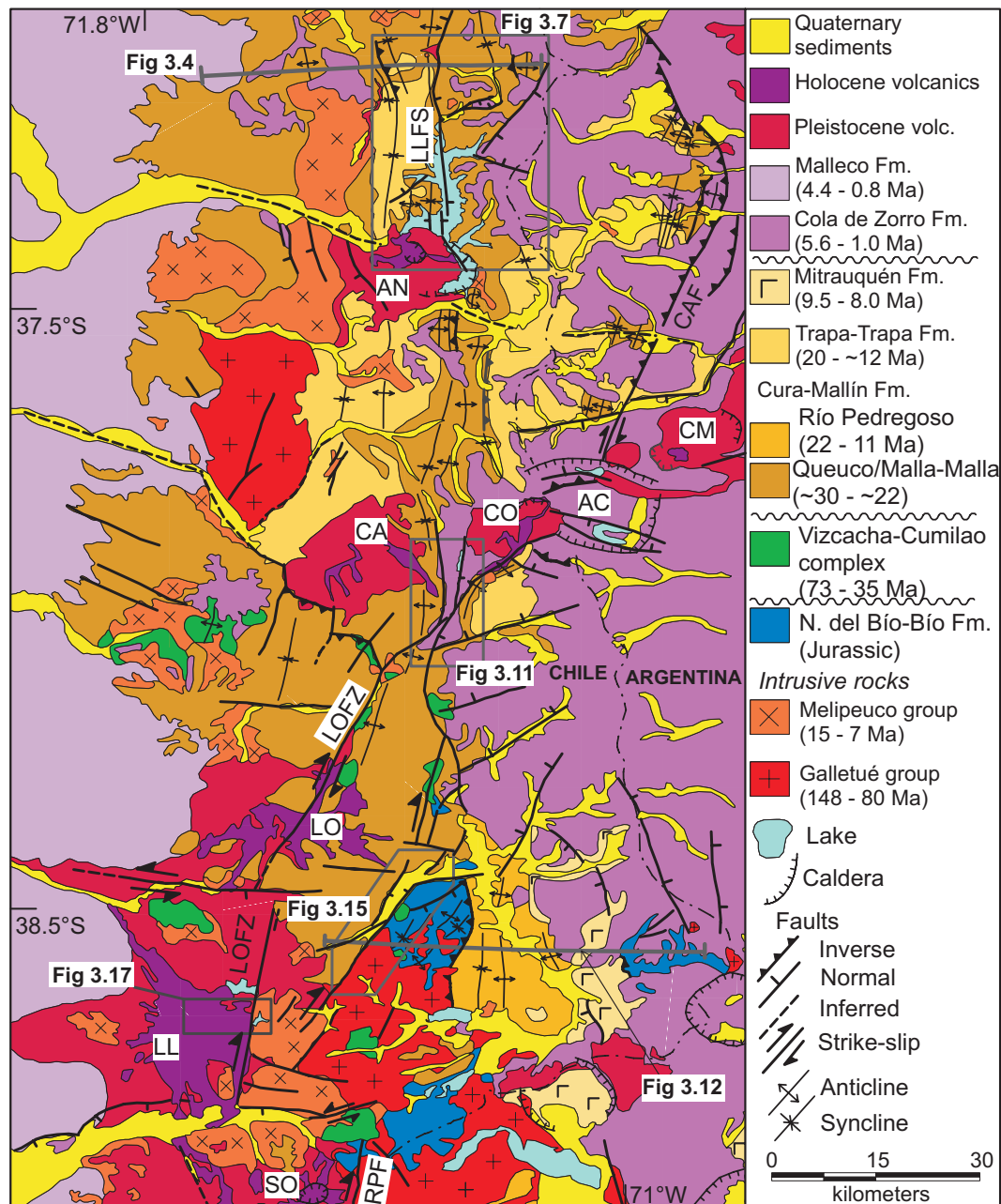


Figure 3.3: Simplified geologic map of the western flank of the Neuquén Andes between 37 and 39°S, compiled from references in the text and our data. Cross sections in Figures 4 and 15 are shown. Areas of Figures 7, 11, 15, and 17 are indicated by boxes. Volcanic centers shown: AN—Antuco—Sierra Velluda, CA—Callaqui, CO—Copahue, AC—Agrio caldera, CM—Cordillera de Mandogüe, LO—Lonquimay, LL—Llaima, SO—Sollipulli. Faults: LOFZ—Liqueñe-Ofqui fault zone, CAF—Copahue-Antiñir fault, LLFS—Lago de la Laja fault system, RPF—Reigolil-Pirihueico fault.

3.3.4 Pliocene to early Pleistocene plateau volcanic rocks

Along most of the drainage divide of the Neuquén Andes, Pliocene to early Pleistocene basic volcanic rocks form extensive plateaus. These rocks are referred to as the Cola de Zorro Formation (González and Vergara, 1962; Vergara and Muñoz, 1982) or Asociación Volcánica de la Precordillera Oriental (Suárez and Emparán, 1997) (Figure 3.3). The Cola de Zorro Formation overlies the older units in a marked angular unconformity of regional extent. Ages of this unit range from 5.6 ± 0.1 to 1.0 ± 0.1 Ma (K-Ar whole rock; Niemeyer and Muñoz, 1983; Suárez and Emparán, 1997; Linares et al., 1999).

Along the western edge of the Main Cordillera, the proximal facies is dominated by lava flows, coarse volcanic breccias, and sills, which grade to the west to a more distal facies

characterized by pyroclastic flows and alluvial and fluvial conglomerates assigned to the Malleco Formation (Suárez and Emparán, 1997). This unit forms the current piedmont and upper infill of the Central Depression (Figure 3.3), with ages ranging from 4.4 ± 0.5 to 0.8 ± 0.3 Ma (K-Ar whole rock; Suárez and Emparán, 1997).

3.3.5 Upper Pleistocene to Holocene volcanic centers

The late Quaternary Southern volcanic zone extends between 33 and 46°S with an ~NNE trend. The study area is within the central petrological province of this volcanic zone, which is characterized by a constant arc-to-trench distance of ~270 km and products mainly of basaltic to andesitic composition (López-Escobar et al., 1995). In the study region, most of the active volcanic centers occur in linear associations that consist of at least two composite stratovolcanoes and several related alignments of minor eruptive centers.

3.4 Segmented tectono-stratigraphy and structural evolution

The stratigraphic descriptions and structural observations of this study are grouped into three geographic areas. These areas represent distinct structural domains with differences in stratigraphy, structural style of deformation, and tectonic evolution. The southern domain is characterized by dominantly strike-slip deformation along the Liquiñe-Ofqui fault zone, the northern domain by extension along the intra-arc and shortening in the Argentinean foothills, and the central domain by a long-lived transfer zone that accommodates the deformation between the northern and southern domains. For the local stratigraphic units of each domain, we follow the terms published by the Chilean Geological Survey.

3.4.1 Northern Domain—Lago de la Laja area (37°–37.7°S)

3.4.1.1 Stratigraphic succession

Oligocene-Miocene volcanic and sedimentary rocks

The northern subbasin of the Cura-Mallín Formation consists of a western part with ~2800 m of late Oligocene to early Miocene sediments attributed to fluvial, lacustrine, and deltaic-alluvial fan facies, whereas an eastern part records only ~400 m of deltaic sediments (Carpinelli, 2000; Radic et al., 2002). The western succession is characterized by two tectono-sedimentary events, leading these authors to relate this subbasin with a dual cycle of continental rifting.

North of 38°S, the Trapa-Trapa Formation conformably overlies the Cura-Mallín Formation (Niemeyer and Muñoz, 1983). The Trapa-Trapa unit is composed of thick pyroclastic breccias, lavas, and minor sedimentary beds. Ages range from 18.2 ± 0.8 to 14.5 ± 1.4 Ma (K-Ar, plagioclase whole rock; Niemeyer and Muñoz, 1983), and in Argentina, an andesitic lava was dated as 16.2 ± 0.2 Ma (Ar-Ar hornblende; Jordan et al., 2001).

Upper Pleistocene to Holocene volcanic venters

The volcanic centers are: the active Antuco stratovolcano, with a basal lava dated as 0.083 ± 0.04 Ma (K-Ar whole rock; Moreno et al., 1985); a valley-confined basaltic plateau of presumably late Pleistocene age; and the Sierra Velluda volcano, a deeply dissected extinct stratovolcano composed of two units: a lower unit, formed by ~1500 m of lavas, breccias, and intercalated pyroclastic flows, dated as 0.495 ± 0.08 Ma; and an upper unit, formed mainly by ~1000 m of lavas and breccias dated as 0.381 ± 0.04 Ma (K-Ar whole rock; Moreno et al., 1985). The Sierra Velluda and Antuco volcanoes are both emplaced in a circular depression, which might represent a Miocene or early Pliocene caldera or the interference of several basement structures (Figure 3.3).

3.4.1.2 Structural evolution

Late Miocene orogenic phase: Ñuble profile

The E-W cross section at ~37.1°S, across the Ñuble National Park, illustrates the bivergent geometry of the orogen in this northern domain (Figure 3.4). In the western part, the Huemules thrust (Figure 3.5A) is a NNW-striking, moderate- to high-angle east-dipping fault, with ~400 m of slip, which truncates the Cura-Mallín and Trapa-Trapa Formations. Two synclines flank this thrust. The central part of the Ñuble section is dominated by an open, ~10-km-wide anticline that turns into a syncline at the upper Polcura River (Figure 3.4). This syncline is detached by the Calabocillo thrust, which truncates lacustrine strata of the Cura-Mallín Formation in the footwall (Figure 3.5B). This east-vergent thrust fault, identified by Niemeyer and Muñoz (1983), has a listric geometry and forms a shallow detachment at depth. East of the Calabocillo thrust, the Cura-

3. Neogene tectonics, western Neuquén Andes

Mallín Formation is deformed in a syncline related to this thrust and an open anticline, which is covered by younger units to the east.

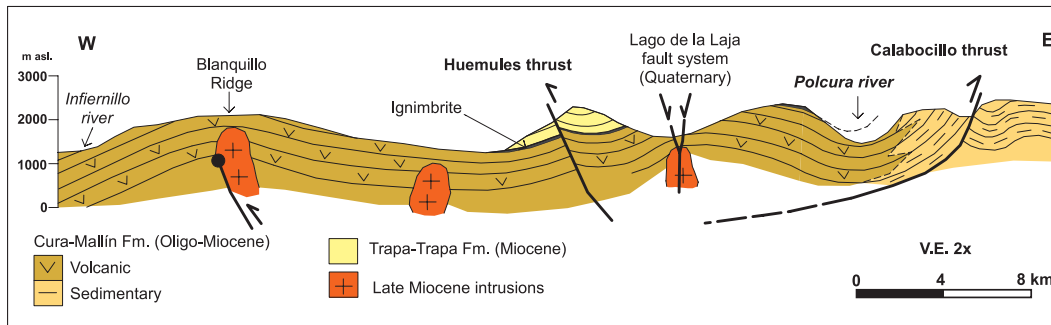


Figure 3.4: Geological cross section along the Ñuble National Park at $\sim 37^\circ\text{S}$, showing the divergent geometry of the Andean orogenic structure of the northern domain.

At this latitude on the Argentinean foothills, Jordan et al. (2001) presented an industry-style seismic reflection line showing that the Cura-Mallín Formation increases in thickness from ~ 400 to ~ 1800 m across a west-dipping normal fault. Based on the occurrence of an anticline in the hanging wall of the fault, they interpreted this structure as an inverted, basin-bounding normal fault.

Along the western margin of the Main Cordillera, the contact with the Central Depression is an area covered by dense vegetation and Pliocene-Quaternary sediments and volcanics. This western edge of the Main Cordillera is formed by Cura-Mallín strata dipping $\sim 30^\circ\text{W}$ on the flank of a slightly asymmetric west-facing wide anticline. Based on the asymmetry of the anticline and the topographic break, we infer a west-vergent blind thrust underneath this fold.

South of the Laja Lake at 37.5°S , a tight, overturned west-vergent fold affects sedimentary rocks of the Cura-Mallín Formation. The geometry of this fold implies a low-angle thrust from a detachment in the sedimentary facies. In this northern domain, low-angle structures linked to shallow-level detachments are located in the eastern sedimentary-dominated part of the basin. In contrast, on the western volcanoclastic-dominated part of the basin, steeper faults, such as the Huemules thrust, and wide folds characterize the structure (Figure 3.5).

Pliocene to early Pleistocene extension: upper Polcura

In the area northeast of Laja Lake (Figure 3.3), the NNE-trending Bejar fault (Figs. 3.6A and 3.7) juxtaposes Oligocene-Miocene lacustrine strata of the Cura-Mallín Formation with volcanic rocks from the Cola de Zorro Formation. This fault has at least 350 m of down-to-east dip-slip displacement and extends along strike for ~ 18 km.

West of the Bejar fault, the Toro graben is an elongated, NE-trending depression hanging over the Polcura River (Figs. 3.6B and 3.7). The two normal faults offset the angular unconformity between the Cura-Mallín and Cola de Zorro Formations by ~ 300 m vertically. On the western part of the graben, a zone of hydrothermal alteration is recognized along the northern-bounding fault of this structure. The southern fault, on the other hand, is well exposed at a road cut along the upper Polcura River.

Late Pleistocene to Holocene deformation: Laja region

The Lago de la Laja is a narrow, 32-km-long, volcanic-dammed lake, located along the axis of the intra-arc zone. The Antuco volcano, immediately southwest of the lake (Figure 3.7A) suffered a Bandai-type caldera collapse event (Lohmar, 2000). The volcanic avalanche emitted during this event and subsequent lava flows dammed the valley, forming the present lake (Vergara and Katsui, 1969). Two Holocene ^{14}C ages have been reported for this event: 9700 ± 600 (Moreno et al., 1985) and 6250 ± 60 yr B.P. (Lohmar, 2000).

Seismic-reflection profiles, collected by the RCMG (Renard Centre for Marine Geology, University of Gent, Belgium) (Charlet et al., 2003), show normal faults forming horst-and-graben structures cutting the lake-bottom sediments (Figure 3.8). These sediments were deposited after the valley was dammed by the Antuco collapse and are thus younger than 6250 ± 60 yr B.P., indicating recent faulting.

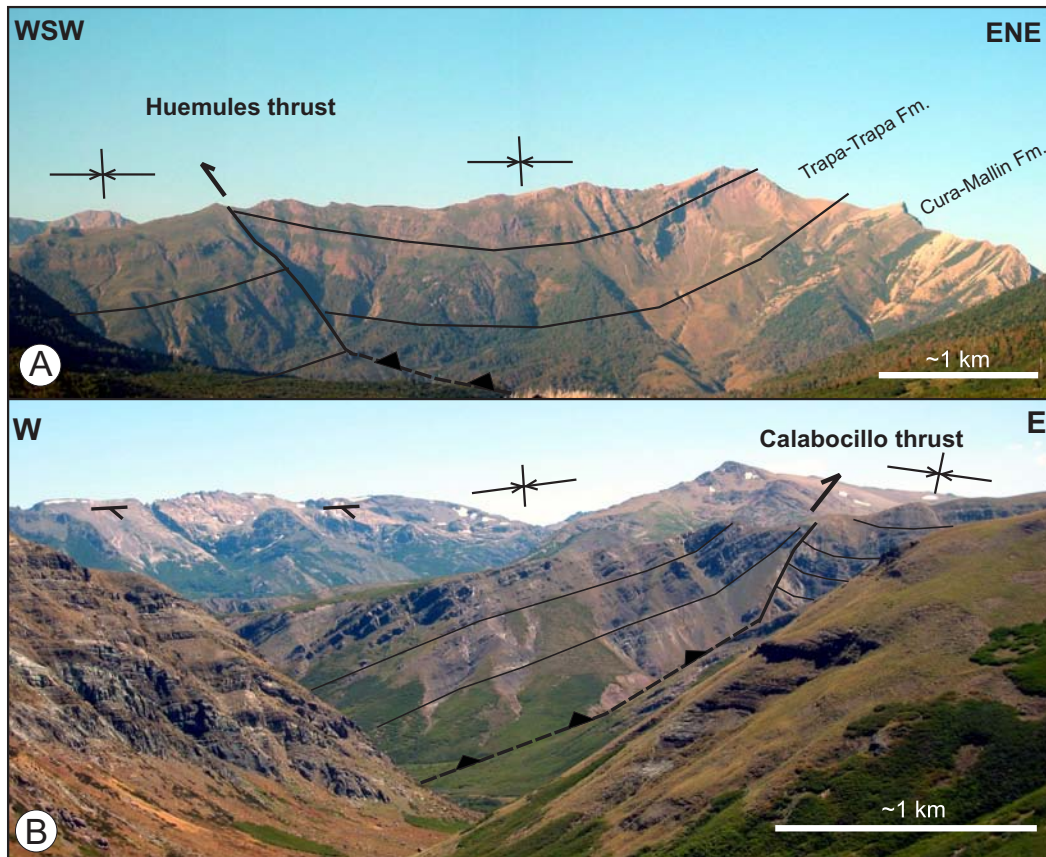


Figure 3.5: (A) View to the NNW of the west-vergent Huemules thrust. (B) View to the north of the Calabocillo thrust, which has a listric-thrust geometry detaching the Cura-Mallin Formation in the hanging wall and truncating the same strata in the footwall.

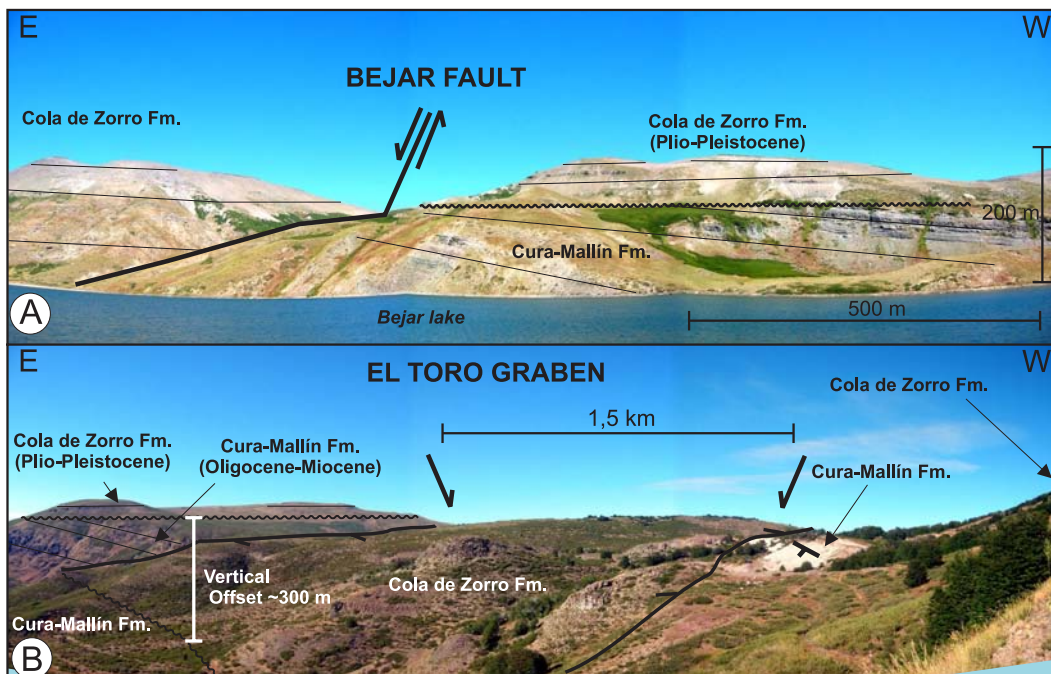


Figure 3.6: (A) View to the southeast of the Bejar fault, juxtaposing Cura-Mallin lacustrine strata with Pliocene-Pleistocene volcanic rocks, with at least 300 m of vertical displacement. (B) View to the SSE of the Toro graben. The normal faults offset the unconformity between the Cura-Mallin and Cola de Zorro Formations by ~300 m. Location is shown on Figure 7.

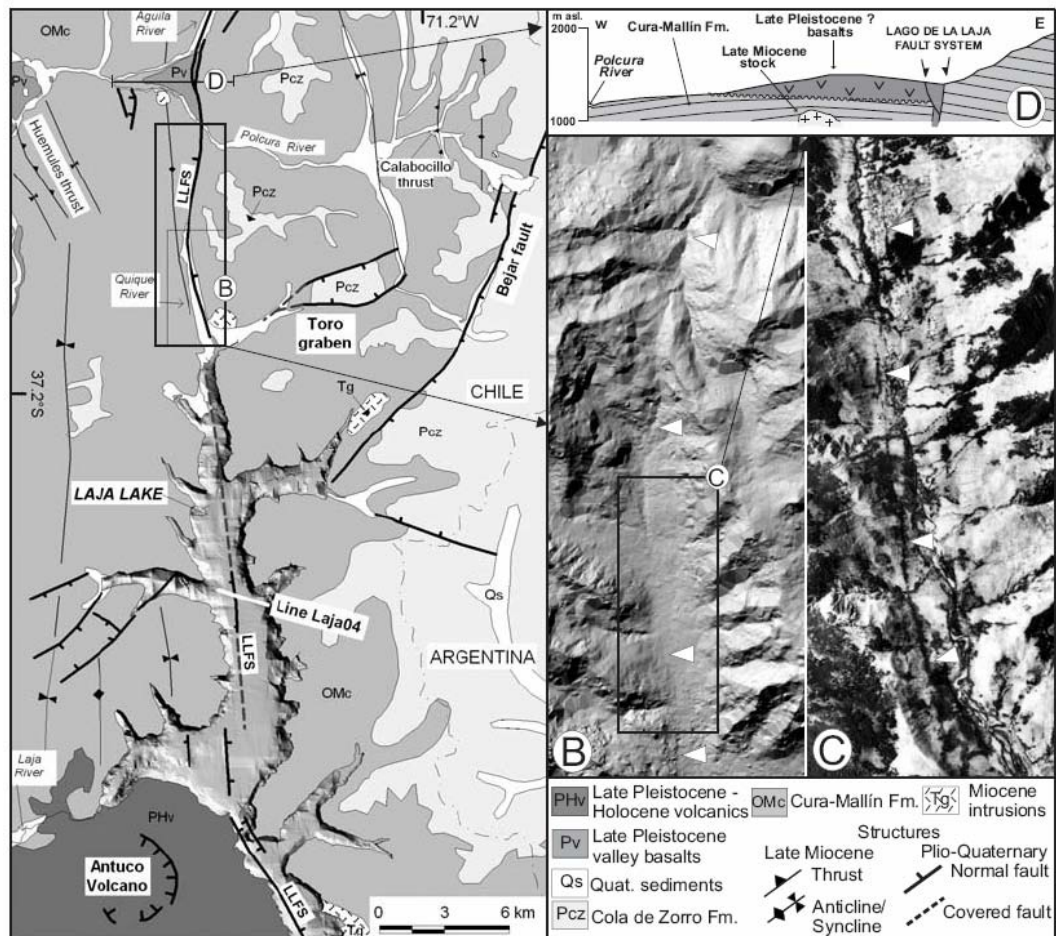


Figure 3.7: Geology of the Lago de la Laja Quaternary fault system. (A) Geologic map with shaded bathymetry from UFZ Leipzig-Halle. LLFS—Lago de la Laja fault system. (B) Photogrammetric shaded-relief digital elevation model (5 m resolution); white triangles show the trace of the Lago de la Laja fault system. (C) Air photo of the Quique valley showing alignment of vegetation along the fault. (D) Profile showing the late Pleistocene valley-confined basaltic plateau controlled by the Lago de la Laja fault system.

The Lago de la Laja fault system (Melnick et al., 2003) runs for ~60 km along the Laja Lake and the Quique and Aguila Rivers (Figure 3.7A). The interpretation of a photogrammetric digital elevation model (5 m resolution) and an air photo of the Quique valley (Figs. 7B and 7C) shows a N-S-trending fault scarp that forms an ~2-km-long alignment of dense vegetation due to the concentration of springs along the fractured fault zone. This scarp marks a topographic break at the bottom of the glacial valley (Figure 3.7B).

Near the junction of the Aguila and Polcura Rivers (Figure 3.7A), a wedge-shaped plateau formed by late Pleistocene valley-confined lavas unconformably covers folded strata of the Cura-Mallín Formation (Figure 3.7D). A steep topographic break marks the contact between the plateau and the higher Cura-Mallín rocks to the east. The plateau morphology, valley confinement, wedge shape, and alignment with the Quique River indicate that the eruption of these flows may have been along the Lago de la Laja fault system. A fault scarp recognized in these lavas indicates that tectonic activity continued after the volcanic eruption (Figure 3.7D).

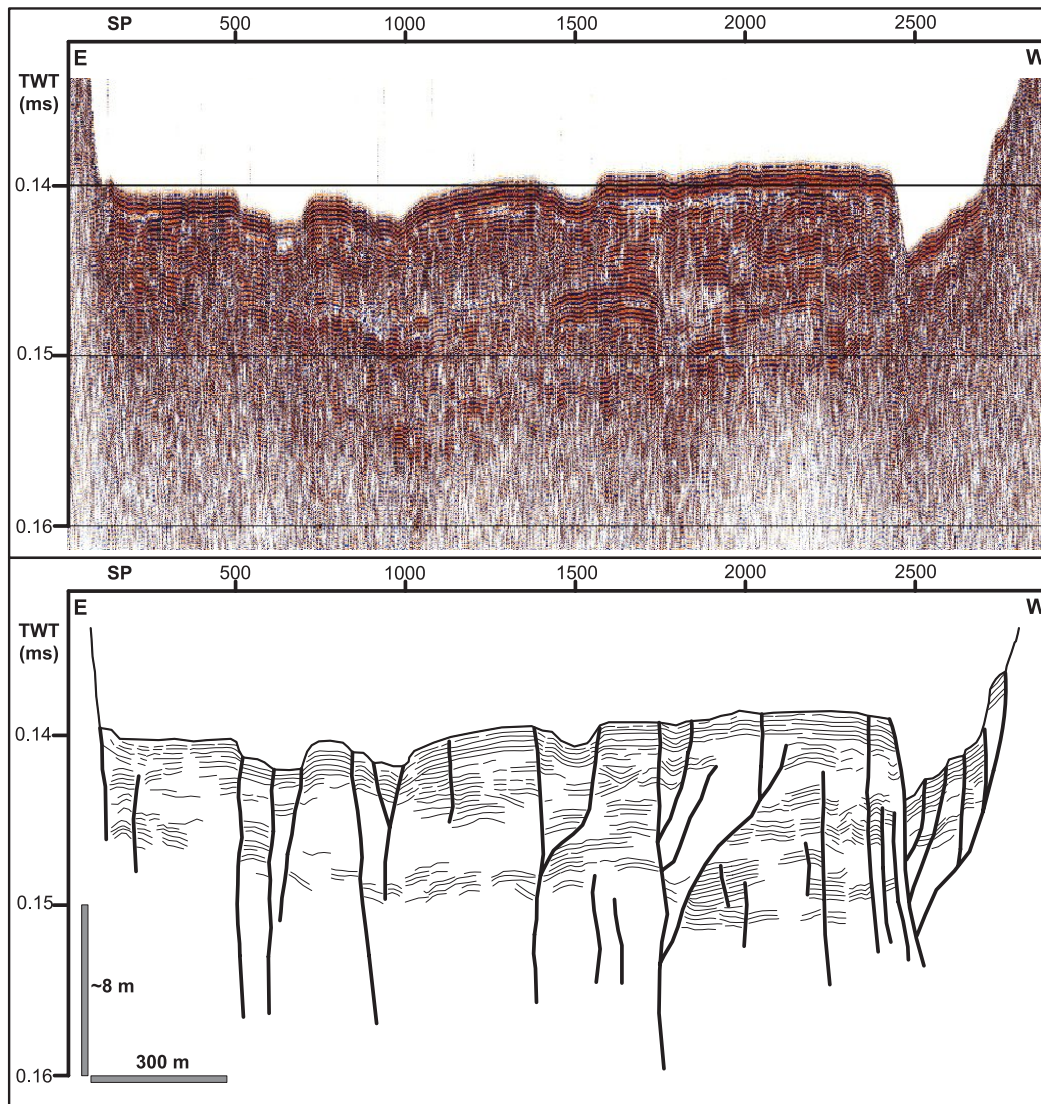


Figure 3.8: The Lago de la Laja fault system in the central part of the lake. Offshore pinger (3.5 kHz) high-resolution seismic-reflection profile Laja04, shot by the RCMG, University of Gent, Belgium (Charlet et al., 2003). Line drawing shows normal faults forming horst-and-graben structures. The faults affect sediments that are younger than 6250 ± 60 yr B.P. (^{14}C age from Lohmar, 2000). Location of seismic line is shown on Figure 7. TWT—two-way traveltime; SP—shot point.

Postglacial pyroclastic fallout deposits from the Chillán volcanic complex, located ~ 30 km to the northwest, cover most of this area. At a road cut south of the plateau, ten N-S-trending normal faults cut these pyroclastic deposits (Figure 3.9). The faults form an asymmetric horst-and-graben structure with a west-down polarity. Maximum slip on a west-dipping fault is 3 m. Dixon et al. (1999) reported nine ^{14}C ages of pyroclastic fallout deposits from the Chillán volcano ranging from 9300 ± 70 to 2270 ± 60 yr B.P. Unfortunately, no datable material was found in the faulted pyroclastics, but we infer that these deposits are equivalent to those dated in the surroundings of the volcano. The horst-and-graben geometry of this outcrop is similar to the structures observed in the seismic line Laja04 (Figure 3.8), and their similar age seems well constrained by our observations.

On the northwestern slope of the Sierra Velluda, a NW-striking, southwest-dipping normal fault was identified cutting an ~ 2000 m vertical section of the volcano, with at least 500 m of down-to-the-west vertical displacement. This fault juxtaposes the upper and lower units of the volcano truncating the pyroclastic flows of the lower unit. No caldera collapse events have been described nor identified in the current survey for this volcano. Two NW-striking normal faults

affecting Pleistocene lavas were recognized ~20 km west of Sierra Velluda. Therefore, we interpret these faults as late Pleistocene extension.



Figure 3.9: Southward view of Holocene fallout pyroclastic deposits affected by normal faults with graben-and-horst geometry. These deposits from the Chillán volcano have ^{14}C ages from ~9 to 2 kyr B.P. (Dixon et al., 1999). Outcrop is located in the upper Polcura River (see Figure 3.7).

3.4.2 Central transitional Domain—Copahue-Agrío area (37.7°S–38°S)

3.4.2.1 Stratigraphic succession

Pliocene to early Pleistocene volcanic rocks

In the inner wall of the Agrío caldera, the Cola de Zorro Formation consists of a homogeneous sequence of lavas and breccias deposited between 4.0 ± 0.2 and 5.67 ± 0.2 Ma (K-Ar whole rock; Linares et al., 1999). Ignimbrites and lavas of the Mellizas volcanic sequence are exposed inside the caldera and surroundings of El Barco Lake in Chile (Melnick et al., 2005), with ages between 2.60 ± 0.2 and 2.68 ± 0.2 Ma (K-Ar whole rock; Linares et al., 1999). The Trollope flows, with ages between 0.8 ± 0.2 and 1.6 ± 0.2 Ma (K-Ar whole rock; Linares et al., 1999), overlie the Mellizas sequence in the northeastern border of the caldera.

Pleistocene to Holocene volcanic centers

At ~38°S, volcanic activity occurs along the 90-km-long Callaqui-Copahue-Mandolegüe NE-trending volcanic lineament. The Upper Pleistocene to Holocene centers emplaced along this structure are: the active Callaqui and Copahue stratovolcanoes, the Agrío caldera, the Trolón minor eruptive center, and the Mandolegüe range. The edifice of the Callaqui stratovolcano defines an 11-km-long, NE-trending morphological ridge (Figure 3.10). The Copahue composite stratovolcano, which is located east of the generally NNE-trending volcanic front, has basal lavas with ages of 1.23 ± 0.3 to 0.76 ± 0.2 Ma (K-Ar whole rock; Muñoz and Stern, 1988; Linares et al., 1999) and is marked by numerous eruptions during the Pleistocene and Holocene (Melnick et al., 2005). In the inner part of the Agrío caldera (AC in Figure 3), isolated subglacial centers of late Pleistocene age are spatially related to WNW-trending extensional faults. In the northern part of the caldera, 1.6 ± 0.2 to 0.8 ± 0.2 Ma lavas and a 0.6 ± 0.2 Ma dome (K-Ar whole rock; Linares et al., 1999). The lavas and domes are emplaced along the normal faults, which control the border of the caldera (Folguera and Ramos, 2000). The Trolón eruptive center, located northeast of the Agrío caldera, is dated as 0.6 ± 0.2 Ma at the base (K-Ar whole rock; Linares et al., 1999) and has two Holocene vents. The Mandolegüe range is an elongated fault-bounded block of Pliocene volcanics covered by eroded Pleistocene stratovolcanoes, calderas, and NE-trending dike swarms.



Figure 3.10: Oblique air photo to the northeast, along strike of the Callaqui-Copahue-Mandolegüe lineament. Morphology of the elongated Callaqui volcano can be appreciated. The darker flows are postglacial; on the lower part of the glacier, a fissure can be seen. Note the axial valley on the ridge where small craters and fissures are aligned. The snow-covered hill in the back is the Copahue volcano.

3.4.2.2 Structural evolution

Late Miocene orogenic phase: Callaqui-Copahue-Mandolegüe transfer zone

Detailed stratigraphic and structural studies (Carpinelli, 2000; Radic et al., 2002) have suggested that the Cura-Mallín basin between 37 and 39°S consists of two diachronic depocenters limited by a major transfer zone located at ~37.7°S. Regional surveys focused on Pliocene-Quaternary deformation and structural control on volcanism (Folguera and Ramos, 2000; Melnick et al., 2002, 2005) identified an alignment of volcanic activity that extends for ~90 km in a N60° direction; it is referred to as the Callaqui-Copahue-Mandolegüe lineament. This lineament divides two domains with different structural styles, the northern domain, characterized by folding and thrusting of the Oligocene-Miocene units with a bivergent geometry (Figure 3.4), and the southern domain, where the Mesozoic units are involved in the deformation (more details in the following). Shortening magnitudes, although not quantified in this study, seem to be larger in the northern domain, as inferred from generally tighter folding in this area. Thus, we suggest that the Callaqui-Copahue-Mandolegüe lineament accommodated the difference in total strain and deformation style during the late Miocene shortening phase and that it represents the Pliocene-Quaternary expression of the major transfer zone postulated by Carpinelli (2000) and Radic et al. (2002) for the Cura-Mallín basin.

Pliocene to early Pleistocene transtension: Agrio caldera

The Agrio caldera is located in the central part of the Callaqui-Copahue-Mandolegüe transfer zone at 37.8°S (Figure 3.3). This depression has a rectangular morphology and is 20 km long in WNW and 15 km in NE directions. The caldera cuts the Cola de Zorro Formation and the first postcaldera unit is the Mellizas volcanic sequence, which constrains the age of the Agrio caldera to the Upper Pliocene.

The Agrio caldera developed between two regional fault zones, the Liquiñe-Ofqui strike-slip and the Copahue-Antiñir thrust systems (LOFZ and CAF in Figure 3, respectively). Around 10 km north of the Agrio caldera, a NE-trending normal fault forms a half-graben with a southeast-down polarity along the Damas River, and ~10 km south of the Agrio caldera along the Chaquilvín River, a north-down normal fault forms another half-graben. These two half-grabens form a symmetrical arrangement with the Agrio caldera in the central part (Figure 3.3). The hanging-wall tilt, up to 30°NW in the Damas half-graben, allows the exposure of folded Miocene sequences in the footwall of both faults. Inside the caldera, two WNW-trending graben systems cut the 1.6 to 0.8 Ma Trollope flows, and strike-slip faults cut glacial-polished surfaces and Holocene lavas of the Copahue volcano (Melnick et al., 2005). The rectangular morphology of the Agrio caldera, its spatial association to regional N-S- to NNE-trending faults, and the related structures are compatible with a pull-apart structure that developed during the late Pliocene-early Pleistocene and have been active since then.

The Agrio caldera and Callaqui-Copahue-Mandolegüe lineament coincide with the southern limit of the backarc Quaternary shortening observed to the north continuously along the Central Andes (Folguera et al., this volume, chapter 12), and with the northern limit of the strike-slip Liquiñe-Ofqui fault zone that extends along the intra-arc zone from 46.5 to 38°S (e.g., Lavenu and Cembrano, 1999). In the Copahue volcano and adjacent Agrio caldera, Pliocene-Quaternary faulting and the orientation of σ_{Hmax} , determined from the alignment and morphologies of volcanic effusions (Nakamura, 1977), display heterogeneous patterns reflected in the clockwise rotation of σ_{Hmax} (Melnick et al., 2005). We interpret this heterogeneous pattern as controlled by the Callaqui-Copahue-Mandolegüe transfer zone, which decouples deformation from the transtensional intra-arc Liquiñe-Ofqui fault zone and the backarc shortening observed along the Copahue-Antiñir fault system north of 37.6°S (Figure 3.3) (Melnick et al., 2002). Pliocene-Quaternary volcanism here is concentrated along a crustal-scale, inherited discontinuity that controls the longest volcanic lineament of the Southern volcanic zone.

Late Pleistocene to Holocene deformation: El Barco

The surroundings of El Barco Lake (Figure 3.11) represent the northern end of the Liquiñe-Ofqui fault zone, which forms a series of splays that cut the late Pliocene Mellizas volcanic sequence (Melnick et al., 2005). The splays trend NNW to ENE, diverging from the main NE-oriented Liquiñe-Ofqui fault zone. Glacial incision followed the trend of the main structures, resulting in narrow elongated valleys. Between the Lomín and Chaquilvín Rivers (Figure 3.11A), lavas of the Mellizas sequence are cut by a NNE-trending east-down normal fault (Figure 3.11C). This fault cuts a glaciated surface, indicating late Pleistocene or younger activity.

El Barco Lake is an elongated depression hanging over the Pelahuenco and Trepureo Rivers (Figure 3.11B). At a gravel quarry on the southern part of the lake, basaltic lavas overlain by fluvial conglomerates and cross-bedded sandstones dip 40°W; this sequence crops out 300 m higher at the Vizcachas area in a horizontal position. This observation suggests block tilting associated with normal faulting. In the upper Trepureo River, a 3-km-long N-S-trending fault scarp was identified from air photos. The scarp is concave to the east, 35 m high in its central part, and loses topographic relief to the north. This fault is probably the postglacial expression of faults that form the northern termination of the Liquiñe-Ofqui fault zone (Figure 3.11A). East of El Barco Lake, fault scarps crosscut postglacial lava flows from the Copahue volcano (Melnick et al., 2005).

3.4.3 Southern Domain—Lonquimay area (38°S–39°S)

3.4.3.1 Stratigraphic succession

Pre-Cenozoic to Paleogene units

The pre-Andean basement in this area is represented by isolated outcrops at 38.7°S of metamorphic rocks of late Paleozoic-Triassic age, named the Huinucal Ivante strata (Suárez and Emparán, 1997). Unconformably overlying this basement, the Nacientes del Bío-Bío Formation (Figure 3.3) integrates volcanic and marine sedimentary rocks of Pliensbachian to Oxfordian age (De la Cruz and Suárez, 1997; Suárez and Emparán, 1997), equivalent to the Cuyo Group in Argentina. The Nacientes del Bío-Bío Formation is in turn unconformably overlain by the Late Cretaceous-Paleogene Vizcacha-Cumilao complex, which is composed of volcanic and continental sedimentary rocks, including subvolcanic intrusive bodies (Suárez and Emparán, 1997).

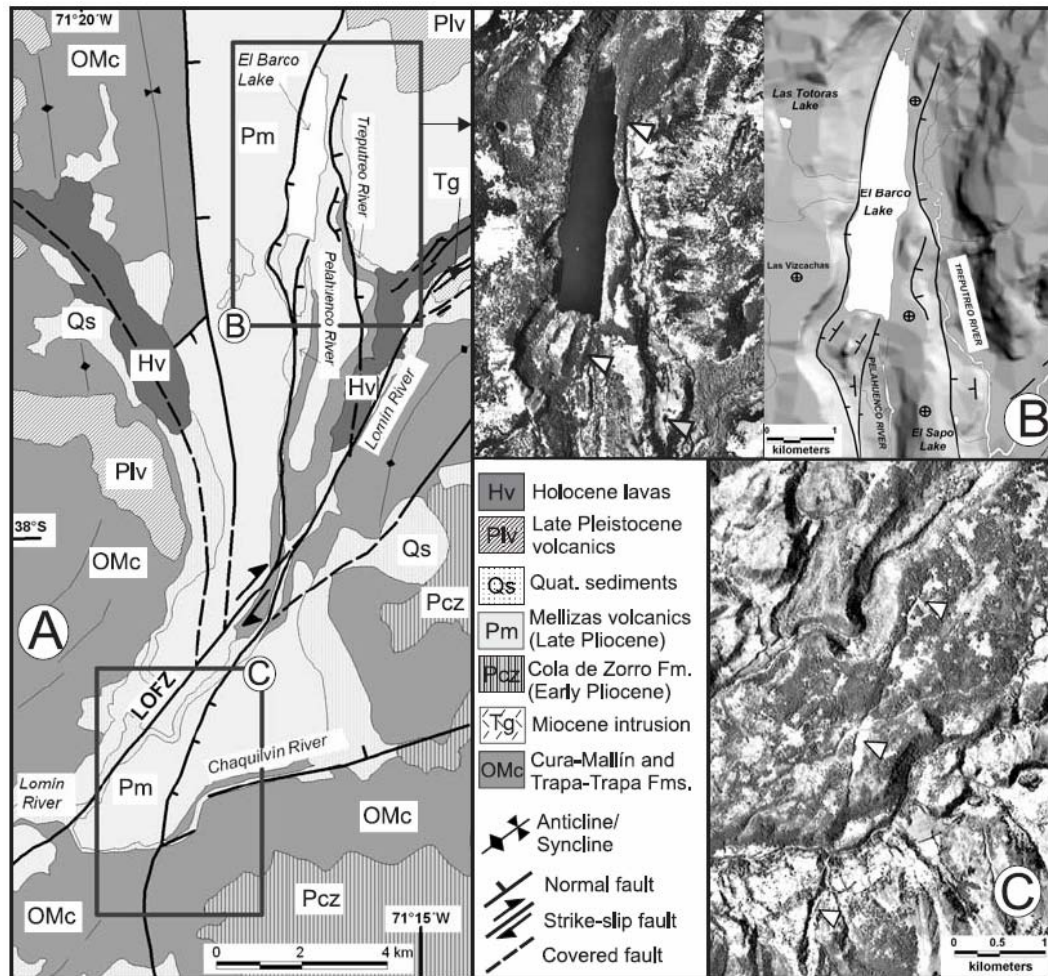


Figure 3.11: Late Quaternary normal faulting at El Barco area. (A) Simplified geologic map. Thick lines indicate Pliocene-Quaternary structures, thin lines, late Miocene structures. LOFZ—Liquiñe-Ofqui fault zone. (B) Air photo (left) and structural map over shaded-relief digital-elevation model (right) of El Barco Lake. White triangles indicate postglacial normal faults; gray triangle indicate sag pond. (C) Air photo showing a late Pleistocene and possibly Holocene NNE-trending east-down normal fault.

Oligocene-Miocene volcanic and sedimentary rocks

The southern Lonquimay subbasin of the Cura-Mallín Formation is characterized by ~2600 m of early Miocene to middle Miocene sediments, similar to the northern subbasin (~37.5°S) but related to a single tectono-sedimentary cycle of continental rifting (Radic et al., 2002). Suárez and Emparán (1995) determined the main development of the southern subbasin based on 23 ages (K-Ar, biotite whole rock), which are between 22.0 ± 0.9 and 11.9 ± 0.8 Ma. Sedimentological studies show that it was an internally drained closed basin between ca. 18 and ca. 11 Ma; subsequently, the basin was opened to the regional drainage system, as indicated by deposition of clasts from Cretaceous quartz diorites from the Galletué Plutonic Group and Jurassic graywackes from the Nacientes del Bío-Bío Formation (Kemnitz et al., 2005).

South of 38.4°S, the Mitrauquén Formation (Suárez and Emparán, 1997) lies conformably above the Cura-Mallín unit. The Mitrauquén Formation is formed by thick dacitic ignimbrites, volcanic breccias, andesitic lavas, and interbedded upward-coarsening fluvial conglomerates. Radiometric ages from this unit from Suárez and Emparán (1997) are: four ignimbrites between 8.0 ± 0.5 and 8.3 ± 0.9 Ma, one of 9.5 ± 2.8 Ma at the base (K-Ar biotite), and two andesitic lavas of 8.0 ± 0.3 and 8.1 ± 0.6 Ma (K-Ar whole rock).

Upper Pleistocene to Holocene volcanic center

South of 38°S, two main active volcanic centers are related to the NNE-trending Liquiñe-Ofqui fault zone. The first is the Lonquimay volcanic system of Holocene age (LO in Figure 3), which is formed by a main cone and a NE-trending, 10-km-long fissure system, including scoria

craters, cinder cones, and vents (Moreno and Gardeweg, 1989). North of the Lonquimay volcano, four small minor eruptive centers form another 24-km-long, NE-trending volcanic alignment. The Llaima volcano is the second volcanic system (LL in Figure 3), which is composed by a Holocene edifice and a 17-km-long, NE- to NNE-trending field of parasite cones and fissure vents. At 39°S, the Rucapillán volcanic complex is located west of the volcanic front, almost in the Central Depression. This complex is formed by a NNW-trending, 3-km-long alignment of Holocene maars (Moreno and López-Escobar, 1994). To the east, the Sollipulli Pleistocene volcano is composed of a 3-km-wide caldera and several scattered Holocene parasite cones oriented in N-S and E-W directions. This center is located in the eastern part of the volcanic front spatially related to the Reigolil-Pirihueico fault (Lara et al., 2001), an eastern branch of the Liquiñe-Ofqui fault zone (Figure 3.3).

3.4.3.2 Structural evolution

Late Miocene orogenic phase: Bio-Bio profile

The E-W profile at ~38.8°S, across the upper Bio-Bio River (Figure 3.12), illustrates the structural style of the southern domain. The Cura-Mallín Formation is exposed in a wide anticline and a west-facing flexure. The limits of this uplifted part of the basin are moderate-angle reverse faults that thrust the Mesozoic on top of the Miocene units.

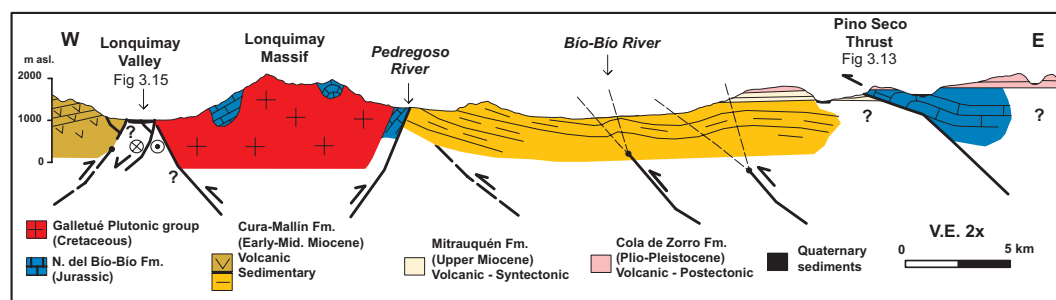


Figure 3.12: Geological cross section of the upper Bio-Bio River at ~38.5°S. The structure is controlled by the thrusting of the Mesozoic sequence over mildly deformed Oligocene-Miocene Cura-Mallín beds.

In the eastern part of the profile, the N-S-trending Pino Seco thrust (Figure 3.13), identified by Suárez and Emparán (1997), superposes the Jurassic Nacientes del Bio-Bio Formation on top of the late Miocene Mitrauquén Formation. This structure is cut by a regional angular unconformity at the base of the Pliocene-Pleistocene Cola de Zorro Formation. Thus, the age of the latest thrusting in this area is between 8.0 ± 0.3 and 4.8 ± 0.5 Ma, which is bracketed by the ages from the Mitrauquén and Cola de Zorro Formations.

In the western part of the section, the contact between the Lonquimay Massif and the Cura-Mallín Formation is not exposed. This contact was interpreted as an unconformity by Suárez and Emparán (1997) and later as an east-dipping inverted normal fault by Radic et al. (2002). On the eastern side of the upper Pedregoso River (Figure 3.12), Cura-Mallín strata dip homogeneously ~20°E and shallow eastward, whereas on the western side, folded Mesozoic rocks intruded by Cretaceous and Miocene granitoids are exposed. Gräfe et al. (2002) reported an apatite fission-track age of 5.8 ± 1.0 Ma for a Miocene granite of the Lonquimay Massif, indicating uplift and exhumation of the massif during the late Miocene. Since the Cura-Mallín Formation is only little deformed east of this contact, we interpret this contact as a west-dipping thrust controlling the bulk of the uplift of the Lonquimay Massif (Rosenau et al., 2001).

The contact between the Mitrauquén and Cura-Mallín Formations is concordant along the eastern Bio-Bio Valley. In contrast with the underlying Cura-Mallín strata, the dip of the Mitrauquén unit decreases upward from locally 40°E to subhorizontal (Figs. 14A and 14B). The present-day drainage network is formed by torrential rivers, but in contrast, the Mitrauquén conglomerates, which represent braided river systems (Suárez and Emparán, 1997), show evidence of an older landscape with much lower relief. The conglomerate sequence is an ~250- m-thick, coarsening upward unit (Figure 3.14B). Along the Mitrauquén Valley, the upper lavas of this unit show a progressive upward-sequence decrease in dip from 20°E at the valley bottom to a horizontal disposition ~300 m higher, where they are conformably overlain by the Cola de Zorro Formation, which suggests syntectonic deposition (Figure 3.14C). Thus, we interpret the Mitrauquén Formation as a syntectonic unit, and relate the deposition of the upward-coarsening conglomerate sequence to surface uplift caused by activity of the Pino Seco thrust. A viable

scenario is that the Pino Seco thrust was blind during the deposition of the Mitrauquén unit, which was being progressively folded during deposition between ca. 9 and 8 Ma. During a later stage, the thrust propagated to the surface, juxtaposing the Nacientes del Bío-Bío and Mitrauquén Formations. Erosion and deposition of the Pliocene Cola de Zorro plateau volcanics removed and covered the Mitrauquén unit from the top and part of the back limb of the fold, respectively.

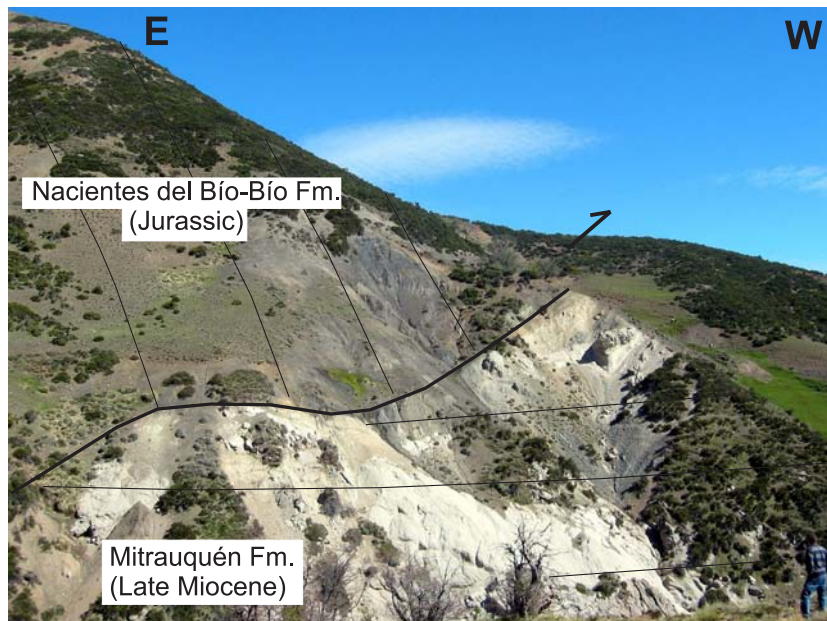


Figure 3.13: View to the south of the Pino Seco thrust, juxtaposing Jurassic turbidites of the Nacientes del Bío-Bío Formation over ignimbrites and conglomerates from the Mitrauquén Formation. The bedding of the Jurassic strata is subvertical, not clearly seen in the photo. This structure is unconformably overlain by Pliocene-Pleistocene volcanic rocks of the Cola de Zorro F Formation, constraining the last pulse of contractional deformation between 8.0 and 5.6 Ma.

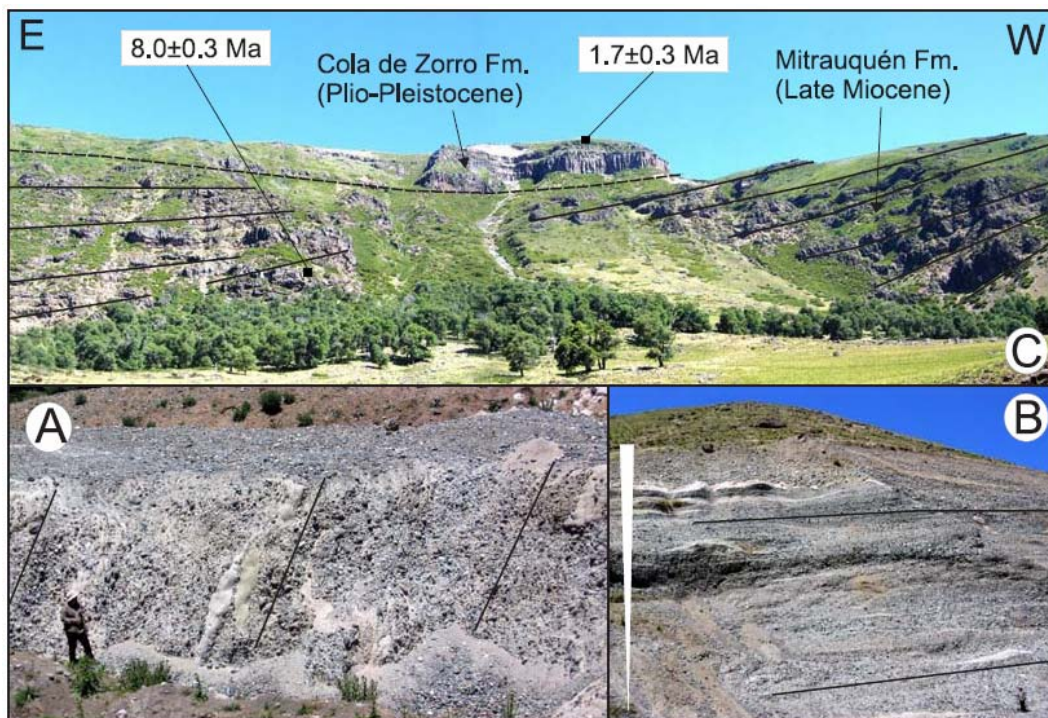


Figure 3.14: Syntectonic deposits of the Mitrauquén Formation. (A) View of steeply dipping fluvial conglomerates. (B) View of subhorizontal, upward-coarsening conglomerates; person on

the lower right for scale. (C) View toward the south of andesitic lavas at the upper Mitrauquén valley. Note the upward decrease in dip. Ages are from Suárez and Emparán (1997).

Pliocene to Quaternary transtension: Lonquimay Valley

The Lonquimay glacial valley trends NNE for ~30 km (Figure 3.3). This linear depression is tectonically controlled and bounded to the west and east by transtensional faults. The following features (Figure 3.15) are interpreted from a LandSat ETM+ image and air photos: (1) the Lonquimay River runs along the eastern side of the valley, presumably parallel to a NNE-trending fault system; (2) the fault system is formed by a series of NNE-trending faults, which delimit the occurrence of small ridges in the generally flat valley bottom; (3) triangular and trapezoidal facets characterize the up to 900-m-high western slope of the Lonquimay Massif, which delimits the Lonquimay valley morphologically to the east; and (4) outlets draining the Lonquimay Massif to the west into the Lonquimay valley are dextrally offset by NNE-trending faults. This is observed in fifteen outlets on the eastern part of the Lonquimay valley and on three at the western side of the Punta Negra River. Dextral offset of the outlets along the eastern side of the valley range from ~500 to 200 m.

Along a road cut 3.5 km east of Lonquimay, postglacial fallout pyroclastic and alluvial deposits are cut by mesoscale N-S-trending normal faults forming a horst-and-graben structure (Figure 3.16). North of this outcrop, a smooth topographic break is observed trending north in the valley floodplain limiting the San Pedro Lake to the east (Figure 3.15). We interpret this lake as a sag pond related to the observed Holocene faulting and graben formation in this area.

These observations indicate that the Lonquimay area experienced dextral transtensional deformation during the Quaternary, resulting in the formation of a half-graben with east-down polarity and an east-bending pull-apart structure to its northern end (Figure 3.15). Dextral offset was accumulated probably during the late Pleistocene–Holocene at this transtensional branch of the northern Liquiñe-Ofqui fault zone.

Holocene volcanism and deformation: Llaima pyroclastic cones

The Llaima volcano, located immediately west of the Liquiñe-Ofqui fault zone (LL in Figure 3) is one of the largest composite Holocene volcanoes in Chile (Figure 3.3). It includes a field of at least 40 parasite scoria cones trending NNE and NE for ~17 km (Naranjo and Moreno, 1991). In the northeastern part of the parasite cone field, interpretation of an air photo shows a set of two en echelon, NE-trending, 400- and 800-m-long faults cutting the side of a postglacial pyroclastic cone (Figure 3.17A). These two very recent faults controlled the subsequent effusion of five small vents. However, no clear field observations allowed determination of the kinematics of these faults.

According to Tibaldi (1995), in aligned pyroclastic cones that overlie a feeder dike or fault, the breaching angle—the angle between the orientation of the alignment of cones and the opening where the lava flows out of the cone (Figure 3.17B)—is indicative of the kinematics of the feeder fault in the substratum. In areas under extension, pyroclastic cones usually have fault-normal breaching angles, which are controlled by the dip of the fault and point to the downthrown block. In areas under a transtensional or strike-slip regime, fault-parallel and fault-oblique breaching dominates.

In the northeastern part of the Llaima volcano, most of the cones have low breaching angles (Figure 3.17C), which is indicative of strike-slip or transtensional deformation in the substratum. Following the geological and seismological observations of strike-slip deformation along the Liquiñe-Ofqui fault zone (e.g., Lavenu and Cembrano, 1999; Barrientos and Acevedo, 1992; Rosenau, 2004; Reinecker et al., 2004), we interpret the Holocene NE-oriented alignments of cones and fissures here as extensional shear fractures, which serve as channels for magma. These observations emphasize the control of the Liquiñe-Ofqui fault zone on the volcanic arc.

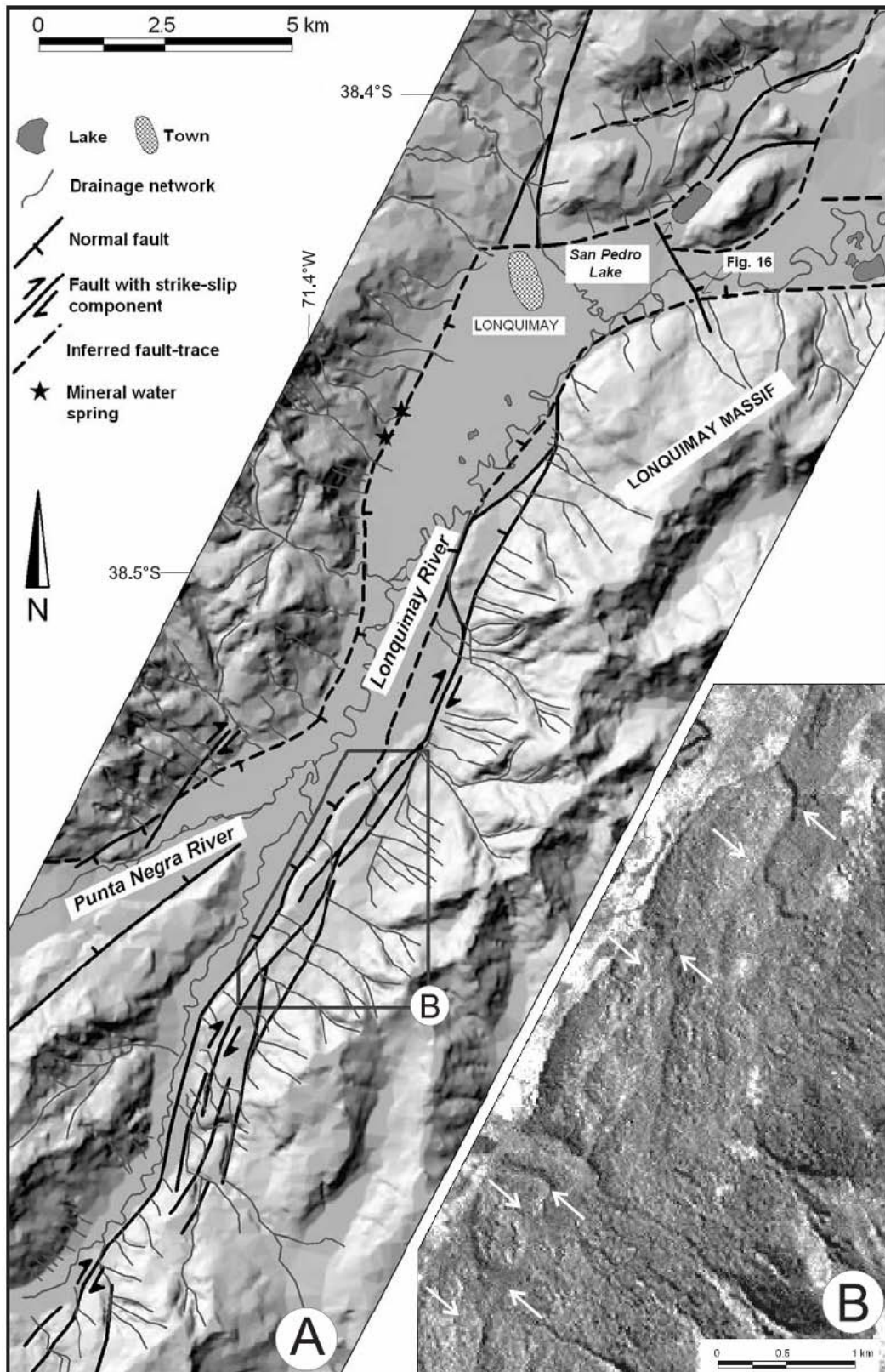


Figure 3.15: Quaternary deformation in the Lonquimay transtensional system. (A) Shaded-relief digital-elevation model with main drainage network and Quaternary faults. The Lonquimay valley is interpreted as a hemigraben. Note that the Lonquimay River north of 38.5°S runs on the eastern side of the valley, which may indicate Holocene tilting of the central block. The San Pedro Lake is a sag pond associated with Holocene normal faults shown on Figure 16. (B) Detail of LandSat ETM+ panchromatic band (14.25 m pixel). The white arrows show dextral offset of outlets by NNE-trending faults.



Figure 3.16: View to the south of Holocene fallout pyroclastic and alluvial deposits affected by normal faults with graben-and-horst geometry. Outcrop along international road, 3.5 km east of Lonquimay (see Figure 15).

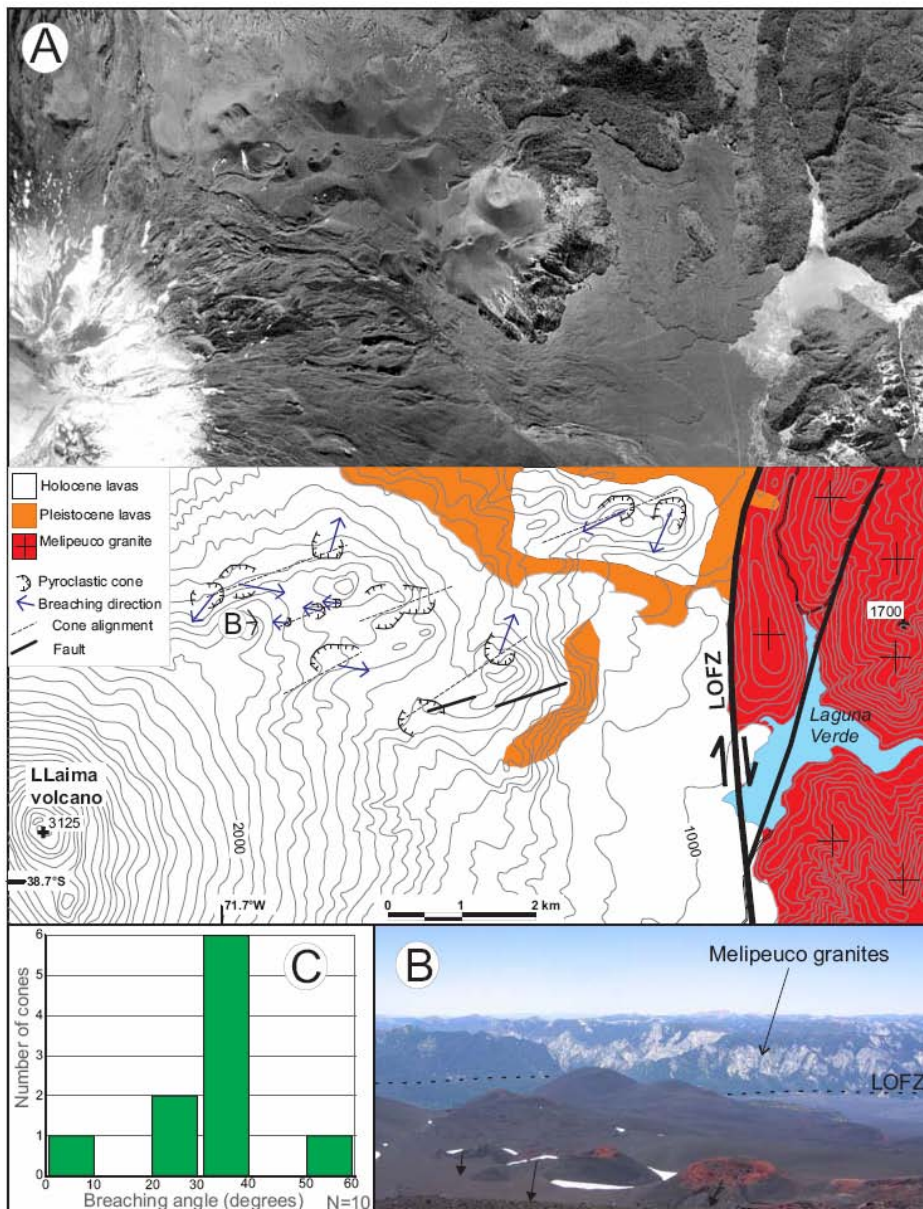


Figure 3.17: (previous page) Holocene volcanism and tectonics at the Llaima volcano. (A) Orthorectified air photo of the northeastern part of the Llaima volcano. (B) Geologic and topographic map of the same area as A. Contour interval is 50 m. (C) Histogram of the breaching angles measured in B (the breaching angle is the angle between the orientation of the alignment of cones and the opening from where the lava flows out of the cone). According to Tibaldi (1995), low breaching angles are indicative of strike-slip deformation along a feeder fault in the substratum. (D) View to the east of three aligned pyroclastic cones. The arrows indicate the direction of breaching. The Liquiñe-Ofqui fault zone (LOFZ) and Melipeuco granite (late Miocene) are shown. Note the pronounced scarp associated with the Liquiñe-Ofqui fault zone.

3.5 Tectonic evolution

Based on the integrated structural and stratigraphic data, we establish the following late Cenozoic tectonic evolution of the western Neuquén Andes between 37 and 39°S (Figure 3.18).

3.5.1 Cura-Mallín Basin formation: late Oligocene–middle Miocene (ca. 28–11 Ma)

During this stage, extensional tectonics and basin formation was contemporaneous with an increase in convergence rate between the Nazca and South American plates (Muñoz et al., 2000; Jordan et al., 2001). The Cura-Mallín volcano-sedimentary intra-arc basin was formed (Burns et al., this volume, chapter 8) as a continental rift with lacustrine sedimentation in internally drained subbasins with volcanoclastic input from the west (Suárez and Emparán, 1995; Kemnitz et al., 2005). The Cura-Mallín basin between 37 and 39°S is divided along-strike into two diachronic subbasins limited by the NE-trending Callaqui-Copahue-Mandolegüe transfer zone (Carpinelli, 2000; Radic et al., 2002; Melnick et al., 2002).

3.5.2 Shortening and uplift: late Miocene (11–6 Ma)

Following extension, a compressional tectonic regime during the late Miocene occurred coeval with the emplacement of large amounts of granitoid melts into the crust. During this compressional stage, the present-day Main Cordillera was built. Shortening resulted in uplift and exhumation of granitoids that intruded at depths of less than 3 km (Seifert et al., 2005). Deformation in the northern structural domain

(37–37.7°S) was characterized by a bivergent wedge geometry, similar to the mid-Tertiary basin at ~34°S (Godoy et al., 1999), although shortening amounts were smaller. Thrusts with a shallow detachment level developed in the eastern, sedimentary part of the basin, while the western volcanoclastic part was characterized by high-angle reverse faults. Deformation style differed in the southern structural domain (38–39°S), where uplift of Mesozoic units occurred along reverse faults. Shortening magnitudes decrease from north to south in the study area. The Callaqui-Copahue-Mandolegüe transfer zone marks the boundary between the northern and the southern structural domains accommodating the differences in total strain. The onset of mountain building, relief formation, and exhumation at ca. 11 Ma in the southern subbasin is constrained by clast-provenance studies (Kemnitz et al., 2005). The 9.5 to 8.0 Ma conglomerates and lavas of the Mitrauquén unit are interpreted as syntectonic deposits of this orogenic phase. Ignimbrites and minor lavas of the Mitrauquén unit are the only volcanic products of late Miocene age in the Main Cordillera at this latitude, where shortening ceased before 5.6 Ma. This volcano-tectonic scenario is similar to the one proposed by Coira et al. (1993) for the ignimbrites to the north in the Puna region.

3.5.3 Liquiñe-Ofqui fault zone transtension: Pliocene–early Pleistocene (5–1 Ma)

Cessation of shortening in the area was accompanied by migration of the volcanic arc from an eastern position at ~69–70°W toward the trench over more than ~150 km (Kay et al., 2006). Volcanism was reestablished in the Main Cordillera, in an ~50-km-wide zone north of 38°S, which may be up to ~90 km wide to the south. Reestablishment of the volcanic arc was temporally coincident with the renewal of extensional deformation. During this stage, as the obliquity of plate convergence was continuously increasing (Somoza, 1998), motion on the Liquiñe-Ofqui fault zone initiated. Transtensional deformation was localized along the northern segment of the Liquiñe-Ofqui fault zone, including the Agrio caldera pull-apart structure and the Lonquimay and El Barco fault zones. Continued slip along the Callaqui-Copahue-Mandolegüe structure controlled the strain transfer from the transtensive northern Liquiñe-Ofqui fault zone to the Copahue-Antiñir thrust front in the backarc flank of the Main Cordillera.

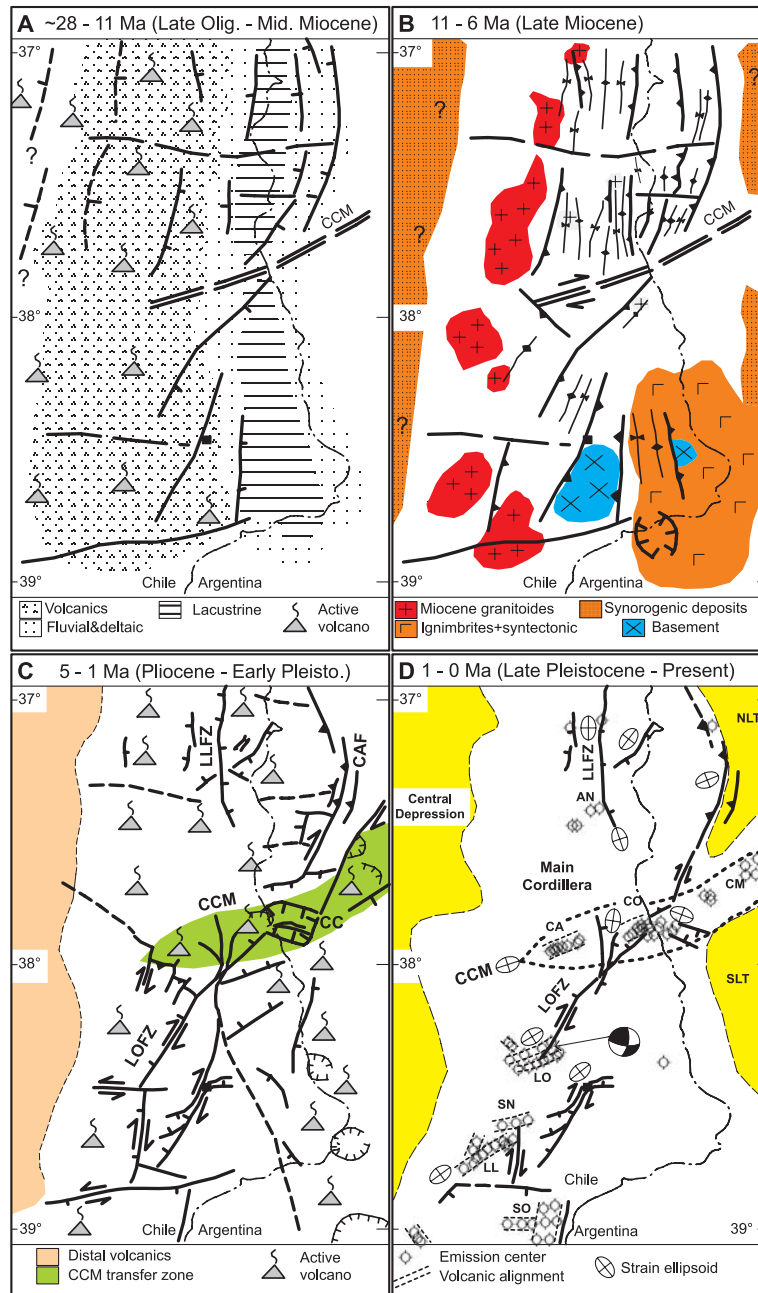


Figure 3.18: Series of interpretative maps summarizing four main phases in the tectonic evolution of the western Neuquén Andes between 37 and 39°S, based on structural data, stratigraphic facies, sediment thickness, interpretation of digital-elevation models and remote-sensing data, and published information. The town of Lonquimay is represented by a black square. (A) Formation of the Cura-Mallín basin during extensional tectonics, CCM—Callaqui-Copahue-Mandolegüe transfer zone; long stippled lines indicate inferred secondary transfer zones. (B) Inversion of the Cura-Mallín basin, exhumation of Miocene granitoids, and hiatus in volcanism except for the Mitrauquén ignimbrites. (C) Reestablishment of the volcanic arc, extension of the former orogenic structure, transtensional deformation associated with the northern Liquiñe-Ofqui fault zone (LOFZ), and along-strike strain decoupling by the CCM transfer zone. Note formation of the Agrio caldera pull-apart (AC), Copahue-Antiñir thrust front (CAF), and Lago de la Laja fault zone (LLFZ). (D) Narrowing of the volcanic arc, localization of the deformation along the axial intra-arc and Liquiñe-Ofqui fault zone. Focal mechanism is from Barrientos and Acevedo (1992). The western extent of the northern and southern Loncopué trough (NLT, SLT) (Ramos, 1977) and associated backarc volcanic centers are shown. Volcanic centers shown: AN—Antuco-Sierra Velluda, CA—Callaqui, CO—Copahue, AC—Agrio caldera, CM—Cordillera de Mandolegüe, LO—Lonquimay, LL—Llaima, SO—Sollipulli.

Scientific Technical Report STR 07/01

DOI: 10.2312/GFZ.b103-07012

3.5.4 Extension and transtension: late Pleistocene–Holocene

During the late Pleistocene, the volcanic arc narrowed to its present position (Stern, 1989). Deformation is closely associated with volcanic activity along the Liquiñe-Ofqui fault zone in the axial intra-arc zone. All the centers south of the Callaqui-Copahue-Mandolegüe transfer zone have Liquiñe-Ofqui fault zone–related strike-slip structural elements. North of this transfer zone, late Pleistocene–Holocene deformation is localized along the Lago de la Laja extensional fault zone and to the north of $\sim 37.5^{\circ}\text{S}$; compressional deformation is continuously present along the backarc (Folguera et al., 2004).

3.6 Discussion: geodynamic implications

The factors controlling extension and shortening in the Southern Andes have been the subject of controversial debate. The late Oligocene plate reorganization in the South Pacific (Tebbens and Cande, 1997) produced an increase in the convergence rate between the Nazca and South American plates (Somoza, 1998). Muñoz et al. (2000) and Jordan et al. (2001) showed that conventional models linking shortening in the overriding plate to high convergence velocities do not account for the Neogene tectonic evolution of the Neuquén Andes, since regional extensional tectonics and basin formation are coeval to high convergence rates in the Andes south of $\sim 33^{\circ}\text{S}$. The onset of shortening in the Neuquén Andes during the late Miocene is coincident with the flattening of the slab, emplacement of shallow crustal granitoids, and a lack of volcanism in the Main Cordillera, as discussed by Kay (2002) and Kay et al. (this volume, chapter 2). Low subduction angles and the onset of shortening in the Miocene have been previously proposed for the Central and Southern Andes between ~ 19 and 39°S (Isacks, 1988; Allmendinger et al., 1997).

Shortening in the Neuquén Andes ceased at ca. 6 Ma and was followed by the reestablishment of volcanic activity in the Main Cordillera and extensional tectonics related to steepening of the slab and a westward trench retreat (Muñoz and Stern, 1988; Stern, 1989). This scenario contrasts with those proposed for the areas north of $\sim 34^{\circ}\text{S}$, where the downgoing plate maintained a lower angle and shortening has been more or less continuous since the Miocene and is still ongoing in the foreland (Giambiagi et al., 2003; Cortés et al., 1999). The steepening of the slab in the Neuquén Andes is considered to be the main driving factor for the cessation of shortening and the onset of extension during the Pliocene.

Two factors may explain the onset of the strike-slip Liquiñe-Ofqui fault zone at ca. 6–5 Ma: (1) the plate reorganization, which caused a continuous increase in the obliquity of the Nazca–South America convergence since the late Miocene (Somoza, 1998); and (2) steepening of the slab and reestablishment of the volcanic front along the Main Cordillera, which causes thermal weakening and strain localization in the intra-arc zone. Arrival of the northward migrating Chile Rise collision zone at the southern end of the volcanic arc might have additionally triggered initiation of the Liquiñe-Ofqui fault zone (Forsythe and Nelson, 1985).

Localization and evolution of the northern end of the Liquiñe-Ofqui fault zone at 38°S may be related to a combination of the following factors: (1) along-strike changes in physical properties of the oceanic plate at the Valdivia fracture zone system, separating a segmented and rough oceanic crust produced by the Chile Rise from a homogeneous and smoother crust produced by the East Pacific Rise (Tebbens and Cande, 1997); (2) widening of the orogen northward by increasing backarc shortening during the Miocene (Kley et al., 1999) and partitioning of oblique subduction over a broad area of deformation in the Central Andes (Folguera et al., 2002); and (3) a probable threshold distance in the ridge-push force exerted by the Chile Rise northward (Cembrano et al., 2000).

3.7 Conclusions

The western flank of the Neuquén Andes between 37 and 39°S records an episodic evolution during the Neogene, which can be summarized in four main tectonic phases: (1) late Oligocene–middle Miocene extension and development of a wide zone of volcanic activity and a segmented intra-arc continental rift basin; (2) late Miocene shallowing of the slab, triggering a gap in volcanic activity in the Main Cordillera and compressional deformation, resulting in shortening, uplift, and exhumation; (3) Pliocene to early Pleistocene steepening of the slab, reestablishment of the volcanic arc, extension of the orogenic structure, and transtension at the northern limit of the intra-arc Liquiñe-Ofqui fault zone; and (4) late Pleistocene to Holocene narrowing of the volcanic arc and localized extensional-transtensional deformation in the axial intra-arc zone.

Acknowledgments

This work was supported by the GFZ-Potsdam Southern Andes project, PIP 4162 and PICT 059 (Conicet to V.A. Ramos) and SFB 267 “Deformation Processes in the Andes” founded by the DFG. Melnick acknowledges founding by the DAAD International Quality Network (IQN) at Potsdam Universität and is grateful to M. Strecker and O. Oncken for their continuous support. We would like to thank: V. Ramos, S. Kay, J. Cembrano, T. Vietor, M. Brandon, D. Sellés, P. Alvarez, and J. Clavero for fruitful discussions, and F. Charlet, M. de Batist, B. Scharf, and O. Buettner for sharing their seismic lines and bathymetry from the Lago de la Laja. Reviews by E. Godoy and A. Meigs greatly helped to improve the ideas presented in this work.

4. Inversion of forearc basins in south-central Chile caused by rapid glacial age trench fill

Abstract

This study examines the response of a forearc to the increase in sediment flux to the trench caused by the onset of glacial denudation in the Patagonian Andes. We investigated shelf-coastal basins in south-central Chile, which generally comprise Eocene-early Miocene near-shore facies overlain by late Miocene-early Pliocene deep-water siltstones and by late Pliocene-Quaternary near-shore deposits. Seismic profiles and coastal exposures reveal Eocene-early Pliocene extension followed by ongoing late Pliocene compression evidenced from growth strata adjacent to seismically active reverse faults. The onset of major global cooling at ca. 6 Ma triggered glacial denudation in the uplifted high Andes. Exhumed material transported along the steep and humid Andean western slope increased trench sedimentation rates and caused continuous accretion and subduction of terrigenous material. We interpret forearc basin inversion as a response to a decrease in slope and basal friction of the wedge caused by frontal accretion and subduction of water-rich material, respectively, in order to reach a critical taper. This process lifted the shelf ~1.5 km during the middle Pliocene. The Juan Fernández Ridge and Chile Rise confined >2-km trench fill between 45–34°S, limiting accretion and basin inversion. Glacial age trench fill and the steady decrease in plate convergence rate shifted this segment of the margin from erosive to accretionary during the Pliocene.

4.1 Introduction

Trench fill and plate convergence rate exert a first-order control on the accretionary or erosive nature of subduction margins (von Huene and Scholl, 1991; Clift and Vannucchi, 2004). Thick trench fill leads to frontal accretion resulting in low-tapered wedges formed by imbricated thrust sheets (Davis et al., 1983). Thin trench fill, in contrast, leads to erosive margins with high-tapered wedges that may be gravitationally unstable and dominated by extension. Material removal from the toe and base of the continent by tectonic erosion explains subsidence evident in the variation from near-shore to deep-water environments in forearc basins (e.g., von Huene and Scholl, 1991). Forearc basins are probably the most suitable archives to study processes relating plate coupling and wedge stability over million year time scales, because of their position above the plate interface and suitable fauna to constrain age and paleobathymetry.

The Andean margin is particularly well suited to study the impact of climate change on tectonic processes due to their extreme along-strike variability, where coeval environments in similar positions have different boundary conditions. The Andes are formed by subduction of the Nazca plate under the South American continent (Figure 4.1) at a modern global positioning system convergence rate of 66 mm/yr, which has decreased ~40% over the last 10 m.y. (Kendrick et al., 2003; Somoza, 1998). Mean precipitation along the Chilean (windward) side of the orogen decreases northward from >3 to <0.3 m/yr, between 46–33°S. The Chile Rise and Juan Fernández Ridge (Figure 4.1) are the main oceanic features causing major segmentation of the margin (Cande and Leslie, 1986; Yáñez et al., 2001). To gain insight into the influence of variable sediment flux caused by climate change on plate coupling, wedge stability, and forearc deformation processes, we investigated the stratigraphy and structure of forearc basins in south-central Chile using field data and reflection-seismic profiles correlated with boreholes from ENAP—the Chilean state oil company (methods and data sources can be found in the Appendix A).

4.2 Tectonic setting of forearc basins in south-central Chile

Numerous basins of differing size developed along the Chilean continental shelf, tapering toward the slope and coast (descriptions and profiles in Mordojovich, 1981; González, 1989). In general, between 34–45°S basin fill comprises a basal late Cretaceous marine unit, Eocene-middle Miocene coastal and coal-bearing lagoon facies, Tortonian-Zanclean (late Miocene, N16-early Pliocene, N19) lower bathyal siltstones, and Gelasian (late Pliocene)-Pleistocene near-shore sands

4. Inversion of forearc basins

(e.g., García, 1968; Le Roux and Elgueta, 1997, 2000; Finger et al., 2007). Cretaceous to Miocene sequences fill discrete depocenters with thicknesses of 0.8–3.1 km bounded by basement highs that segment individual basins (Figure 4.1). These units are unconformably covered by the Plio-Quaternary sequence, which in turn is continuous over most of the shelf. In the Navidad, Arauco, and Chiloé basins, as well as in boreholes H and D1 (Figure 4.1), the Tortonian-Zanclean unit consists of slope apron sediments with benthic foraminifers and ostracodes that indicate down-slope transport, deposition at lower bathyal depths, and rapid subsidence (Finger et al., 2007; Encinas et al., 2005). Thus between 10.9–3.6 Ma, the present shelf and sectors of the coast in most, if not the entire 34–45°S segment subsided >1.5 km.

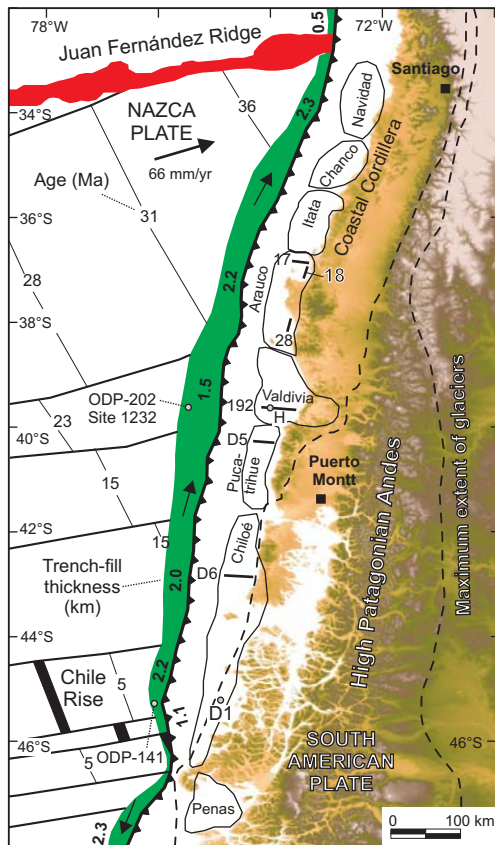


Figure 4.1: Tectonic setting of the south-central Chile margin. Forearc basins after González (1989). Nazca plate and trench-fill thickness from Bangs and Cande (1997). Maximum extent of glaciers from Rabassa and Clapperton (1990). ENAP reflection-seismic profiles discussed in the text are shown.

Coal engineers recognized normal faults displacing Eocene seams several hundred meters in the Arauco Basin, and extensional structures are widespread in the 34–45°S basins (Mordojovich, 1981). Seismic profiles and borehole data show that thicknesses of the Eocene-early Pliocene units increase across normal faults (Figure 4.2C), suggesting syn-extensional deposition followed by minor compressional folding (González, 1989). Coeval subsidence has also been documented by stratigraphy (e.g., García, 1968; Le Roux and Elgueta, 2000), and syndepositional normal faults are observed at various scales (Figs. A2 and A3).

4.3 Middle Pliocene forearc basin inversion and uplift

Chilean forearc basins have a complex structure controlled by heterogeneous basement fabrics (González, 1989). However, these basins have some similarities: the thicker section is in the center of the present shelf; pre-late Pliocene units have strong variations in thickness controlled by normal faults, which are locally inverted; and, the late Pliocene-Quaternary unit is continuous over most of the shelf and locally affected by reverse faults and fault-propagation folds. Near these folds, onlaps, an increase in thickness of continuous strata, and progressively upward-decreasing dip indicate syn-contractual deposition (Figure 4.2). In the axial zone of anticlines, small bending-moment normal faults are imaged in reflection profiles (Figure 4.2A) and are common in exposed rocks as well.

Strain magnitudes are higher and exposures better in the Arauco Basin. Here, seismic profiles image inversion of selected Eocene-early Pliocene normal faults in the mid-Pliocene and

4. Inversion of forearc basins

shortening since (Figure 4.2C). Clusters of shallow seismicity and focal mechanisms show that some reverse faults that controlled syntectonic deposition are active (Figure A1) (Melnick et al., 2005). Compression normal to the margin is consistent from seismological data as well as growth strata in reflection profiles (Figure 4.2) and Plio-Pleistocene outcrops (Figure 4.3). Similarly, Lavenu and Encinas (2005) proposed late Pliocene inversion of the extensional Navidad Basin (34°S) and ongoing compression. In the Valdivia Basin (39°S), seismic profile 192 images inverted normal faults, folding of Miocene strata, and continuous late Pliocene-Quaternary syntectonic deposition (Figure 4.2D). In the Pucatrihue (41°S) and Chiloé (43°S) basins, profiles D5–06 and D6–40, respectively (location in Figure 4.1), also image similar inversion structures and syntectonic sequences (Figs. 14 and 16 of Mordojovich, 1981).

At least 1.5 km of uplift during the middle Pliocene is evident from coastal exposures of early Pliocene lower bathyal siltstones overlain by late Pliocene near-shore sandstones (Figure A2). This is the case in the Navidad, Arauco, and Chiloé basins, as well as boreholes H and D1 (Finger et al., 2007; Encinas et al., 2005). Therefore this seems to be common to the entire coastal forearc region between 34 and 45°S, although local processes like selective reactivation of inherited discontinuities caused segmentation and gradients in shortening magnitudes.

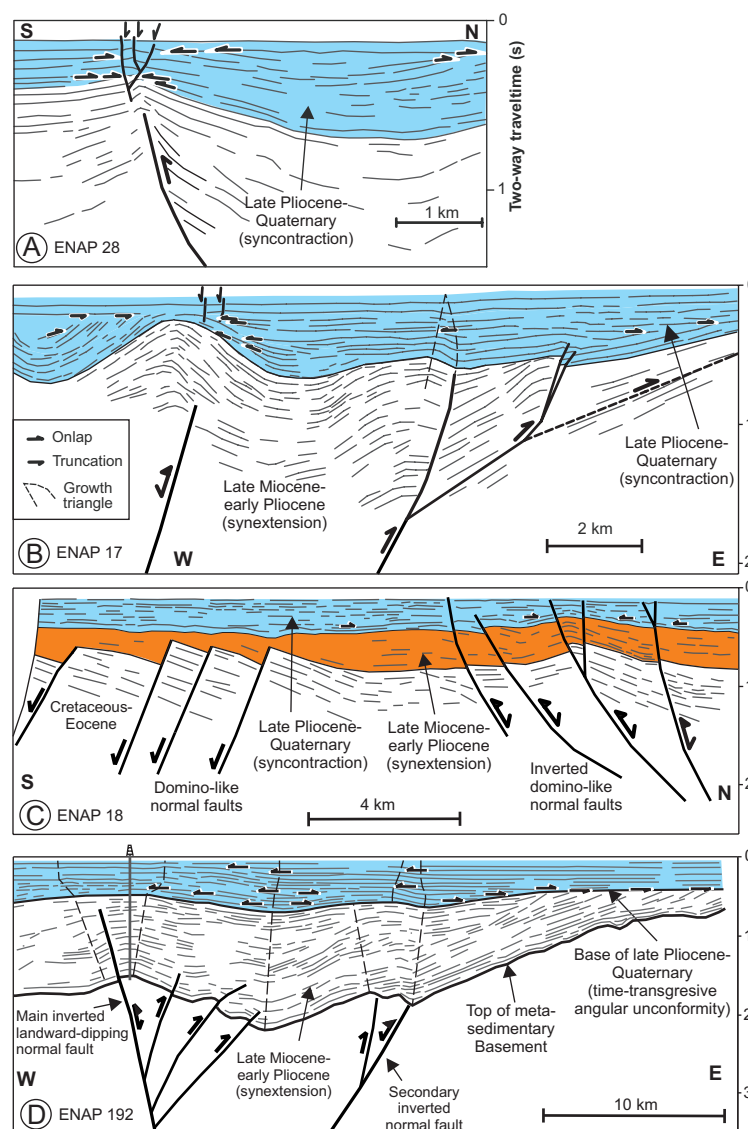


Figure 4.2: Line drawing of ENAP time-migrated, reflection-seismic profiles showing inversion of Eocene-early Pliocene extensional forearc basins and late Pliocene-Quaternary syn-contraction sequences. Stratigraphy correlated with nearby boreholes (descriptions and profiles in Figure A4).



Figure 4.3: Late Pliocene-Pleistocene near-shore syntectonic sequence at Coi-Coi, 38.5°S. Person for scale.

4.4 Mountain building, glacial denudation and trench fill

The onset of glacial erosion and denudation in the high Andes requires two factors: (1) topographic relief and (2) cooling. (1) Oligocene-early Miocene continental and marine extensional basins dominated the Andes between 33 and 45°S, and thus elevations and relief were low (Jordan et al., 2001). These basins were inverted and uplifted during the Miocene forming the modern mountains (Figure 4.5B). At 37–39°S, syntectonic deposits indicate shortening and uplift between 11 and 8 Ma (Melnick et al., 2006a). At 42–46°S, fission-track data show that transpression and exhumation started between 16 and 10 Ma and, in addition to landscape analysis, that glacial erosion has been the main contributor to denudation since ca. 7 Ma (Thomson, 2002). Likewise, at 47.5°S changing patterns of carbon and oxygen isotopes reflect >1 km of surface uplift between 16 and 14 Ma (Blisniuk et al., 2005). (2) The onset of major Antarctic ice-sheet expansion at 7–5 Ma (Zachos et al., 2001) is consistent with the oldest glacial deposits in Patagonia bracketed between 7–4.6 Ma (Mercer and Sutter, 1982), and various proxies indicating significant cooling since ca. 6 Ma (Lear et al., 2000) (Figure 4.5A). Thus conditions required for the onset of glacial denudation in the Patagonian Andes were achieved by latest Miocene-earliest Pliocene. Rivers along the steep and humid western flank of the Andes have transported the eroded material to the trench, and south of 42°S glaciers reached the coast (Figure 4.1). High Pliocene-Quaternary trench sedimentation rates of 0.3–1 mm/yr at sites of Ocean Drilling Program (ODP) Leg 141 (location in Figure 4.1) resulted from the extreme humidity and frequently extended glaciations (Kilian and Behrmann, 2003). Site 1232 of ODP Leg 202 (location in Figure 4.1) drilled into 0.78-Ma turbidites yielding a similar average sedimentation rate of 0.47 mm/yr (Shipboard Scientific Party, 2003).

South of the Juan Fernández Ridge, 1.5–2.3 km of terrigenous sediments fill the trench (Figure 4.1), leading to an accretionary margin (Bangs and Cande, 1997). In contrast, north of the Juan Fernández Ridge trench fill consists of <0.5-km-thick slope debris and the margin is erosive (Yáñez et al., 2001). The northward-increasing age of the Nazca plate (Figure 4.1) causes its top to plunge northward controlling sediment transport in the trench. Most of the sediments are supplied from the southern region limited by the Chile Rise, while the Juan Fernández Ridge forms a barrier blocking transport farther north (Figure 4.1) (Bangs and Cande, 1997). The Juan Fernández Ridge migrated southward until 10 Ma and has been stationary at 33°S since (Yáñez et al., 2001), while the Chile Rise has migrated continuously northward since 14 Ma (Cande and Leslie, 1986) (Figure 4.5E). The position of these oceanic ridges played a key role in restraining and enhancing trench sediment storage between 33 and 45°S.

4.5 Discussion

The nature and thickness of trench fill has a first-order control on Andean subduction dynamics (Lamb and Davis, 2003). During Oligo-Miocene times, low relief and slow exhumation in the Patagonian Andes resulted in a sediment-starved trench, which in addition to high plate convergence rates caused subduction erosion (Figs. 4.5C and 4.5D). This process explains >1.5 km of forearc subsidence evident from coastal sequences overlain by 10.9–3.6-Ma lower bathyal

sediments (Encinas et al., 2005). Kay et al. (2005), based on eastward migration of the frontal volcanic arc, also proposed subduction erosion during ~19–3 Ma (Figure 4.5B). Lower bathyal sediments overlain by near-shore deposits between 34 and 45°S imply >1.5 km uplift during the mid Pliocene, entailing an uplift rate of ~1.3 mm/yr, which is similar to the late Quaternary uplift rate at Arauco (Melnick et al., 2005). However, unsteady uplift, coastal erosion and possibly migration of deformation arcward causing uplift of the Coastal Cordillera (Figure 4.1) inhibited complete emergence of the shelf.

Considering the onset of glacial denudation at ca. 6–5 Ma and ODP trench sedimentation rates, we believe that by mid-Pliocene times trench fill was >1 km, the minimum thickness for accretion (Clift and Vannucchi, 2004). Thus we relate mid-Pliocene forearc uplift to accretion of glacial trench fill. In contrast, vertical movements in coastal basins north of the Juan Fernández Ridge, where trench fill has been <0.5 km, have not exceeded ~210 m, at rates <0.1 mm/yr, in the last 15 m.y. (Le Roux et al., 2005). The northward increase in slab age could contribute to the decrease in coastal uplift north of the Juan Fernández Ridge, but no clear correlation is observed in the available uplift rates of the margin (Figure 4.4).

Continuous syntectonic deposition evidence compression and ongoing shortening over the last ~3 m.y. As predicted by the taper theory, a Coulomb wedge will deform internally when material is accreted to its toe in order to reach the critical taper angle (Davis et al., 1983). Compression in the forearc reflects a low taper and wide seismogenic coupling zone needed for the plate interface shear stress to exceed the lateral tension caused by margin topography (Wang and He, 1999). The taper is lowered by continuous frontal accretion of glacial-derived trench fill, which decrease the slope, and by subduction of these water-rich sediments that reduce basal effective friction (Davis et al., 1983). These processes and the decreasing plate convergence rate that reduced frictional heat allowing wider coupling (Lamb and Davis, 2003) resulted in forearc compression after glacial age filling of the south Chile trench. Contrastingly, in north Chile where taper is higher and coupling narrower extension dominates the forearc (Lamb and Davis, 2003, and references therein).

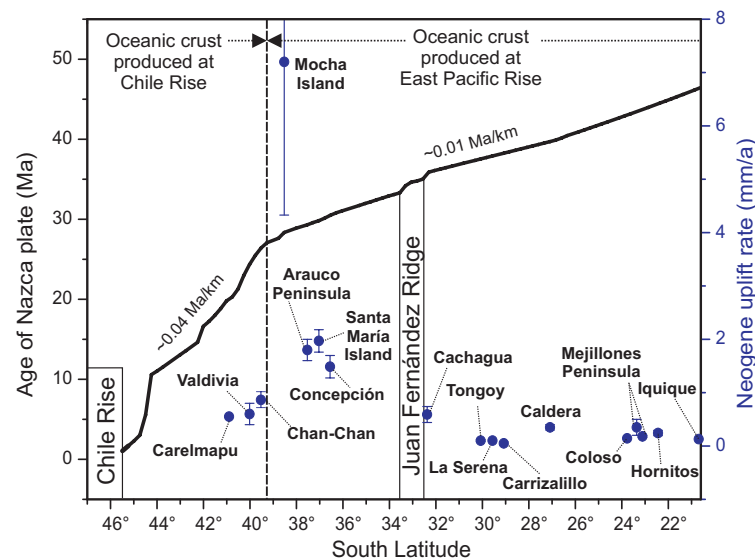


Figure 4.4: Age of the Nazca plate at the trench and Neogene uplift rates along the coast of Chile. Uplift rates decrease north of the Juan Fernández Ridge, which we relate to the lack of significant trench fill and subduction erosion. No clear correlation between slab age and coastal uplift rate is observed in these data. The kink in the age curve is caused by the transition between oceanic crust formed at the Chile Rise to the south and at the East Pacific Rise to the north (Tebbens and Cande, 1997). Uplift rates compiled from: Carelmapu—Atwater et al. (1992); Valdivia—Pino et al. (2002); Chan-Chan—Pino and Navarro (2005); Mocha Island—Kaizuka et al. (1973), Radtke (1989), Nelson and Manley (1992); Arauco—Kaizuka et al. (1973) and Melnick et al. (2005); Isla Santa María—Melnick et al. (2006b), Bookhagen et al. (2006); Tongoy—Le Roux et al. (2006); Carrizalillo—Le Roux et al. (2005); Caldera—Marquardt et al. (2004); Mejillones Peninsula—Ortlieb et al. (1996a), Marquardt (2005); Hornitos—Ortlieb et al. (1996b); Concepción, La Serena, Cachagua, Coloso, Iquique—Radtke (1989). Age of the Nazca plate from Müller et al. (1997).

We propose that the shift from erosive to accretionary conditions during the Pliocene and inversion of forearc basins were caused by (1) the increased sediment flux to the trench produced by the onset of glacial denudation in the uplifted high Andes (Figs. 4.5B and 4.5D); (2) a steady decrease in plate convergence rate (Figure 4.5C); and, (3) the stationary position of the JFR (Figure 4.5E), which blocked trench sediment transport farther north. Glaciations started at ca. 6 Ma, but our observations constrain the onset of inversion as ca. 3 Ma. Considering ODP sedimentation rates and that trench fill is frontally accreted and subducted, this lag should represent the time required to reach the minimum thickness for accretion and to lubricate the entire coupling zone. We conclude that the shift to accretion and onset of forearc compression in south-central Chile resulted primarily from Miocene mountain building and climate change, decreasing plate convergence rate, and position of oceanic ridges.

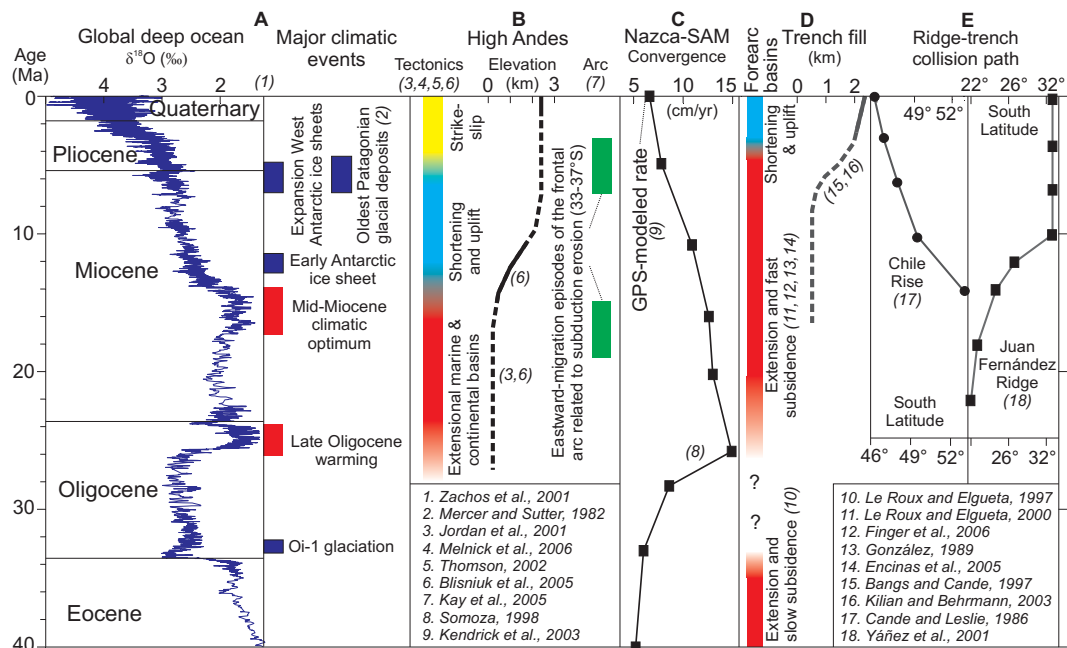


Figure 4.5: Climate and tectonics of the Patagonian Andes. A, Major climatic events and long-term trends in benthic oxygen isotope ratios, reflecting changes in ice volumes. B, Tectonic phases of the high Patagonian Andes, postulated mean elevations, and eastward arc migration episodes related to subduction erosion. C, Plate convergence velocity at 30°S. GPS—global positioning system; SAM—South America; D, Tectonic phases in 34–45°S forearc basins and estimated mean trench-fill thickness. E, Path of Chile Rise and Juan Fernández Ridge.

Acknowledgments

We thank Empresa Nacional del Petróleo (ENAP-Chile) for providing seismic profiles and M. Strecker, A. Tassara, and S. Nielsen for discussions and comments. This is publication GEOTECH-219 of the TIPTEQ project of BMBF and DFG, grant 03G0594. S. Cande and an anonymous reviewer provided constructive comments.

5. Coastal deformation and great subduction earthquakes, Isla Santa María, Chile (37°S)

Abstract

Isla Santa María at the active margin of south-central Chile is the result of earthquake-related uplift and deformation in the forearc since at least late Pleistocene time. Field mapping, dating of key depositional horizons, and analysis of seismic reflection profiles reveal ongoing deformation in this sector of the Chilean forearc. The 30 km² island is located ~12 km above the interplate seismogenic zone and 75 km landward of the trench. It is situated near the southern termination of the Concepción earthquake rupture segment, where Charles Darwin measured 3 m of coseismic uplift during a M>8 megathrust earthquake in 1835. Permanent post-earthquake deformation from this earthquake and an earlier event in 1751 is registered by emerged, landward tilted abrasion surfaces. Uplift at ~2 m/k.y. and tilting at ~0.025°/ka of the island have been fairly constant throughout the late Quaternary and have resulted in emergence of the island above sea level ~31 ka ago. The island comprises a late Pleistocene upper, tilted surface with two asymmetric tilt domains, and Holocene lowlands characterized by uplifted and tilted strandlines. Industry off-shore seismic reflection profiles covering an area of ~1800 km² and crustal seismicity reveal active reverse-fault cored anticlines surrounding Isla Santa María; the principal fault apparently roots in the plate-interface thrust. These reverse faults in the upper plate result from inversion of late Cretaceous to early Pliocene normal faults and rift structure of the Arauco forearc basin. Positive inversion of these inherited structures started between 3.6 and 2.5 Ma and resulted in continuous shortening rates of ~0.8 mm/yr. The seismic reflection profiles show that the asymmetric tilt domains and progressive syntectonic sedimentation are linked to the position of the island in the forelimbs of two converging anticlines, whereas their backlimbs have been removed by cliff retreat. The 2 m uplift contour of the 1835 earthquake is parallel to the strike of active faults and antiforms in the Arauco-Concepción region. The close relation between the asymmetric uplift and tilt of the island, modern deformation patterns, and reverse faults rooted in the plate interface suggests that slip on the plate interface thrust influences, localizes, and segments surface deformation during large interplate earthquakes. Furthermore, the link between positive inversion of pre-existing structures, uplift and tilt patterns in the forearc emphasizes the importance of inherited structural fabrics in guiding plate-boundary deformation.

5.1 Introduction

Uplift and subsidence are first-order phenomena of tectonically active coasts along subduction margins (e.g., Plafker, 1972; Ando, 1975). Emergent coasts are usually characterized by differential uplift within distinct segments that may be sustained as morphotectonic units on timescales of 10⁵ to 10⁶ years. During earthquakes these areas appear to act as semi-independent rupture zones that guide deformation (e.g., Kaizuka et al., 1973; Ando, 1975; Matsuda, 1978; Taylor et al., 1986; Thatcher, 1990; Berryman, 1993b; Pandolfi et al., 1994; Ota and Yamaguchi, 2004). Coseismic land-level changes caused by subduction earthquakes follow a sinusoidal deformation pattern across the margin, with uplift along the shelf and coast, and subsidence farther inland (e.g., Plafker and Savage, 1970; Savage, 1983; Hyndman and Wang, 1995). This idealized distribution of coseismic deformation is dramatically altered, however, when pre-existing faults in the upper plate are triggered by a megathrust event, such as during the M 9.2 Alaskan earthquake in 1964 (Plafker, 1972). In some subduction zones, crustal faults have controlled coastal deformation patterns and forearc basin formation over million-year time scales, and their subdivisions seem to govern seismotectonic segmentation, rupture propagation, and susceptibility to local earthquake hazards (e.g., Berryman et al., 1989; Goldfinger et al., 1992; Barnes et al., 2002; Johnson et al., 2004; Bruhn and Hauessler, 2006; Briggs et al., 2006). Some of these faults are rooted in the plate-interface thrust, and mechanical coupling with the megathrust during the earthquake cycle is thus expected (e.g., Park et al., 2000; Barnes et al., 2002; Bruhn and Hauessler, 2006).

This study focuses on the Chile active margin, which comprises distinct coastal segments undergoing long-term differential uplift and subsidence manifested in a rich array of coastal landforms. Historic accounts of great subduction earthquakes in Chile indicate the protracted existence of discrete rupture segments (Lomnitz, 1970; 2004; Kelleher, 1972; Nishenko, 1985; Comte et al., 1986; Thatcher, 1990; Beck et al., 1998), refer to Figure 5.1A for the southern segments. However, it is not known over what timescales these rupture segments prevail and what their influence is with respect to overall landscape development. We present the deformation history for Isla Santa María in the south-central Chile margin (Figure 5.1A), where continuous late Quaternary uplift and tilting are recorded in the geomorphology and coastal deposits of this island which experienced meter-scale coseismic uplift during the last great interplate earthquake (Figure 5.2C). The island is located near the transition between two distinct seismotectonic sectors, the Concepción and Valdivia segments (Figure 5.1A). We use detailed geologic mapping, stratigraphy, geomorphology, and radiocarbon dating to demonstrate that the island is being differentially uplifted and tilted. Furthermore, we analyze seismic reflection profiles and crustal seismicity patterns to show that active reverse faults rooted in the plate interface have been responsible for the progressive uplift and tilting of this island. Our results demonstrate that morphotectonic segmentation along this part of the Chile margin is fundamentally controlled by inverted crustal-scale faults that highlight the importance of structural inheritance in tectonically active regions.

5.2 Methods and data sources

For geological mapping and geomorphic analysis of Isla Santa María we used aerial photos at a scale of 1:20.000 and a photogrammetrically derived digital elevation model at 5 m resolution (Figure 3). Detailed stratigraphic sections were surveyed and sampled at sea-cliff exposures, which allowed measuring the elevation of the Tertiary/Pleistocene unconformity at 80 locations. Fourteen accelerator mass spectrometry (AMS) radiocarbon ages were obtained from wood and charcoal collected in paleosols, peat, and clay layers from the Pleistocene units and Holocene debris flow deposits (Table 5.1). The ages were calibrated with the Calpal software (www.calpal.de) using the *Calpal 2004 January* calibration curve (Stuiver et al., 1998; Hughen et al., 2004). We believe that the sampled material is uncontaminated because: (1) stratigraphic concordance, ages of lower stratigraphic levels are older; (2) thickness of the sedimentary sequence, the samples were taken from fresh sea-cliff exposures where no roots or other exotic material was present, several meters below the top of the sequence; and (3) type of material, dating was performed on centimeter-size charcoal and large pieces of well-preserved wood.

Tectonic uplift rates were calculated using the radiocarbon ages and the sea-level curve from Siddall et al. (2003). Uplift rates derived from optically stimulated luminescence ages of late Holocene strandlines and a detailed topographic survey based on measurements with a laser theodolite are presented in Bookhagen et al. (2006). Active structures off-shore were interpreted from migrated seismic reflection profiles provided by Empresa Nacional del Petróleo (ENAP—the Chilean state oil company) (Figure 5.2C), and crustal seismicity data recorded by the ISSA (Integrated Seismological experiment in the Southern Andes) local network (Figure 5.2D). The seismic stratigraphy was correlated with ENAP exploration boreholes and outcrops in the Arauco Bay area (Figures 5.2A and 5.2C) (Mordojovich, 1981; González, 1989; Vietyes et al., 1993; Elgueta and Arcos, 1994). The ISSA data was collected during a three-month-long experiment using 62 broadband instruments and 16 OBH/OBS deployed between 36 and 40°S (Bohm et al., 2002; Bruhn, 2003).

5.3 Regional tectonic and geologic setting

The Chile margin is formed by subduction of the Nazca plate under the South American continent, at a convergence rate of ~80 mm/yr averaged for the past ~3 m.y. (Somoza, 1998) or 66 mm/yr determined from GPS modeling (Angermann et al., 1999). The Juan Fernández Ridge and Chile Rise constitute major bathymetric anomalies and tectonic discontinuities of the Nazca plate, and are located to the north and south of the study area, respectively (Figure 5.1A). At 37°S, seismic reflection profiles image a filled trench with up to 2.2 km of turbidites and a small accretionary wedge (Figure 5.1C). Part of the trench fill is frontally accreted to the margin, while the rest is underthrust into a subduction channel (Bangs and Cande, 1997). The top of the subducting Nazca plate lies at ~12-20 km depth below the shelf and coastal region where it dips ~10° eastward (Krawczyk et al., 2003).

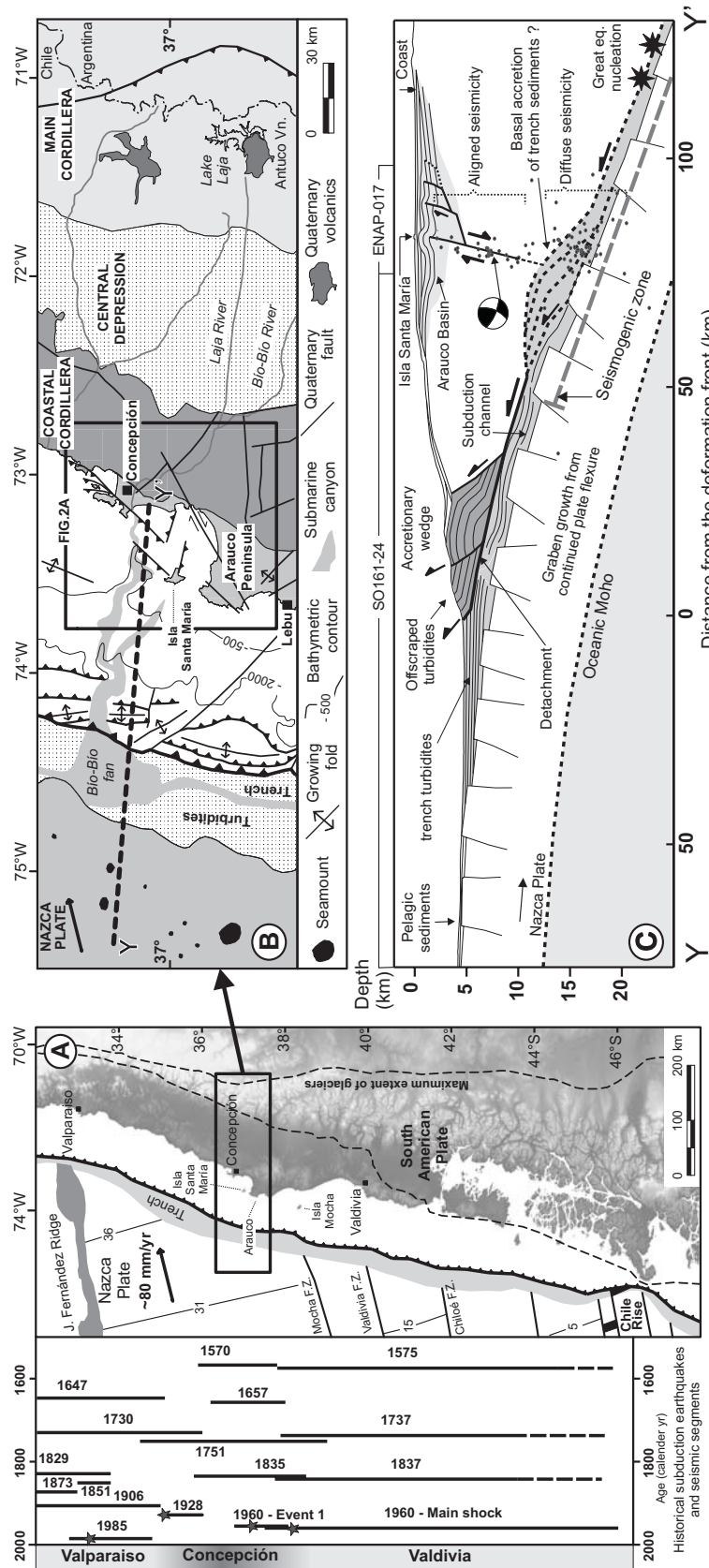


Figure 5.1: A: Seismotectonic segments, rupture zones of historical subduction earthquakes, and main tectonic features of the south-central Andean convergent margin. Earthquakes compiled from Lomnitz (1970; 2004), Kelleher (1972), Comte et al. (1986), Cifuentes (1989), Beck et al. (1998), and Campos et al. (2002). Nazca plate and trench from Bangs and Cande (1997) and Tebbens and Cande (1997). Maximum extension of glaciers from Rabassa and Clapperton (1990). B: Regional morphotectonic units, Quaternary faults, and location of the study area. Trench and slope interpreted from multibeam bathymetry and seismic reflection profiles acquired by Reichert et al. (2002). C: Profile of the off-shore Chile margin at ~37°S, indicated by thick stippled line on the map and based on seismic reflection profiles SO161-24 and ENAP-017. ISSA local network seismicity (Bohm et al., 2002) shown by dots, focal mechanism from Bruhn (2003). Up-dip limit of seismogenic coupling zone from heat-flow measurements (Grevemeyer et al., 2003). Basal accretion of trench sediments from sandbox models (Lohmann, 2002; Glodny et al., 2005). Convergence parameters from Somoza (1998).

5. Coastal deformation and subduction earthquakes

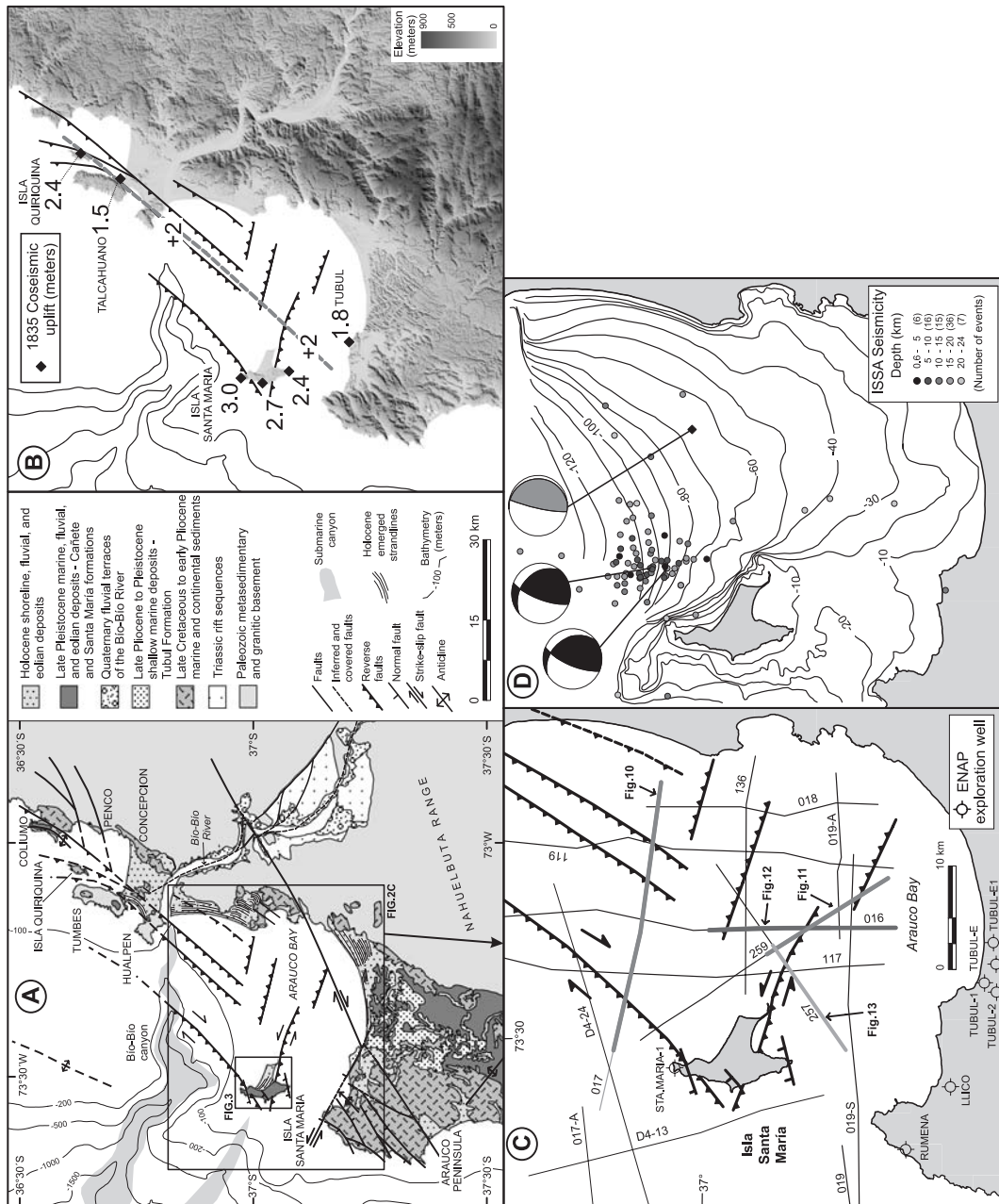


Figure 5.2: Regional geology, structures, and geophysical data sets of the Arauco-Concepción region. A: Simplified geologic map compiled from Pineda (1986), Elgueta and Arcos (1994), and own field observations. Off-shore structures interpreted from ENAP seismic profiles. Bathymetric contours from Reichert et al. (2002). B: Measurements of coseismic uplift during the 20 Feb 1835, $M=8.25$ subduction earthquake from Darwin (1839). Note that the 2 m uplift contour derived from this data is parallel to the northeast striking reverse fault system as well as the en échelon arrangement formed by Isla Quiriquina and the Hualpén, Tumbes, and Colilmo peninsulas. Shaded-relief DEM from SRTM data. C: ENAP seismic reflection profiles and boreholes used in this study. Late Pliocene to Quaternary off-shore structures interpreted from these data. D: Depth-coded seismicity from the ISSA local network (Bohm et al., 2002). Black focal mechanisms from ISSA data (Bruhn, 2003), grey focal mechanism from the USGS-NEIC catalogue (21 May 1990, $M_w=6.3$, 5 km depth). Bathymetric contours in meters from Pineda (1999).

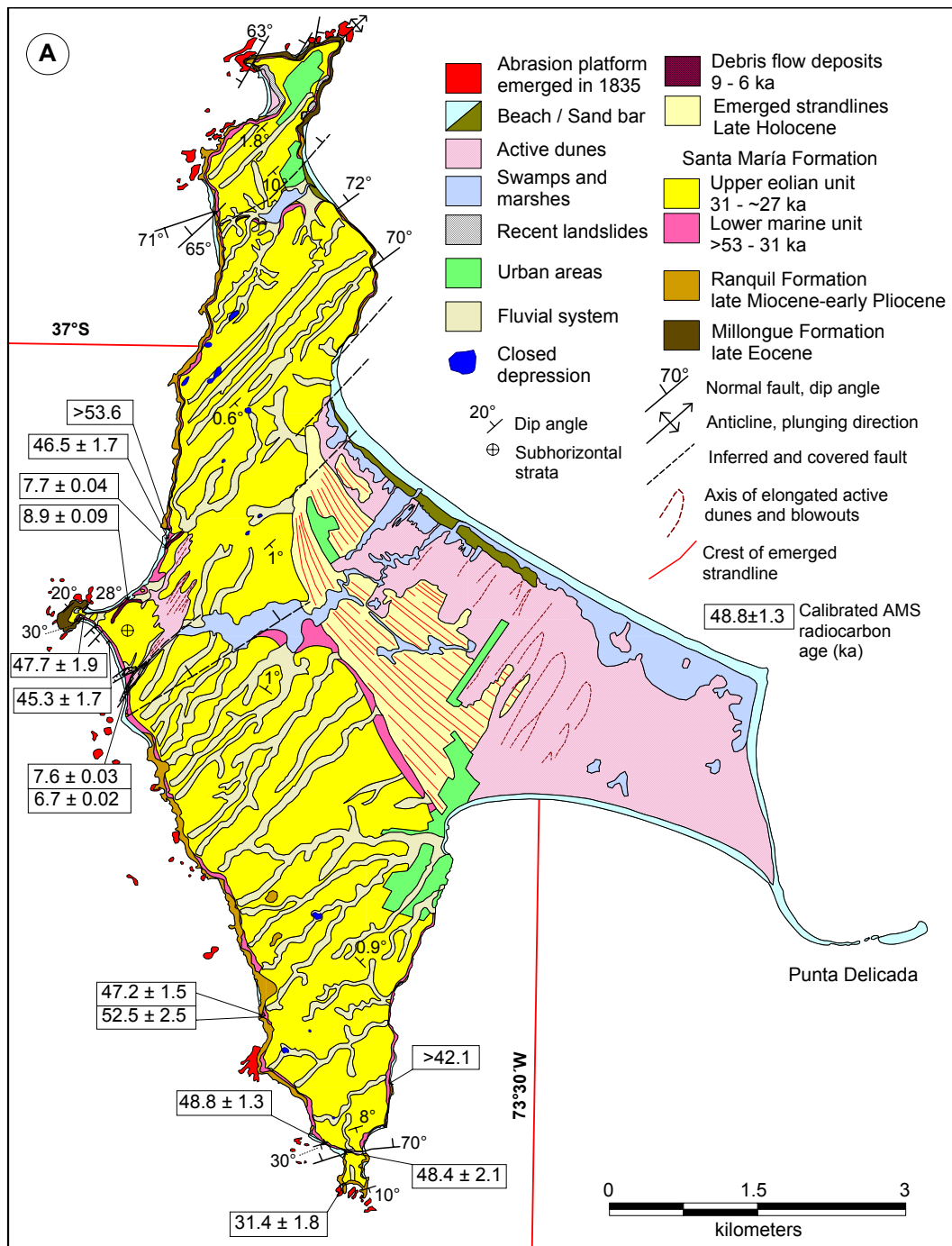


Figure 5.3: A: Geologic and geomorphic map of Isla Santa María and calibrated ^{14}C ages.

The onshore area consists of four main morphotectonic units (Figure 5.1B): (1) the Coastal Platform, formed by uplifted Cenozoic marine and continental sediments, and the focus of this paper; (2) the Coastal Cordillera, a Paleozoic accretionary complex and magmatic arc constituting the crystalline continental basement; (3) the Central Depression, a low-lying basin filled by Plio-Quaternary conglomerates; and (4) the Main Cordillera, characterized by high topography and active volcanic arc (e.g., Mpodozis and Ramos, 1989).

Isla Santa María is in the Coastal Platform and part of the Arauco Basin, a late Cretaceous to Quaternary forearc depocenter filled with at least 3.1 km of marine and continental sediments, as revealed by ENAP exploration wells (Mordojovich, 1981; González, 1989; Elgueta and Arcos, 1994). The Arauco basin contains the Campanian to Maastrichtian Quiriquina Formation, the Paleocene to Eocene Lebu Group, the late Miocene to early Pliocene Ranquil Formation, and the late Pliocene to Pleistocene Tubul Formation (e.g., Biró, 1979; Pineda, 1986; Elgueta and Arcos,

5. Coastal deformation and subduction earthquakes

1994; Le Roux and Elgueta, 1997; Finger et al., 2007) (Figure 5.2A). Hydrocarbon exploration models of forearc basins in Chile between 34 and 45°S, supported by structural data from coal mines in the Arauco Basin, suggest that various phases of subsidence and extension occurred between the late Cretaceous and early Pliocene (Mordojovich, 1981; González, 1989; Melnick and Echtler, 2006a). Normal faults associated with these basins apparently reactivated inherited fabrics of the Paleozoic metasedimentary basement (González, 1989). In this study and Melnick and Echtler (2006a), we show that inversion of the Arauco rift basin inversion started between 3.6 and 2.5 Ma, and that shortening has been continuous at relatively low rates during deposition of the late Pliocene to Pleistocene Tubul Formation and is active today.

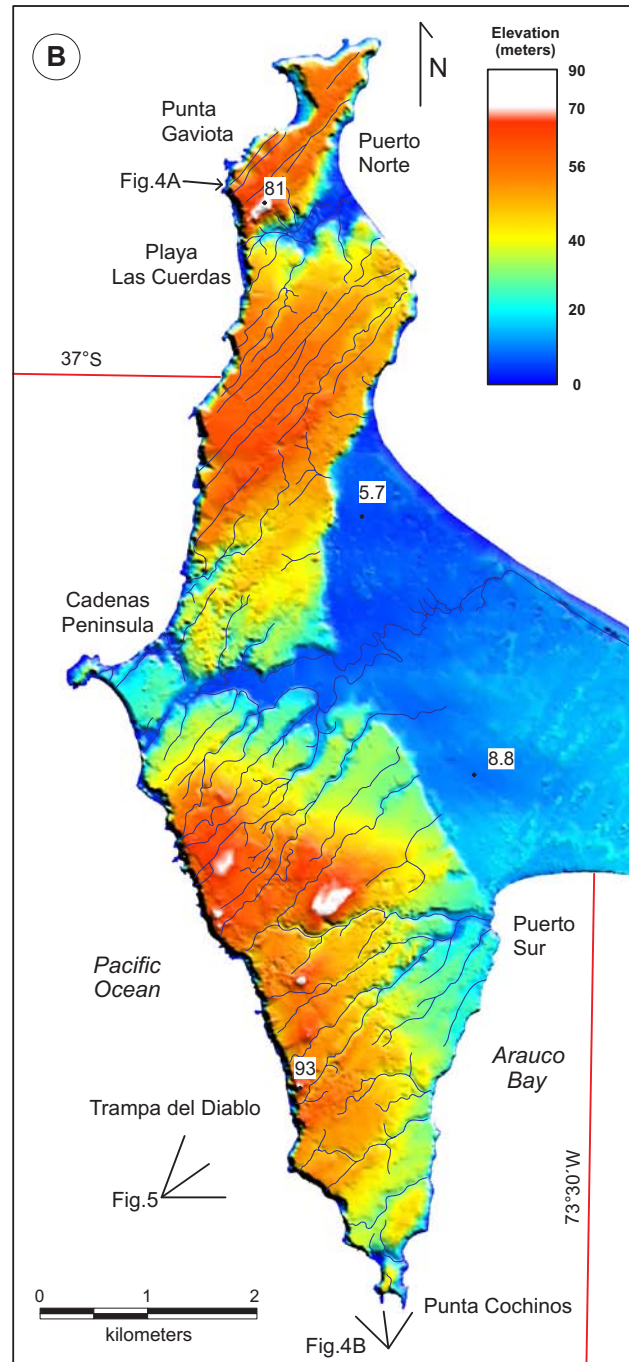


Figure 5.3: B: Shaded-relief digital elevation model (5 m horizontal resolution, derived from photogrammetric restitution of 1:20.000 aerial photos) and drainage network. Labels indicate elevations in meters.

5. Coastal deformation and subduction earthquakes

Lab ID	Material	Stratigraphic Position	Age (yr BP)	2 σ error (yr)	Calibrated age (yr BP)	2 σ error (yr)	Sea-level elevation (m)	Sample elevation (m)
KIA24186	Paleosol	Base eolian unit	27380	1750	31463	1885	-93.1	33.0
KIA25772	Paleosol	Base marine unit	47600	1250	48826	1318	-78	3.5
KIA24181	Paleosol	Base marine unit	52750	2530			-46.1	12.5
KIA25771	Clay	Base marine unit	>42130				-82	5.4
KIA24182	Peat	Base marine unit	>53600				-68	6.0
KIA24188*	Clay	Int. marine unit	43780	1500	45319	1760	-77	3.1+15.3
KIA25773	Clay	Int. marine unit	44480	725	47250	1505	-85	24.8
KIA24190	Peat	Int. marine unit	45450	1300	46540	1735	-70	6.2
KIA24182	Peat	Int. marine unit	47280	1760	47769	1976	-78.8	5.0
KIA24187*	Paleosol	Int. marine unit	48080	1900	48442	2180	-84.8	15.0+20.4
KIA24178	Peat /df.	Filling channel	5890	30	6703	26		3.6
KIA24179	Peat /df.	Filling channel	6835	40	7660	33		2.6
KIA24189	Peat /df.	Filling channel	6900	45	7731	40		7.2
KIA24180	Peat /df.	Filling channel	8020	35	8900	93		10.2

*Beds tilted by adjacent normal growth faults and affected by post-depositional subsidence. The added elevation value has been estimated considering bed dip and distance from sampling point to half-graben hinge. Int: interbedded; df.: debris flow deposit

Table 5.1: Radiocarbon ages obtained by Accelerator Mass Spectrometry dating of charcoal and large pieces of wood of the Santa María Formation. Dating was performed at the Leibnitz-Labor AMS facility in Kiel, Germany. Calibration was made with the Calpal software (www.calpal.de) using the *January 2004 calibration curve*. Sea-level elevations are from Siddall et al. (2003) and have a 2 σ error of 12 m. The latter and the present elevation of the samples were added to obtain the uplift by assuming that the samples were deposited at, or very near to, sea level. The uplift rates are also presented in Figure 5.9.

Only a few previous studies have addressed late Quaternary and historic deformation along the south-central Chile margin. The pioneer work of Kaizuka et al. (1973) and detailed study by Nelson and Manley (1992) reported Holocene uplift rates between 5.5 and 10 m/k.y. at Mocha Island (Figure 5.1A), based on ^{14}C ages of emerged strandlines. Marine terraces of the Arauco Peninsula and surroundings were described by Kaizuka et al. (1973) as three sequences of uplifted Pleistocene marine surfaces containing shallow marine deposits, fluvial conglomerates, and eolian sands. These surfaces are folded around a northwest oriented anticline in the center of the peninsula (Figures 5.1B and 5.2A). Based on its width and lateral extension, Kaizuka et al. (1973) inferred that the broadest surface, the Cañete surface, was formed during the last interglacial sea-level highstand ~125 ka ago, and the upper two surfaces during the preceding interglacial highstands. If this inference is true, an uplift rate of ~1.8 m/k.y. results for the center of the folded peninsula. Surfaces with similar near-shore deposits but narrower, less pronounced, and lacking longitudinal continuity exist at lower elevations in the Arauco-Concepción region, and were correlated with late Pleistocene interstadials (Kaizuka et al., 1973). Based on the rupture zones of historical earthquakes (Figure 5.1A) they concluded that the Arauco peninsula exists as a result of overlap between the Valdivia and Concepción seismic rupture zones (see section on historical earthquakes below). However, the mechanistic explanation for the relation between the broad megathrust ruptures, localized folding and uplift of Pleistocene surfaces, and the general coastal geomorphology have remained unsolved.

5.4 Historic earthquakes

Five hundred years of historic records of subduction earthquakes in Chile show that Isla Santa María is within the southern part of the Concepción seismic segment (Lomnitz, 1970; Barrientos, 1987; Thatcher, 1990; Beck et al., 1998; Campos et al., 2002), which nucleated M>8 subduction earthquakes in 1570, 1657, 1751, and 1835 (Lomnitz, 1970; 2004) (Figure 5.1A). Until the last event in 1835, this segment followed a rather periodic pattern with a recurrence of 88 ± 5 year (mean $\pm 1\sigma$ SD), which is very similar to the 82 ± 7 year recurrence interval of the Valparaíso

segment immediately to the north (Comte et al., 1986), but lower than the 128 ± 31 year of the Valdivia segment to the south. The 1960 seismic sequence, which produced the largest earthquake ever recorded instrumentally, started with a $M_w=8.1$ foreshock that nucleated at $37^\circ 10'S$, immediately north of the Arauco Peninsula with a rupture length of ~ 150 km (Cifuentes, 1989) (Figure 5.1A). The $M_w=9.5$ mainshock nucleated a day after at $38^\circ 30'S$ and ruptured the entire Valdivia segment between $37^\circ 30'$ and $46^\circ 30'S$ (Plafker and Savage, 1970; Kanamori, 1977; Cifuentes, 1989).

The Concepción segment is considered to be a seismic gap because it has not ruptured since 1835 (Barrientos, 1987; Campos et al., 2002); however the northern extent of the rupture associated with the 1960 $M_w=8.1$ foreshock is not clear (Cifuentes, 1989). Campos et al. (2002) assumed that this rupture propagated only southward because no land-level changes were reported north of $\sim 37^\circ 30'S$ by Plafker and Savage (1970), including Isla Santa María. However, their survey was done eight years after the earthquake, and thus the $M_w=8.1$ foreshock could have ruptured at least part of the Concepción segment releasing some of the accumulated strain and preventing the occurrence of an interplate earthquake since.

Coseismic uplift on Isla Santa María had been previously described, but not quantified for the $M \sim 8.5$ earthquake in 1751, whose related tsunami completely destroyed the city of Penco causing the relocation of this former regional capital to its present-day position in Concepción (Lomnitz, 1970). The island is also located in the rupture zone of the February 20, 1835 earthquake, which had an estimated magnitude of 8.25 (Lomnitz, 1970). Coincidentally, Charles Darwin and Captain Robert FitzRoy were in this area during the earthquake and visited the island twice, from March 4 to 7 and from March 27 to April 17 (Darwin, 1839; FitzRoy, 1839; Darwin, 1851). During the first visit they concluded from dead shell-fish, water marks, soundings, and verbal testimony of the inhabitants that the land had been raised about 2.7 m; during their second visit three precise measurements were made: 2.4, 2.7, and 3.0 m in the southern, central, and northern sectors of the island, respectively (Figure 5.2B). These land-level changes were obtained using the emerged upper limit of dead *Mytilus* shells exposed at rocky cliffs as a pre-earthquake marker of the upper limit of the intertidal zone. They also measured uplift on the mainland of 1.8, 2.4, and 1.5 m at Tubul, Isla Quiriquina, and Talcahuano harbor, respectively (Figure 5.2B). At the latter locality $\sim 50\%$ of postseismic recovery was observed during the two months following the earthquake. One month after the earthquake, Simón Rodríguez made a formal report of the damages, which also mentions 2.4 to 3.0 m of uplift at Isla Santa María (Rodríguez, 1835).

The abrasion platform that emerged during the 1835 earthquake is exposed as a prominent feature around the entire island (Figure 5.4). Interestingly, the present-day elevation of the platform is similar to its position as measured by Darwin. The abrasion platform is tilted to the east with heights of 2.6 to 3.2 m above the high-tide level along the western coast, whereas it only reaches 1.6 to 2.0 m at the eastern coast.

5.5 Stratigraphy of Isla Santa María

Isla Santa María is composed of two distinct sedimentary units: the Tertiary substrate formed by well-lithified sedimentary rocks, and Pleistocene marine and continental, poorly consolidated deposits that follow over a marked angular unconformity (Figure 5.5). Our radiocarbon ages obtained from the base of the Pleistocene sequence (Table 5.1) constrain the onset of renewed marine sedimentation to a minimum age of 53 ka. We define and name this sequence the Santa María Formation.

5.5.1 Tertiary sedimentary rocks

The Tertiary sedimentary units include (Figure 5.3A) the late Eocene Millongue Formation (Muñoz-Cristi, 1946) and the late Miocene to early Pliocene Ranquil Formation. These units comprise sandstone and shale containing coal seams, and massive white siltstone and fine sandstone, respectively. The Millongue Formation is only locally exposed, whereas the Ranquil Formation crops out almost continuously along the cliffs, except at the center of the island (Figure 5.3A).

5.5.2 Pleistocene Santa María Formation

The Santa María Formation (SMF) can be differentiated into two distinct units: a lower, dominantly marine shore unit with interbedded near-shore terrestrial beds and an upper unit composed of eolian sands (Figure 5.6).

5.5.2.1 Lower marine unit

The lower unit of the SMF is continuously exposed along the western coast, whereas in the east it is discontinuous (Figure 5.3A). The maximum thickness of 78 m is on the southwestern coast, where marine deposition occurred in topographic lows in the undulatory Tertiary substrate (Figure 5.5). In our latitudinal transects the thickness was found to always increase eastward (Table B1). These beds consist of predominately medium to coarse sandstone with interbedded layers of paleosol, peat and clay. Descriptions of facies, grain-sizes, and sections are in the Appendix B. We propose that this unit was deposited in a marine nearshore environment based on the occurrence of coarse landward-inclined cross-bedding, wavy flaser bedding, intense vertical bioturbation, occasional occurrence of shell fragments, and similarities in grain-size distribution with present-day deposits.

We obtained four radiocarbon ages from paleosol, peat, and clay layers at the base of this unit (Figure 5.3A and Table 5.1). The sample at the southeastern coast yielded a lower bound of 42 ka, and north of the Cadenas Peninsula a lower bound of 53 ka; in the southwestern sector, we obtained ages of 52.7 ± 2.5 ka and 48.8 ± 1.3 cal-ka (cal-ka=calibrated thousand years before present). From similar layers interbedded in the marine sands, we obtained five ages, which range between 45.3 ± 1.7 and 48.4 ± 2.1 cal-ka (Table 5.1). The sample constitute centimeter-size wood fragments devoid of any sign of contamination by younger roots.

5.5.2.2 Upper eolian unit

In map view most of the SMF consists of very well sorted, semi-consolidated grey to brownish sandstone. We distinguish this succession as the upper stratigraphic unit of the SMF. The contact with the underlying marine-dominated unit is conformable and transitional. The thickness reaches a maximum of 14 m at the western, and 37 m at the eastern coast, increasing northeastward in the southern domain, and southeastward in the northern domain. It thus mimics the depositional pattern of the underlying marine unit. This unit comprises a characteristic rhythmic succession of homogenous beds with alternating horizontal and inclined parallel lamination (Figures 5.6 and 5.7). Descriptions of facies, trace fossils, and sedimentary sections are in the Appendix B. The beds with inclined laminations uniformly dip 20 to 30° throughout the island, and the dip-direction is parallel to the northeast direction of the prevailing Pacific winds. Grain-size distributions from this unit and from active dunes of the island are very similar and contrast markedly with the underlying unit (Figure B1). We interpret a continental, eolian depositional environment for the upper unit of the SMF. A paleosol at the base of this sequence yielded a radiocarbon age of 31.5 ± 1.8 cal-ka (Table 5.1; Figure 5.3A; Figure B8).

Compared to recent depositional environments, eolian sand dunes in low-relief coastal regions and islands are active only when they are at elevations below ~15 to 20 m, as seen in the present-day distribution of coastal eolian environments in south-central Chile (Paskoff and Manríquez, 2004) and a detailed correlation between late Quaternary sea-level highstands and eolian activity (Carr et al., 2006). The sea-level curve of Siddall et al. (2003) shows that between the onset of eolian activity at 31.5 ka and 27.5 ka sea level was fairly stable at -82.2 ± 6.1 m. At 27.5 ka, sea level started to fall continuously to reach its lowermost level of -114 m during the last glacial maximum (LGM) at 19.5 ka. Thus based on the onset of eolian deposition at 31.5 ka, we infer that the dune fields were deposited between 31.5 ± 1.8 and 27 ± 2 ka.

5.5.3 Fluvial system and channelized Holocene debris-flow deposits

The eolian unit of the SMF is incised by linear ephemeral channels (fluvial system in Figure 5.3A). In the southern domain, the drainage channels follow the slope of the upper surface due to the tilt of the island about a west-northwest axis. In contrast, in the northern domain the drainages have a marked parallel pattern, which is influenced by the orientation of recent faults and fractures (Figure 5.3). The channels are carved into the SMF and near the Cadenas Peninsula they are filled by debris-flow deposits (Figure 5.3A). These deposits are massive, monomict and are comprised of brownish sandstone clasts from the eolian unit of the SMF (Figure B5); the matrix constitutes brown sand and peat containing wood. In the southern channels, at least three superimposed debris-flow deposits occur, the upper two provided radiocarbon ages of 7.66 ± 0.03 and 6.70 ± 0.02 cal-ka (Figure 5.3A). In the northern part of the peninsula, we obtained ages of 8.90 ± 0.09 and 7.73 ± 0.04 cal-ka from similar deposits (Table 5.1). These debris-flow deposits, however, cannot be used to calculate uplift rates as their position with respect to paleo-sea level is ambiguous, because of cliff-retreat and eastward tilting. In addition, the southern deposits occur in the hanging wall of normal faults (Figure B7).

The age of these deposits indicates that by ~9 ka, processes leading to the semi-consolidated eolianites of the SMF had been long inactive. Incision and development of the

5. Coastal deformation and subduction earthquakes

drainage network must thus have started between ~27 and 9 ka, and was probably related to sea-level fall during the LGM at ~19.5 ka.

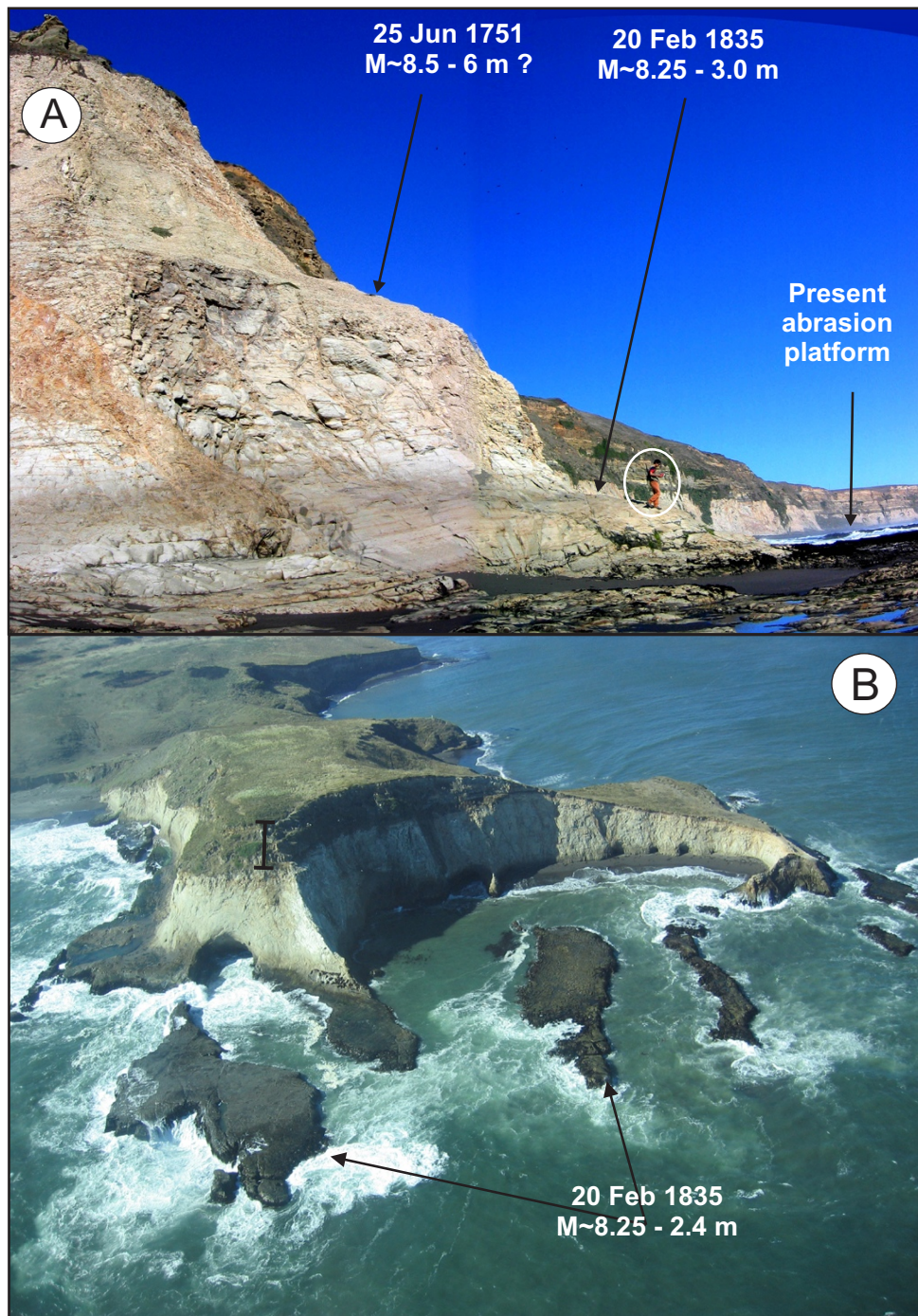


Figure 5.4: A: View of the two preserved uplifted abrasion platforms on the northwestern coast. These surfaces were abandoned due to coseismic uplift, probably during the two last great earthquakes. The lower platform was abandoned by the 3.0 m of coseismic uplift during the 1835 M~8.25 earthquake (Darwin, 1839; magnitude from Lomnitz, 1970). Uplift was also described, but not quantified, during the 1751 M~8.5 earthquake (Lomnitz, 1970), which may have reached ~6 m. Person in white circle for scale. B: Aerial view of the abrasion platform emerged during the 1835 earthquake at the southern tip of the island. This surface is at 2.6 to 3.2 m along the western and 1.6 to 2.0 m along the eastern coast, which is consistent with the amount of coseismic uplift documented by Darwin (1839), and is indicative of coseismic eastward tilting. The bar indicates the location of the Punta Cochinos section shown on Figure B2.

5. Coastal deformation and subduction earthquakes

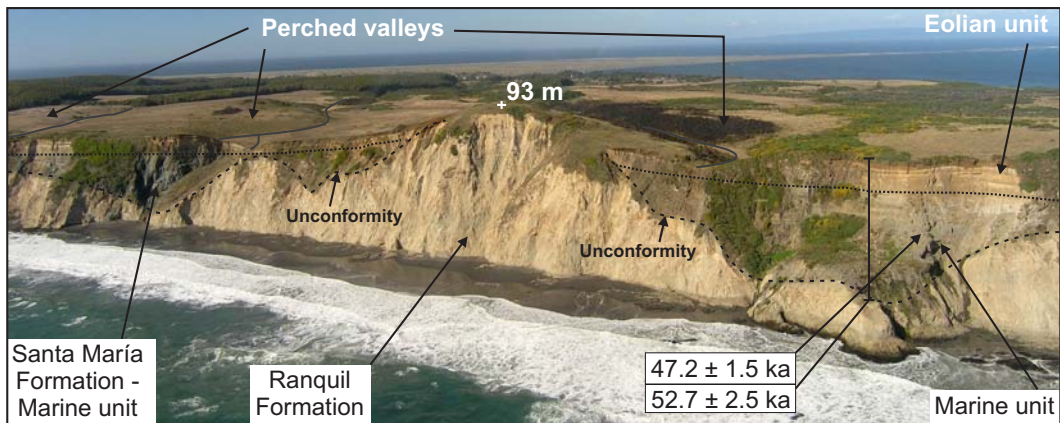


Figure 5.5: Oblique aerial view to the east in the south of the island, see Figure 3B for location. Note the marked unconformity between the Tertiary siltstone and the late Pleistocene Santa María Formation, and the color contrast between the marine and eolian units. The perched morphology of the valleys is interpreted as produced by progressive cliff retreat. The bar indicates the location of the Trampa del Diablo section shown on Figure DR2.

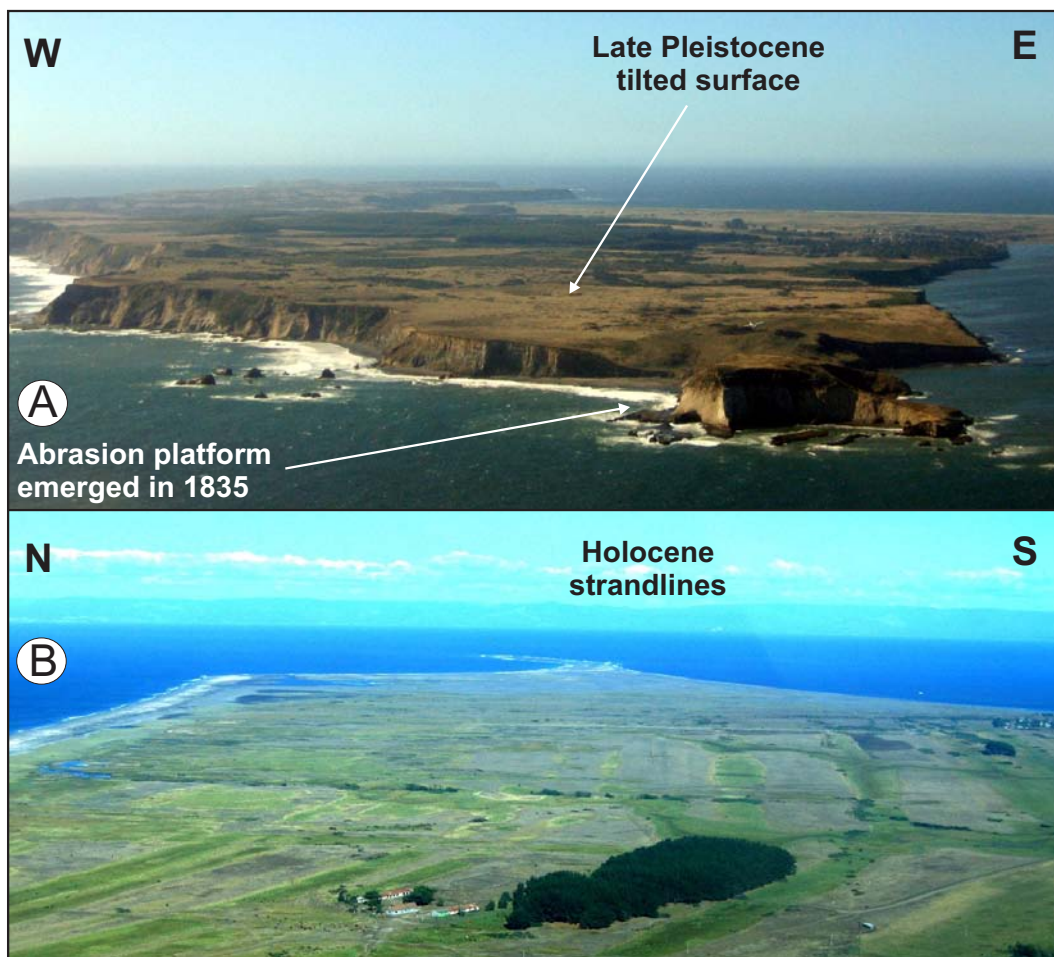


Figure 5.6: A: Oblique aerial view to the north of Isla Santa María. Note the eastward tilt of the upper surface and the lowlands on the eastern part. The abrasion platform abandoned after the 1835 earthquake can be seen. B: Oblique aerial view to the east of the Holocene lowlands with emerged strandlines forming the undulatory landscape.

5.6 Geomorphology of Isla Santa María

In map view, Isla Santa María has an east-pointing triangular shape (Figure 5.3A). We subdivide the island in two main geomorphic units: (1) a central part formed by a higher surface tilted $<2^\circ$ landward and bounded by steep cliffs (Figures 5.3 and 5.6A), here denoted as the upper surface; and (2) east of the upper surface, lowlands forming an east-pointing wedge and comprising a sequence of emerged strandlines, marshes, and dunes (Figures 5.3 and 5.6B). The upper surface is formed by poorly consolidated sediments of the SMF (Figure 5.5).

5.6.1 Upper surface

The upper surface consists of a northern and southern domain, divided by an east-west-oriented central valley, which integrates the main drainage of the island (Figure 5.3). We derived a hypsometric curve for each domain, which shows the asymmetric distribution of topography (Figure 5.7B). The eastward tilt of the upper surface is also asymmetric and with different tilt axes as also seen on topographic swath profiles (Figure 5.7C) and the thickness distribution of the SMF (Table B1). The southern domain is tilted to the north-northeast, along a west-northwest striking axis, while the northern domain is tilted to the southeast, along a northeast striking axis.

5.6.2 Lowlands – Holocene emergent strandlines

The emerged strandlines, marshes, and dunes in the lowlands occur at elevations up to 18 m (Figure 5.6B). The southern part of these lowlands is exposed to the strong southwesterly Pacific winds and thus governed by northeast-oriented blowouts and dunes. However, the northern part is in the lee of the upper surface allowing the preservation of emerged strandlines (Figure 5.3). Twenty strandlines are well preserved and approximately five more are covered by dunes. The strandline sequence is formed by parallel pairs of beach berms and back-swamps that result in an undulating, shore-parallel landscape of ridges and depressions (Figure 5.6B). The berms consist of medium well-sorted black sand, while the back-swamp areas consist of organic-rich, homogeneous silty sand. The crests reach 12 m elevation and are late Holocene in age as shown by eight 3.4- to 1.8-ka luminescence ages obtained from the central part of the sequence (Bookhagen et al., 2006).

The formation of such a landscape in a shoreline environment is only plausible with a rather stable sea level affected by successive episodes of relative sea-level fall, caused by tectonic uplift and/or post-glacial isostatic rebound (e.g., Matsuda et al., 1978; Nelson and Manley, 1992; Berryman, 1993a; Ota and Yamaguchi, 2004; Steward et al., 2000). At Isla Santa María post-glacial rebound can be rejected because at this latitude Pleistocene glaciers were restricted to the Main Cordillera at elevations above ~ 2000 m (Rabassa and Clapperton, 1990), about 180 km east of the island (Figure 5.1A). Thus tectonic uplift by either repeated coseismic events and/or protracted aseismic movements must have caused the emergence of these strandlines.

5.7 Paleogeography of the Santa María Formation

Identical depositional environments with which we correlate the late Pleistocene SMF exist on the island today: beaches with black sands surround the island; swamps occur in the lowlands and central valley; and dune fields cover the lowlands (Figure 5.3A). We interpret that the cyclic interbedding of black marine sandstone and clay-rich continental layers, and the graded sandstone represent a mixed signal of tectonic uplift and eustatic sea-level oscillations. The fact that the upper unit of the SMF is exclusively eolian, and that its base is ~ 31 ka old when sea level must have been about 90 m lower than at present, emphasizes that tectonic uplift during the late Pleistocene has outpaced glacio-eustatic oscillations in this environment.

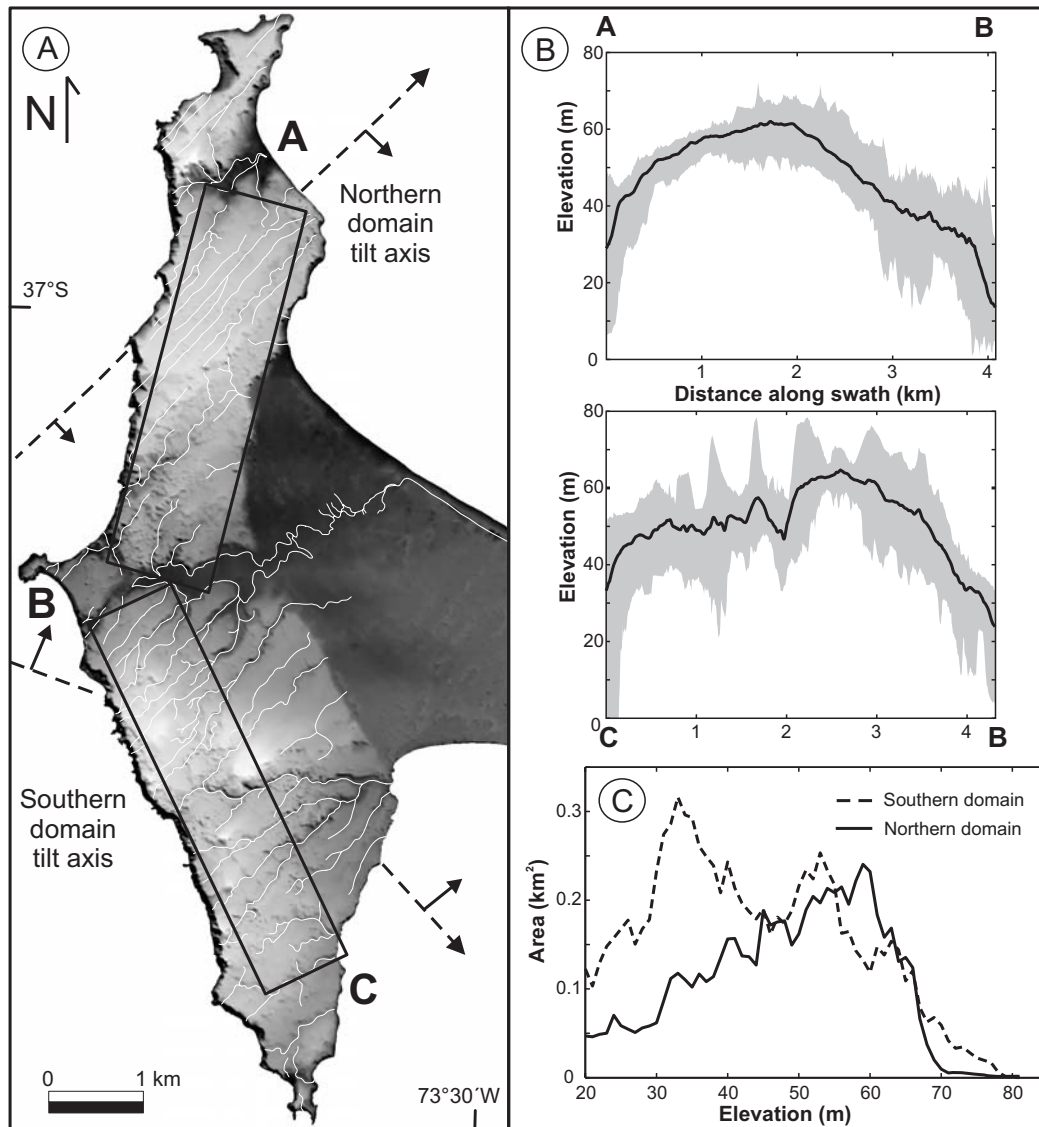


Figure 5.7: Topographic asymmetry of the upper surface of Isla Santa María. A: DEM with drainage network. Note the asymmetric tilt of the upper surface. B: Swath topographic profiles, areas shown on the DEM. The thick line represents the mean topography and the shaded area the maximum and minimum values, respectively. C: Hypsometric curves derived from the DEM for the entire northern and southern domains of the upper surface. The DEM was splitted along the central valley to derive these curves. Note the differences in morphology and distribution of topography in both domains.

5.8 Topography of the Tertiary-Pleistocene unconformity and marine-eolian transition surfaces

Exposures of the unconformity between the Tertiary and Pleistocene units are ubiquitous along the western and northeastern coasts of the island and show a pronounced variation in elevations (Figures 5.5 and 5.8). The geometry of the unconformity has a marked north-south asymmetry, segmented by the central valley where the unconformity is below sea level. The north-south profile shown on Figure 5.8 was constructed with measurements obtained at the western coast. This profile illustrates the longitudinal asymmetry of the island and the pronounced paleorelief in the southern part. There, the unconformity is very undulatory, reaching over 80 m elevation in the highest hills of the island (Figures 5.5 and 5.8). The strong paleorelief in the south contrasts with the north where the unconformity is subhorizontal and at elevations between 10 and 20 m.

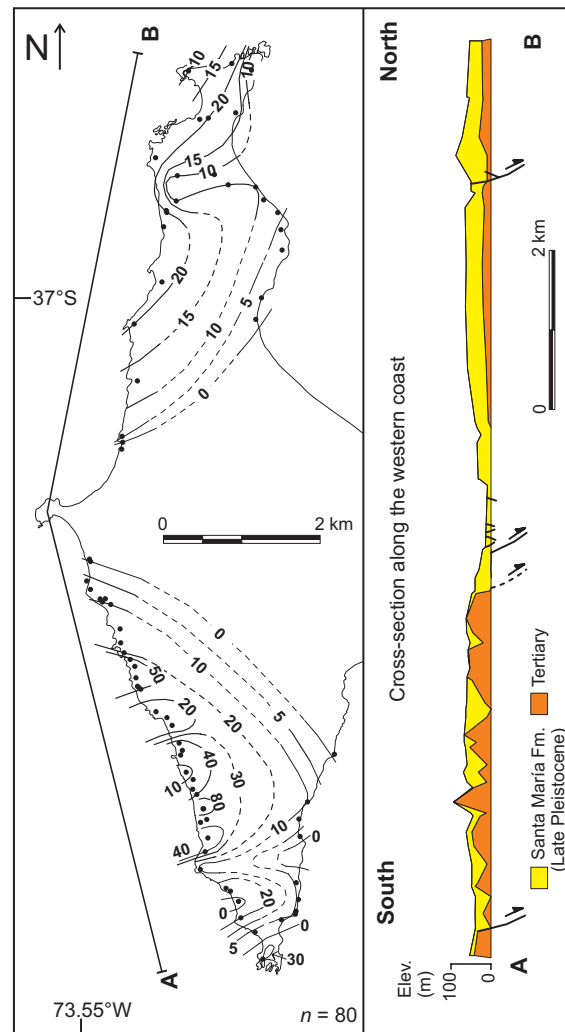


Figure 5.8: Contour map of the base of the Santa María Formation and N-S profile along the western coast of the island. Note the marked asymmetry of the island in both map-view and cross-section. The southern domain is tilted to the NNE along a WNW striking axis, while the northern domain is tilted to the WSW along a NNE striking axis. Black dots on the map correspond to data points measured at sea cliffs with a digital altimeter and tape. Note the similarity between the surface of the island (see DEM on Figures 5.3B and 5.7) and the Tertiary/Pleistocene unconformity surface.

The contour map of the Tertiary/Pleistocene unconformity also exhibits a contrasting geometry between the south and north of the island (Figure 5.8). The surface is inclined, northeast striking and southeast dipping in the northern part, whereas in the south, it strikes northwest and dips northeast. Interestingly, the asymmetric tilt of the unconformity is very similar, but steeper, when compared to the inclination and geometry of the present-day surface of the island (Figure 5.7A). We interpret the strong paleorelief of the unconformity in the south of the island to result from fluvial erosion of the continental shelf region during early Pleistocene sea-level lowstands. The bathymetric map (Pineda, 1999) has similar undulatory contour lines southwest of the island (Figure 5.2D) and multibeam bathymetry (Reichert et al., 2002) reveals a submarine canyon immediately west of the island (Figures 5.1B and 5.2A), related to former fluvial systems. Subsequently, the former channels were filled with marine near-shore deposits of the SMF.

The conformable transition between the marine and eolian units in the SMF also has a similar geometry as the Tertiary/Pleistocene unconformity, involving a general decrease in elevation eastward along the entire island, and the same asymmetric geometry in map view. These observations indicate that Pleistocene marine and eolian deposition was synchronous with progressive asymmetric tilting. Hence, uplift and tilting of the island during the Pleistocene must have been governed by identical processes responsible for the present-day tilting of the island (Figures 5.6A and 5.7A).

5.9 Normal faulting and syntectonic sedimentation

In contrast to the pervasively faulted and fractured Tertiary rocks, the SMF is cut by faults only in three areas. All Quaternary faults are extensional, steeply dipping, and strike northeast to east-northeast. They are located at the north, center, and south of the island at ~ 5 km from each other (Figures 5.3A and 5.8). Adjacent to the faults liquefaction features and growth strata are ubiquitous in the marine unit of the SMF. Well preserved ruptures indicate very recent activity along the northern and central faults. Detail descriptions and photos are in the Data Repository (Figures B6, B7, B8). The constant dip of individual growth strata is indicative of domino-style block rotation controlled by high-angle normal fault.

5.10 Late Quaternary deformation rates of isla santa María

5.10.1 Uplift rates

We calculated uplift rates from dated paleosols, peat and clay layers from the SMF. We interpret these beds as geomorphic markers of back-swamp areas in immediate vicinity to corresponding paleo-sea level positions, since at present identical depositional environments and facies associations are exclusively found near sea level or at elevations that are within the error of the sea-level curve (± 12 m). Table 5.1 presents ten AMS radiocarbon ages from these layers. In order to derive realistic uplift values and uplift rates, we viewed the sample elevations with respect to the position of their present counterparts and the late Pleistocene sea-level curve of Siddall et al. (2003). The obtained ages from the marine unit result in uplift rates between 1.2 ± 0.35 and 2.3 ± 0.36 m/k.y., but the age of a single sample from the base of the fixed dunes at the southern point of the island provided a significantly higher rate of 4.0 ± 0.28 m/k.y. (Figure 5.9 and Table 5.1).

We attribute the two-fold difference in uplift rate between the sample at the southern point of the island and the rest of the samples from the marine unit, to be related to normal faulting rather than an acceleration of uplift. Since the marine unit is absent at the southern tip of the island, footwall uplift caused by normal faulting may be responsible for its absence and the higher degree of uplift there (Figure B8). Samples collected in the central depression are in the downthrown blocks of normal faults and hence, have lower uplift rates. Averaging all the ages yields an uplift rate of 2.01 ± 0.38 m/k.y.; however, by removing the footwall sample we obtain a more realistic rate of 1.79 ± 0.39 m/k.y. Because the radiocarbon ages are on the analytical limit of the dating method, this uplift rate should be considered a maximum value. Interestingly, despite this uncertainty, the late Pleistocene uplift rate agrees within error with the late Holocene uplift rate of 2.3 ± 0.2 m/k.y. derived from the strandline sequence (Bookhagen et al., 2006).

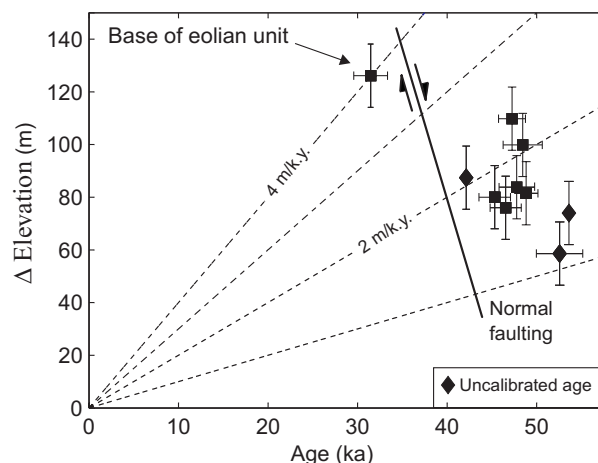


Figure 5.9: Uplift rates of Isla Santa María. Squares are calibrated AMS ^{14}C ages with 2σ error bars. The samples are from paleosol, peat, and clay layers from the near-shore marine unit, and one from the paleosol at the base of the eolian unit of the Santa María Formation, respectively. We assumed that they originated near sea level because at present the same depositional environments occur only near sea level at the island. Δ Elevation is equal to the present altitude of the samples minus the paleo sea-level elevation from Siddall et al. (2003) data set, which has 12-m 2σ error. We attribute the difference between the 4.0 ± 0.28 m/k.y. uplift rate calculated for the sample at the base of the fixed dunes and the rest of the samples to the effects of normal faulting. The mean uplift rate is 2.0 ± 0.38 m/k.y., and by removing the footwall sample 1.79 ± 0.39 m/k.y..

5.10.2 Tilt rates

We used three reference surfaces to calculate late Pleistocene tilt rates of the island: (1) the ~50-ka-old Tertiary/Pleistocene unconformity and base of the marine unit; (2) the horizon of the marine/eolian transition, which marks the emergence of the island and onset of subaerial deposition at 31.5 ± 1.8 ka; and (3) the present surface of the island, which is depositional and has an age of 27 ± 2 ka. From our field observations we infer that these erosional/depositional surfaces were subhorizontal at the time of their abandonment. The elevation of each of these surfaces was correlated across eight detailed sections normal to the tilt axes of each domain (Figure B9 and Table B1). We obtained average tilt rates of $0.024 \pm 0.014^\circ/\text{ka}$ for the Tertiary/Pleistocene unconformity, $0.039 \pm 0.022^\circ/\text{ka}$ for the base of the eolian unit, and $0.031 \pm 0.016^\circ/\text{ka}$ for the present surface of the island. Averaging all these values yields an integrated tilt rate for the island of $0.032 \pm 0.018^\circ/\text{ka}$ during the past ~50 k.y. (Table B2).

The average late Holocene tilt rate calculated from a detailed topographic survey of the emergent strandlines and luminescence ages is $0.020 \pm 0.001^\circ/\text{ka}$ (Bookhagen et al., 2006), suggesting rather steady tilting during the late Quaternary.

5.11 Active shortening and basin Inversion structures

Our observations clearly show that Isla Santa María has been uplifting and tilting in two asymmetric tilt domains at a relatively constant rate during the late Quaternary. In order to explain and decipher the mechanisms responsible for this deformation, we first view our interpretations in the framework of off-shore seismic reflection profiles, local network seismicity data, and focal mechanism solutions. In a second step, we integrate these geophysical data with the geologic and geomorphic observations to propose that active crustal reverse faults are responsible for the differential surface deformation on the island and in the neighboring Arauco-Concepción area.

5.11.1 Crustal seismicity

Data from the temporary ISSA local network show that most of the seismicity within the upper plate is concentrated in the forearc below the coast and shelf. Sixty-one crustal events cluster 7 km north of Isla Santa María in an area of ~90 km². In an east-west section seismicity has a linear alignment inclined 67°W and extending from 0.6 km depth to the plate interface at ~12 km; below this depth seismicity becomes scattered (Figure 5.1C). Bruhn (2003) calculated focal mechanism solutions for two $M_w=4.0$ events, which are both very similar and compatible with a 022°E striking, 72°W dipping reverse fault with a minor dextral strike-slip component (Figure 5.2C). The fact that the dip of the two focal mechanisms is very similar to the inclination of the earthquake alignment suggests that this concentration of seismicity underneath Isla Santa María is caused by a crustal-scale reverse fault. The 21st May 1990, a 5-km-depth, $M_w=6.2$ earthquake reported in the USGS-NEIC catalogue occurred east of the island, also with a focal mechanism compatible with a north-northeast striking steep reverse fault (Figure 5.2D). Recent data from another local network confirms the cluster of shallow seismic activity northeast of the island (Rietbrock et al., 2005).

5.11.2 Shortening features imaged from seismic reflection profiles

We interpreted off-shore seismic reflection profiles that cover an area of ~1800 km² surrounding Isla Santa María (Figure 5.2C). The base of the late Pliocene to Pleistocene Tubul Formation has been correlated with a high-amplitude reflector recognized in all profiles truncating older sequences, and in four ENAP hydrocarbon exploration boreholes located southeast of the island (Figure 5.2C) (Mordojovich, 1981; González, 1989; Elgueta and Arcos, 1994; Vietyes et al., 1993). The base of the Tubul Formation is a key horizon that brackets the minimum age for the onset of basin inversion and syn-contractual sedimentation at 2.5 Ma. The maximum age for inversion of 3.6 Ma is provided by foraminifera and ostracodes from the underlying syn-extensional Ranquil Formation.

5.11.2.1 East vergent faults and folds northeast of Isla Santa María

Reflection profile 017 is oriented west-northwest and situated 6 km north of the island crossing the cluster of crustal seismicity (Figures 5.2C and 5.2D). This profile reveals three shortening structures (Figure 5.10): (1) an asymmetric anticline at shotpoint (SP) 500; (2) an east dipping monocline at SP 250; and (3) an east vergent ramp at SP 150. The crest of the anticline is obscured by horizontal sea-floor multiples at ~0.4 and ~0.3 s depth (two-way travel time). Several small discontinuous reflectors are offset below the anticline, which we relate to a west dipping

5. Coastal deformation and subduction earthquakes

reverse fault responsible for propagating this fold. Below the monocline, a reverse fault with an east dipping asymmetric anticline in the hanging wall is clearly seen.

We identify a lower sequence, characterized by the lack of well-defined internal onlaps and truncations, and folding of subparallel, discontinuous reflectors. This unit consists of the Lebu Group and Ranquil Formation. The unconformably overlying upper unit corresponds to the Tubul Formation and exhibits onlaps, truncations, variations in thickness, progressive upward decrease in dip, and pinch-out of reflectors, which are indicative of syn-contractual deposition. Two minor normal faults cut the strong uppermost reflectors above the anticline, which we interpret as crestal-bending faults. The axial surfaces of the monocline define an upward-narrowing zone above 0.4 s. Active growth here can be inferred because the apex of this growth triangle is at the present surface, which is depositional (Suppe et al., 1992). Line-length balancing of the 2.5-Ma-old base of the syntectonic Tubul Formation accounts for about 8 % of shortening, and thus a minimum late Pliocene to Holocene shortening rate of about 0.8 mm/yr. The spatial coincidence of these structures with the inclined plane of crustal seismicity suggests that they are genetically linked with a ramp-flat-ramp geometry rooted in the plate-boundary thrust at ~12 km depth (Figure 5.1C).

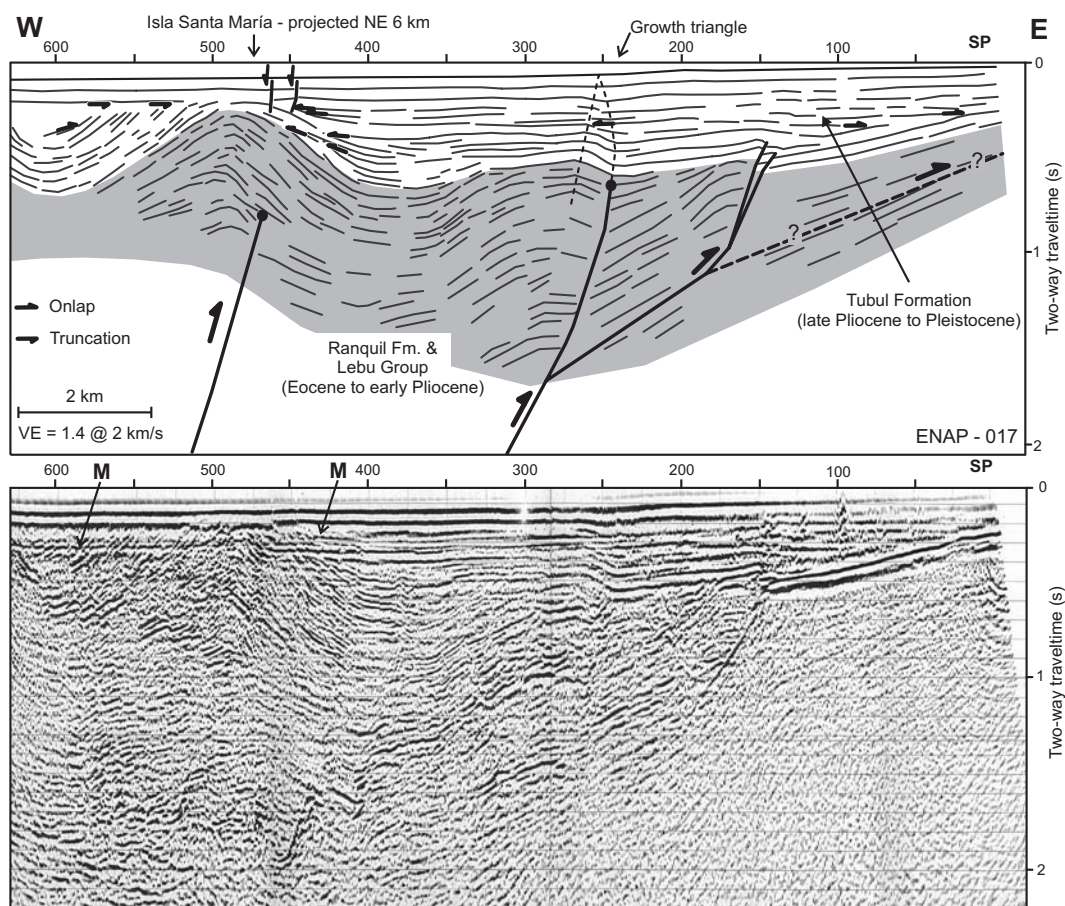


Figure 5.10: Migrated seismic reflection profile ENAP-017 (24-channel). See Figure 5.2C for location. The syntectonic sequence shows eastward propagation of the deformation by footwall shortcuts. The fault below the anticline is inferred to be rooted in the plate interface area at ~12 km depth, which is supported by the continuous alignment of seismicity (see Figure 5.1C). M: sea-floor multiple.

5.11.2.2 North vergent faults and folds east of Isla Santa María

Reflection profiles east of the island (Figure 5.2C) reveal complex lower sequences corresponding to the Quiriquina Formation, Lebu Group, and Ranquil Formation (Vietes et al., 1993), which are affected by normal faults (Figures 5.11 and 5.12). Some of these faults are inverted and control the occurrence of folds deforming the unconformably overlying Tubul Formation. These inverted faults are recognized in all profiles of the southeastern Arauco Bay (Figure 5.2C), from which we deduced a west-northwest strike.

5. Coastal deformation and subduction earthquakes

Profile 016 images five south dipping normal faults between SPs 400 and 800 and one north dipping normal fault to the north of SP 400 (Figure 5.11). These structures controlled tilting of domino-style blocks and syn-extensional deposition of the Lebu Group and Ranquil Formation. Two faults cut the Tubul Formation and determine the occurrence of fault-related folds. Onlaps within the Tubul Formation occur on the limbs of these fault-related folds, indicating syn-contractual deposition. The reverse faults at the core of these anticlines have normal offsets in the lower units, and thus are likely inverted normal faults of the late Cretaceous to early Pliocene extensional Arauco Basin. The anticline at SP 630 has a west-northwest striking axis, which passes nearly through the easternmost point of the island and the southern shore of the lowlands; it appears to be an active structure deforming the uppermost reflectors (Figure 5.11). Profiles 259 (Figure 5.12) and 257 (Figure 5.13) image similar normal faults that controlled domino-style block tilting and syn-extensional deposition of the Lebu Group and the Ranquil Formation in half-grabens. Folding of the unconformably overlying Tubul Formation and internal onlaps are observed in the vicinity of inverted normal faults. Profiles 016, 259, and 257 (Figure 5.2C) show that structural relief across the north-vergent fault increases toward the island.

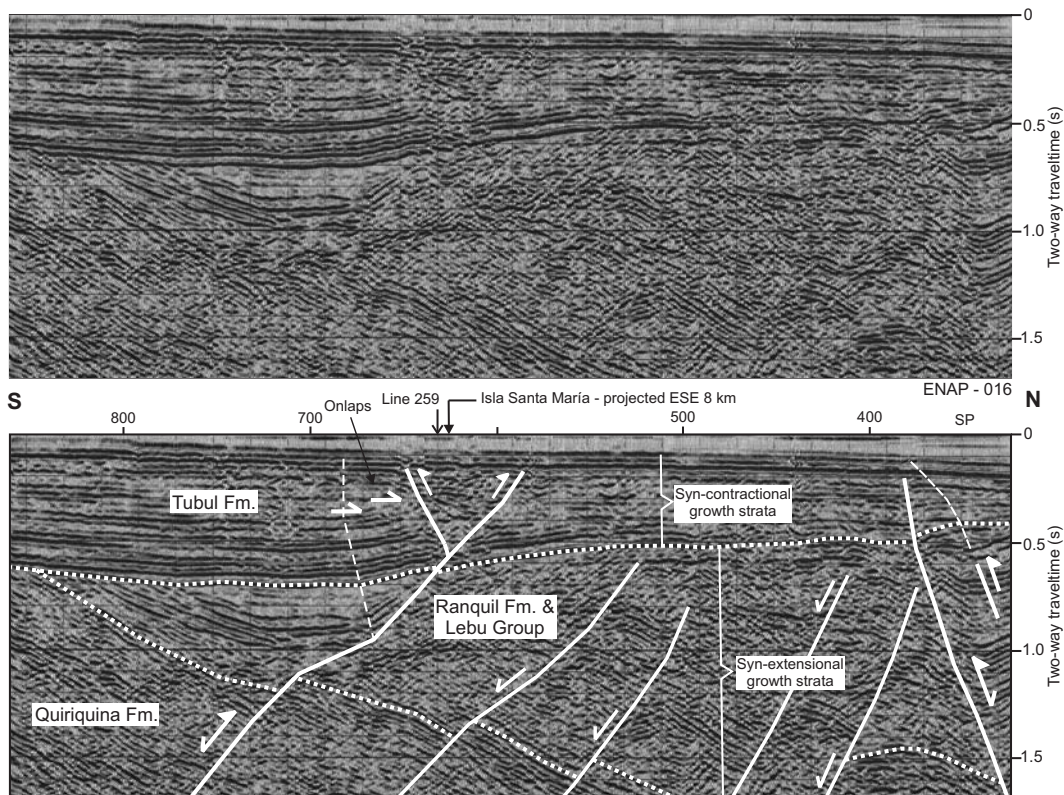


Figure 5.11: Migrated seismic reflection profile ENAP-016 (48-channel). See Figure 5.2C for location. Stratigraphy correlated with nearby exploration boreholes.

5. Coastal deformation and subduction earthquakes

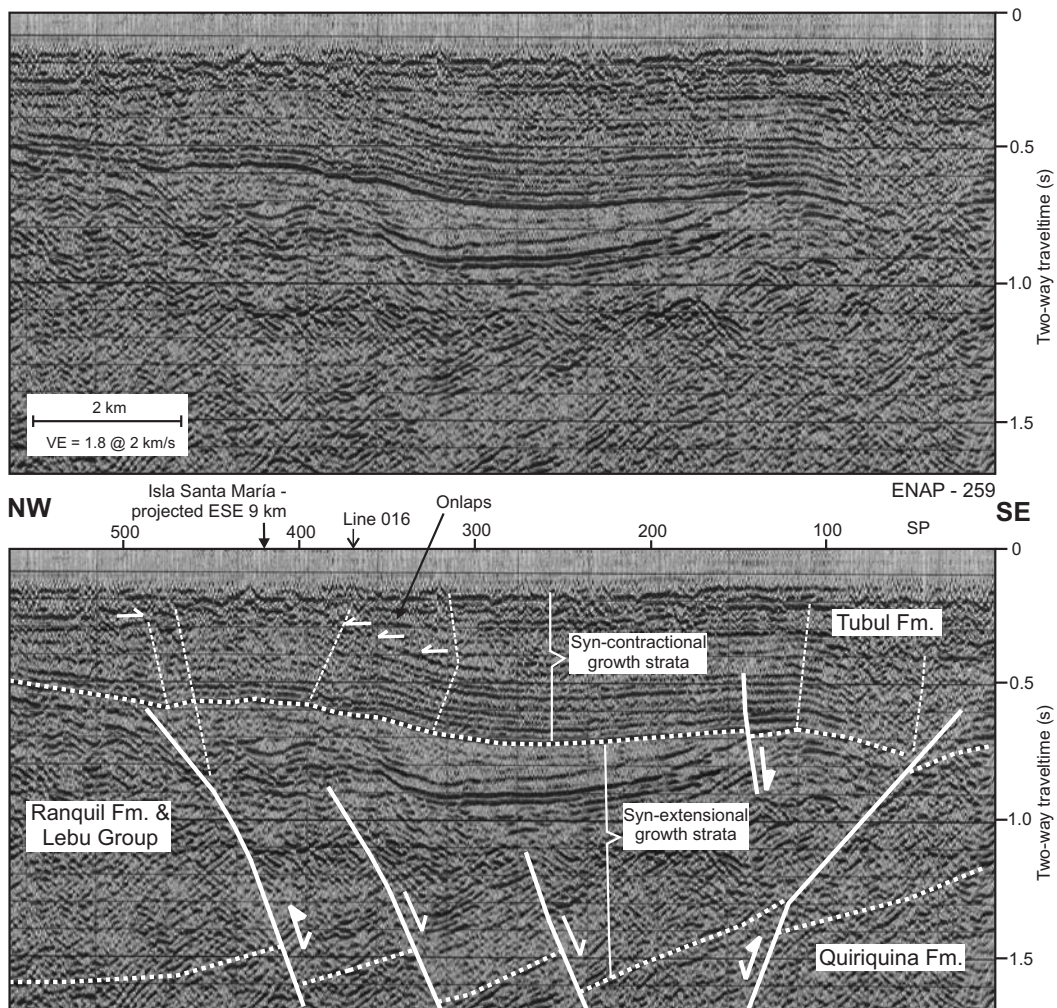


Figure 5.12: Migrated seismic reflection profile ENAP-259 (48-channel). See Figure 5.2C for location. Stratigraphy correlated with nearby exploration boreholes.

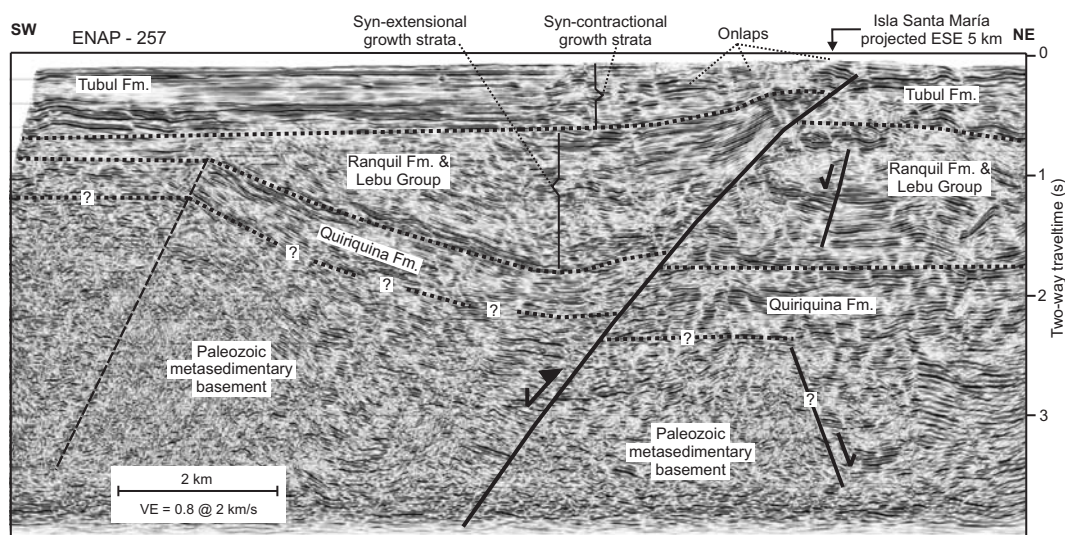


Figure 5.13: Reprocessed migrated seismic reflection profile ENAP-257 (48-channel). See Figure 2C for location. Stratigraphy correlated with nearby exploration boreholes. The syn-extensional Lebu Group and Ranquil Formation (Eocene to early Pliocene) were deposited in a half-graben controlled by a south-dipping normal fault. This fault was inverted between 3.6 and 2.5 Ma and since has controlled deposition of the syn-contractual Tubul Formation. Note the increase in structural relief of the reverse-fault cored anticline below Isla Santa María between this profile and sections 016 and 259 (Figures. 5.11 and 5.12).

Scientific Technical Report STR 07/01

DOI: 10.2312/GFZ.b103-07012

5.12 Discussion

5.12.1 Uplift and deformation mechanisms of Isla Santa María

We have shown that the topography of the Tertiary/Pleistocene unconformity, marine/eolian transition surface of the SMF, and the present-day surface of the island are asymmetrically tilted in two separate domains. In the southern domain, these reference surfaces are progressively tilted to the north-northeast along a west-northwest striking axis; while in the northern domain, they are gradually tilted to the southeast along a northeast striking axis (Figures 5.7 and 5.8; Table B1). Furthermore, our analysis of seismic profiles revealed two systems of fault-cored anticlines in the Arauco Bay area: a northeast striking system located northeast of the island and a west-northwest striking one to the southeast (Figure 5.2C). Both systems converge at the center of the island and control the tilt asymmetry. Increased structural relief islandward indicates lateral growth of the anticlines. The observed structural and geomorphic features of the island can thus be attributed to the convergence of two laterally propagating fault-cored anticlines. The eastward-tilted surfaces represent growth strata in the forelimbs of both folds, whereas their backlimbs have been removed by cliff retreat along the western coast of the island, which is exposed to strong wave attack by the Pacific Ocean (Figure 5.14). Seismic reflection profiles and exploratory well data reveal that the reverse faults in the core of the anticlines are inverted normal faults of the late Cretaceous to early Pliocene extensional Arauco Basin, which explains their oblique orientation with respect to the margin.

The high-angle normal faults on the island are interpreted to be caused by tensile bending stresses in the crestral areas of these anticlines. The marine growth strata adjacent to these faults corroborate extension as an integral part of folding, at least over the last ~50 k.y. The 10-15° angle between the axes of the anticlines and the strike of the crestral faults possibly reflects a small component of oblique shear (e.g., Philip and Meghraoui, 1983). This would result in oblique shortening with a small right-lateral component along the northeast striking fold-fault system north of the island, which is corroborated by focal mechanisms (Figure 5.2D).

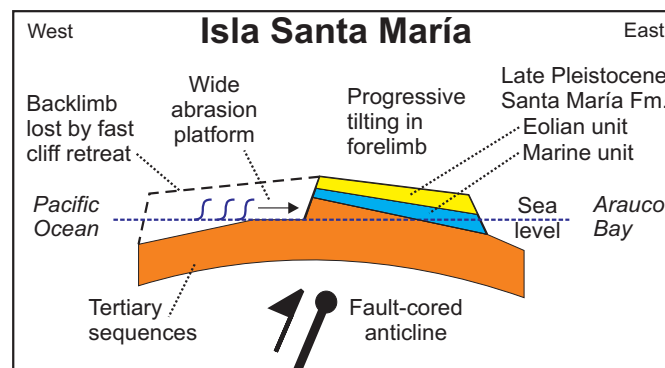


Figure 5.14: Schematic profile of Isla Santa María showing the relation between fault-cored anticline, progressive tilting and sedimentation in the forelimb, and backlimb removal by fast cliff retreat along the western coast exposed to the open Pacific Ocean.

5.12.2 Crustal reverse faulting, coastal geomorphology, and megathrust earthquakes

Based on our interpretation of seismic lines, we infer that the northeast striking system of reverse faults and folds in the Arauco Bay extends from Isla Santa María to the Concepción area, where it apparently controls the morphology of the Hualpén, Tumbes, and Coliumo peninsulas, as well as Quiriquina Island (Figure 5.2A). These are also topographic features related to anticlines that form a northeast-oriented en échelon arrangement. We therefore propose that in the Arauco-Concepción area, active upper-crustal reverse faults are responsible for creating topography. Furthermore, that their orientation and distribution fundamentally controls the coastal geomorphology reflected in elongated and aligned peninsulas, islands, and embayments. The reverse faults result from inversion of former Tertiary normal faults, whose orientation was controlled by Paleozoic basement fabrics (González, 1989), emphasizing the importance of inherited structures in guiding deformation in tectonically active regions. Inverted faults at Isla Santa María are analogous to inverted faults rooted in the Hikurangi subduction zone (Barnes et al., 2002).

The highest coseismic uplift recorded during the 1835 earthquake occurred along the fault-controlled islands and peninsulas of the Arauco-Concepción area (Figure 5.2B). Interestingly, the 2 m uplift contour related to this event is oriented northeast, and parallel to the elongation of these topographic features, as well as the reverse fault system (Figure 5.2B). This spatial coincidence of geomorphic phenomena and inverted structures, as well as the fact that the uplifted abrasion platform at Isla Santa María is steeply tilted to the east, suggests that interplate mega-earthquakes may trigger slip on reverse faults in the upper plate. Consequently, these structures would in turn control and localize the distribution of surface deformation. This assessment is supported by observations during the 1964, M 9.2 Alaskan earthquake, which caused a maximum coseismic uplift of 11.3 m adjacent to the Patton and Hanning bays reverse faults. Both structures were triggered by this event causing at least 7.9 and 6.0 m of surface displacement, respectively (Plafker, 1972). Similarly, crustal-scale transverse faults along the Cascadia margin propagate surface folds, which apparently control localized coseismic subsidence during megathrust ruptures (Goldfinger et al., 1992).

Coseismic warping and tilting caused by earthquakes nucleated in the low-angle megathrust are predicted by dislocation models (e.g., Savage, 1983) and are widely observed in geodetic data (e.g., Hyndman and Wang, 1995). The deformation patterns, and consequently the landforms associated with cumulative ruptures have wavelength on the order of a 100 km. In contrast, the tilted and warped peninsulas and islands in the Arauco-Concepción area are narrow features, with wavelengths of less than 5 km, indicating that their emergence is instead dictated by the contractional reactivation of pre-existing steep normal faults imaged in seismic reflection profiles.

5.12.3 Modern versus millennial uplift rates

The earthquake-cycle model of subduction zones predicts inverse patterns during the interseismic strain accumulation and coseismic strain-release phases (Savage, 1983). This model, supported by geodetic measurements (e.g., Hyndman and Wang, 1995; Klotz et al., 2001), also predicts that most of the strain released during earthquakes is elastic and that only a small amount of permanent strain, which is the interseismic strain not recovered during coseismic deformation, accumulates after each cycle. The ~ 2 m/k.y. uplift rate calculated from the geological record for the last ~ 50 k.y. at Isla Santa María should thus represent the cumulative permanent strain averaged from many earthquake cycles.

At Isla Santa María, Darwin (1839) measured 2.4- to 3-m coseismic uplift during the M ~ 8.25 earthquake in 1835 (Figure 5.2B), but the abrasion platform uplifted during this earthquake is at the same elevation today (Figure 5.4). The previous earthquake in 1751 is inferred to have had a larger magnitude of ~ 8.5 (Lomnitz, 2004). Coseismic uplift on the island during this event could have been ~ 6 m, judging by the elevation of a partially preserved abrasion platform above the 1835 surface (Figure 5.4A). Therefore, these two surfaces should represent the permanent strain of the 1751 and 1835 cycles, implying a modern uplift rate which is over an order of magnitude higher than the millennial rate. This might indicate that the Concepción segment is neither slip nor time-predictable, as has been shown for the Valdivia segment to the south (Cisternas et al., 2005).

Darwin noticed $\sim 50\%$ of post-earthquake recovery at Talcahuano (Figure 5.2B). This raises the question as to whether Isla Santa María also subsided after the earthquake, and subsequently emerged back to the same level or if it has remained at the same elevation since 1835. We cannot reconcile these issues with our data, but we can state that the island is slowly uplifting today in response to the seismically active reverse fault imaged below. In this region, GPS data shows shortening inferred to be caused by locking of the plate interface (Klotz et al., 2001), and thus ongoing thrust-type shear of the upper plate by megathrust loading. Because no mega-earthquakes have ruptured the Concepción segment since 1835, loading here is expected to be in an advanced phase promoting thrust faulting and surface uplift.

5.13 Conclusions

The uplifting Isla Santa María was part of a submerged bedrock erosional platform at the edge of the Chilean shelf during the Pleistocene. Tectonic uplift and eustatic oscillations of sea level caused the onset of coastal marine sedimentation at least ~ 50 ka ago. Due to continuous tectonic uplift at ~ 2 m/k.y., the island emerged ~ 31 ka ago and eolian sedimentary conditions prevailed. The eastward-inclined present-day surface of the island, the eastward increase in thickness of both the marine and eolian units of the late Pleistocene Santa María Formation, and a minimum of twenty emerged Holocene strandlines indicate progressive tilting at $\sim 0.025^\circ/\text{ka}$ during the late Quaternary.

Crustal seismicity and seismic reflection profiles revealed active reverse faults, fault-cored anticlines, and growth strata that document ongoing shortening over the last 2.5 m.y. Deformation is distributed in folds and faults that individually accommodate low magnitudes of shortening. Focal mechanism solutions and the inclined alignment of crustal seismicity along a master fault indicate that it is rooted in the plate interface at ~12 km depth.

Isla Santa María is located at the intersection of two growing fault-cored anticlines; their lateral propagation produced progressive asymmetric tilting recorded in the Pleistocene marine and eolian units and the present-day surface of the island, which are growth strata in the forelimbs of both folds. Their backlimbs have been removed by cliff-retreat along the western side of the island, which is exposed to stronger erosion through waves from the open Pacific Ocean.

The highest coseismic uplift measured by Darwin during the 1835 earthquake is parallel to the seismogenic reverse fault system that extends from Isla Santa María across the Arauco Bay to the city of Concepción and surrounding areas. Importantly, this geometry suggests that blind reverse faults in the upper plate of a subduction zone can be triggered by great interplate earthquakes. In turn, these crustal faults control the distribution of low-wavelength surface features by folding of the upper crust between and probably also during interplate events. Consequently, subduction zone interplate earthquakes and upper plate faults control the degree and areal extent of surface deformation, uplift, and associated seismic hazards. In the Arauco-Concepción area, active reverse faults result from inversion of late Cretaceous to early Pliocene normal faults, and thus their inherited orientations control the geometry and distribution of emergent coastal landforms, emphasizing the fundamental role of inherited structures in seismotectonic segmentation of convergent margins.

Acknowledgments

We thank Empresa Nacional del Petróleo–ENAP Chile for providing seismic profiles and to L. Rojas, C. Mpodozis, and J.P. Radic (ENAP-Sipetrol) for fruitful discussions and permission to publish these data. A. Manzanares, M. Bohm, and G. Asch (GFZ) provided the ISSA seismicity data; M. Moreno and J. Jara helped in the field. This is publication GEOTECH-220, of the TIPTEQ project. DM acknowledges support from the DAAD-IQN program at Potsdam University, Leibniz-funds from O. Oncken, and GFZ-Potsdam. MS acknowledges additional funding by the German Science Foundation and A. Cox fund of Stanford University. Constructive reviews by R. Allmendinger and Associate Editor P. Mann greatly helped clarify the ideas presented in this work.

6. Incipient axial collapse of the Main Cordillera and strain partitioning gradient between the Central and Patagonian Andes, Lago Laja, Chile

Abstract

Lago Laja is a late Quaternary volcanic-dammed lake located near the drainage divide of the south-central Andes. Field observations, lake reflection-seismic profiles, bathymetry, and remote sensing data reveal an active fault system that runs parallel to the volcanic arc along the axis of the Main Cordillera, the Lago Laja fault system (LLFS). Normal faults of this extensional system cut late Pleistocene volcanics, <7.1-ka-old still-water lacustrine sediments, 6.3-ka pyroclastic deposits, and Holocene alluvial fans. We divide the LLFS in three segments based on fault geometry, width, and slip magnitude. The underwater faults of the central segment in the lake's deepest part have the maximum Holocene vertical slip rate of >2.7 mm/yr. Since 7.1 ka, the LLFS accounts for ~0.7% of arc-normal extension at an average minimum rate of 1.2 mm/yr and strain rate of $\sim 10^{-14} \text{ s}^{-1}$. Seismites and surface ruptures evidence $M > 6$ paleoearthquakes. The Main Cordillera at $\sim 37^\circ\text{S}$ is a large-scale pop-up structure uplifted by thrusting along its foothills. In this light, we interpret extension in the axial and highest part of the Andes as incipient synorogenic gravitational collapse in response to uplift and crustal thickening. Thermal weakening due to elevated heat flow and post-glacial lithospheric rebound and unbending have probably contributed to the arc-limited collapse and Holocene acceleration of deformation rates. The lack of significant strike-slip offsets along the LLFS as well as along both foothills-thrust systems at 37°S contrasts with the intra-arc dextral fault zone south of 38°S . Regional structural data indicates that north of 38°S , diffusely-distributed strain reflects low partitioning of oblique subduction, while to the south deformation is localized in a discrete strike-slip fault zone along the volcanic arc, reflecting a higher degree of partitioning. We relate this strain partitioning gradient to favorable fault orientations in the forearc north of the Arauco Peninsula, a major seismotectonic boundary.

6.1 Introduction

Continental margins usually deform over broad regions (e.g., Molnar, 1988), and in oblique plate convergent settings strain is frequently partitioned in a discrete strike-slip fault system and zones of diffuse deformation (e.g., Fitch, 1972; Jarrard, 1986; Tikoff and Teyssier, 1994; Teyssier et al., 1995; Avé Lallemant and Oldow, 2000). Mountain belts result from crustal shortening and thickening, but depending on its evolutionary state and on the physical properties of the lithosphere, strain may be partitioned into contraction along the mountain's foothills and coeval extension or transtension along its axis (e.g., Dalmayrac and Molnar, 1981; Mercier et al., 1987; Molnar and Lyon-Caen, 1988; Buck and Sokoutis, 1994; Royden, 1996; Liu et al., 2000).

Active strain partitioning occurs at crustal scale along the Andean subduction margin (e.g., Dewey and Lamb, 1992; Siame et al., 2005), but although plate convergence is constant along the margin (Somoza, 1998; Kendrick et al., 2003), the degree of partitioning and consequent structural styles, and distribution of strain magnitude and seismic moment release vary markedly along strike. Major along-strike segmentation of the Andes has been correlated with changes in dip and age of the subducting plate, as well as with the presence of oceanic ridges and inherited continental discontinuities (e.g., Jordan et al., 1983; Mpodozis and Ramos, 1989; Ramos, 1999; Yáñez and Cembrano, 2004). However, the detailed structure of some transitional zones and their control on the seismotectonic segmentation of the margin remain poorly understood.

A high degree of partitioning characterize the Patagonian Andes ($38\text{--}46^\circ\text{S}$), where most of the margin-parallel component of oblique convergence has been accommodated by a strike-slip fault zone along the volcanic arc (Figure 1) (Lavenu and Cembrano, 1999; Rosenau et al., 2006). The margin-normal component is absorbed by the subduction interface and crustal faults in the coastal region as no thrusting has occurred in the foreland since late Miocene time (Giacosa and Heredia, 2004; Melnick et al., 2006a). The Patagonian intra-arc region has relatively low crustal seismicity and only two studies have reported focal mechanisms from shallow earthquakes that

6. Incipient collapse and strain partitioning at Lago Laja

can be related to the geometry and kinematics of a surface fault (Chinn and Isacks, 1983; Barrientos and Acevedo, 1992). In contrast, along the flat-slab segment of the Central Andes (33–28°S) abundant shallow seismicity and Pliocene to Recent deformation has occurred mainly in the foreland region, partitioned into wide thrust belts and subordinated zones of strike-slip faulting (Siame et al., 2005). The transitional region (33–38°S) between the flat-slab and Patagonian segments lacks previous detailed neotectonic studies, although three shallow $M > 7$ earthquakes related to upper crustal faults of the intra-arc region are described in the <500-years historical record (Lomnitz, 2004); no causative structures have been proposed yet and virtually nothing is known about seismogenic faults in this part of the high Andes. Between 33–34°S, superficial microearthquake clusters have been tentatively related to mapped faults or lineaments (Barrientos et al., 2004), still, their paleoseismicity and relation to the historical $M > 7$ events remain unexplored. Many lakes exist in this region of the high Andes, most are of glacial or volcanic origin while others result from natural damming by landslides or volcanic deposits, and from artificial barriers made for hydropower generation, irrigation, or to store mining residue. Since these lakes are in a seismically and volcanically active region, where related processes could lead to the sudden opening of a lake's dam, the generation of outburst megafloods along the steep western flank of the Andes pose one of the highest hazards to settlements in the foothills, the Central Depression, and even the coastal region. Wide fans with volcanic boulders spread in the flat Central Depression are testimonies of past catastrophic outburst floods (e.g., Thiele et al., 1998).

We focus on the southernmost Central Andes, where most of the studied active deformation has been east vergent thrusting in the back-arc and foreland regions. The aim of this study is mainly to document an active extensional fault system adjacent to a volcanic-dammed lake in the higher part of the Main Cordillera, the Lago Laja fault system. We describe the kinematics, deformation rates, and earthquake hazards of this fault system by integrating field observations with offshore-lake seismic profiles, bathymetry, and remote sensing images. Soft-sediment deformation structures affecting late Pleistocene glacio-lacustrine deposits adjacent to the fault system are discussed as indicators of paleoseismicity. Furthermore, we document Quaternary folding in response to shortening locally along the western foothills of the Main Cordillera and integrate regional neotectonic data in an arc-normal profile. In this light, the extensional deformation along the Main Cordillera's axis is interpreted as caused by incipient gravitational collapse in response to coeval shortening along both its eastern and western foothills. Active structures in the forearc and intra-arc regions are integrated to propose a transition zone in the degree of strain partitioning and to discuss the causes and resulting changes of the distribution of active deformation, structural styles, and topography along the margin.

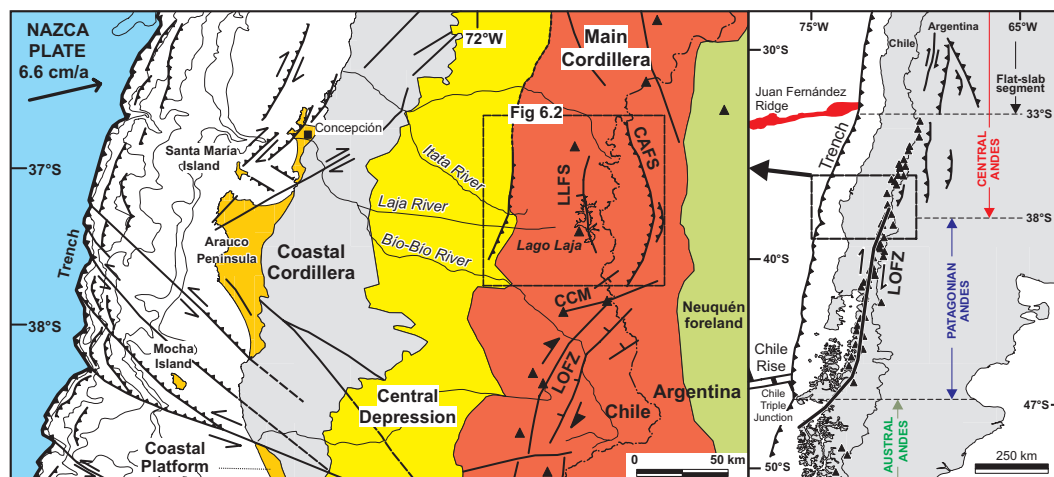


Figure 6.1: Right: Location map with main neotectonic structures and Andean segments (Mpodozis and Ramos, 1989). LOFZ: Liquiñe-Ofqui fault zone. Flat-slab foreland structures from Siame et al. (2005). Triangles denote Holocene volcanoes. Left: Regional morphotectonic units and Plio-Quaternary faults of the study region. LLFS: Lago Laja fault system; CAFS: Copahue-Antiñir fault system. The offshore and coastal structures have been interpreted from multibeam bathymetry acquired by Reichert et al., (2001), crustal seismicity, focal mechanisms, and industry reflection-seismic profiles (Melnick et al., 2006b; Melnick and Echtler, 2006a).

6.2 Methods

Active faulting along the Lago Laja fault system is documented through field geologic, geomorphic, and structural mapping, interpretation of rectified aerial photos and satellite imagery. Digital Elevation Models (DEM) made from digitized 1:50.000 topographic maps, SRTM-Nasa data, and photogrammetric restitutions of 1:70.000 scale aerial photos aided in the identification and mapping of landforms and active structures. Published isotopic ages from the youngest deposits cut by the fault system were compiled to estimate deformation rates. Radiocarbon ages were calibrated using the CalPal 2005 software – www.calpal.de (Stuiver et al., 1998; Hughens et al., 2004). Within the framework of paleoclimatic and limnologic research, high-resolution reflection-seismic data were collected at Lago Laja by the Renard Center for Marine Geology, University of Ghent, Belgium (RCMG) (Charlet et al., 2003). They were recorded using a “Centipede” multi-electrode sparker, which operated at 500 J with a signal frequency range of 100-1500 Hz, and a subbottom-profiler (Transducer Mount Model 132B, 3.5 kHz) composed of a transmitter Model 5430A and a receiver Model 5210A. A total of 72 km of reflection lines were shot, 25 km sparker and 47 km pinger (3.5 kHz). The subaqueous faults of Lago Laja were mapped from selected 3.5 kHz profiles using the software package KINGDOM[®] at RCMG. In this cooperation, bathymetric profiles were collected by the UmweltForschungsZentrum Leipzig-Halle, Germany (UFZ), using a two-frequency echo sounder system (Simrad EA400) and a differential GPS. About 160 cross-profiles were measured covering 350 km of tracklines. The data was linearly interpolated to produce a DEM. To quantify fault throw, individual bathymetric profiles were correlated with the structures interpreted from the seismic lines.

6.3 Regional tectonic and geologic setting

The Andean margin is formed by subduction of the Nazca oceanic plate under the South American continent (Figure 1); this collision is responsible for the growth of the Andean orogeny over the last ~200 m.y. (e.g., Mpodozis and Ramos, 1989). The subducting Nazca plate at 37°S is formed by ~32-Ma-old oceanic crust (Tebbens and Cande, 1997), which converges at 80 mm/yr averaged over the last ~3 m.y. (Somoza, 1998), or 66 mm/yr determined on the base of GPS modeling (Kendrick et al., 2003).

The Andes at ~37°S are subdivided in five major morphotectonic units (Figure 1): (1) the Coastal Platform, which consists of uplifted Cenozoic coastal sequences; (2) the Coastal Cordillera that integrates a late Paleozoic accretionary complex and magmatic arc; (3) the Central Depression, a low-relief area formed by Oligo-Miocene sedimentary and volcanic rocks covered by Plio-Quaternary sediments; (4) the Main Cordillera, focus area of this paper, consists of a long-lived Meso-Cenozoic magmatic arc and intra-arc volcano-sedimentary basins; and (5) the Neuquén Mesozoic embayment and late Cretaceous-Miocene foreland basin. Crustal thickness below the Main Cordillera is between 40 and 45 km in the 37-39°S region, as estimated from refraction-seismic profiles (Lüth et al., 2003), P-wave tomography (Bohm et al., 2002), receiver functions (Yuan et al., 2006), and gravity modeling (Tassara et al., 2006).

Between 36-39°S, the Main Cordillera integrates the late Oligocene-middle Miocene Cura-Mallín and Trapa-Trapa Formations (Niemeyer and Muñoz, 1983), which have been interpreted as the infill of the Cura-Mallín extensional intra-arc basin (Jordan et al., 2001; Kemnitz et al., 2005). The Main Cordillera was uplifted during the late Miocene through inversion of the Cura-Mallín basin (Jordan et al., 2001; Melnick et al., 2006a). Orogenic shortening formed a mountain belt about 2 to 2.5 km high and 80 km wide. This mountain building phase is recorded along most of the Central and Southern Andes and has a diachronic evolution and marked along-strike variations in shortening magnitude and deformation style (e.g., Kley et al., 1999). Between 38-39°S, shortening in the intra-arc started at ~11 Ma and stopped before 5.6 Ma, as shown by ages of the synorogenic and oldest post-tectonic deposits, respectively (Melnick et al., 2006a). Plateau volcanic rocks, referred to as the Cola de Zorro Formation of Pliocene-early Pleistocene in age (Vergara and Muñoz, 1982), overlay the former units in a marked angular unconformity (Figure 2).

At 37°S in the coastal region, shallow crustal seismicity registered by a temporary network (Bohm et al., 2002), focal mechanisms (Bruhn, 2003), and industry reflection-seismic profiles show that dextral oblique shortening is occurring along northeast-striking reverse faults, which extend from Isla Santa María to the northeast (Figure 1) (Melnick et al., 2006b). In contrast, south of the Arauco Peninsula, the same data sets image similar active faults, which in turn strike northwest and accommodate left-lateral oblique shortening. Therefore, two coastal kinematic domains exist, the domain south of Arauco where active faults strike northwest and have a left-

lateral component, and the domain to the north where in turn active faults strike northeast and have a right-lateral component (Figure 1). Seismic stratigraphy of syntectonic deposits correlated with ENAP hydrocarbon-exploration boreholes indicate that these structures have been continuously active since the late Pliocene with constant kinematics (Melnick et al., 2006b; Melnick and Ehtler, 2006a).

After the southeast Pacific plates reorganization at ~10 Ma (Tebbens and Cande, 1997), convergence obliquity along the Andean margin increased continuously south of ~20°S, inducing strain partitioning along the margin (e.g., Dewey and Lamb, 1992). No Pliocene-Quaternary foreland fold-and-thrust belt has been recognized in the Patagonian Andes (38-47°S), where about half of the margin-parallel component of oblique subduction has been accommodated along the intra-arc region by the strike-slip Liquiñe-Ofqui fault zone (LOFZ in Figure 1) (Rosenau et al., 2006). The LOFZ is a ~1200-km-long dextral system that extends from 47°S, immediately south of the Chile Triple Junction, until 38°S (e.g., Cembrano et al., 1996; Lavenu and Cembrano, 1999). At its northern end, the Callaqui-Copahue-Mandolegüe crustal-scale transfer zone (CCM in Figure 1) (Melnick et al., 2006a) decouples the LOFZ-related strike-slip deformation from the Copahue-Antiñir contractional back-arc system and the Lago Laja extensional intra-arc system, the focus of this paper.

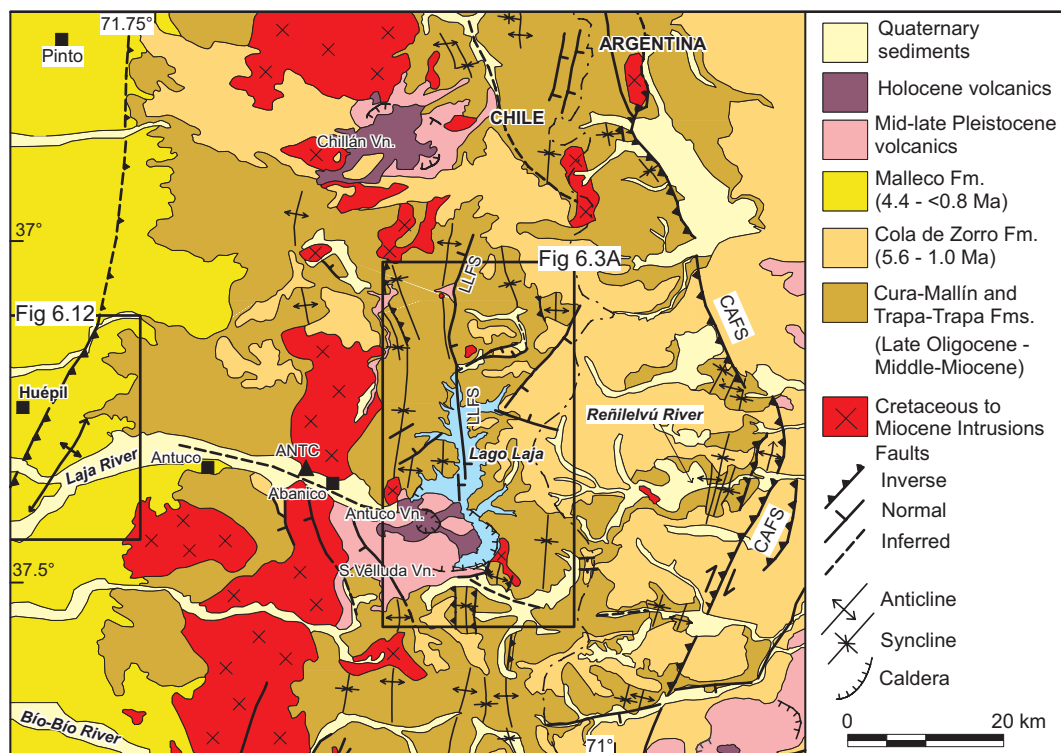


Figure 6.2: Regional geologic map of the Main Cordillera. LLFS: Lago Laja fault system, CATF: Copahue-Antiñir thrust front. Compiled from Niemeyer and Muñoz (1983), Delpino and Deza (1995), Folguera et al. (2004), Melnick et al. (2006b), and new field observations.

6.4 Study area: Lago Laja

Lago Laja, also known as Laguna de la Laja, is a narrow volcanic-dammed lake located along the axis of the volcanic arc (Figures 1 and 2). The lake has a surface of 95 km² and a watershed area of 975 km². The maximum length and width are 32 and 9 km, respectively, and the total shoreline length is 136 km. The lake is formed by three connected sub-basins, two shallow parts in the south and north, and a central deeper part (Figure 3). At a water level of 1346 m, the maximum depth is 134 m and the estimated volume is 4.7 km³. The lake is fed by several small streams, torrential rivers, and the meandering Pinos River on the southern part, and is drained by the Laja River and two artificial tunnels made for hydropower generation. Mean annual precipitation is 2170 mm/yr, mostly as snow during the winter (Dirección Meteorológica de Chile, 2005). Many strandlines are present along the shore due to the large fluctuations of the water level.

Annual variations in lake level have reached 60 m, causing volume changes of up to 3 km³, due to management by hydroelectric power stations during dry years (Bevis et al., 2004).

6.4.1 Origin of Lago Laja

The 2979-m-high Antuco and 3585-m-high Sierra Velluda stratovolcanoes are located on the southwestern border of Lago Laja (Figures 2 and 3A). Both are Quaternary edifices with ages at the base of <124 and 495 ± 88 ka, respectively (K-Ar/whole rock; Moreno et al., 1985). The Sierra Velluda is inactive and deeply eroded by glaciations, while the Antuco erupted at least 19 times since 1624, latest in 1911 (Petit-Breuilh, 1994). In contrast to most of the stratovolcanoes in the Southern Andes, the base of these edifices is topographically lower than their surrounding Tertiary basement. Both volcanoes are emplaced in the western part of an ~18-km-diameter annular depression (Figures 2 and 3A), where they dam the drainage network forming the Laja intramontane basin.

The Antuco volcano evolved in two stages: Antuco 1, started erupting at ~130 ka with the building of the basaltic-andesitic edifice and culminated with a Bandai-type caldera collapse event; and during the ongoing Antuco 2 stage a 500-m-high cone formed in the center of the cuspidate caldera created at the end of the previous stage, as well as six flank vents and cinder cones (Domeyko, 1846; Brügggen, 1941; Vergara and Katsui, 1969; Moreno et al., 1985; 2000; Thiele et al., 1998; Lohmar, 2000) (Figure 3A). The volcanic avalanche ejected at the end of the first stage caused the opening of Lago Laja's dam generating an outburst megaflood (Vergara and Katsui, 1969; Thiele et al., 1998). Subsequent lava flows emitted during the second stage dammed the Laja River forming the present-day Lago Laja. Two radiocarbon ages have been reported for this volcanic avalanche: 9.70 ± 0.6 (Moreno et al., 1985) and 6.25 ± 0.06 ka BP (Lohmar, 2000). We favor the latter age because the analytic error is much lower. This age was obtained from a large piece of *Nothofagus dombeyi* found 2 km northwest of Abanico (Figure 2) inside a hummock of the volcanic avalanche; it has a calibrated value of 7.143 ± 0.09 cal-ka BP (calibrated thousand years before present). The lava flows emitted during the Antuco's last major eruption in 1852-1853 (Figure 4) covered the outlet of Lago Laja causing the waters to rise ~20 m (Petit-Breuilh, 1994).

6.4.2 Lake stratigraphy from reflection-seismic profiles

The sparker and pinger (3.5 kHz) data show a complex seismic stratigraphy with limited penetration. The profiles indicate a strong influence in the southern part of the lake by volcanic input from the Antuco. Several units, which could correspond to successive volcanic events, are thinning out northward away from the volcano. Fluid-escape features and free-gas pockets are observed locally. In the central and northern sectors, a lacustrine drape overlies these volcanic-lacustrine units above an erosive unconformity (Figure 5). This drape is formed by continuous parallel reflectors, typical of Holocene lacustrine sediments in glaciated environments (e.g., Eyles et al., 2000). This acoustically-laminated seismic facies—however, without confirmation from sediment cores—suggests that the sediments are typical still-water lacustrine deposits, composed of laminations formed by suspension settling, similar to the sediments recovered in other lakes in the region (e.g. Bertrand et al., 2005). The lacustrine drape has a fairly uniform thickness of 2 to 3 milliseconds TWT (two-way traveltime), about 1.6 to 2.4 m. We relate this erosional surface to the Holocene caldera-collapse event at the end of the Antuco 1 stage, which caused the opening of Lago Laja generating an outburst megaflood. The lake was probably emptied during this event because the >150-m-high present-day dam, which is exclusively formed by post-collapse lava flows (Figure 4), is higher than the maximum depth of the lake. Therefore after the opening of the dam the fluvial systems that feed the lake advanced into the deeper parts of the basin eroding the poorly-consolidated lacustrine sediments. This erosional surface is thus synchronous to the Antuco 1 caldera-collapse event dated at 7.1 ± 0.09 cal-ka (Lohmar, 2000). This horizon is observed in most of the seismic profiles and is therefore an excellent marker for structural analysis. The Holocene sedimentation rate would be 0.2-0.3 mm/yr, which is consistently lower than the 0.7-0.9 mm/yr rate determined for Lago Puyehue at 40°S by coring (Bertrand et al., 2005). Puyehue is a glacial lake located at much lower elevation (185 m asl.), with much higher watershed-to-lake area ratio and elevated mean annual precipitation and sediment supply, therefore a higher sedimentation rate than at Laja should be expected.

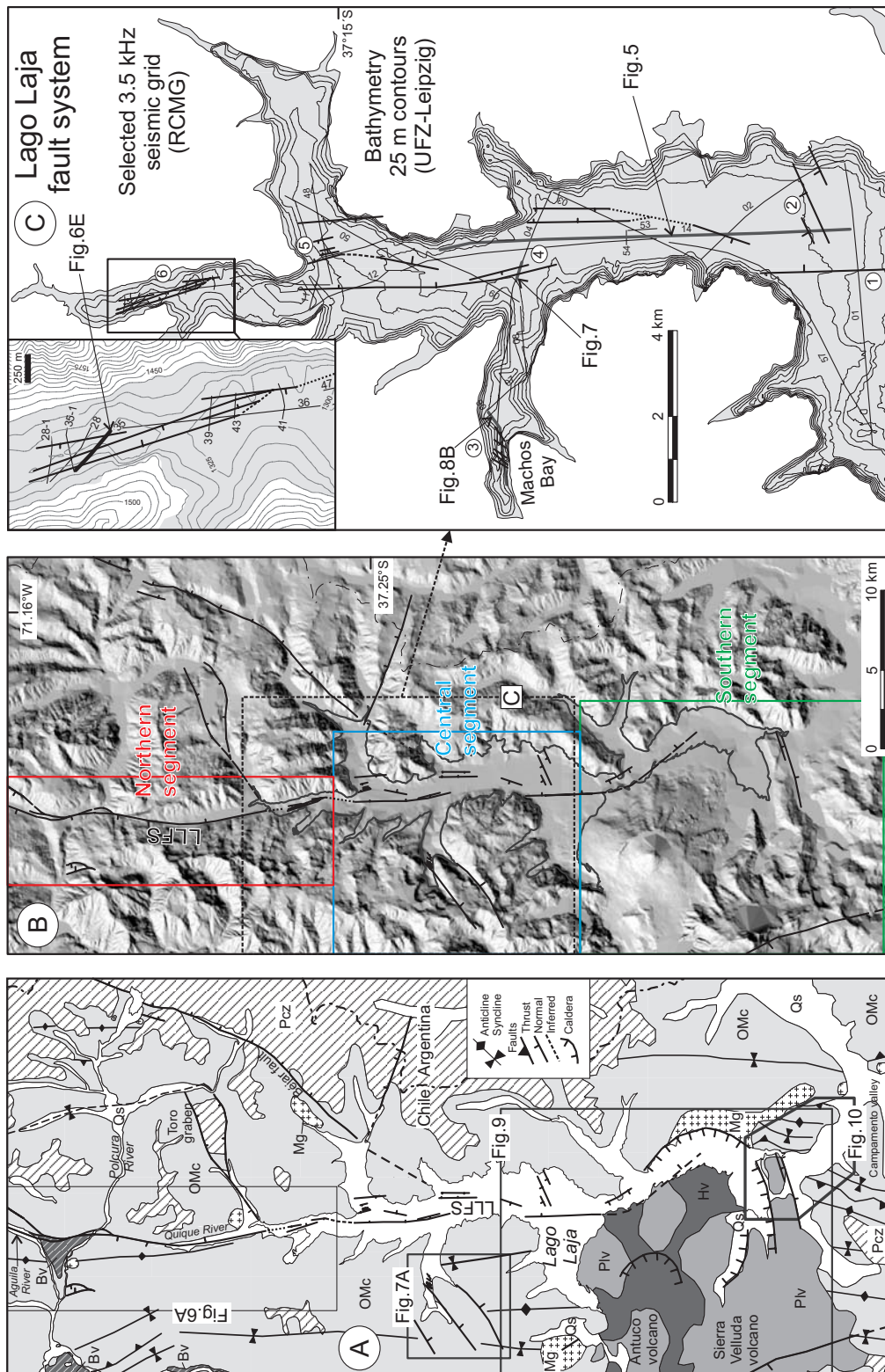


Figure 6.3: A: Geologic map of Lago Laja region, modified from Niemeyer and Muñoz (1983) and Melnick et al. (2006a). Geologic units: OMc—Cura-Mallín and Trapa-Trapa Fms. (Oligocene-middle Miocene), Mg—Intrusives (Late Miocene), Pcz—Cola de Zorro Fm. (Pliocene-early Pleistocene), Plv—Middle-late Pleistocene volcanics, Bv—late Pleistocene valley-confined basalts, Hv—Holocene volcanics, Qs—Quaternary sediments. B: Shaded-relief DEM made from 1:50.000 topographic maps (50-m contours) and detailed bathymetric profiles. Quaternary extensional faults are shown. The white boxes indicate the three segments of the Lago Laja fault system discussed in the text. C: Location of selected 3.5 kHz reflection-seismic profiles and map of Holocene faults interpreted from these lines.



Figure 6.4: Panoramic view from the foothills of the Antuco volcano toward the northwest (see Figure 6.9 for location). The Holocene volcanic avalanche can be seen on the lower left. Calibrated radiocarbon age from Lohmar (2000). The late Holocene lava flows on the lower part conform the dam of the present lake. The darker flows on the lower right were emitted during the 1853 eruption and dammed the outlet of Lago Laja causing its waters to rise about 20 m (Petit-Breuilh, 1994). In the central part a relict late Pleistocene lacustrine surface is seen. Crosses indicate reference elevations in meters.

In the central part of Lago Laja, homogeneous, non-reflective massive layers are locally interbedded in the lacustrine sequence (Figure 5). These discontinuous beds thin out rapidly and are thus interpreted as debris or mass flow deposits, based on similarities with other lake-seismic surveys in mountain regions where they have been verified by coring (e.g., Chapron et al., 1999; Schnellmann et al., 2002). These instantaneous deposits could have been triggered by earthquake-induced ground shaking or by abnormally-high precipitation events. However, the mass flow deposit imaged on profile 14 (Figure 5) increases in thickness toward the main northwest-dipping fault, and may have been related to an earthquake that caused slip on this fault.

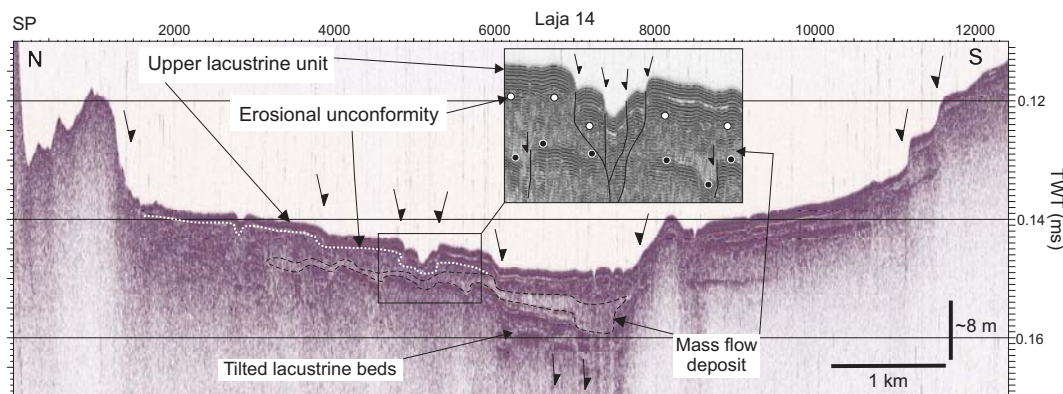


Figure 6.5: Reflection-seismic profile Laja 14 (3.5 kHz) illustrating the stratigraphy and structure of the central part of Lago Laja. For location see Figure 3C. SP–Shot Point, TWT–Two-way traveltime. The upper lacustrine drape covers the older sequences in an erosional unconformity. We relate this erosional phase to the 7.1-ka-od Antuco 1 caldera-collapse event, which broke Lago Laja’s dam causing an outburst megaflood. The lake was totally emptied and the fluvial systems advanced into the lacustrine basin eroding the unconsolidated sediments and forming the unconformity, see text for details.

6.5 The Lago Laja fault system (LLFS)

The LLFS strikes north-south and extends for ~60 km along the bottom of Lago Laja, Quique and Aguila valleys (Figure 3A). During their regional survey, Niemeyer and Muñoz (1983) first mapped the fault along the Quique valley, but kinematics and age were not determined. Recent faulting along this system was first recognized in offshore seismic profiles. These faults offset the most recent sediments of the lake-bottom (Figure 5), generating relief on the lake bed. During consecutive field investigations, faults cutting Holocene pyroclastic deposits and alluvial fans were found north and southeast of the lake, and merged with the interpretation of seismic profiles to define and map the fault system.

We subdivide the LLFS in three segments (Figure 3B): (1) the northern segment, where faulting occurs along a relatively narrow, north-south-striking zone with meter-scale slip magnitude; (2) the central segment, which consists of a ~7-km-wide north-south-striking zone of faulting and also oblique structures, and where slip can reach 20 m on individual faults; and (3) the southern segment, which has a poorly-defined fault geometry masked by the Antuco volcanics and integrates soft-sediment deformation structures interpreted as seismites. Slip magnitude decreases in the southern segment and the fault-pattern becomes irregular. Evidence for recent extensional tectonics is documented from surface ruptures, fault-controlled volcanic eruptions, and seismic and bathymetric profiles for each segment.

6.5.1 Northern LLFS segment

6.5.1.1 Surface ruptures

North of Lago Laja along the Quique valley (Figures 3A and 6A), Holocene surface ruptures can be traced as fairly continuous features on aerial photos. The main fault strikes north-south and forms a ~1.5-m-high east-down scarp that cuts alluvial fans along the western flank of the valley. The rupture area is covered by dense vegetation, which probably concentrates here due to waters springing through the densely fractured fault zone. The dense vegetation area is about 15-20 m wide and can be followed on the aerial photo for 3.5 km along the western flank of the valley, and northward for 1.5 km along the eastern flank (Figure 6B).

Postglacial fallout pyroclastic deposits from the Chillán volcano, which is located ~25 km to the northwest (see Figure 2), cover most of the area north of Lago Laja. At a road-cut along the Polcura River, ten north-south-striking normal faults cut these pyroclastic deposits (Figure 6D). The faults form an asymmetric horst-and-graben structure with west-down polarity and 3.2 m slip on the main fault. Dixon et al. (1999) reported nine radiocarbon ages of pyroclastic deposits from the Chillán volcano, which range from 9.30 ± 0.07 to 2.27 ± 0.06 ka BP; calibrated values range from 10.46 ± 0.1 to 2.25 ± 0.07 cal-ka. They subdivided these deposits based on their ages, facies, and spatial distribution in three groups: the ~10-ka-old basal sequence, the intermediate sequence that ranges from 6.1 to 6.5 cal-ka, and the proximal deposits that have a ~2.2 cal-ka age. Unfortunately, no datable material was found in the faulted pyroclastics of the Polcura River, but based on their strong lithological and stratigraphical similarities and equivalent distance to the source, we correlate them with Dixon's intermediate group, which has a pooled age of 6.3 ± 0.2 ka. Assuming this age range, a slip rate of 0.50 ± 0.02 mm/yr is derived for the main west-dipping fault.

At the crossing of the Aguila and Polcura Rivers (Figure 3A), a wedge-shaped plateau formed by late Pleistocene valley-confined lava covers folded strata of the Cura-Mallín Formation (Figure 6C). The plateau consists of ~1 km³ of basaltic lavas that probably erupted during a single event because there are no interbedded slope deposits expected from the steep topographic gradient to the east. The plateau morphology, valley confinement, wedge shape, and alignment with the surface ruptures of the Quique River indicate that the ascension of these flows occurred along the LLFS. Two uneroded fault scarps probably of Holocene age cut the surface of the plateau bounding a small depression (Figure 6C).

Immediately north of the Chillán volcano, two parallel ~north-south to north-northeast-oriented glacial valleys are located along the northward prolongation of the LLFS (Figure 2). The valleys run parallel to the axis of Tertiary folds and are probably controlled by basement faults. The eastern valley, which would correspond to the direct along-strike northward prolongation of the LLFS, is filled by a lava flow dated as 641 ± 20 ka (Ar-Ar/whole rock; Dixon et al., 1999). No field evidence of faults cutting either this lava or unconsolidated deposits were found in this area.

6.5.1.2 Seismic reflection and bathymetric profiles

Near the northern end of the lake, bathymetric profiles image several relatively small north-south-oriented scarps, which increase in relief southward. Seismic profiles 28, 28-1, 35, and 35-1 image three main north-northwest-striking faults that form a complex horst-and-graben structure with many secondary faults (inset map, Figure 3C; profile, Figure 6E). The faults seem to have an anastomosed pattern hard to follow along these four profiles, but the major graben-bounding fault can be well correlated to a continuous bathymetric break.

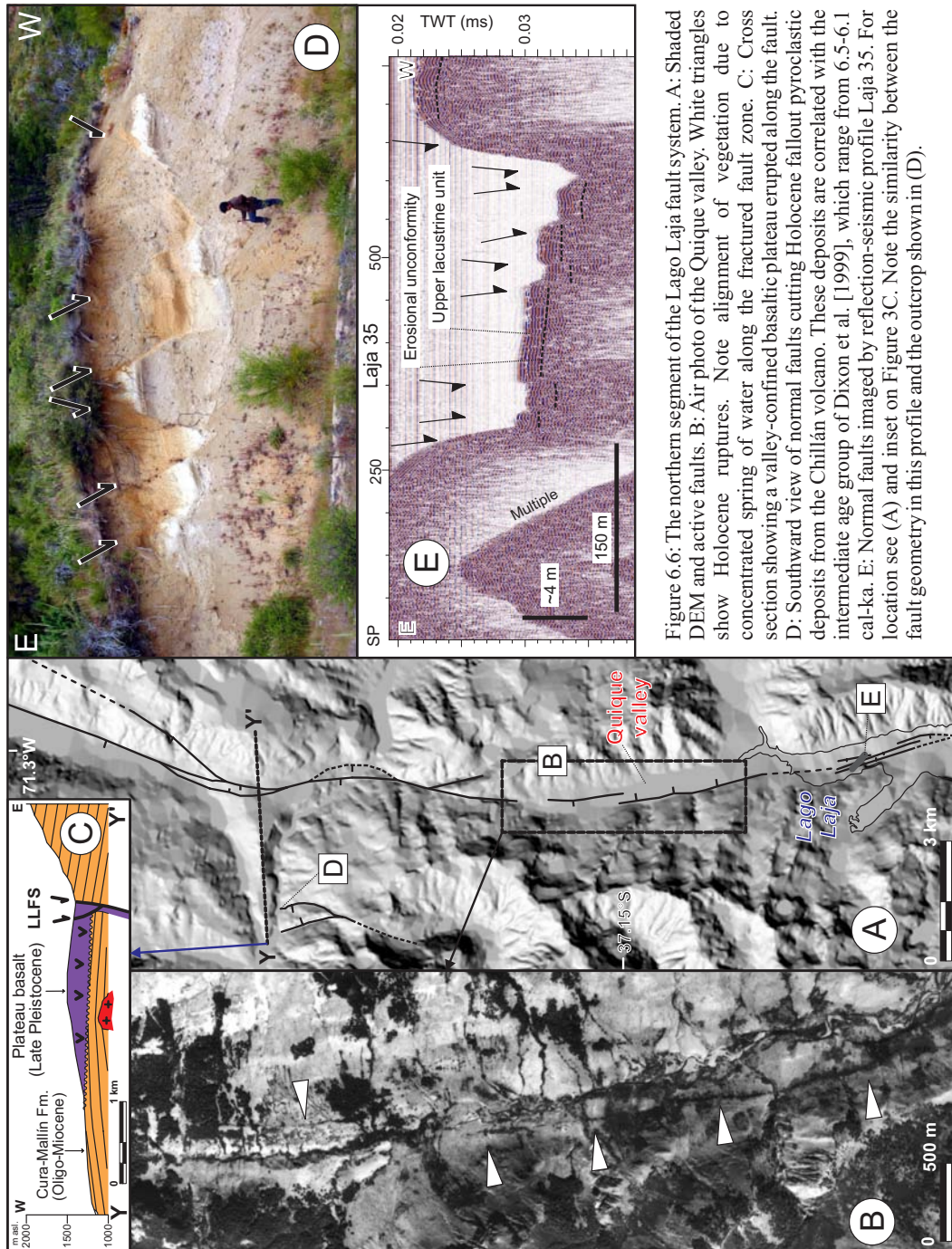


Figure 6.6: The northern segment of the Lago Laja fault system. A: Shaded DEM and active faults. B: Air photo of the Quique valley. White triangles show Holocene ruptures. Note alignment of vegetation due to concentrated spring of water along the fractured fault zone. C: Cross section showing a valley-confined basaltic plateau erupted along the fault. D: Southward view of normal faults cutting Holocene fallout pyroclastic deposits from the Chillán volcano. These deposits are correlated with the intermediate age group of Dixon et al. [1999], which range from 6.5-6.1 cal-ka. E: Normal faults imaged by reflection-seismic profile Laja 35. For location see (A) and inset on Figure 3C. Note the similarity between the fault geometry in this profile and the outcrop shown in (D).

The seismic and bathymetric profiles indicate that slip magnitude increase toward the center of the lake. Along the shore, recent slope debris and the strong variations in water level have eroded all the evidence of surface ruptures. Normal faults that control tilted hanging wall blocks are imaged in the north-south-oriented profile 47, but as cross-profiles are not available here, fault strikes are undefined and thus not confidently extended southward. Anyway, east-west bathymetric profiles show continuous breaks suggesting that faults are connected with the seismically-imaged system farther south (Figure 3C).

The highest fault scarps of this northern segment generate about 5.5 m of relief in the flat lake bottom. Assuming that the upper lacustrine drape cut by these faults is younger than 7.1 cal-ka, the faults would have a minimum slip rate of 0.77 mm/yr, which is consistent with the rate determined for the faulted pyroclastics of the Polcura River (Figure 6D). However, the faults cut the lake bottom and thus their latest increment must be younger. Slip along this segment increase toward the center of the lake.

6.5.2 Central LLFS segment

6.5.2.1 Surface ruptures

On the western shore of the central part of the lake, Niemeyer and Muñoz (1983) mapped several northeast-striking normal faults that cut the Cura-Mallín Formation. These faults are prominent features on the aerial photo and cut a glaciated surface indicating recent activity (Figure 7A). Two normal faults juxtapose the Cola de Zorro and Cura-Mallín Formations at the eastern shore of Lago Laja (Figure 3A). Here, the northeast-striking Béjar fault converges with a west-northwest-striking normal fault; both have about 300 m throw but their prolongation into the lake is not imaged on the seismic data and thus their late Quaternary activity is uncertain.

6.5.2.2 Seismic reflection and bathymetric profiles

Seismic profile 04 is east-west-oriented and located in the central part of the lake (Figure 3C). The center of this profile images two half-graben structures with associated antithetic faults in the hanging wall and a central horst pillar. The eastern half-graben is shown in Figure 8. Profile 06 is east-west-oriented, located in the western sector of the Machos Bay (Figure 3C) and images three east-down normal faults. The eastern at shotpoint (SP) 750 tilted a hanging wall block; the fault at SP 1100 generates an about 12-m-high scarp formed by two steps that cut the tilted block (Figure 7B). These faults have a northeast strike as correlated with profile 04, a parallel line immediately north, and are interpreted as the extension of the northeast-striking on-shore normal faults observed in the aerial photo (Figure 7A). The fresh fault traces are consistent with the Holocene activity determined from the seismic profiles.

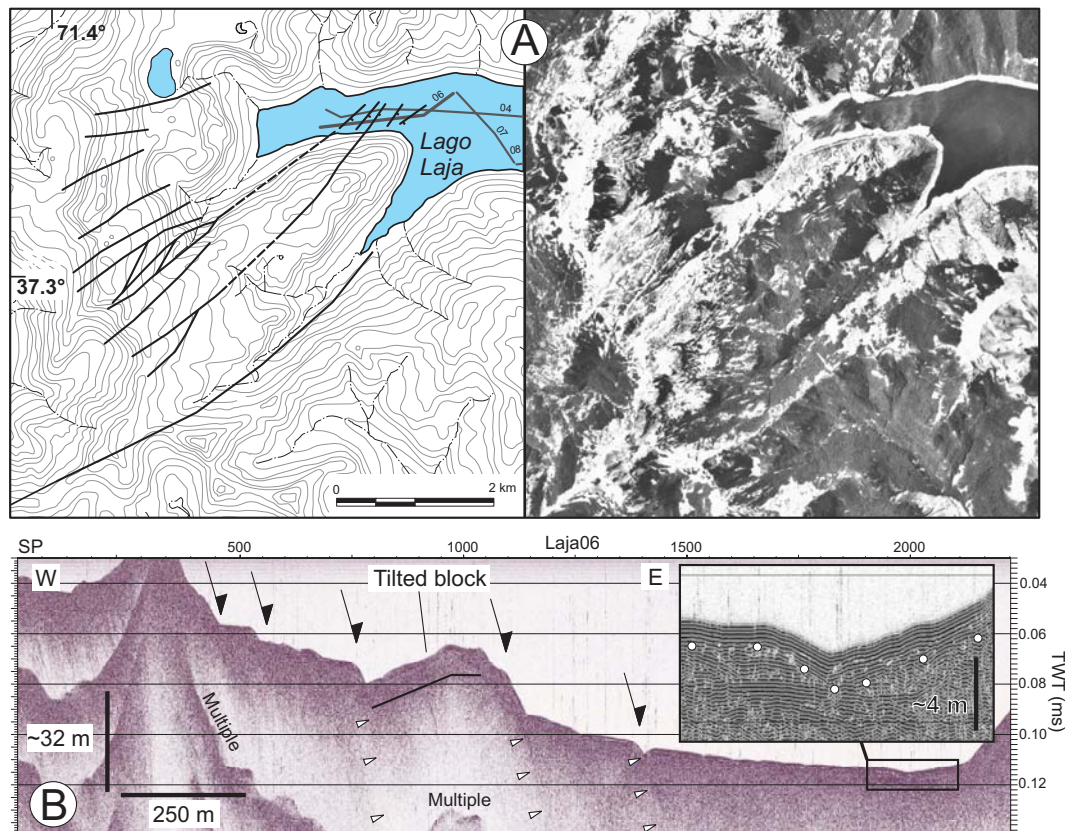


Figure 6.7: Western part of the central Lago Laja fault system segment. A: Topographic map and aerial photo of the Machos Bay area showing fresh surface ruptures. These faults cut a glacially-polished surface on Tertiary rocks, and their extension into the lake is correlated with subaqueous faults imaged by seismic profiles Laja 06 and 04. B: Reflection-seismic profile Laja 06 showing the subaqueous expression of the faults interpreted from the aerial photo. Inset shows the erosional unconformity and the upper lacustrine drape.

In the eastern part of profile 06, the high-resolution 3.5 kHz data images a paleochannel that truncates subhorizontal sediments and produced about 3.5 m of incision. Subsequently, ~1.8 to 2 m of well-bedded sediments corresponding to the uppermost lacustrine drape downlap against

the erosional surface and cover the paleorelief formed by channel incision (inset, Figure 7B). This erosional unconformity is related to the opening of the lake's dam during the Antuco 1 collapse event at 7.1 ± 0.09 cal-ka. This implies that the fault at SP 1100 that offsets this horizon by 12 m has a minimum slip rate of 1.7 mm/yr, which is significantly higher than rates along the northern segment.

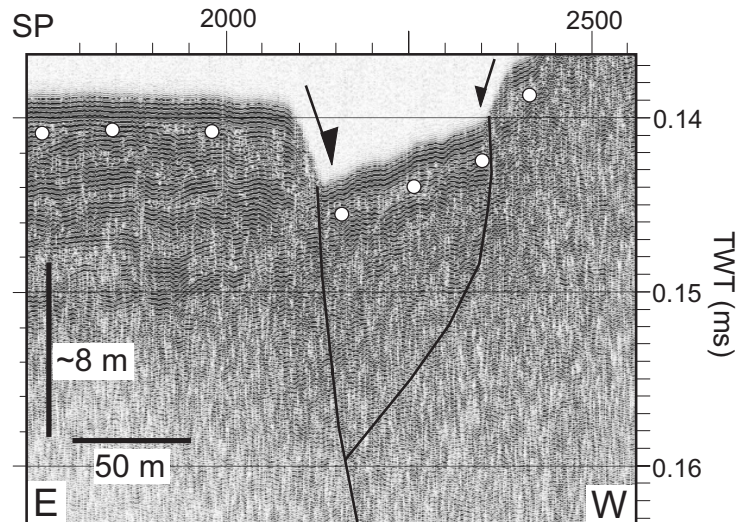


Figure 6.8: The central Lago Laja fault system. Extract of reflection-seismic profile Laja 04 showing a hemigraben structure with an antithetic fault in the center of the lake. For location see Figure 3C. The white dots indicate the 7.1-ka-old erosional unconformity.

6.5.3 Southern LLFS segment

6.5.3.1 Surface ruptures

South of Lago Laja, along the Campamento River (Figure 3), Holocene fallout pyroclastic deposits from the nearby Antuco volcano and unconsolidated fluvial conglomerates are locally cut by east-west-striking subvertical normal faults, which have 50 to 80 cm of slip. In contrast to the faults of the other segments, the structures here are not clearly related to a topographic break in the landscape and are only observed in incised fluvial terraces. Slip magnitude is much lower in this area, and no evidence of Quaternary normal faults were found farther south along the Trapa-Trapa River.

6.5.3.2 Seismic reflection and bathymetric profiles

Immediately north of the Antuco volcano in the widest part of the lake, a ~2-km-long, north-south-striking scarp is observed in three east-west-oriented parallel bathymetric profiles (Figure 3C). Seismic profile 01 crosses this scarp and images an east-dipping normal fault that cuts the uppermost sediments. Due to the proximity of the Antuco volcano, the sediments are imaged as less continuous and slightly undulated reflecting input of volcanoclastic material. This east-facing scarp is up to 19 m high and thus the causative normal fault would have a minimum vertical slip rate of 2.6 mm/yr on its southern part.

6.5.3.3 Structure of the Antuco and C ndor volcanoes

Mount C ndor is an eroded Pleistocene volcanic center located on the western flank of the Antuco volcano (Figure 9). A dyke swarm is exposed on the glaciated flat top surface of this center. The dykes have a mean azimuth of $039 \pm 5^\circ$ (1σ SD; $n=16$). If these dykes are andersonian as has been proposed for northeast-oriented neotectonic volcanic conduits along the Patagonian Andes (Nakamura, 1977; L pez-Escobar et al., 1995; Lara et al., 2004), their orientation should be parallel to the axis of maximum horizontal stress (SH_{max}) (Anderson, 1951). The Antuco's active summit crater and three vents located on the southwestern flank also form a northeast-oriented alignment (Figure 9), which should also be parallel to SH_{max} (Nakamura, 1977). Two other vents are emplaced along the rim of the Antuco 1 collapse caldera. The Herradura minor eruptive center is located near the lake's shore on the northeastern base of the Antuco, and is probably related to the fault imaged immediately north (Figure 9).

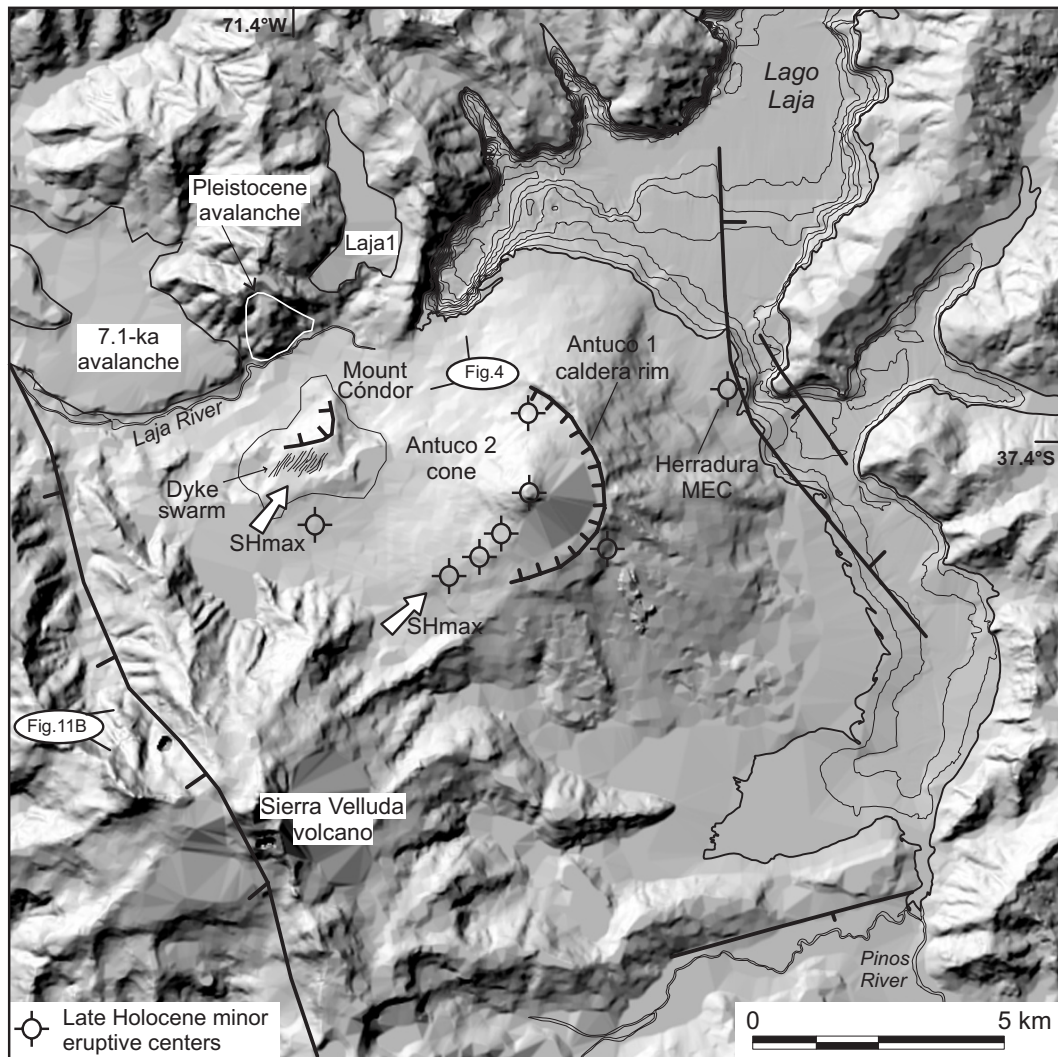


Figure 6.9: Shaded-relief DEM and Map of the Antuco volcano area illustrating the distribution of late Quaternary minor eruption centers, recent faults, and volcanotectonic features discussed in the text.

6.6 Soft-sediment deformation structures adjacent to the LLFS: paleoseismic significance

Southeast of Lago Laja along the Pinos River (Figure 3), fluvial incision exposed a sequence of glacio-lacustrine sediments. The paleolake covered $\sim 10 \text{ km}^2$ and its surface was above 1400 m asl., at least 50 m higher than the maximum level of the present lake (Figure 10A). This paleolake was probably not connected to the modern Laja basin, as no similar lacustrine deposits were found in its surroundings and both areas are separated by a ridge formed by Tertiary bedrock (Figures 3A and 10A). Subsequent incision of the ridge by the Pinos River connected this region to the present Laja basin.

The lacustrine sequence consists of clay, fine ash, occasionally fine to medium sand with pumice clasts, and rarely fine conglomerate (Figure 10B). The sequence has a minimum thickness of 20 m, its base is not exposed and the top is an erosional surface covered by colluvial and

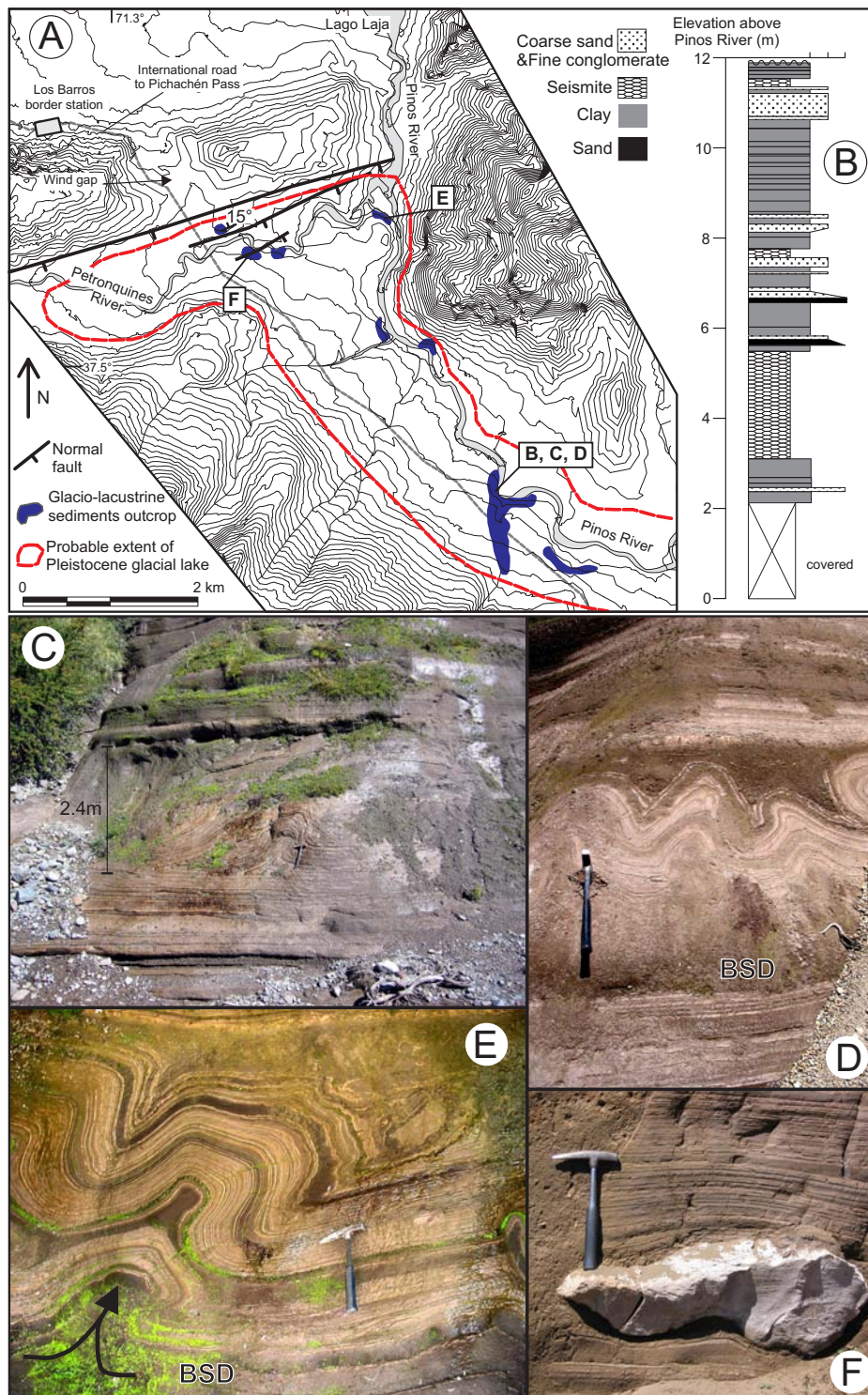


Figure 6.10: Soft-sediment deformation structures. A: Map showing outcrops of late Pleistocene glacio-lacustrine sediments, estimated extent of the former lake, and recent normal faults. 20-m topographic contours derived from the photogrammetric restitution of 1:70.000 aerial photos (photos were taken in 1998, a dry year when the border of the lake was lower than in Figure 3). B: Stratigraphic column of the late Pleistocene glacio-lacustrine sequence. C: The thickest soft-sediment deformation structures interpreted as seismites. Note that it is sandwiched by horizontally undeformed beds. D: A sandwiched seismitic layer with a basal layer of sand at its base. During lateral compression caused by seismic waves, this water-saturated porous layer, which is confined by the less permeable overlying clay, would liquefy and act as a basal detachment (BSD) allowing the clay beds to deform plastically. E: Pillow-like deformed bed with sand blows injected into the axial plane of the anticline. F: Drop-stone in lacustrine sediments.

pyroclastic deposits. The lack of organic material and the presence of drop-stones (Figure 10F) indicate deposition during a glacial period, probably in a proglacial lake formed during the ice-retreat phase. Because the preservation potential of soft-sediments deposited during old glacial periods is very low (Gibbons et al., 1984), these lacustrine sediments presumably date from the last glaciation, whose end is well dated at ~10 ka in the 40°S region (Lowell et al., 1995). Judging from the distribution of frontal moraines and previous glacial reconstructions (Laugenie, 1982), the whole Lago Laja area was covered by glaciers during the last glacial maximum (LGM) at ~19 ka. Thus the lacustrine sediments should postdate the LGM but predate the end of the last glaciation at ~10 ka.

In the northern part of the paleolake, east-northeast–striking normal faults with centimeter-scale offsets cut the lacustrine deposits. Generally, these sediments are horizontal, but on the flank of the bedrock ridge they are tilted 15°N and unconformably covered by horizontal conglomerates. A steep east-northeast–oriented topographic break separates the tilted beds from similar horizontal layers, which crop out 25 m below. This scarp is parallel to the tilted beds and extends westward for at least 5 km into the Petronquines River. We relate it to a south-southeast–dipping normal fault (Figure 10A). In the footwall ridge, a small depression filled with fluvial conglomerates overlays the lacustrine sediments. This saddle-like depression, which hosts the international road to Pichachén Pass, is interpreted as the result of fluvial erosion by a former tributary of Lago Laja, which was then abandoned due to normal faulting and footwall uplift forming a wind gap (Figure 10A).

Layers affected by soft-sediment deformation are present in the lacustrine sequence. The deformed beds range from 10 cm to 2.4 m in thickness. The deformation structures are centimeter- to meter-scale tight isoclinal, asymmetric, and overturned folds, with linear wavy geometries and locally pillow-like structures (Figures 10C and 10E). A layer of medium-grained sand is present at the base of all but one of the deformed beds (BSD in Figures 10D and 10E).

The deformed soft-sediment layers meet the six field criteria for their relation to “seismites” and paleoearthquakes proposed among others by Sims (1975), Hempton and Dewey (1983), Obermeier (1996), and Bowman et al. (2004) (Table 1): (1) Clay-rich sediments are not the most susceptible to liquefaction because of their cohesion, but almost all of the deformed beds have a basal layer of fine to medium sand. This basal water-saturated porous sand is confined by the less permeable overlying clay. During an earthquake, the sand layer would lose cohesion, liquefy and act as a detachment for the overlying clay that would deform plastically. (2) Three beds with similar deformation structures are exposed in the thicker section (Figure 10B). (3) The fine laminated clay suggests still-water lacustrine conditions and the lack of rotational slips or displaced material typical of slumps, decreases the possibility of slope control as a cause for soft-sediment deformation. Moreover, the friable laminated sediments are expected to be pulverized during turbulent transport. (4) A sandwiched position is observed in all the deformed horizons. Clear rhythmic alternation of deformed and undisturbed layers may also indicate the instantaneous nature of seismic triggering, implying that deformation occurred shortly after deposition (Jones and Omoto, 2000). (5) From a total of ten outcrops of lacustrine sediments, nine have deformed layers and in the tenth the sediments are cut by normal faults. (6) The linear wavy geometry shown in Figure 10E is very similar to the seismites described in the Dead Sea Basin by Heifetz et al. (2005), which have been precisely dated and correlated to historical earthquakes (Migowski et al., 2004). Thus we interpret the soft-sediment deformation structures as seismites, and relate them to earthquakes nucleated along the LLFS during the late Pleistocene. The >2-m-thick seismites and existence of surface ruptures indicates that the LLFS is capable of generating M>6 events (Allen, 1982; Wells and Coppersmith, 1994).

No.	Field criteria for the identification of seismites
1	Suitable sediments—loosely consolidated
2	Cyclic repetitions of similar structures
3	Preclusion of trigger by gravity flows or slope instabilities
4	A stratigraphically sandwiched position
5	Lateral continuity and regional abundance
6	Similarity to structures reported elsewhere or formed in experiments under earthquake-induced shaking

Table 6.1: Field criteria for the relation of soft-sediment structures to seismites, proposed among others by Sims (1975), Hempton and Dewey (1983), Obermeier (1996), and Bowman et al. (2004). Scientific Technical Report STR 07/01

6.7 Quaternary extensional structures in the Laja region

Since the end of orogenic shortening at ~5 Ma, extensional and transtensional tectonics have dominated the intra-arc region between ~36–39°S (Folguera et al., 2002; 2003; Melnick et al., 2006a). Northeast of Lago Laja, the north-northeast–striking Béjar fault juxtaposes Oligo-Miocene sediments of the Cura-Mallín Formation with Pliocene-early Pleistocene volcanic rocks from the Cola de Zorro Formation (Figure 3A). This steep fault has at least 350 m of down-to-east throw and has a clear topographic expression extending for ~18 km (Figure 3B). The Cola de Zorro Formation is continuously exposed from this area to the eastern foothills of the Main Cordillera in Argentina, where it has an age range of 4.0 to 1.2 Ma (K-Ar/whole rock; Folguera et al., 2004; Miranda et al., 2006). West of the Béjar fault, the Toro graben is an elongated 3 x 1.7 km², northeast-oriented tectonic depression that hangs over the upper Polcura River (Figure 3A). The two graben-bounding normal faults offset the angular unconformity between the Cura-Mallín and Cola de Zorro Formations by 300 m vertically. On the western part of the graben, a zone of hydrothermal alteration is localized along the steep northern fault. The southern fault, on the other hand, is well exposed at a road-cut along the upper Polcura River where it dips 80°NW. Both the Toro and Béjar faults have vertical slip rates of ~0.1–0.2 mm/yr. However, no clear evidences of Holocene activity were observed along these faults.

Deep glacial erosion exposed the interior of the Sierra Velluda volcano, which consists of two units: the lower unit, dated as 495 ± 88 ka, is formed by ~1500 m of lavas and breccias with interbedded pyroclastic flows; and the upper unit dated as 381 ± 40 ka is formed mainly by ~1000 m of lavas and breccias (K-Ar/whole rock; Moreno et al., 1985). On the northwestern slope of the volcano, a northwest-striking southwest-dipping normal fault cuts a 2000-m-high section of the volcano with 500 ± 50 m throw (Figure 11A). This fault juxtaposes the upper and lower units of the volcano truncating the pyroclastic flows of the lower sequence (Figure 11B), and has a vertical slip rate of 1.3 ± 0.3 mm/yr. As no caldera collapse events have been described nor identified in the current survey for this Pleistocene volcano, we relate this fault to extensional tectonics.

6.8 Deformation rates of the Lago Laja fault system

Slip rates have been calculated for the faulted pyroclastic deposits and subaqueous faults of the northern and central LLFS, respectively, which have age-constrained stratigraphic markers. Because the time seismic sections do not allow estimating true inclinations, a 10° error is assigned to the dips of the subaqueous faults, which range from 60 to 85°. This range estimate is consistent with the rather steep exposed Holocene faults (Figure 6D). The fault parameters, slip rates, and seismic profiles used to derive these data are presented in Table 2, and fault-group numbers are shown in Figure 3B. These rates should be considered as minimum because they are mostly based on the 7.1-ka age of the erosional unconformity, but most faults cut through this layer implying younger activity and thus faster rates. The average minimum east-west extension rate for the whole fault system is 1.2 ± 0.6 mm/yr (1σ SD), obtained by adding fault groups in latitudinal sections and averaging them (Table 2). The higher averaged rate of 2.0 ± 1.0 mm/yr occurs in the central and deepest part of the lake. Total post-7.1 ka east-west extension is about 0.7% and the average strain rate is in the order of 3 x 10⁻¹⁴ s⁻¹.

The Holocene extension rate is about an order of magnitude higher than the rates estimated for the Pliocene-early Pleistocene Toro and Béjar faults (<0.1 mm/yr) and still about twice the rate of the mid-Pleistocene Sierra Velluda fault (~0.7 mm/yr). Even if these estimates are limited, they indicate an acceleration over the Quaternary.

6.9 Quaternary shortening along the foothills of the Main Cordillera

6.9.1 Eastern foothills: Copahue-Antiñir fault system (CAFS)

The CAFS (Figures 1 and 2) extends for over 110 km along the Argentinean back-arc region from 37.8°S northward, and represents the southernmost expression of the active central Andean orogenic front. This system consists of east-vergent reverse faults and folds that affect 4.0- to 1.2-Ma-old plateau lavas from the Cola de Zorro Formation (K-Ar/whole rock; Folguera et al., 2004; Miranda et al., 2006), Pleistocene conglomerates, and lacustrine sediments (Iaffa et al., 2002; Melnick et al., 2002). Dextral offsets of ephemeral streams and a lava flow are well exposed along the southern sector of the CAFS leading Folguera et al. (2004) to interpret the whole fault system as transpressional. In the southern sector a 3.1 ± 0.2-Ma-old lava flow is dextrally displaced 195 m, yielding a low strike-slip rate of 0.06 mm/yr. However, there is no clear evidence of dextral deformation along the central and northern sectors of this fault system. The CAFS has a

marked concave-to-the-west trace (Figure 2) and higher shortening magnitude occurred in its central sector. Therefore the subordinated right-lateral deformation in the southern sector is likely an effect of the concave trace and accommodation of the along-strike gradient in shortening, rather than bulk transpression.

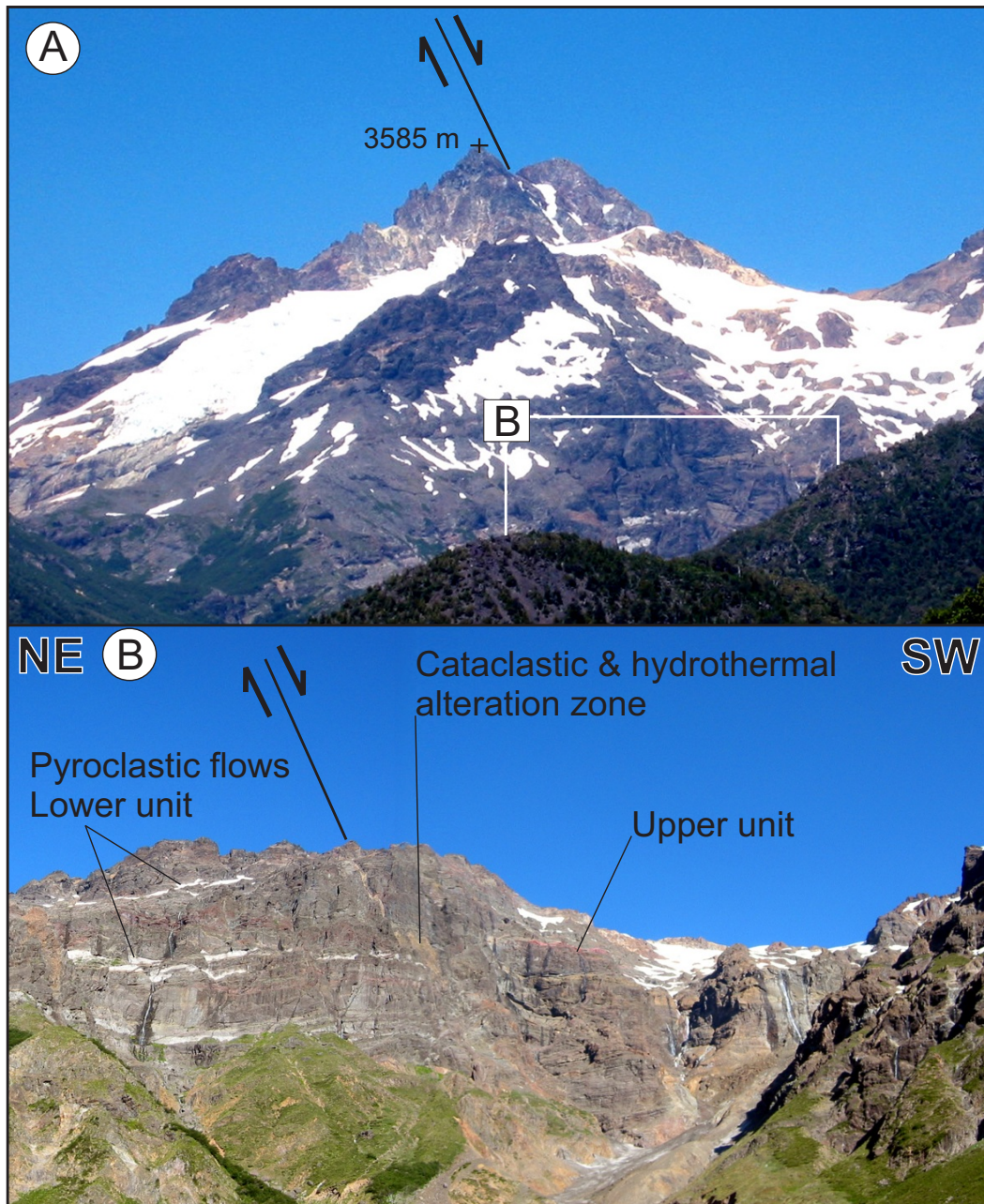


Figure 6.11: A: View to the southeast of the Sierra Velluda volcano from the intermediate Laja valley. Note the trace of the southwest-dipping normal fault that cuts a 2500-m-high section of the volcano with ~500 m throw. B: Detailed view of the fault at the upper Malalcura valley (see Figure 9 for location). The fault juxtaposes the upper and lower units of the volcano truncating the pyroclastic flows from the inferior unit. A 15-m-wide cataclastic zone overprinted by hydrothermal alteration fills the fault zone. Normal drag is observed in the hanging wall beds.

Age of faulted unit (calibrated ka BP)	Seismic profiles used	No. of faults	Fault parameters			Vertical Slip rate ⁴ (mm/a)	Horizontal Slip rate (mm/a)	E-W Slip rate (mm/a)				
			Throw ¹ (m)	Dip ± ² (°)	Azimuth ± ³ (°)	±	±	±				
Pyroclastics		6	6.5	0.1	75	2	5	0.05	0.28	0.04	0.28	0.04
Fault group 1	1,57	2	18.5	1.9	70	10	0	0.29	0.94	0.49	0.94	0.49
Fault group 2	2,14	3	20.5	2.1	70	10	65	0.32	1.05	0.54	0.44	0.23
Fault group 3	3,4	5	42.5	4.3	70	10	35	0.66	2.17	1.12	1.78	0.91
Fault group 4	4,9,3	5	23	2.3	80	10	355	0.36	0.57	0.57	0.57	0.57
Fault group 5	11,12,48,50	6	40	4.0	70	10	0	0.62	2.04	1.05	2.04	1.05
Fault group 6	28,35,39,43	9	22	2.2	80	10	355	0.34	0.55	0.54	0.54	0.54
Average ⁵								0.68	1.90	0.74	1.24	0.63

¹Cumulative throw for all faults in the respective group. ²We assume 10% error in measurements from seismic lines. ³Since our seismic lines are not depth converted, we assume 10° error in dip estimates. ⁴Minimum cumulative vertical slip rate for all faults in the respective group. ⁵Vertical rate average per fault. Horizontal averages for groups in latitudinal sections: 1+2, 3+4, 5, and 6 (1σ errors).

Table 6.2: Holocene slip rates of the Lago Laja fault system. Subaqueous fault group numbers and location of seismic lines shown in Figure 3C.

Along the Reñilelvú section, which represents the central sector of the CAFS, about 0.5-0.8 km of shortening have occurred since 1.2 ± 0.1 Ma at an average shortening rate of 0.5 ± 0.2 mm/yr. In this sector deformation has occurred along a 13-km-wide zone accounting thus for ~5% of shortening and an average east-west strain rate in the order of -10^{-14} s^{-1} . The strain rate of the northern and southern sectors should be similar as deformation occurs along a narrower area and shortening magnitudes are lower.

6.9.2 Western foothills: Huépil fault

Near Huépil, the piedmont of the Main Cordillera is deformed by a ~10-km-wide, north-northeast–striking anticline and cut by a parallel reverse fault (Figures 2 and 12). This piedmont surface is formed by alluvial breccias, pyroclastic flows, and fluvial conglomerates of the Malleco Formation (Suárez and Emparán, 1997). The age of this unit is bracketed by several 4.4 ± 0.5 - to 0.8 ± 0.3 -Ma-old lava flows interbedded near the base and top of the predominantly fluvial-alluvial sequence, respectively (K-Ar/whole rock; Suárez and Emparán, 1997). Thus the folded surface near Huépil should be younger than 0.8 ± 0.3 Ma.

Immediately west of Tucapel, alluvial beds of the Malleco Formation strike north-south and dip 15°E (Figure 12). This eastward inclination is opposite to the usual dip direction of the Malleco beds, which follow the westward-inclined depositional slope. These folded beds conform the eastern flank of a small range, which we interpret as an asymmetric anticline. The Laja River cuts the anticline forming a gorge; on its walls two ~50-m-thick polygenic sequences are exposed with a marked contact surface, which is smoothly folded parallel to the depositional surface. Several small internally-drained basins formed in the crestal region of the northern anticline, and are probably related to continuous channel slope decrease due to uplift and abandonment from the Laja drainage. The Huépil anticline has a maximum relief of 130 m from the present Laja River bed, so assuming an age of 0.8 ± 0.3 Ma for the upper part of the Malleco Formation yields a minimum growth rate of 0.18 ± 0.07 mm/yr for the central part of the anticline. This is a conservative estimate since the upper surface is probably younger and the Laja River bed is filled with recent terraces that have decreased relief.

On the western flank of the fold, a north-northeast–striking, west-facing scarp cuts the Malleco beds generating about 30 m of relief. This scarp is interpreted to be caused by an east-dipping Quaternary reverse or thrust fault to which the anticline is related. Northward, the fault continues along the Cholguán River where two marked west-facing scarps control the development of range-parallel drainages (Figure 12). Late Miocene west-vergent reverse faults and fault-related folds have been widely described along the western edge and foothills of the Main Cordillera between 33 – 38°S (e.g., Godoy et al., 1999; Melnick et al., 2006a; Sernageomin, 2003). We interpret the Huépil fault as the neotectonic expression of such a structure. More Quaternary contractional structures probably exist along the western foothills, but the lack of good exposures due to low relief and extensive vegetation has made their identification difficult. Crustal microearthquakes registered by the ISSA local network (Bohm et al., 2002) occur below the western foothills (Figure 13), and are probably related to the Huépil contractional structure.

6.10 Discussion

6.10.1 Tectonic interpretation of intra-arc extensional deformation

Our observations suggest regionally-limited Quaternary extensional deformation along the axis of the intra-arc. The LLFS extent (36.9 – 37.6°S) is coincident with the Copahue-Antiñir contractional system located ~40 km east along the Andean foothills (Figure 2). Folding and faulting of Quaternary sediments also occurs at this latitude along the western piedmont of the Main Cordillera (Figure 12). In consequence, Quaternary shortening concentrates along its foothills forming a large-scale pop-up structure, while coeval extension is localized along its axial, volcanically-active, and topographically-highest zone (Figure 13). The strain rates of the LLFS and back-arc reverse fault system are of the same magnitude ($\sim 10^{-14}$ s $^{-1}$).

One plausible interpretation for the synorogenic extension along the LLFS is incipient gravitational collapse of the Main Cordillera's core. Limited collapse, which extracts potential energy from the thickened crust is induced by ongoing crustal shortening (e.g., Molnar and Lyon-Caen, 1988; Buck and Sokoutis, 1994; Liu et al., 2000). This phenomena—coeval shortening and extension—has been described along the Andes in Perú (e.g., Dalmayrac and Molnar, 1981) and the Altiplano-Puna plateau (e.g., Allmendinger et al., 1997), as well as in other mountain belts in the world (e.g., Mercier et al., 1987; Echtler and Malavieille, 1990; Selverstone, 2005). The Laja Andes are rather triangular in cross-section and thrusting occurs along both foothills; so, considering modeling by Royden (1996), its collapse implies the absence of an intra-crustal low viscosity layer and coupling between the crust and motion of the mantle. In fact, no crustal discontinuity has been imaged by receiver function (Yuan et al., 2006) and tomography surveys (Bohm et al., 2002) in the Laja region, while similar data imaged a large mid-crustal low viscosity layer across the flat-topped Altiplano plateau (Yuan et al., 2000).

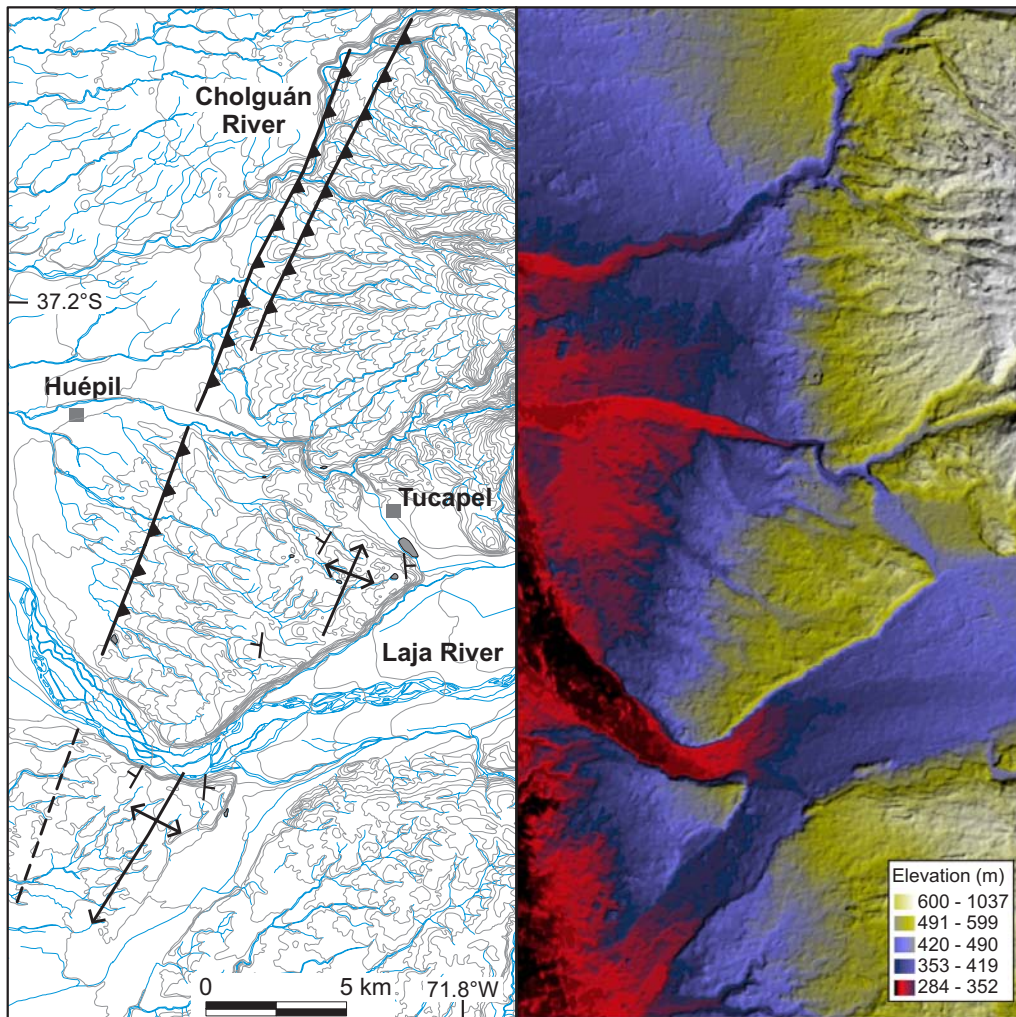


Figure 6.12: Map of the Huépil contractional structures along the western foothills of the Main Cordillera. See Figure 2 for location. Right: Shaded-relief DEM (15-m and 4-m horizontal and vertical resolution, respectively) derived from ASTER (Advanced Spaceborne Thermal Emission and Reflection Radiometer) satellite imagery. Left: Structural map, 25-m topographic contours, and drainage network.

The elevated heat-flow along the volcanic arc most likely contributed to a rheological weakening of structures in the Lago Laja region, facilitating and localizing deformation. It is also plausible that synorogenic extension is enhanced by cooling of intrusions below the arc. As most of this area was completely covered by glaciers during the Quaternary ice ages, post-glacial lithospheric rebound and unbending have probably also contributed to uplift causing subsequent isostatic compensation of surface loads during the Holocene (see below). Lower crustal flow in this region has probably not contributed significantly to synorogenic extension (e.g., Bird, 1991), because here the lower crust should consist of high viscosity restites produced by ~150 m.y. of stationary arc magmatism (Mpodozis and Ramos, 1989; Tassara and Yáñez, 2003).

6.10.2 Transient unloading and localization of faulting

Bevis et al. (2004) showed that the vertical component of the continuous GPS record from the ANTC site, located 20 km west of Lago Laja (Figure 2), is experiencing non-steady fluctuations with a range of 50 mm since 1997. They found that these variations are very well correlated with changes in Lago Laja's volume due to the seasonal hydropower management, and thus the fluctuations of the GPS data are dominated by the earth's local elastic response to the changing weight of water. Hetzel and Hampel (2005) modeled the extensional deformation of the Wasatch region showing that lithospheric rebound caused by fast unloading, in this case by postglacial emptying of Lake Boneville, led to an increase in slip rates and localized deformation. Thereon this is a reasonable explanation for the paleo-earthquake clustering and slip acceleration observed during the last ~10 k.y. in the Wasatch region. A parameter study of this process showed

Scientific Technical Report STR 07/01

that loading magnitude mostly controls the slip rate increase after unloading (Hampel and Hetzel, 2006).

The Holocene faults of the LLFS that have the largest displacements and slip rates are in the central, deepest part of the lake. Here, slip rates are at least three times higher than along the shallow northern part as well as onshore sectors of the fault system (Table 2). These observations raise the question as whether the Holocene unloading episode caused by deglaciation and the outburst megaflood event at 7.1 ka enhanced fault activity in the deeper part of Lago Laja, where loading magnitudes were higher and which should be rebounding faster.

6.10.3 The Lago Laja fault system and strain partitioning along the margin

Along the Patagonian Andes (38–46°S), most of the margin-parallel component of oblique plate convergence has been accommodated along the intra-arc region by the Liquiñe-Ofqui strike-slip fault zone, and thus a high degree of strain partitioning occurs (Dewey and Lamb, 1992; Lavenu and Cembrano, 1999; Rosenau et al., 2006). This is supported by the oblique orientation of SH_{max} along the volcanic arc, fault-kinematic and regional structural data, and focal mechanisms. The northernmost geomorphic evidence of Holocene dextral strike-slip deformation along the volcanic arc come from the Lonquimay Valley (38.5°S) and Copahue area (38°S) (Melnick et al., 2006a).

In contrast, no geomorphic evidence for strike-slip deformation were found along the LLFS in the field and in the detailed examination of stereo aerial photos. A strike-slip component may be inferred from: (1) some of the seismically-imaged fault arrays in the center of the lake, which suggest negative flower structures (Figure 5); (2) the general fault pattern of the LLFS conformed by a main north-south-striking branch and several northeast-striking subsidiary faults; and (3) the prominent northeast strike of the dykes at Mount Cónдор and the aligned flank vents of the Antuco volcano both suggesting a northeast orientation of SH_{max} (Figure 9). However, if some margin-parallel dextral shear has occurred along the LLFS, it must have been of much lower magnitude than the rate of geomorphic decay of the landscape and thus not observable in the field, in contrast to the structures south of 38°S. This raises the question as to how oblique convergence is partitioned at 37°S. Probably very minor dextral shear has occurred diffusely along the arc but surely much less than south of 38°S.

In order to visualize and understand the major along-strike kinematic variations between the Central and Patagonian Andes, we integrate the forearc structures. At this latitude, the forearc is divided in two kinematic domains limited by the Arauco Peninsula (Figures 1 and 13). In the southern domain oblique shortening occurs along northwest-striking faults with a left-lateral component, while along the northern domain oblique shortening occurs along northeast-striking faults, which in turn have a right-lateral component. This forearc kinematic boundary across Arauco is spatially coincident with the intra-arc kinematic boundary over the Callaqui-Copahue-Mandolegüe transfer zone (CCM in Figure 13), which decouples the discrete Liquiñe-Ofqui strike-slip system from the LLFS and Copahue-Antiñir dip-slip systems (Melnick et al., 2006a). These observations emphasize that north of Arauco and Copahue (37.5°–38°S) a higher magnitude of the margin-parallel component of oblique subduction has been accommodated in the coastal region due to the favorable fault orientations, while in turn to the south a higher magnitude has been accommodated by dextral strike-slip faulting along the intra-arc region. This segment boundary, named Arauco transition zone, marks the change from the low and narrow Patagonian Andes to the high and broad Central Andes, and a steep gradient in the degree of strain partitioning. North of the Arauco transition the margin-parallel shear induced by oblique convergence is absorbed along a wide zone with small amounts of diffuse strike-slip deformation, while to the south strain is partitioned into the discrete Liquiñe-Ofqui strike-slip fault zone. The Arauco Peninsula is the largest deflection of the coastline along the Pacific of South America, and like other peninsulas of the Andean margin (i.e., Pisco–14°S, Mejillones–23°S, and Taitao–46.5°S Peninsulas (e.g., Mpodozis and Ramos, 1989)), is related to a major along-strike change in deformation style, subduction-earthquake ruptures, tectonic evolution, and topography of the entire orogen.

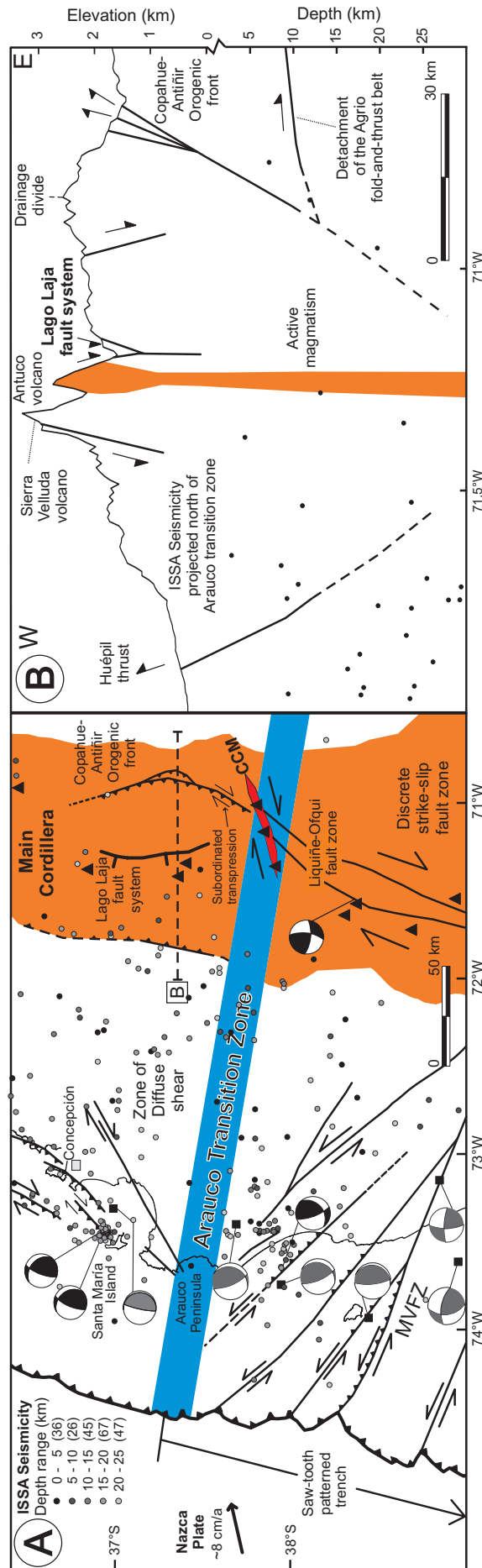


Figure 6.13: A: Neotectonic map of the Andean margin illustrating the kinematic changes across the Arauco transition zone, which integrates the Arauco Peninsula in the forearc and Callaqui-Copahue-Mandolegüe transfer zone (CCM) in the intra-arc. Two contrasting kinematic domains are differentiated across this segment boundary: (1) the southern domain, which in the forearc is dominated by oblique shortening along northwest-striking faults that have a left-lateral component controlling the saw-tooth pattern of the trench (interpreted from multibeam bathymetry collected by Reichert et al. (2002)). The major fault is the Mocha-Villarica fault zone (MVFZ) (Melnick et al., 2003). In the intra-arc of this southern domain, dextral strike-slip deformation occurs along the Liqueñe-Ofqui fault zone (LOFZ). (2) the northern domain in turn is characterized by oblique shortening along northeast-striking reverse faults with right-lateral component in the forearc, and in the intra-arc by shortening along the Copahue-Antifir fault system in the eastern foothills of the Main Cordillera and locally along its western piedmont region as well, while extension occurs along the Lago Laja fault system in the axial region. The Arauco transition zone marks a northward-decreasing gradient in the degree of strain partitioning, as deduced from the distribution of margin-parallel shear in a broad zone to the north and in the discrete Liqueñe-Ofqui fault zone to the south and the boundary between the Central and Patagonian Andes. Depth-coded crustal seismicity from the ISSA local network (Bohm et al., 2002), number of events in brackets. Black focal mechanisms in the forearc from Bruhn (2003) and in the arc from Barrientos and Acevedo (1992). Grey structures interpreted from ENAP-Chile industry reflection-seismic profiles (Melnick et al., 2006b; Melnick and Echlter, 2006). B: Maximum topography over a 30-km-wide swath of the Main Cordillera illustrating the active structures. See (A) for location. Seismicity projected from the region north of the Arauco transition zone. Agrío fold-and-thrust belt detachment extrapolated from seismic reflection profiles acquired immediately east in the Neuquén Basin (Zapata and Folguera, 2005).

6.10.4 Seismic hazards posed by the Lago Laja fault system

Although the Laja region is mostly uninhabited, earthquakes here pose a regional hazard. Surface ruptures along the northern active faults could damage the two hydrocarbon pipelines along the upper Polcura River. The seiche waves caused by an earthquake nucleated in one of the subaqueous faults of the lake could damage the hydroelectric power stations, which are the major hydropower suppliers in Chile. In any case, the highest hazard is posed by the eventual rupture of the narrow dam of Lago Laja by tectonic and/or volcanic activity, retaining 4.7 km³ of water. The opening of the dam would trigger an outburst megaflood as has happened at least twice before, latest at 7.1 ka, presenting a severe risk to many settlements in the Central Depression and along the Bío-Bío River including Concepción, the second largest city of Chile.

6.11 Conclusions

Field observations, interpretation of reflection-seismic profiles, aerial photos, and combined bathymetric-topographic DEMs indicate late Pleistocene-Holocene extensional faulting along the Andean intra-arc zone at ~37°S. The deformation pattern defines the Lago Laja fault system, which has an average minimum east-west Holocene extensional rate of 1.2 mm/yr. Soft-sediment deformation structures in late Pleistocene glacio-lacustrine deposits are interpreted as seismites and related to M>6 paleoearthquakes. No strike-slip component in the deformation has been recorded in geomorphic markers.

Extensional deformation occurs along the axial, higher region of the Main Cordillera, and is coeval and spatially related to two contractional systems. These systems are located along the eastern and western foothills and have opposite vergence defining a large-scale pop-up structure responsible for uplift of the Main Cordillera. In this context, we interpret extension in terms of incipient gravitational collapse of the highest part of the Andes in response to crustal thickening in a thermally-weakened volcanic domain. Extension is over-imposed to the isostatic compensation of surface loads caused by post-glacial rebound, which could have led to the observed acceleration of the deformation during the latest Quaternary.

The lack of strike-slip deformation expected from oblique convergence at 37°S contrasts with the dextral fault zone that extends continuously south of 38°S along the Patagonian Andes volcanic arc. We interpret this kinematic change along the volcanic arc to be caused by a first-order seismotectonic segment boundary, the Arauco transition zone, located at the Arauco Peninsula in the forearc (37.5°S). Favorable fault orientations north of Arauco accommodate oblique shortening absorbing and distributing the margin-parallel component of plate convergence in the forearc. The structures in the Laja region result from regional tectonic changes along the orogen, underlining the necessity of integrating regional and local observations to gain insight into processes responsible for seismotectonic segmentation of convergent margins.

Acknowledgments

This work was supported by: International Quality Network (IQN) project at U. of Potsdam founded by the German Academic Exchange Found (DAAD), GeoForschungsZentrum Potsdam Southern Andes Project, and Collaborative Research Center SFB 267 “Deformation Processes in the Andes” founded by the German Science Foundation (DFG). The seismic data were collected in the framework of the Belgian OSTC project EV/12/10B “A continuous Holocene record of ENSO variability in southern Chile”, and with the support in the field of K. De Rycker, E. Chapron, and R. Brümmer and M. Pino at U. Austral de Chile (Valdivia) and W. San Martín and R. Urrutia of EULA at the U. of Concepción. DM is grateful to O. Oncken and M. Strecker for their continuous support. This work benefits from discussions with A. Folguera, M. Rosenau, A. Tassara, V.A. Ramos, E. Godoy, and B. Bookhagen. We thank K. Bataille and G. Hermosilla (U. of Concepción), E. Bartulovic (Oleoducto Transandino S.A.), R. Verdugo (CONAF), and the staff of “Avanzada Cuatro Juntas” for logistical support and to R. Fuenzalida, H. Muñoz, and M. Sanchez for assistance during fieldwork. B. Scharf and O. Buettner (UFZ Leipzig-Halle) kindly shared their bathymetry of Lago Laja, acquired within the chilean-german cooperation project “Water Resources and Energy: Aquatic ecosystem responses to water level” (WTZ 00/002), EULA supported their field work. C. Garzione, an anonymous reviewer, and Associate Editor C. Andronicos provided constructive comments.

7. Conclusions

The tectonic investigations of the south-central Chile margin at various spatial and temporal scales provide new insights on seismotectonic segmentation processes in subduction margins and on the influence of climate-induced increase in sediment flux on wedge mechanics. This study integrates geomorphic, structural, and stratigraphic data obtained from extensive field work, and from the integration of geophysical data as well as constraints from hydrocarbon exploration boreholes. It focuses on two regions, the Main Cordillera or intra-arc and the coastal forearc, in two temporal scales, the Neogene and the late Quaternary.

The evolution of the Main Cordillera during the Neogene is subdivided in four main tectonic episodes: (1) Oligocene to early Miocene extension and formation of volcano-sedimentary intra-arc, rift-like basins. (2) Late Miocene flattening of the subduction zone resulting in a shift of volcanism toward the foreland and inversion of the former rift basins. The present topographic relief and elevation of the Main Cordillera in the south-central Andes was achieved during this episode. (3) Pliocene to early Pleistocene steepening of the slab resulting in renewed arc volcanism and local extension of the former orogenic structure. Onset of dextral strike-slip deformation along the Liquiñe-Ofqui fault zone due to increasing plate convergence obliquity. (4) Late Pleistocene to Holocene narrowing of the volcanic arc. North of 38°S, active contractional deformation occurs along the eastern and locally western foothills of the Main Cordillera, whereas extension and transtension is localized along its axial and topographically higher region. The latter is interpreted as incipient gravitationally-driven collapse in response to crustal thickening and shortening. The newly defined Lago Laja extensional fault system accounts for an averaged minimum arc-normal extension rate of 1.2 mm/yr since 7.1 ka, and strain rate of $\sim 10^{-14} \text{ s}^{-1}$. In the glaciated Lake Laja region, the Holocene normal faults have the highest slip rate of $>2.7 \text{ mm/yr}$ in the deeper parts of the basin, where ice thicknesses were maximum. Thus probably the differential isostatic compensation of surface loads overimposed to the regional extensional regime may be an important contributor to local changes in fault slip rates. Although historical earthquakes have not been reported along these active faults, soft-sediment deformation structures interpreted as seismites and fault scarps of several meters imply that these structures are capable of generating $M > 6$ events.

The coastal forearc of the south-central Andes hosts several basins that developed principally during the Cenozoic. The integration of on- and off-shore data showed that most of the basins between 34° and 45°S share common stratigraphic and structural features, which can be integrated in a common tectonic evolution for this segment. These basins record an initial phase of Eocene to early Pliocene extension and subsidence, coeval to a high plate convergence rate. During this stage topographic relief was low and exhumation slow in the hinterland, resulting in reduced sediment supply to the trench. These observations, in addition to synchronous eastward migration episodes of the volcanic arc, are consistent with tectonic erosion. The late Miocene orogenic pulse that uplifted the Main Cordillera, in addition to global cooling, triggered the onset of Patagonian glaciations and denudation at $\sim 6 \text{ Ma}$, which is also consistent with thermochronological data. This resulted in a dramatic increase in sediment flux to the trench and in consequence the elevated sedimentation rates during the Pliocene and Quaternary derived from cores of Ocean Drilling Projects. The unconformity between deep-water siltstone and near-shore sandstone in the 34-45°S forearc basins indicates that they were uplifted $>1.5 \text{ km}$ between 3.6 and 2.5 Ma, entailing an uplift rate of $\sim 1.3 \text{ mm/yr}$. This uplift was congruent with tectonic inversion and contractional deformation. Syntectonic deposition adjacent to seismically-active reverse faults indicate continuous compression since $\sim 2.5 \text{ Ma}$ with shortening rates of $\sim 0.8 \text{ mm/yr}$. During the Quaternary, deformation migrated arcwards causing uplift of the Coastal Cordillera. The theory of critical Coulomb wedges provides a viable explanation for this inversion. This theory predicts that when the taper angle of an accretionary wedge decreases, the wedge will grow by deforming internally in order to reach the critical taper angle. Frontal accretion of glacial-derived trench fill to the toe of the wedge in south-central Chile has decreased its taper angle continuously during the Pliocene and Quaternary. Subduction of these water-rich terrigenous material decreases also basal effective friction, which also resulted in lowering of the taper angle. It has been shown that frictional heating is the main source of heat in cold forearcs. Hence, the $\sim 40 \%$ decrease in plate convergence rate over the past 10 m.y. reduced frictional heating, which allowed wider seismogenic coupling and thus higher shear stress transmission to the forearc wedge. Because the wedge's slope is continuously lowered by frontal accretion, the lateral tension caused by margin

7. Conclusions

bathymetry diminishes and when the shear stress along the plate interface exceeds this lateral tension, the entire wedge is under compression. Thus the inversion of forearc basins and the onset of the present compressional stress regime are related to Miocene mountain building and climate change and to the continuous decreasing plate convergence rate. Nevertheless, another important factor is the stationary position of the Juan Fernández sea-mount ridge over the past 10 m.y. at 33.5°S, which blocked sediment transport northward along the trench and thus enhanced sediment storage to the south.

The close inspection of marine terraces at Isla Santa María and reflection-seismic profiles from the Arauco Bay area revealed that the coastal geomorphology and segmentation of active deformation is controlled by reverse fault-cored anticlines. At Isla Santa María, radiocarbon ages of paleosols interbedded in a lower, marine-dominated sequence and at the base of an upper, eolian unit yielded a maximum uplift rate of 1.79 ± 0.39 m/k.y. and landward tilt rate of 0.032 ± 0.018 °/k.y. The position of the island in the forelimbs of two growing anticline has controlled the ongoing tilt and syntectonic sedimentation over at least the past 50 k.y. The close inspection of seismic profiles correlated with nearby exploration boreholes reveals that these reverse faults are inverted structures from the Eocene to early Pliocene extensional phase of the Arauco forearc basin. The distribution of maximum coseismic uplift in the Arauco Bay area during a $M > 8$ earthquake in 1835 is parallel to the main reverse fault-and-fold system. In addition, the abrasion platform that emerged during this event at Isla Santa María is steeply tilted landward, similarly to the late Pleistocene marine and eolian units and to a sequence of Holocene emergent strandlines. The reverse fault that propagates the anticline below Isla Santa María appears to be rooted in the plate interface as suggested by the continuous alignment of microseismicity that reaches ~18 km depth. This implies that crustal-scale faults may be mechanically coupled to the megathrust and that slip during great subduction earthquakes would trigger movement on upper plate structures. In the case of upper-plate fault triggering by a subduction earthquake, strong ground motion and surface deformation would be localized along the defined upper-plate structures. This conclusion has strong implications for the seismic hazard assessment in this region as well as in other subduction margins sharing similar features.

These results emphasize the important role of inherited structures in guiding active plate-boundary deformation and the necessity to study processes at various temporal and spatial scales using a variety of methods in order to contribute to the understanding of earthquake-related segmentation processes in convergent margins. The relationship between coastal geomorphology and segmentation of deformation caused by subduction earthquakes can be attributed to the possible mechanical coupling between the subduction-zone megathrust and local, inherited upper-plate structures.

8. Bibliography

- Adriasola, A.C., S.N. Thomson, M.R. Brix, F. Hervé, and B. Stöckhert (2006), Postmagmatic cooling and late Cenozoic denudation of the North Patagonian Batholith in the Los Lagos region of Chile, 41°-42°15'S, *International Journal of Earth Sciences*, 95, 504-528.
- Allen, J.R.L. (1982), *Sedimentary Structures: Their Character and Physical Basis*, 663 pp., Elsevier, Amsterdam.
- Allmendinger, R.W., V.A. Ramos, T.E. Jordan, M. Palma, and B.L. Isacks (1983), Paleogeography and Andean structural geometry, northwest Argentina, *Tectonics*, 2, 1-16.
- Allmendinger, R.W., T.E. Jordan, S.M. Kay, and B.L. Isacks (1997), The evolution of the Altiplano-Puna plateau of the Central Andes, *Annual Review of Earth and Planetary Sciences*, 25, 139-174.
- Anderson, E.M. (1951), *The Dynamics of Faulting*, 191 pp., Oliver and Boyd.
- Ando, M. (1975), Source mechanisms and tectonic significance of historical earthquakes along the Nankai trough, Japan, *Tectonophysics*, 27, 119-140.
- Angermann, D., J. Klotz, and C. Reiberg (1999), Space-geodetic estimation of the Nazca-South American Euler vector, *Earth and Planetary Science Letters*, 171, 329-334.
- Arcos, R., and S. Elgueta (1993), Geología y modelo de sedimentación de la secuencia Cretácico-Terciaria de la Cuenca de Arauco, 34 pp., Empresa Nacional del Petróleo, Santiago.
- Atwater, B.F., H.J. Núñez, and C. Vita-Finzi (1992), Net late Holocene emergence despite earthquake-induced submergence, south-central Chile, *Quaternary International*, 15/16, 77-85.
- Avé Lallemant, H.G., and J.S. Oldow (2000), Active displacement partitioning and arc-parallel extension of the Aleutian volcanic arc based on Global Positioning System geodesy and kinematic analysis, *Geology*, 28, 739-742.
- Bangs, N., and S.C. Cande (1997), Episodic development of a convergent margin inferred from structures and processes along the southern Chile margin, *Tectonics*, 16, 489-503.
- Barnes, P.M., A. Nicol, and T. Harrison (2002), Late Cenozoic evolution and earthquake potential of an active listric thrust complex above the Hikurangi subduction zone, New Zealand, *Geological Society of America Bulletin*, 114, 1379-1405.
- Barrientos, S. (1987), Is the Pichilemu-Talcahuano (Chile) a seismic gap?, *Seismological Research Letters*, 61, 43-48.
- Barrientos, S., and P.S. Acevedo-Aránguiz (1992), Seismological aspects of the 1988-1989 Lonquimay (Chile) volcanic eruption, *Journal of Volcanology and Geothermal Research*, 53, 73-87.
- Barrientos, S., E. Vera, P. Alvarado, and T. Monfret (2004), Crustal seismicity in central Chile, *Journal of South American Earth Sciences*, 16, 759-768.
- Beck, S., S. Barrientos, E. Kausel, and M. Reyes (1998), Source characteristics of historic earthquakes along the Central Chile subduction zone, *Journal of South American Earth Sciences*, 11, 115-129.
- Berryman, K.R., Y. Ota, and A.G. Hull (1989), Holocene paleoseismicity in the fold and thrust belt of the Hikurangi subduction zone, eastern North Island, New Zealand, *Tectonophysics*, 163, 185-195.
- Berryman, K.R. (1993), Distribution, age, and deformation of late Plesitocene marine terraces at Mahia Peninsula, Hikurangi Subduction margin, New Zealand, *Tectonics*, 12, 1365-1379.
- Berryman, K.R. (1993), Age, height, and deformation of Holocene marine terraces at Mahia Peninsula, Hikurangi Subduction margin, New Zealand, *Tectonics*, 12, 1347-1364.
- Bertrand, S., X. Boes, J. Castiaux, F. Charlet, R. Urrutia, C. Espinoza, G. Lepoint, B. Charlier, and N. Fagel (2005), Temporal evolution of sediment supply in Lago Puyehue (Southern Chile) during the last 600 yr and its climatic significance, *Quaternary Research*, 64, 163-175.
- Bevis, M., E. Kendrick, A. Cser, and R. Smalley Jr. (2004), Geodetic measurement of the local elastic response to the changing mass of water in Lago Laja, Chile, *Physics of the Earth and Planetary Interiors*, 141, 71-78.
- Bird, P. (1991), Lateral extrusion of lower crust from under high topography, in the isostatic limit, *Journal of Geophysical Research*, 96, 10275-10286.
- Bird, P. (2003), An updated digital model of plate boundaries, *Geochemistry, Geophysics, Geosystems*, 4, 1027.
- Biró, L. (1979), Contribución al conocimiento de la Formación Tubul, Plioceno Superior, Provincia de Arauco (37°14'S), in *II Congreso Geológico Chileno*, vol. 3, pp. H33-H44, Arica.
- Blisniuk, P.M., L.A. Stern, C.P. Chamberlain, B. Idleman, and P.K. Zeitler (2005), Climatic and ecologic changes during Miocene surface uplift in the Southern Patagonian Andes, *Earth and Planetary Science Letters*, 230, 125-142.
- Bohm, M., S. Lüth, H. Echtler, G. Asch, K. Bataille, C. Bruhn, A. Rietbrock, and P. Wigger (2002), The Southern Andes between 36°S and 40°S latitude: seismicity and average velocities, *Tectonophysics*, 356, 275-289.
- Bohm, M. (2004), 3-D lokal earthquake tomography of the southern Andes between 36° and 40°S, Ph.D. thesis, 135 pp., Free University, Berlin.
- Bookhagen, B., H.P. Echtler, D. Melnick, M.R. Strecker, and J.Q.G. Spencer (2006), Using uplifted Holocene beach berms for paleoseismic analysis on the Santa María Island, south-central Chile, *Geophysical Research Letters*, 33, L15302.

- Bowman, D., A. Korjenkov, and N. Porat (2004), Late-Pleistocene seismites from Lake Issyk-Kul, the Tien Shan range, Kyrgyzstan, *Sedimentary Geology*, 163, 211-228.
- Briggs, R.W., K. Sieh, A.J. Meltzner, D. Natawidjaja, J. Galetzka, B. Suwargadi, Y.-J. Hsu, M. Simons, N. Hananto, I. Suprihanto, D. Prayudi, J.-P. Avouac, L. Prawirodirdjo, and Y. Bock (2006), Deformation and slip along the Sunda megathrust in the great 2005 Nias-Simeulue earthquake, *Science*, 311, 1897-1901.
- Bruhn, C. (2003), Momententensoren hochfrequenter Ereignisse in Sudchile, Ph.D. thesis, 181 pp., University of Potsdam, Potsdam.
- Bruhn, R.L., and P.J. Haeussler (2006), Deformation driven by subduction and microplate collision: Geodynamics of Cook Inlet basin, Alaska, *Geological Society of America Bulletin*, 118, 289-303.
- Brüggen, J. (1941), El volcán Antuco y la geología glacial del valle del Laja, *Revista Chilena de Historia y Geografía*, 91, 356-385.
- Brüggen, J. (1950), *Fundamentos de la Geología de Chile*, 374 pp., Instituto Geográfico Militar, Santiago.
- Buck, W.R., and D. Sokoutis (1994), Analogue model of gravitational collapse and surface extension during continental convergence, *Nature*, 369, 737-740.
- Burns, M.W., T.E. Jordan, P. Copeland, and S.A. Kelley (2006), The case for extensional tectonics in the Oligo-Miocene Southern Andes as recorded in the Cura-Mallín basin (36°-38°S), in *Evolution of an Andean margin: A tectonic and magmatic view from the Andes to the Neuquén Basin (35°-39°S lat)*, vol. 407, edited by S.M. Kay and V.A. Ramos, pp. 162-184, Geological Society of America Special Paper.
- Campos, J., D. Hatzfeld, R. Madariaga, G. López, E. Kausel, A. Zollo, G. Iannacone, R. Fromm, S. Barrientos, and H. Lyon-Caen (2002), A seismological study of the 1835 seismic gap in south-central Chile, *Physics of The Earth and Planetary Interiors*, 132, 177-195.
- Cande, S.C., and R.B. Leslie (1986), Late Cenozoic tectonics of the southern Chile Trench, *Journal of Geophysical Research*, 91, 471-496.
- Carpinelli, A. (2000), Análisis estratigráfico, paleoambiental, estructural y modelo tectono-estratigráfico de la cuenca de Cura-Mallín, VIII y IX Región, Chile, Provincia de Neuquén, Argentina, master thesis, 158 pp., Universidad de Concepción, Concepción.
- Carr, A.S., D.S.G. Thomas, and M.D. Bateman (2006), Climatic and sea level controls on Late Quaternary eolian activity on the Agulhas Plain, South Africa, *Quaternary Research*, 65, 252-263.
- Cembrano, J., F. Hervé, and A. Lavenu (1996), The Liquiñe Ofqui fault zone: A long-lived intra-arc fault system in southern Chile, *Tectonophysics*, 259, 55-66.
- Cembrano, J., E. Schermer, A. Lavenu, and A. Sanhueza (2000), Contrasting nature of deformation along an intra-arc shear zone, the Liquiñe-Ofqui fault zone, southern Chilean Andes, *Tectonophysics*, 319, 129-149.
- Cembrano, J., A. Lavenu, P. Reynolds, G. Arancibia, G. López, and A. Sanhueza (2002), Late Cenozoic transpressional ductile deformation north of the Nazca-South America-Antarctica triple junction, *Tectonophysics*, 354, 289-314.
- Chapron, E., C. Beck, M. Pouchet, and J.F. Deconinck (1999), 1822 earthquake-triggered homogenite in Lake Le Bourget (NW Alps), *Terra Nova*, 11, 86-92.
- Charlet, F., C. Marchand, S. Volland, M. Pino, R. Urrutia, M. J., E. Chapron, and M. De Batist (2003), Reflection-seismic study of six lakes in South-Central Chile (37°S-42°S): Lagos Laja, Lleulleu, Icalma, Villarrica, Puyehue & Todos Los Santos, in *X Congreso Geológico Chileno*, vol. CD-Rom, Universidad de Concepción, Concepción.
- Chinn, D.S., and B.L. Isacks (1983), Accurate source depths and focal mechanisms of shallow earthquakes in western South America and in the New Hebrides island arc, *Tectonics*, 2, 529-563.
- Cifuentes, I.L. (1989), The 1960 Chilean earthquake, *Journal of Geophysical Research*, 94, 665-680.
- Cisternas, M., B.F. Atwater, F. Torrejón, Y. Sawai, G. Machuca, M. Lagos, A. Eipert, C. Youlton, I. Salgado, T. Kamataki, M. Shishikura, C.P. Rajendran, J.K. Malik, Y. Rizal, and M. Husni (2005), Predecessors of the giant 1960 Chile earthquake, *Nature*, 437, 404-407.
- Clift, P., and P. Vannucchi (2004), Controls on tectonic accretion versus erosion in subduction zones: Implications for the origin and recycling of the continental crust, *Reviews of Geophysics*, 42, RG2001 1-31.
- Coira, B., S.M. Kay, and J. Viramonte (1993), Upper Cenozoic magmatic evolution of the Argentine Puna - a model for changing subduction geometry, *International Geology Review*, 35, 677-720.
- Comte, D., A. Eisenberg, E. Lorca, M. Pardo, L. Ponce, R. Saragoni, S. Singh, and G. Suárez (1986), The 1985 central Chile earthquake, a repeat of previous earthquakes in the region?, *Science*, 233, 449-453.
- Comte, D., H. Haessler, L. Dorbath, M. Pardo, T. Monfred, A. Lavenu, B. Pontoise, and Y. Hello (2002), Seismicity and stress distribution in the Copiapo, northern Chile subduction zone using combined on- and off-shore seismic observations, *Physics of The Earth and Planetary Interiors*, 417, 1-21.
- Cortés, J.M., P. Vinciguerra, M. Yamin, and M.M. Pasini (1999), Tectónica Cuaternaria de la región Andina del Nuevo Cuyo (28°-38°LS), in *Geología Argentina*, edited by R. Caminos, pp. 760-778, Subsecretaría de Minería, Servicio Geológico y Minero Argentino, Buenos Aires.
- Dalmayrac, D., and P. Molnar (1981), Parallel thrust and normal faulting in Peru and constraints on the state of stress, *Earth and Planetary Science Letters*, 55, 473-481.
- Darwin, C. (1839), Journal and Remarks 1832-1836, in *Narrative of the Surveying Voyages of His Majesty's Ships Adventure and Beagle between the Years 1826 and 1836, Describing their Examination of the Southern Shores of*

Bibliography

- South America, and the Beagle's Circumnavigation of the globe*, vol. III, edited by H. Colburn, 370-381 pp., London; reprint 1966, New York, AMS press.
- Darwin, C. (1851), Geological observations of South America, in *Geological Observations on Coral Reefs, Volcanic Islands and on South America-Being the Voyage of the Beagle, Under the Command of Captain Fitzroy, R.N., During the years 1832 to 1836*, Part III, 279 pp., Smith, Elder, London.
- Davis, D., J. Suppe, and F.A. Dahlen (1983), Mechanics of fold-and-thrust belts and accretionary wedges, *Journal of Geophysical Research*, 88, 1153-1172.
- De La Cruz, R., and M. Suárez (1997), El Jurásico de la cuenca de Neuquén en Lonquimay, Chile: Formación Nacientes del Bio-Bio (38-39°S), *Revista Geológica de Chile*, 24, 3-24.
- De Mets, C., R.G. Gordon, D.F. Argus, and S. Stein (1994), Effect of recent revisions to the geomagnetic reversal time scale on estimates of current plate motions, *Geophysical Research Letters*, 21, 2191-2194.
- Delpino, D., and M. Deza (1995), Mapa Geológico y de recursos minerales de la provincia de Neuquén, 1:500.000 scale, República Argentina, *Servicio Geológico y Minero Argentino*, Neuquén.
- Dewey, J.F., and S.H. Lamb (1992), Active tectonics of the Andes, *Tectonophysics*, 205, 79-95.
- Dixon, H.J., M.D. Murphy, S.J. Sparks, R. Chavez, J.A. Naranjo, P.N. Dunkley, S.R. Young, J.S. Gilbert, and M.R. Pringle (1999), The geology of Nevados de Chillan volcano, Chile, *Revista Geológica de Chile*, 26, 227-253.
- Domeyko, I. (1846), Memoria sobre la Estructura Geológica de Chile en la Latitud de Concepción, desde la Bahía de Talcahuano hasta la Cumbre de la Cordillera de Pichachén y Descripción del Volcán Antuco, in *Geología*, vol. 5, edited by I. Domeyko, pp. 123-172, Imprenta Cervantes, Santiago.
- Echtler, H., and J. Malavieille (1990), Extensional tectonics, basement uplift and Stephano-Permian collapse basin in a late Variscan metamorphic core complex (Montagne Noire, southern Massif Central), *Tectonophysics*, 177, 125-138.
- Elger, K., O. Oncken, and J. Glodny (2005), Plateau-style accumulation of deformation: Southern Altiplano, *Tectonics*, 24, 1-19.
- Elgueta, S., and R. Arcos (1994), Geología y modelo de sedimentación de la secuencia Cretácico Terciaria de la Cuenca de Arauco, 34 pp., Empresa Nacional del Petróleo, Santiago.
- Encinas, A., K. Finger, S. Nielsen, A. Lavenue, L. Buatois, and D. Peterson (2005), Late Miocene coastal subsidence in Central Chile: Tectonic implications, in *6th International Symposium of Andean Geodynamics*, pp. 246-249, IRD, Barcelona.
- England, P., and P. Molnar (1990), Surface uplift, uplift of rocks, and exhumation of rocks, *Geology*, 18, 1173-1177.
- Eyles, N., B. Koseoglu, J.I. Boyce, and J.D. Halfman (2000), Seismic stratigraphy of Waterton Lake, a sediment-starved glaciated basin in the Rocky Mountains of Alberta, Canada and Montana, USA, *Sedimentary Geology*, 130, 283-311.
- Finger, K., A. Encinas, S. Nielsen, and D. Peterson (2003), Microfaunal indications of late Miocene deep-water basins off the central coast of Chile, in *X Congreso Geológico Chileno*, vol. CD-Rom, Universidad de Concepción, Concepción.
- Finger, K., S. Nielsen, T. DeVries, A. Encinas, and D. Peterson (2007), Paleontologic evidence for sedimentary displacement in Neogene forearc basins of Central Chile, *Palaios*, 22, 2-16.
- Fitch, T.J. (1972), Plate convergence, transcurrent faults, and internal deformation adjacent to southeast Asia and the western Pacific, *Journal of Geophysical Research*, 77, 4432-4460.
- Fitzroy, R. (1839), Proceedings of the Second Expedition 1831-1836, in *Narrative of the Surveying Voyages of His Majesty's Ships Adventure and Beagle between the Years 1826 and 1836, Describing their Examination of the southern shores of South America, and the Beagle's circumnavigation of the globe*, vol. II, edited by H. Colburn, 695 pp., London; reprint 1966, New York, AMS press.
- Flynn, J.J., and C.C. Swisher III (1995), *Cenozoic South American land mammal ages: correlation to global geochronologies*, 317-333 pp.
- Folguera, A., and V.A. Ramos (2000), Control estructural del volcán Copahue (38°S-71°O): Implicancias tectónicas para el arco volcánico cuaternario (36-39°S), *Revista Asociación Geológica Argentina*, 55, 229-244.
- Folguera, A., V.A. Ramos, and D. Melnick (2002), Transición de los Andes Patagónicos a los Andes Centrales: Extremo norte del sistema de Liquiñe-Ofqui (38°S), *Revista Geológica de Chile*, 29, 227-240.
- Folguera, A., V.A. Ramos, and D. Melnick (2003), Recurrencia en el desarrollo de cuencas de intraarco Cordillera Neuquina (37°30'-38°S), *Revista Asociación Geológica Argentina*, 58, 3-19.
- Folguera, A., V.A. Ramos, R.L. Hermanns, and J. Naranjo (2004), Neotectonics in the foothills of the southernmost central Andes (37°-38°S): Evidence of strike-slip displacement along the Antifiñir-Copahue fault zone, *Tectonics*, 23, TC5008.
- Folguera, A., V.A. Ramos, E. González Díaz, and R.L. Hermanns (2006), Miocene to Quaternary Deformation of the Guañacos fold and thrust belt in the Neuquén Andes between 37° and 37°30'S, in *Evolution of an Andean margin: A tectonic and magmatic view from the Andes to the Neuquén Basin (35°-39°S lat)*, vol. 407, edited by S.M. Kay and V.A. Ramos, pp. 247-266, Geological Society of America Special Paper.
- Forsythe, R., and E. Nelson (1985), Geological manifestations of ridge collision: evidence from the Golfo de Penas-Taitao basin, southern Chile., *Tectonics*, 4, 477-495.

Bibliography

- Fuller, C.W., S.D. Willett, and M.T. Brandon (2006), Formation of forearc basins and their influence on subduction zone earthquakes, *Geology*, *34*, 65-68.
- Gansser, A. (1973), Facts and theories on the Andes, *Journal of the Geological Society of London*, *129*, 93-131.
- García, F. (1968), Estratigrafía del Terciario de Chile Central, in *Terciario de Chile*, edited by G. Cecioni, pp. 25-56, Sociedad Geológica de Chile, Santiago.
- Garzzone, C.N., P. Molnar, J.C. Libarkin, and B.J. MacFadden (2006), Rapid late Miocene rise of the Bolivian Altiplano: Evidence for removal of mantle lithosphere, *Earth and Planetary Science Letters*, *241*, 543-556.
- Giacosa, R.E., and C. N. Heredia (2004), Structure of the North Patagonian thick-skinned fold-and-thrust belt, southern central Andes, Argentina (41°-42°S), *Journal of South American Earth Sciences*, *18*, 61-72.
- Giambiagi, L.B., V.A. Ramos, E. Godoy, P.P. Alvarez, and S. Orts (2003), Cenozoic deformation and tectonic style of the Andes, between 33° and 34° south latitude, *Tectonics*, *22*, 1-15.
- Gibbons, A., J. Megeath, and K. Pierce (1984), Probability of moraine survival in a succession of glacial advances, *Geology*, *12*, 327-330.
- Glodny, J., J. Lohrmann, H. Echtler, K. Gräfe, W. Seifert, S. Collao, and O. Figueroa (2005), Internal dynamics of a paleoaccretionary wedge: Insights from combined isotope tectonochronology and sandbox modelling of the South-Central Chilean forearc, *Earth and Planetary Science Letters*, *231*, 23-39.
- Godoy, E., G. Yañez, and E. Vera (1999), Inversion of an Oligocene volcano-tectonic basin and uplifting of its superimposed Miocene magmatic arc in the Chilean Central Andes: First seismic and gravity evidences, *Tectonophysics*, *306*, 217-236.
- Goldfinger, C., L.D. Kulm, R.S. Yeats, B. Appelgate, M.E. Mackay, and G.F. Moore (1992), Transverse structural trends along the Oregon convergent margin: implications for Cascadia earthquake potential and crustal rotations, *Geology*, *20*, 141-144.
- González, O., and M. Vergara (1962), *Reconocimiento geológico de la Cordillera de Los Andes entre los paralelos 35° y 38°S*, 119 pp., Universidad de Chile, Instituto de Geología, Santiago.
- González, E. (1989), Hydrocarbon Resources in the Coastal Zone of Chile, in *Geology of the Andes and Its Relation to Hydrocarbon and Mineral Resources*, edited by G.E. Erickson, M.T. Cañas Pinochet and J.A. Reinemund, pp. 383-404, Cricum-Pacific Council for Energy and Mineral Resources, Houston, Texas.
- Gräfe, K., J. Glodny, W. Seifert, M. Rosenau, and H. Echtler (2002), Apatite fission track thermochronology of granitoids at the South Chilean active continental margin (37°S, 42°S): Implications for denudation, tectonics and mass transfer since the Cretaceous, in *5th International Symposium of Andean Geodynamics*, pp. 275-278, IRD, Toulouse.
- Grevemeyer, I., J.L. Díaz-Naveas, C.R. Ranero, and H.W. Villinger (2003), Heat flow over the descending Nazca plate in central Chile, 32°S to 41°S: Observations from ODP Leg 202 and the occurrence of natural gas hydrates, *Earth and Planetary Science Letters*, *213*, 285-298.
- Hampel, A., and R. Hetzel (2006), Response of normal faults to glacial-interglacial fluctuations of ice and water masses on Earth's surface, *Journal of Geophysical Research*, *111*, B06406.
- Hartley, A.J. (2003), Andean uplift and climate change, in *Journal of the Geological Society*, vol. 160, pp. 7-10.
- Heifetz, E., A. Agnon, and S. Marco (2005), Soft sediment deformation by Kelvin Helmholtz Instability: A case from Dead Sea earthquakes, *Earth and Planetary Science Letters*, *236*, 497-504.
- Hempton, M.R., and J.F. Dewey (1983), Earthquake-induced deformational structures in young lacustrine sediments, East Anatolian Fault, southeast Turkey, *Tectonophysics*, *98*.
- Hervé, M. (1976), Estudio geológico de la falla Liquiñe-Reloncaví en el área de Liquiñe; antecedentes de un movimiento transcurrente (Provincia de Valdivia), in *I Congreso Geológico Chileno*, vol. B, pp. 39-56, Sociedad Geológica Chilena, Santiago.
- Hervé, F. (1988), Late Paleozoic subduction and accretion in southern Chile, *Episodes*, *11*, 183-188.
- Hervé, F. (1994), The southern Andes between 39° and 44°S latitude: The geological signature of a transpressive tectonic regime related to a magmatic arc, in *Tectonics of the Southern Central Andes*, edited by K.J. Reutter, E. Scheuber and P.J. Wigger, pp. 243-248, Springer, Berlin.
- Hetzel, R., and A. Hampel (2005), Slip rate variations on normal faults during glacial-interglacial changes in surface loads, *Nature*, *435*, 81-84.
- Hilley, G.E., and M.R. Strecker (2004), Steady state erosion of critical Coulomb wedges with applications to Taiwan and the Himalaya, *Journal of Geophysical Research*, *109*, B01411.
- Hughen, K., C. Herring, O. Marchal, S. Lehman, J. Turnbull, J. Southon, and J. Overpeck (2004), 14C Activity and Global Carbon Cycle Changes over the Past 50,000 Years, *Science*, *303*, 202-207.
- Hyndman, R.D., and K. Wang (1995), The rupture zone of Cascadia great earthquakes from current deformation and the thermal regime, *Journal of Geophysical Research*, *100*, 22133-22154.
- Iaffa, D., E. González-Díaz, and A. Folguera (2002), Tectónica postglaciar en la Cordillera Neuquina: Río Picunleo (37°30' S), in *XV Congreso Geológico Argentino*, vol. CD-Rom, Sociedad Geológica Argentina, El Calafate.
- Isacks, B.L. (1988), Uplift of the central Andean Plateau and bending of the Bolivian Orocline., *Journal of Geophysical Research*, *93*, 3211-3231.
- Jara, J. (2006), Análisis del alzamiento tectónico en Isla Santa María, evidencias sedimentológicas y geomorfológicas, master thesis, 110 pp., Universidad de Concepción, Concepción.

Bibliography

- Jarrard, R.D. (1986), Relations among subduction parameters, *Reviews of Geophysics*, 24, 217-284.
- Johnson, S.Y., R.J. Blakely, W.J. Stephenson, S.V. Dadisman, and M.A. Fisher (2004), Active shortening of the Cascadia forearc and implications for seismic hazards of the Puget Lowland, *Tectonics*, 23, TC1011.
- Jones, A.P., and K. Omoto (2000), Towards establishing criteria for identifying trigger mechanisms for soft-sediment deformation: A case study of late pleistocene lacustrine sands and clays, Onikobe and Nakayamadaira Basins, Northeastern Japan, *Sedimentology*, 47, 1211-1226.
- Jordan, T.E., B.L. Isacks, R.W. Allmendinger, J.A. Brewer, V.A. Ramos, and C.J. Ando (1983), Andean tectonics related to geometry of subducted Nazca plate., *Geological Society of America Bulletin*, 94, 341-361.
- Jordan, T.E., J.H. Reynolds, and J.P. Erikson (1997), Variability in age of initial shortening and uplift in the central Andes, 16-33°S, *Tectonic Uplift and Climate Change*, 41-61.
- Jordan, T.E., W. Matthew Burns, R. Veiga, F. Pángaro, P. Copeland, S. Kelley, and C. Mpodozis (2001), Extension and basin formation in the southern Andes caused by increased convergence rate: A mid-Cenozoic trigger for the Andes, *Tectonics*, 20, 308-324.
- Kaizuka, S., T. Matsuda, M. Nogami, and N. Yonekura (1973), Quaternary tectonic and recent seismic crustal movements in the Arauco Peninsula and its environs, Central Chile, *Geographical Reports Tokyo Metropolitan University*, 8, 1-49.
- Kanamori, H. (1977), The energy release in great earthquakes, *Journal of Geophysical Research*, 82, 2981-2987.
- Kanamori, H. (1983), Magnitude scale and quantification of earthquakes., *Tectonophysics*, 93, 185-199.
- Kay, S.M., V.A. Ramos, C. Mpodozis, and P. Sruoga (1989), Late Paleozoic to Jurassic silicic magmatism at the Gondwana margin: analogy to the Middle Proterozoic in North America?, *Geology*, 17, 324-328.
- Kay, S.M. (2002), Tertiary to Recent transient shallow subduction zones in the Central and Southern Andes, in *XV Congreso Geológico Argentino*, vol. CD-Rom, Sociedad Geológica Argentina, El Calafate.
- Kay, S.M., E. Godoy, and A. Kurtz (2005), Episodic arc migration, crustal thickening, subduction erosion, and magmatism in the south-central Andes, *Bulletin of the Geological Society of America*, 117, 67-88.
- Kay, S.M., M.W. Burns, P. Copeland, and O. Mancilla (2006), Upper Cretaceous to Holocene Magmatism and Evidence for Transient Miocene Shallowing of the Andean Subduction Zone under the Northern Neuquén Basin, in *Evolution of an Andean margin: A tectonic and magmatic view from the Andes to the Neuquén Basin (35°-39°S lat)*, vol. 407, edited by S.M. Kay and V.A. Ramos, pp. 19-60, Geological Society of America Special Paper.
- Kelleher, J.A. (1972), Rupture zones of large South American earthquakes and some predictions, *Journal of Geophysical Research*, 77, 2089-2103.
- Kemnitz, H., W. Kramer, and M. Rosenau (2005), Jurassic of Tertiary tectonic, volcanic, and sedimentary evolution of the Southern Andean intra-arc zone, Chile (38 - 39°S): A survey, *Neues Jahrbuch für Geologie und Paläontologie - Abhandlungen*, 236, 19-42.
- Kendrick, E., M. Bevis, R. Smalley Jr., B. Brooks, R.C. Vargas, E. Lauria, and L.P.S. Fortes (2003), The Nazca-South America Euler vector and its rate of change, *Journal of South American Earth Sciences*, 16, 125-131.
- Kilian, R., and J.H. Behrmann (2003), Geochemical constraints on the sources of Southern Chile Trench sediments and their recycling in arc magmas of the Southern Andes, *Journal of the Geological Society*, 160, 57-70.
- Kley, J., C.R. Monaldi, and J.A. Salfity (1999), Along-strike segmentation of the Andean foreland: Causes and consequences, *Tectonophysics*, 301, 75-94.
- Kley, J., and C.R. Monaldi (2002), Tectonic inversion in the Santa Barbara System of the central Andean foreland thrust belt, northwestern Argentina, in *Tectonics*, vol. 21, pp. 11-1.
- Klotz, J., G. Khazaradze, D. Angermann, C. Reigber, R. Perdomo, and O. Cifuentes (2001), Earthquake cycle dominates contemporary crustal deformation in central and southern Andes, *Earth and Planetary Science Letters*, 193, 437-446.
- Krawczyk, C., and the SPOC team (2003), Amphibious seismic survey images plate interface at 1960 Chile earthquake, *Eos*, 84, 304-305.
- Lamb, S., and P. Davis (2003), Cenozoic climate change as a possible cause for the rise of the Andes, *Nature*, 425, 792-797.
- Lamb, S. (2006), Shear stresses on megathrusts: Implications for mountain building behind subduction zones, *Journal of Geophysical Research*, 111, B07401.
- Lara, L., C. Rodríguez, H. Moreno, and C. Pérez de Arce (2001), Geocronología K-Ar y geoquímica del volcanismo Plioceno superior-pleistoceno de los Andes del sur (39-42°S), *Revista Geológica de Chile*, 28, 67-90.
- Lara, L.E., J.A. Naranjo, and H. Moreno (2004), Rhyodacitic fissure eruption in Southern Andes (Cordón Caulle; 40.5°S) after the 1960 (Mw:9.5) Chilean earthquake: A structural interpretation, *Journal of Volcanology and Geothermal Research*, 138, 127-138.
- Laugenie, C. (1982), La Région des Lacs, Chili Meridional, Recherches sur l'Evolution Geomorphologique d'Un Piemont Glaciaire Quaternaire Andin, Ph.D. thesis, 822 pp., Université de Bordeaux III, Bordeaux.
- Lavenu, A., and J. Cembrano (1999), Compressional- and transpressional-stress pattern for Pliocene and Quaternary brittle deformation in fore arc and intra-arc zones (Andes of Central and Southern Chile), *Journal of Structural Geology*, 21, 1669-1691.
- Lavenu, A., and A. Encinas (2005), Análisis de la deformación frágil de los depósitos neógenos de la cuenca de Navidad (Cordillera de la Costa-34°S, Chile central), *Revista Geológica de Chile*, 32, 229-248.

- Le Roux, J.P., and S. Elgueta (1997), Paralic parasequences associated with Eocene sea-level oscillations in an active margin setting: Trihuco Formation of the Arauco Basin, Chile, *Sedimentary Geology*, *110*, 257-276.
- Le Roux, J.P., and S. Elgueta (2000), Sedimentologic development of a Late Oligocene-Miocene forearc embayment, Valdivia Basin Complex, southern Chile, *Sedimentary Geology*, *130*, 27-44.
- Le Roux, J.P., C.A. Gómez, D.M. Olivares, and H. Middleton (2005), Determining the Neogene behavior of the Nazca plate by geohistory analysis, *Geology*, *33*, 165-168.
- Le Roux, J.P., C. Gómez, C. Venegas, J. Fenner, H. Middleton, M. Marchant, B. Buchbinder, D. Frassinetti, C. Marquardt, K.M. Gregory-Wodzicki, and A. Lavenu (2005), Neogene-Quaternary coastal and offshore sedimentation in north central Chile: Record of sea-level changes and implications for Andean tectonism, *Journal of South American Earth Sciences*, *19*, 83-98.
- Le Roux, J.P., D.M. Olivares, S.N. Nielsen, N.D. Smith, H. Middleton, J. Fenner, and S.E. Ishman (2006), Bay sedimentation as controlled by regional crustal behaviour, local tectonics and eustatic sea-level changes: Coquimbo Formation (Miocene-Pliocene), Bay of Tongoy, central Chile, *Sedimentary Geology*, *184*, 133-153.
- Lear, C.H., H. Elderfield, and P.A. Wilson (2000), Cenozoic deep-sea temperatures and global ice volumes from Mg/Ca in benthic foraminiferal calcite, *Science*, *287*, 269-272.
- Linares, E., and R.R. González (1990), *Catálogo de Edades Radimétricas de la República Argentina 1957-1987*, 628 pp., Buenos Aires.
- Linares, E., H.A. Osters, and L.C. Mas (1999), Cronología potasio-argón del Complejo Efusivo Copahue-Caviahue, Provincia del Neuquén, *Revista Asociación Geológica Argentina*, *54*, 240-247.
- Liu, M., Y. Shen, and Y. Yang (2000), Gravitational collapse of orogenic crust: A preliminary three-dimensional finite element study, *Journal of Geophysical Research*, *105*, 3159-3173.
- Lohmar, S. (2000), Estratigrafía, Petrografía y Geoquímica del Volcán Antuco y sus depósitos (Andes del Sur, 37°25'S), master thesis, 115 pp., Universidad de Concepción, Concepción.
- Lohmann, J. (2002), Identification of parameters controlling the accretive and tectonically erosive mass-transfer mode at the South-Central and North Chilean forearc using scaled 2D sandbox experiments, Ph.D. thesis, 236 pp., Freie University Berlin, Berlin.
- Lomnitz, C. (1970), Major earthquakes and tsunamis in Chile during the period 1535 to 1955, *Geologische Rundschau*, *59*, 938-960.
- Lomnitz, C. (2004), Major earthquakes of Chile: a historical survey, 1535-1960, *Seismological Research Letters*, *75*, 368-378.
- Lowell, T.V., C.J. Heusser, B.G. Andersen, P.I. Moreno, A. Hauser, L.E. Heusser, C. Schlüchter, D.R. Marchant, and G.H. Denton (1995), Interhemispheric correlation of late pleistocene glacial events, *Science*, *269*, 1541-1549.
- López-Escobar, L., J. Cembrano, and H. Moreno (1995), Geochemistry and tectonics of the Chilean Southern Andes basaltic Quaternary volcanism (37-46°S), *Revista Geológica de Chile*, *22*, 219-234.
- Lüth, S., P. Wigger, M. Araneda, G. Asch, K. Bataille, M. Bohm, C. Bruhn, P. Giese, J. Quezada, A. Rietbrock, and P. Wigger (2003), A crustal model along 39°S from a seismic refraction profile-ISSA 2000, *Revista Geológica de Chile*, *30*, 83-94.
- Marquardt, C., A. Lavenu, L. Ortlieb, E. Godoy, and D. Comte (2004), Coastal neotectonics in Southern Central Andes: Uplift and deformation of marine terraces in Northern Chile (27°S), *Tectonophysics*, *394*, 193-219.
- Marquardt, C. (2005), Neogene deformation along the coast of northern Chile (23-27°S), forearc of the Central Andes, Ph.D. thesis, 219 pp., University of Toulouse III - Paul Sabatier, Toulouse.
- Marrett, R., and M. Strecker (2000), Response of intracontinental deformation in the central Andes to late Cenozoic reorganization of South American Plate motions, *Tectonics*, *19*, 452-467.
- Martínez-Pardo, R. (1990), Major Neogene events of the Southeastern Pacific: the Chilean and Peruvian record, *Palaeogeography, Palaeoclimatology, Palaeoecology*, *77*, 263-278.
- Matsuda, T., Y. Ota, M. Ando, and N. Yonekura (1978), Fault mechanism and recurrence time of major earthquakes in southern Kanto district, Japan, as deduced from coastal terrace data, *Geological Society of America Bulletin*, *89*, 1610-1618.
- Melnick, D., A. Folguera, M. Rosenau, H. Echtler, and S. Potent (2002), Tectonics from the northern segment of the Liquiñe-Ofqui fault system (37°-39°S), Patagonian Andes, in *5th International Symposium of Andean Geodynamics*, pp. 413-417, IRD, Toulouse.
- Melnick, D., M. Sanchez, H. Echtler, and V. Pineda (2003), Structural geology of Mocha Island, south-central Chile (38°30'S, 74°W): Regional tectonic implications, in *X Congreso Geológico Chileno*, vol. CD-Rom, Universidad de Concepción, Concepción.
- Melnick, D., A. Folguera, H. Echtler, F. Charlet, O. Buettner, E. Chapron, B. Scharf, M. De Batist, and T. Vietor (2003), The Lago de la Laja fault system: Active intra-arc collapse in the southern Central Andes (37°15'S), in *X Congreso Geológico Chileno*, vol. CD-ROM, Universidad de Concepción, Concepción.
- Melnick, D., B. Bookhagen, H. Echtler, and M. Strecker (2005), Active shortening, surface deformation and late Neogene coastal geomorphology of the Arauco Region, Chile, in *6th International Symposium on Andean Geodynamic*, pp. 502-503, IRD, Barcelona.
- Melnick, D., M. Rosenau, A. Folguera, and H. Echtler (2006a), Neogene tectonic evolution of the Neuquén Andes western flank (37-39°S), in *Evolution of an Andean margin: A tectonic and magmatic view from the Andes to the Neuquén*

Bibliography

- Basin (35°-39°S lat)*, vol. 407, edited by S.M. Kay and V.A. Ramos, pp. 79-95, Geological Society of America Special Paper.
- Melnick, D., B. Bookhagen, H. Echtler, and M. Strecker (2006b), Coastal deformation and great subduction earthquakes, Isla Santa María, Chile (37°S), *Geological Society of America Bulletin*, 118, 1463-1480.
- Melnick, D., F. Charlet, H. Echtler, and M. De Batist (2006c), Incipient axial collapse of the Main Cordillera and strain partitioning gradient between the Central and Patagonian Andes, Lago Laja, Chile, *Tectonics*, 25, TC5004.
- Melnick, D., and H.P. Echtler (2006a), Inversion of forearc basins in south-central Chile caused by rapid glacial age trench fill, *Geology*, 34, 709-712.
- Melnick, D., and H.P. Echtler (2006b), Morphotectonic and geologic digital map compilations of the south-central Andes (36°-42°S), in *The Andes - Active Subduction Orogeny*, vol. 1, *Frontiers in Earth Sciences*, edited by O. Oncken, G. Chong, G. Franz, P. Giese, H.-J. Götze, V.A. Ramos, M. Strecker and P. Wigger, pp. 565-568, Springer-Verlag, Berlin Heidelberg New York.
- Melnick, D., A. Folguera, and V.A. Ramos (2006d), Structural control on arc volcanism: The Caviahué-Copahué complex, Central to Patagonian Andes transition (38°S), *Journal of South American Earth Sciences*, 22, 66-88.
- Mercer, J.H., and J.F. Sutter (1982), Late Miocene - earliest Pliocene glaciation in southern Argentina: implications for global ice-sheet history, *Palaeogeography, Palaeoclimatology, Palaeoecology*, 38, 185-206.
- Mercier, J.L., R. Armijo, P. Tapponnier, E. Carey-Gailhardis, and H. Tong Lin (1987), Change from late Tertiary compression to Quaternary extension in southern Tibet during the India-Asia collision, *Tectonics*, 6, 275-304.
- Migowski, C., A. Agnon, R. Bookman, J.F.W. Negendank, and M. Stein (2004), Recurrence pattern of Holocene earthquakes along the Dead Sea transform revealed by varve-counting and radiocarbon dating of lacustrine sediments, *Earth and Planetary Science Letters*, 222, 301-314.
- Miranda, F., A. Folguera, P.R. Leal, J.A. Naranjo, and A. Pesce (2006), Upper Pliocene to Lower Pleistocene Volcanic Complexes and Late Neogene Deformation in the South Central Andes (36°30'-38°S), in *Evolution of an Andean margin: A tectonic and magmatic view from the Andes to the Neuquén Basin (35°-39°S lat)*, vol. 407, edited by S.M. Kay and V.A. Ramos, pp. 287-298, Geological Society of America Special Paper.
- Molnar, P. (1988), Continental tectonics in the aftermath of plate tectonics, *Nature*, 35, 131-137.
- Molnar, P., and H. Lyon-Caen (1988), Some simple physical aspects of the support, structure, and evolution of mountain belts, in *Processes in Continental Lithospheric Deformation*, vol. 218, edited by B.C. Clark, J. Burchfiel and J. Suppe, pp. 179-207, Geological Society of America Special Paper.
- Molnar, P., and P. England (1990), Late Cenozoic uplift of mountain ranges and global climate change: Chicken or egg?, *Nature*, 346, 29-34.
- Molnar, P., P. England, and J. Martinod (1993), Mantle dynamics, uplift of the Tibetan Plateau, and the Indian monsoon, *Reviews of Geophysics*, 31, 357-396.
- Molnar, P., and M.A. Cane (2002), El Niño's tropical climate and teleconnections as a blueprint for pre-Ice Age climates, *Paleoceanography*, 17, 11-1.
- Montgomery, D.R., G. Balco, and S.D. Willett (2001), Climate, tectonics, and the morphology of the Andes, *Geology*, 29, 579-582.
- Mordojovich, C. (1974), Geology of a part of the Pacific margin of Chile, in *The Geology of Continental Margins*, edited by C.A. Burk and C.L. Drake, pp. 591-598, Springer, New York.
- Mordojovich, C. (1981), Sedimentary basins of Chilean Pacific Offshore, in *Energy Resources of the Pacific Region*, vol. 12, edited by M.T. Halbouty, pp. 63-82, American Association of Petroleum Geologists Studies in Geology.
- Moreno, H., R. Thiele, A. Lahsen, J. Varela, L. López-Escobar, and M. Vergara (1985), Geocronología de Rocas Volcánicas Cuaternarias en los Andes del Sur entre las latitudes 37° y 38°S, Chile, *Revista Asociación Geológica Argentina*, 40, 297-299.
- Moreno, H., and M. Gardeweg (1989), La erupción reciente del complejo volcánico Lonquimay (Diciembre de 1988), Andes del Sur, *Revista Geológica de Chile*, 16, 93-117.
- Moreno, H., and L. López-Escobar (1994), Los centros eruptivos de Rucapillán: Actividad volcánica reciente en la Depresión Central de los Andes del Sur (39°S), in *VII Congreso Geológico Chileno*, vol. 2, pp. 334-339, Universidad de Concepción, Concepción.
- Moreno, H., S. Lohmar, L. López-Escobar, and M.E. Petit-Breuilh (2000), Contribución a la evolución geológica, geoquímica e impacto ambiental del Volcán Antuco (Andes del Sur, 37°25'S), in *IX Congreso Geológico Chileno*, vol. 2, pp. 44-48, Sociedad Geológica de Chile, Puerto Varas.
- Mpodozis, C., and V. Ramos (1989), The Andes of Chile and Argentina, in *Geology of the Andes and Its Relation to Hydrocarbon and Mineral Resources*, edited by G.E. Erickson, M.T. Cañas Pinochet and J.A. Reinemund, pp. 59-90, Cricum-Pacific Council for Energy and Mineral Resources, Texas.
- Muñoz, J., and H. Niemeyer (1984), Hoja Laguna del Maule, Regiones del Maule y del Bío-Bío, 1:250.000, Servicio Nacional de Geología y Minería, Santiago.
- Muñoz, J., and C.R. Stern (1988), The Quaternary volcanic belt of the southern continental margin of South America: transverse structural and petrochemical variations across the segment between 38°S and 39°S, *Journal of South American Earth Sciences*, 1, 147-161.
- Muñoz, J., R. Troncoso, P. Duhart, P. Crignola, L. Farmer, and C.R. Stern (2000), La relación de Cinturón Magmático del Terciario-medio del centro-sur de Chile con el incremento de la razón de convergencia de placas en el Oligoceno superior, *Revista Geológica de Chile*, 27, 177-203.

Scientific Technical Report STR 07/01

Bibliography

- Muñoz-Cristi, J. (1946), Estado actual del conocimiento sobre la geología de la provincia de Arauco, *Anales Universidad de Chile*, 3, 30-63.
- Müller, R.D., W.R. Roest, J.-Y. Royer, L.M. Gahagan, and J.G. Sclater (1997), Digital isochrons of the world's ocean floor, *Journal of Geophysical Research*, 102, 3211-3214.
- Nakamura, K. (1977), Volcanoes as possible indicators of tectonic stress orientation - Principle and proposal, *Journal of Volcanology and Geothermal Research*, 2, 1-16.
- Naranjo, J.A., and M. H. (1991), Actividad explosiva postglacial en el volcán Llaima, Andes del Sur (38°45'S), *Revista Geológica de Chile*, 18, 69-80.
- Nelson, R., and W. Manley (1992), Holocene coseismic and aseismic uplift of the Isla Mocha, south-central Chile, *Quaternary International*, 15/16, 61-76.
- Nielsen, S., and T. DeVries (2002), Tertiary Xenophoridae (Gastropoda) of western South America, *The Nautilus*, 116, 71-78.
- Nielsen, S.N., D. Frassinetti, and K. Bandel (2004), Miocene Vetigastropoda and Neritimorpha (Mollusca, Gastropoda) of central Chile, *Journal of South American Earth Sciences*, 17, 73-88.
- Nielsen, S. (2005), *Exilia alanbeu*, a new species from the Neogene of central Chile: the first record of *Exilia* (Gastropoda: Ptychactinidae) from South America, *The Nautilus*, 119, 153-156.
- Niemeyer, H., and J. Muñoz (1983), Geología de la hoja Laguna de La Laja, Región de Bío-Bío, 1:250.000, Servicio Nacional de Geología y Minería, Santiago.
- Nishenko, S. (1985), Seismic potential for large and great interplate earthquakes along the Chilean and southern Peruvian margins of South America: a quantitative reappraisal, *Journal of Geophysical Research*, 90, 3589-3615.
- Obermeier, S.F. (1996), Using liquefaction-induced features for paleoseismic analysis, *Paleoseismology*, 331-396.
- Oncken, O., D. Hindle, J. Kley, K. Elger, P. Victor, and K. Schemmann (2006), Deformation of the Central Andean upper plate system – facts, fiction, and constraints for plateau models, in *The Andes - Active Subduction Orogeny*, vol. 1, edited by O. Oncken, G. Chong, G. Franz, P. Giese, H.-J. Götze, V.A. Ramos, M. Strecker and P. Wigger, Springer, Berlin.
- Ortlieb, L., C. Zazo, J.L. Goy, C. Hillaire-Marcel, B. Ghaleb, and L. Cournoyer (1996), Coastal deformation and sea-level changes in the northern Chile subduction area (23°S) during the last 330 ky, *Quaternary Science Reviews*, 15, 819-831.
- Ortlieb, L., A. Diaz, and N. Guzman (1996), A warm interglacial episode during oxygen isotope stage 11 in northern Chile, *Quaternary Science Reviews*, 15, 857-871.
- Ota, Y., and M. Yamaguchi (2004), Holocene coastal uplift in the western Pacific Rim in the context of late Quaternary uplift, *Quaternary International*, 120, 105-117.
- Pandolfi, M., M.R. Best, and S.P. Murray (1994), Coseismic event of May 15, 1992, Huon Peninsula, Papua New Guinea, *Geology*, 22, 239-240.
- Pankhurst, R.J., S.D. Weaver, F. Hervé, and P. Larrondo (1999), Mesozoic-Cenozoic evolution of the North Patagonian Batholith in Aysen, southern Chile, *Journal of the Geological Society*, 156, 673-694.
- Park, J.-O., T. Tsuru, S. Kodaira, A. Nakanishi, S. Miura, Y. Kaneda, and Y. Kono (2000), Out-of-sequence thrust faults developed in the coseismic slip zone of the 1946 Nankai earthquake (Mw=8.2) off Shikoku, southwest Japan, *Geophysical Research Letters*, 27, 1033-1036.
- Paskoff, R., and H. Manríquez (2004), *Las Dunas de las Costas de Chile*, 113 pp., Instituto Geográfico Militar, Sanitago.
- Pearson, D.L. (1988), Biology of Tiger Beetles, *Annual Review of Entomology*, 33, 123-147.
- Petit-Breuilh, M.E. (1994), Actividad volcánica y cronología eruptiva histórica del volcán Antuco (37°24'S-71°22'W), Chile, *Revista Geográfica de Chile Terra Australis*, 39, 79-102.
- Philip, H., and M. Meghraoui (1983), Structural analysis and interpretation of the surface deformation during El Asnam earthquake of October 10, 1980, *Tectonics*, 2, 17-49.
- Pineda, V. (1986), Evolución paleográfica de la cuenca sedimentaria Cretácico-Terciaria de Arauco, in *Geología y Recursos Minerales de Chile*, vol. 1, edited by J. Frutos, R. Oyarzún and M. Pincheira, pp. 375-390, Universidad de Concepción, Concepción.
- Pineda, V. (1999), El cañón submarino del Bío-Bío: aspectos dinámicos y ambientales, Ph.D. thesis, 151 pp., Universidad de Concepción, Concepción.
- Pino, M., K. Moreno, and M.P. Riedemann (2002), La terraza del último interglacial en la costa de Valdivia: observaciones, interpretaciones y desafíos, in *International Symposium on Environmental Geology for Land Use Planning*, vol. 1, pp. 165-168, Sernageomin, Puerto Varas.
- Pino, M., and R.X. Navarro (2005), Geoarqueología del sitio arcaico Chan-Chan 18, costa de Valdivia: Discriminación de ambientes de ocupación humana y su relación con la transgresión marina del Holoceno Medio, *Revista Geológica de Chile*, 32, 59-75.
- Plafker, G., and J.C. Savage (1970), Mechanism of the Chilean earthquake of May 21 and 22, 1960, *Geological Society of America Bulletin*, 81, 1001-1030.
- Plafker, G. (1972), Alaskan earthquake of 1964 and Chilean earthquake of 1960 - Implications for arc tectonics, *Journal of Geophysical Research*, 77, 901-925.

- Potent, S., and C.-D. Reuther (2001), Neogene Deformationsprozesse im aktiven magmatischen Bogen Südzentralchiles zwischen 37° und 39°S, *Mitteilung Geologische und Paläontologische Institute Universität Hamburg*, 85, 1-22.
- Rabassa, J., and C.M. Clapperton (1990), Quaternary glaciations of the southern Andes, *Quaternary Science Reviews*, 9, 153-174.
- Rabassa, J., A.M. Coronato, and M. Salemme (2005), Chronology of the Late Cenozoic Patagonian glaciations and their correlation with biostratigraphic units of the Pampean region (Argentina), *Journal of South American Earth Sciences*, 20, 81-103.
- Radic, J., L. Rojas, A. Carpinelli, and E. Zurita (2002), Evolución tectónica de la Cuenca Terciaria de Cura Mallín, región cordillerana chileno-argentina (36°30'-39°S), in *XV Congreso Geológico Argentino*, vol. 3, pp. 233-237, Sociedad Geológica Argentina, El Calafate.
- Radtke, U. (1989), *Marine Terrassen und Korallenriffe - Das Problem der Quatären Meeresspiegelschwankungen erläutert an Fallstudien aus Chile, Argentinien und Barbados*, 245 pp., Heinrich-Heine-Universität Düsseldorf.
- Ramos, V.A. (1977), Estructura, in *Geología y Recursos Naturales de la provincia del Neuquén*, edited by E.O. Roller, pp. 9-24, Relatorio 7° Congreso Geológico Argentino, Buenos Aires.
- Ramos, V.A. (1999), Plate tectonic setting of the Andean Cordillera, *Episodes*, 22, 183-190.
- Rauch, K. (2005), Cyclicity of Perú-Chile trench sediments between 36° and 38°S: A footprint of paleoclimatic variations?, *Geophysical Research Letters*, 32, 1-4.
- Raymo, M.E., and W.F. Ruddiman (1992), Tectonic forcing of late Cenozoic climate, *Nature*, 359, 117-122.
- Reichert, C., and the SPOC Team (2002), Fahrbericht SONNE-Fahrt SO-161 Leg 2&3 SPOC -Subduktionsprozesse vor Chile- BMBF-Forschungsvorhaben 03G0161A, in *Bundesanstalt für Geowissenschaften und Rohstoffe*, pp. 154, Hannover.
- Reinecker, J., O. Heibach, M. Tingay, P. Connolly, and B. Müller (2004), The 2004 release of the World Stress Map (available online at www.world-stress-map.org).
- Rietbrock, A., C. Haberland, K. Bataille, T. Dahm, and O. Oncken (2005), Studying the Seismogenic Coupling Zone with a Passive Seismic Array, *Eos*, 86, 293.
- Rodríguez, S. (1835), *Informe Presentado a la Intendencia de la Provincia de Concepción de Chile, por Ambrosio Lozier, Simón Rodríguez y Juan José Arteaga, nombrados para reconocer la ciudad de Concepción y sus cercanías, después del terremoto de 20 Febrero de 1835*, 471-507 pp., Universidad Simón Rodríguez, Caracas.
- Rosenau, M., D. Melnick, W. Seifert, J. Glodny, K. Graefe, H. Ehtler, and H. Kemnitz (2001), Exhumation of intra-arc basement in the Southern Andes: A kinematic model and implication for mountain building in subduction settings, *Schriftenreihe DGG*, 14, 171-172.
- Rosenau, M. (2004), Tectonics of the Southern Andean intra-arc zone (38°-42°S), Ph.D. thesis, 159 pp., Free University Berlin, Berlin.
- Rosenau, M., D. Melnick, and H. Ehtler (2006), Kinematic constraints on intra-arc shear and strain partitioning in the Southern Andes between 38°S and 42°S latitude, *Tectonics*, 25, TC4013.
- Rossetti, D.D.F. (1999), Soft-sediment deformation structures in late Albian to Cenomanian deposits, Sao Luis Basin, northern Brazil: Evidence for palaeoseismicity, *Sedimentology*, 46, 1065-1081.
- Royden, L. (1996), Coupling and decoupling of crust and mantle in convergent orogens: Implications for strain partitioning in the crust, *Journal of Geophysical Research*, 101, 17679-17705.
- Savage, J.C. (1983), A Dislocation Model of Strain Accumulation and Release at a Subduction Zone, *Journal of Geophysical Research*, 88, 4984-4996.
- Schnellmann, M., F.S. Anselmetti, D. Giardini, J.A. McKenzie, and S.N. Ward (2002), Prehistoric earthquake history revealed by lacustrine slump deposits, *Geology*, 30, 1131-1134.
- Seifert, W., M. Rosenau, and H. Ehtler (2005), Crystallization depths of granitoids of South Central Chile estimated by Al-in-hornblende geobarometry: Implications for mass transfer processes along the active continental margin, *Neues Jahrbuch für Geologie und Paläontologie - Abhandlungen*, 236, 115-127.
- Selverstone, J. (2005), Are the Alps collapsing?, *Annual Review of Earth and Planetary Sciences*, 33, 113-132.
- Sernageomin (2003), Geologic map of Chile digital version, 1:1.000.000, Servicio Nacional de Geología y Minería, Santiago.
- Shipboard Scientific Party (2003), Site 1232, in *Proceedings of the Ocean Drilling Program, Initial reports*, vol. 3, edited by Mix, A.C., R. Tiedemann, et al., College Station, Texas.
- Siame, L.L., O. Bellier, M. Sébrier, and M. Araujo (2005), Deformation partitioning in flat subduction setting: Case of the Andean foreland of western Argentina (28°S-33°S), *Tectonics*, 24, TC5003.
- Siddall, M., E.J. Rohling, A. Almogi-Labin, C. Hemleben, D. Meischner, I. Schmelzer, and D.A. Smeed (2003), Sea-level fluctuations during the last glacial cycle, *Nature*, 423, 853-858.
- Sims, J.D. (1975), Determining earthquake recurrence intervals from deformational structures in young lacustrine sediments, *Tectonophysics*, 29, 141-152.
- Sobolev, S.V., and A.Y. Babeyko (2005), What drives orogeny in the Andes?, *Geology*, 33, 617-620.
- Somoza, R. (1998), Updated Nazca (Farallon)-South America relative motions during the last 40 My: Implications for mountain building in the central Andean region, *Journal of South American Earth Sciences*, 11, 211-215.

- Stern, C.R. (1989), Pliocene to present migration of the volcanic front, Andean Southern Volcanic Zone, *Revista Geológica de Chile*, 16, 145-162.
- Stern, C.R. (2004), Active Andean volcanism: Its geologic and tectonic setting, *Revista Geológica de Chile*, 31, 161-206.
- Stewart, I.S., J. Sauber, and J. Rose (2000), Glacio-seismotectonics: Ice sheets, crustal deformation and seismicity, *Quaternary Science Reviews*, 19, 1367-1389.
- Stuiver, M., P.J. Reimer, E. Bard, J.W. Beck, G.S. Burr, K.A. Hughen, B. Kromer, G. McCormac, J. Van Der Plicht, and M. Spurk (1998), INTCAL98 radiocarbon age calibration, 24,000-0 cal BP, *Radiocarbon*, 40, 1041-1083.
- Suárez, M., and C. Emparán (1995), The stratigraphy, geochronology and paleogeography of a Miocene fresh-water interarc basin, southern Chile, *Journal of South American Earth Sciences*, 8, 17-31.
- Suárez, M., and C. Emparán (1997), Hoja Curacautín, Regiones de la Araucanía y del Bío-Bío, 1:250.000, Servicio Nacional de Geología y Minería, Santiago.
- Suppe, J., G.T. Chou, and S.C. Hook (1992), Rates of folding and faulting determined from growth strata, in *Thrust Tectonics*, edited by K.R. McClay, pp. 105-121, Chapman and Hall, New York.
- Tassara, A., and G. Yáñez (2003), Relationship between elastic thickness and the tectonic segmentation of the Andean margin (15-47°S), *Revista Geológica de Chile*, 30, 159-186.
- Tassara, A., H.J. Götze, S. Schmidt, and R. Hackney (2006), Three-dimensional density model of the Nazca plate and the Andean continental margin, *Journal of Geophysical Research*, 111, B09404.
- Taylor, F., C. Frohlich, J. Lecolle, and M. Strecker (1987), Analysis of partially emerged corals and reef terraces in the central Vanuatu Arc: comparison of contemporary coseismic and nonseismic with Quaternary vertical movements, *Journal of Geophysical Research*, 92, 4905-4933.
- Tebbens, S.F., and S.C. Cande (1997), Southeast Pacific tectonic evolution from early Oligocene to present, *Journal of Geophysical Research*, 102, 12061-12084.
- Teyssier, C., B. Tikoff, and M. Markley (1995), Oblique plate motion and continental tectonics, *Geology*, 23, 447-450.
- Thatcher, W. (1990), Order and diversity in modes of circum-Pacific earthquake recurrence, *Journal of Geophysical Research*, 95, 2609-2624.
- Thiede, R.C., J.R. Arrowsmith, B. Bookhagen, M.O. McWilliams, E.R. Sobel, and M.R. Strecker (2005), From tectonically to erosionally controlled development of the Himalayan orogen, *Geology*, 33, 689-692.
- Thiele, R., H. Moreno, S. Elgueta, A. Lahsen, S. Rebolledo, and M.E. Petit-Breuilh (1998), Evolución geológico-geomorfológica cuaternaria del tramo superior del valle del río Laja, *Revista Geológica de Chile*, 25, 229-253.
- Thomson, S.N. (2002), Late Cenozoic geomorphic and tectonic evolution of the Patagonian Andes between latitudes 42°S and 46°S: An appraisal based on fission-track results from the transpressional intra-arc Liquiñe-Ofqui fault zone, *Geological Society of America Bulletin*, 114, 1159-1173.
- Tibaldi, A. (1995), Morphology of pyroclastic cones and tectonics, *Journal of Geophysical Research*, 100, 24521-24535.
- Tikoff, B., and C. Teyssier (1994), Strain modeling of displacement-field partitioning in transpressional orogens, *Journal of Structural Geology*, 16, 1575-1588.
- Vergara, M., and Y. Katsui (1969), Contribución a la geología y petrología del volcán Antuco, Cordillera de los Andes, Chile Central, *Departamento de Geología, Universidad de Chile, Publicación* 35, 25-47.
- Vergara, M., and J. Muñoz (1982), La Formación Cola de Zorro en la Alta cordillera Andina Chilena (36°-39°S), sus características petrográficas y petrológicas: Una revisión, *Revista Geológica de Chile*, 17, 31-46.
- Vietes, H., R. Arcos, and A. González (1993), Interpretación Geológica de Sísmica Marina del Golfo de Arauco, pp. 17, Empresa Nacional del Petróleo, Santiago.
- Von Huene, R., and D.W. Scholl (1991), Observations at convergent margins concerning sediment subduction, subduction erosion, and the growth of continental crust, *Reviews of Geophysics*, 29, 279-316.
- von Huene, R., C.R. Ranero, and P. Vannucchi (2004), Generic model of subduction erosion, *Geology*, 32, 913-916.
- Wang, K., and J. He (1999), Mechanics of low-stress forearcs: Nankai and Cascadia, *Journal of Geophysical Research*, 104, 15191-15205.
- Wang, K., and Y. Hu (2006), Accretionary prisms in subduction earthquake cycles: The theory of dynamic Coulomb wedge, *Journal of Geophysical Research*, 111, B06410.
- Wells, D.L., and K.J. Coppersmith (1994), New empirical relationships among magnitude, rupture length, rupture width, rupture area, and surface displacement, *Bulletin of the Seismological Society of America*, 84, 974-1002.
- Wells, R.E., R.J. Blakely, Y. Sugiyama, D.W. Scholl, and P.A. Dinterman (2003), Basin-centred asperities in great subduction zone earthquakes: A link between slip, subsidence, and subduction erosion, *J. Geophys. Res.*, 108, 2507-2537.
- Willett, S. (1999), Orogeny and orography: The effects of erosion on the structure of mountain belts, *Journal of Geophysical Research*, 104, 28957-28981.
- Yáñez, G.A., C.R. Ranero, R. Von Huene, and J. Díaz (2001), Magnetic anomaly interpretation across the southern central Andes (32°-34°S): The role of the Juan Fernández Ridge in the late Tertiary evolution of the margin, *Journal of Geophysical Research*, 106, 6325-6345.

Bibliography

- Yáñez, G., J. Cembrano, M. Pardo, C. Ranero, and D. Selles (2002), The Challenger-Juan Fernández-Maipo major tectonic transition of the Nazca-Andean subduction system at 33-34°S: Geodynamic evidence and implications, *Journal of South American Earth Sciences*, 15, 23-38.
- Yáñez, G., and J. Cembrano (2004), Role of viscous plate coupling in the late Tertiary Andean tectonics, *Journal of Geophysical Research*, 109, B02407.
- Yuan, X., S.V. Sobolev, R. Kind, O. Oncken, G. Bock, G. Asch, B. Schurr, F. Graeber, A. Rudloff, W. Hanka, K. Wylegalla, R. Tibi, C. Haberland, A. Rietbrock, P. Giese, P. Wigger, P. Röwer, G. Zandt, S. Beck, T. Wallace, M. Pardo, and D. Comte (2000), Subduction and collision processes in the Central Andes constrained by converted seismic phases, *Nature*, 408, 958-961.
- Yuan, X., G. Asch, K. Bataille, G. Bock, M. Bohm, H. Echtler, R. Kind, O. Oncken, and I. Wolbern (2006), Deep Seismic Images of the Southern Andes, in *Evolution of an Andean margin: A tectonic and magmatic view from the Andes to the Neuquén Basin (35°-39°S lat)*, vol. 407, edited by S.M. Kay and V.A. Ramos, pp. 61-72, Geological Society of America Special Paper.
- Zachos, J., H. Pagani, L. Sloan, E. Thomas, and K. Billups (2001), Trends, rhythms, and aberrations in global climate 65 Ma to present, *Science*, 292, 686-693.
- Zapata, T., and A. Folguera (2005), Tectonic evolution of the Andean Fold and thrust belt of the southern Neuquén Basin, Argentina, in *The Neuquén Basin: A Case Study in Sequence: Stratigraphy and Basin Dynamics*, vol. 252, edited by G.D. Veiga, L.A. Spalletti, J.A. Howell and E. Schwartz, pp. 37-56, Geological Society Special Publication, London.

Appendix A

A1. Methods and data sources

Structural field observations were combined with time-migrated reflection-seismic profiles obtained from ENAP (Empresa Nacional del Petróleo—the Chilean state oil company), and published stratigraphic, sedimentologic, and paleontologic data from forearc basins in south-central Chile (García, 1968; Biró, 1979; Pineda, 1986; Martínez-Pardo, 1990; Le Roux and Elgueta, 1997; Le Roux and Elgueta, 2000; Nielsen and DeVries, 2002; Finger et al., 2003; Nielsen et al., 2004; Encinas et al., 2005; Nielsen, 2005; Finger et al., 2006). About forty reflection profiles were inspected and the seismic stratigraphy of selected lines was correlated with the available exploration boreholes from ENAP (Mordojovich, 1974; Mordojovich, 1981; González, 1989; Arcos and Elgueta, 1993). Multibeam bathymetry and depth-migrated reflection profiles from the trench and slope regions (Reichert et al., 2002; Rauch, 2005) were used to interpret along-strike variability and deformation of the trench fill. Crustal seismicity and focal mechanisms from the ISSA (Integrated Seismological experiment in the Southern Andes) temporary network in the Arauco region were integrated with data from the NEIC and USGS catalogues and reflection profiles to identify active faults and define the present-day stress regime of the forearc. The ISSA experiment deployed 62 three-component broadband instruments and 16 OBH/OBS between January and March 2000 in the 36–40°S region (Bohm et al., 2002; Bruhn, 2003; Bohm, 2004). Recent data from the TIPTEQ network, which deployed 140 onshore stations and 30 OBH/OBS in the same region and has been operating since November 2004, shows that the faults identified with the ISSA data (Melnick et al., 2005) continue its strong activity nucleating up to $m_b=5.2$ shallow events (Rietbrock et al., 2005).

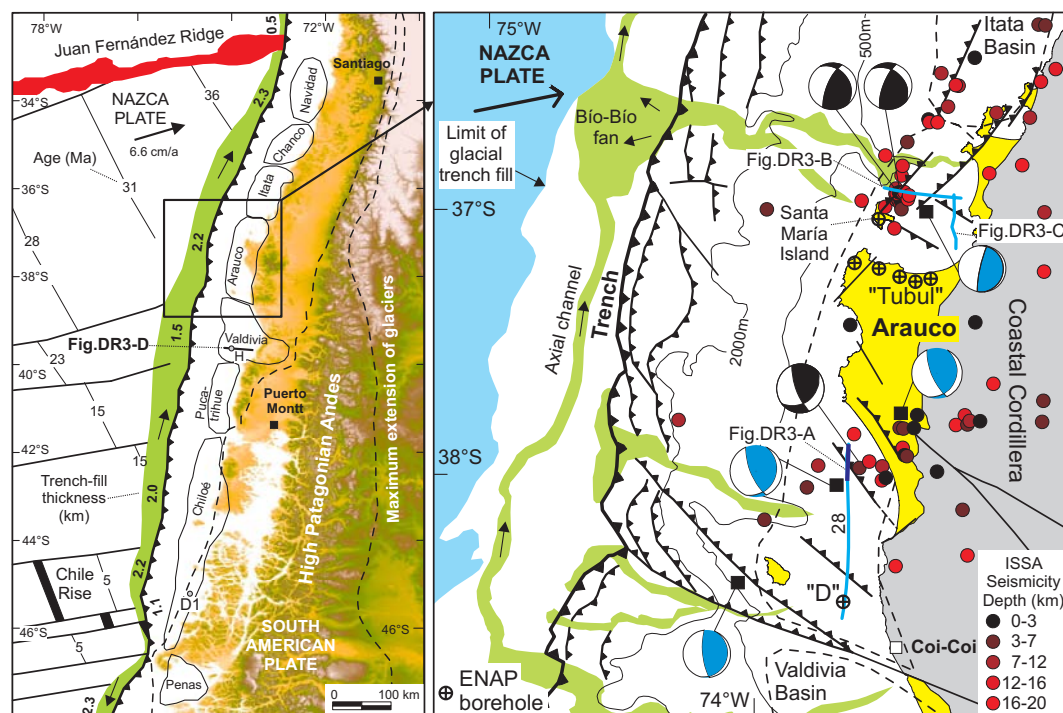


Figure A1: Regional map of forearc basins in south-central Chile and tectonic setting of the Arauco Basin. Location of ENAP seismic-reflection profiles shown in Figures 2 and DR3. ENAP exploration wells used to correlate the seismic stratigraphy are also shown (Mordojovich, 1974; Mordojovich, 1981; González, 1989; Arcos and Elgueta, 1993). Trench and slope interpreted from SPOC swath bathymetry and depth-migrated reflection profiles (Reichert et al., 2002; Rauch, 2005), shelf from ENAP seismic-reflection profiles and coastal exposures (Melnick et al., 2005). Depth-coded seismicity and black focal mechanisms from the ISSA network (Bohm et al., 2002; Bruhn, 2003). Blue focal mechanisms from shallow (<15 km) earthquakes of the NEIC and USGS catalogues.

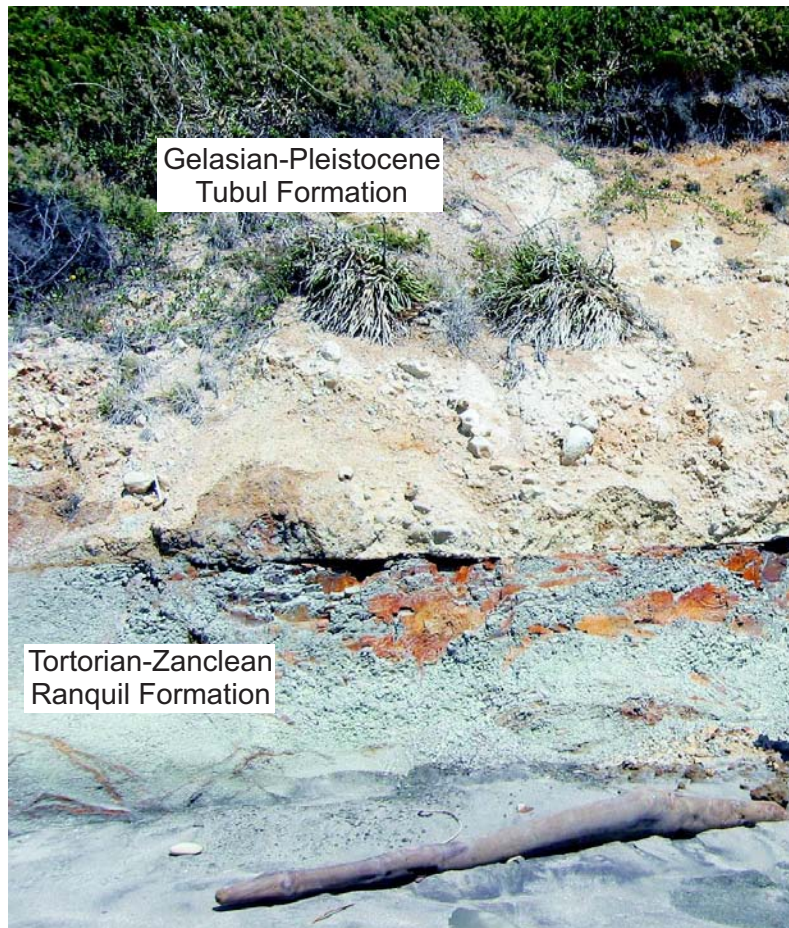


Figure A2: Unconformity between the late Miocene-early Pliocene lower bathyal siltstones of the Ranquil Formation and late Pliocene-Pleistocene near-shore sandstones of the Tubul Formation, Arauco Basin, in the area studied by García (1968), Biró (1979), Pineda (1986), Finger et al. (2003), Nielsen et al. (2004), Encinas et al. (2005), Nielsen (2005) and Finger et al. (2006). The stem lying on the beach is 3 meters long.



Figure A3: Left: Syntectonic deposition across a normal fault in the late Miocene-early Pliocene lower bathyal siltstones of the Ranquil Formation. Stratigraphy and age in this region studied by Encinas et al. (2005), Finger et al. (2003), Nielsen et al. (2004), Nielsen (2005) and Finger et al. (2006). Slip is 0.5 meters. Right: Syntectonic deposition across a normal fault in near-shore, coal-bearing facies of the Eocene Trihueco Formation. Stratigraphy and age studied by Pineda (1986) and LeRoux and Elgueta (1997).

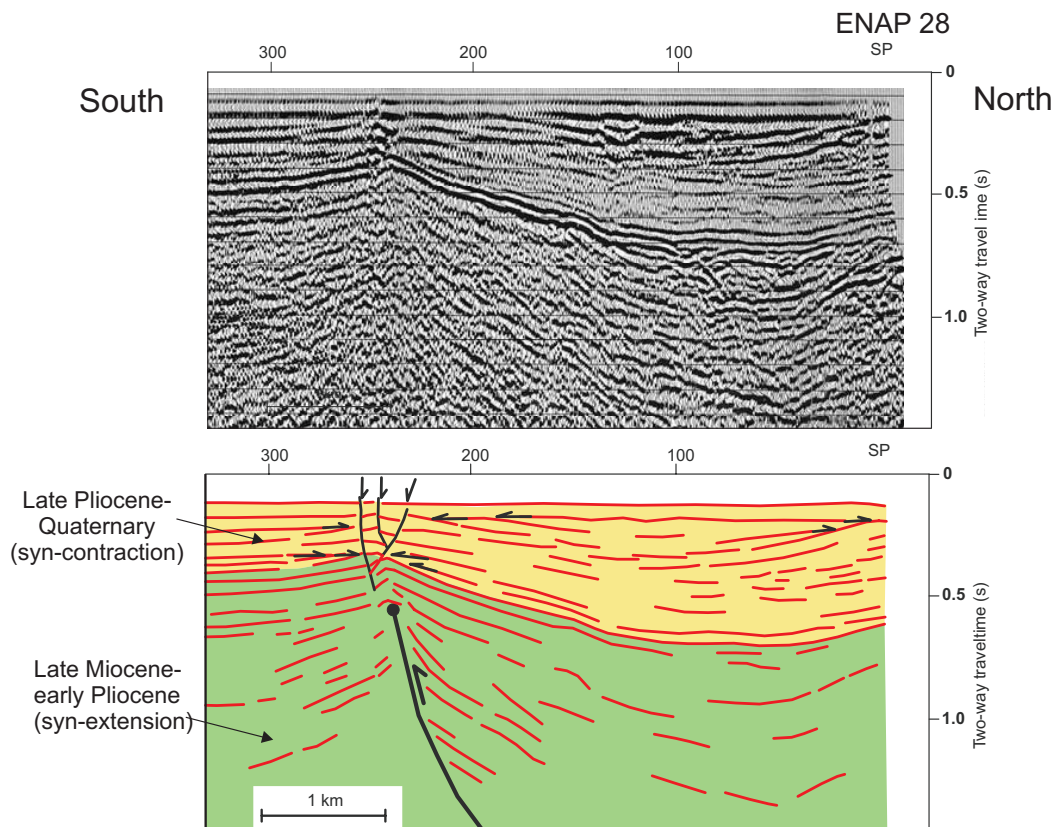


Figure A4-A: ENAP time-migrated reflection-seismic Profile 28 is north-south-oriented and located south of the Arauco Peninsula. The image shown here corresponds only to the northern part of the profile (see Fig. DR1 for location). The stratigraphy is correlated with ENAP borehole 'D', located farther south along the same line (Mordojovich, 1981; González, 1989; Bangs and Cande, 1997). Profile 28 images the late Miocene-early Pliocene Ranquil Formation, which is formed by parallel discontinuous reflectors, unconformably overlain by the late Pliocene-Quaternary Tubul Formation. The latter unit exhibit onlaps, thickness increase of continuous reflectors and a wedge-top geometry. In this light, the Ranquil unit is interpreted as a pre-growth unit and the Tubul Formation as syngrowth sequence. Here, syntectonic deposition has been controlled by a northwest-striking, landward-dipping reverse fault that blinds at ~ 0.5 s depth (two-way travel time) propagating an anticline. A small hinge graben developed at the tip of the anticline, probably reflecting bending-related extension. Shallow seismicity of the ISSA and TIPTEQ temporary networks cluster below this structure, and focal mechanisms are compatible with shortening along a northwest-striking fault. Continuous syntectonic deposition of the Tubul Formation indicates that shortening has been steady since the late Pliocene.

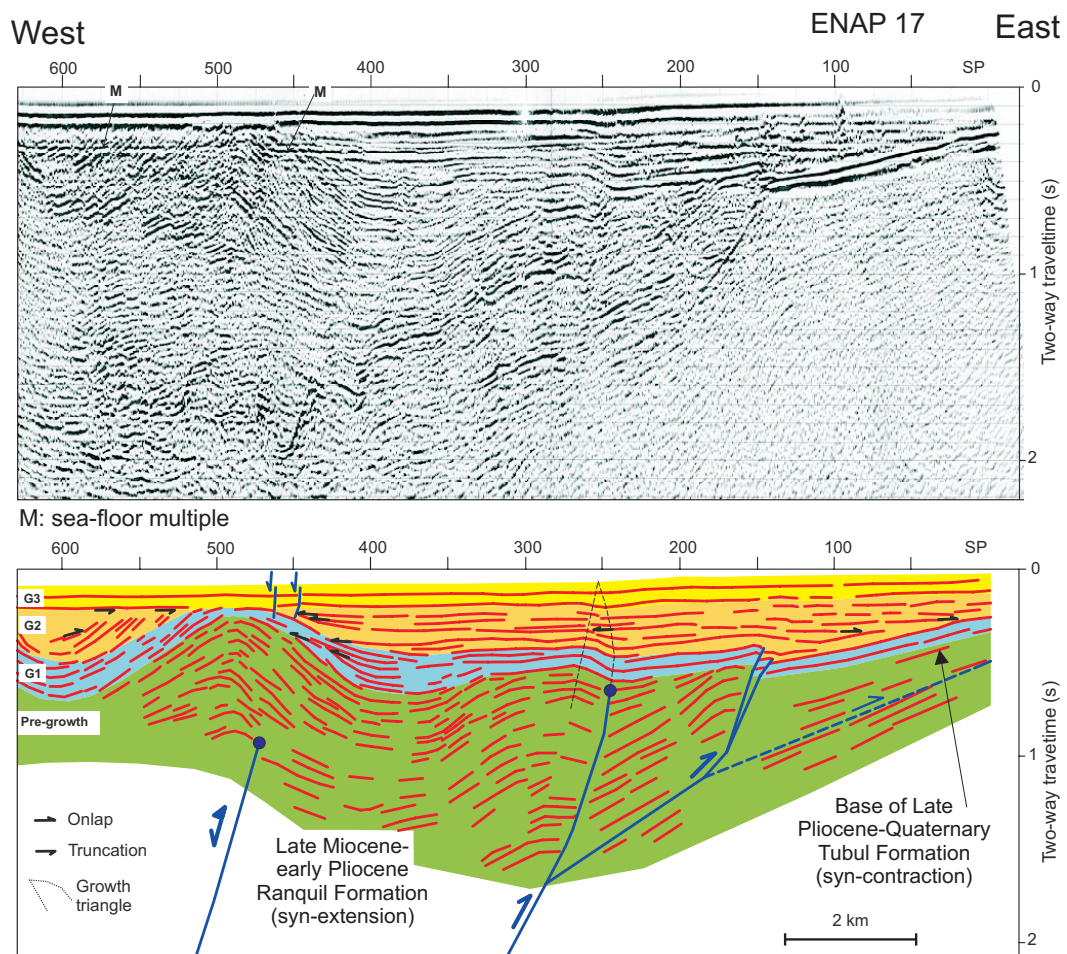


Figure A4-B: ENAP time-migrated reflection-seismic profile 17 is east-west-oriented and located in the Arauco Bay area, immediately north of the Santa María Island (see Fig. DR1 for location). This profile images a thrust-top basin filled by the late Pliocene-Quaternary Tubul Formation. Syntectonic deposition has been controlled by a master seaward-dipping reverse fault and two splaying branches forming a ramp-flat-ramp structure. The pre-growth basal unit has no internal truncations nor thickness change and is overlain by the syntectonic sequence. We differentiate three growth units in this sequence (G1,G2,G3), which reveal eastward propagation of the deformation coeval with slip along the western master fault, and continuous deformation since the Late Pliocene. The inflection of the axial surfaces, or kink bands, above the monocline at SP 150 define the onset of growth. The apex of this growth triangle is at the present surface, which is depositional, and allows to infer that this structure is actively growing (Suppe et al., 1992). Two small normal faults are located above the anticline at shotpoint 450, interpreted as bending-related extension.

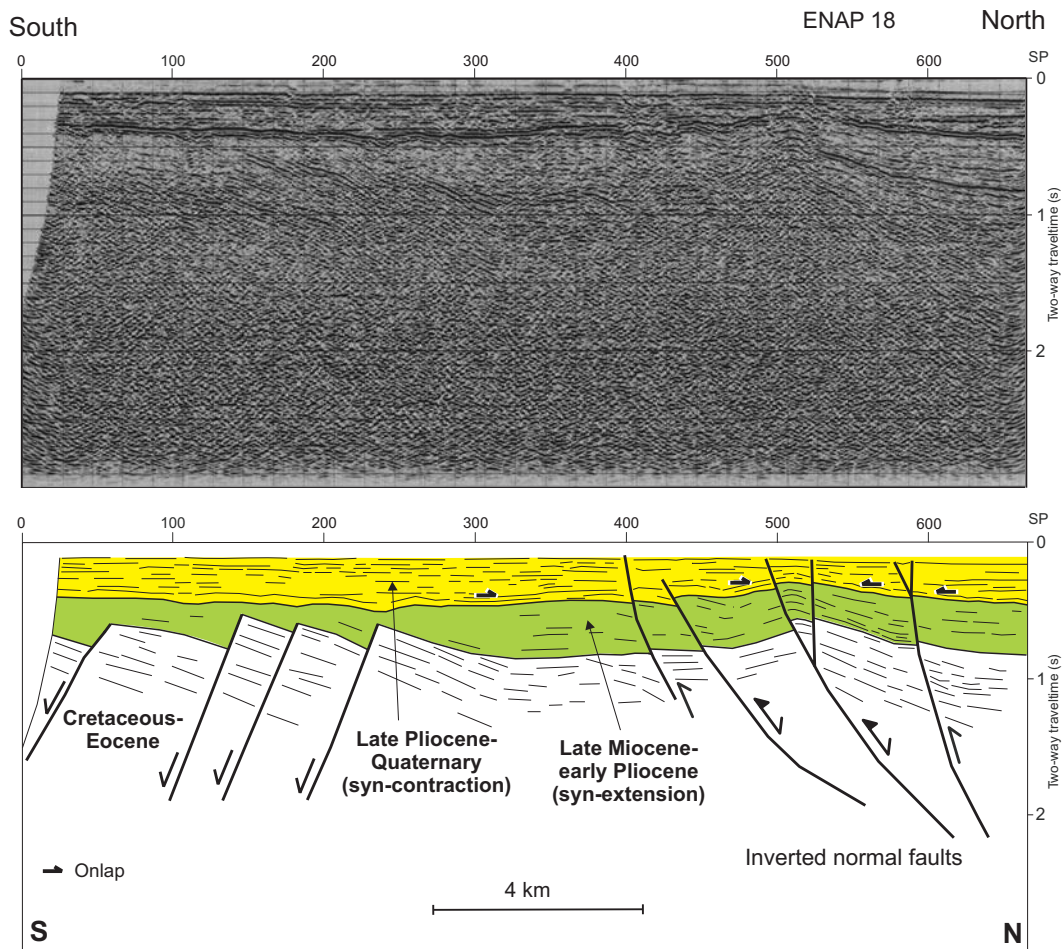


Figure A4-C: ENAP time-migrated reflection-seismic profile 18 is north-south-oriented and located in the Arauco Bay area east of the Santa María Island (see Fig. DR1 for location). In the southern sector, between shotpoints (SP) 50 and 250, this profile images south-dipping normal faults displacing the Eocene Millongue and late Miocene-early Pliocene Ranquil Formations, which are unconformably covered by subhorizontal sediments of the late Pliocene-Quaternary Tubul Formation. The stratigraphy has been correlated with ENAP wells Tubul-1 and Tubul-Este-1 (Arcos and Elgueta, 1993), which are located immediately to the south onshore (see Fig. DR1 for location), as well as exposed rocks along the coast to the east and a borehole at Santa María Island. Synextensional deposition of the late Miocene-early Pliocene Ranquil Formation deposition occurred in half-grabens bounded by domino-like south-dipping normal faults. In the northern sector, reverse faults and folds affect the sequence between SP 400 and 600, which we interpret as inverted domino-like normal faults similar to the faults imaged in the southern sector but with an opposite dip angle. The late Pliocene-Quaternary unit exhibits growth strata above these faults and folds. In this sector of the Arauco Basin, late Miocene-early Pliocene deposition occurred in two hemigrabens with opposite polarity limited by a central horst. Only the northern hemigrabens were inverted during late Pliocene-Quaternary compression. Some of the reverse faults seem to cut the uppermost reflectors indicating recent activity.

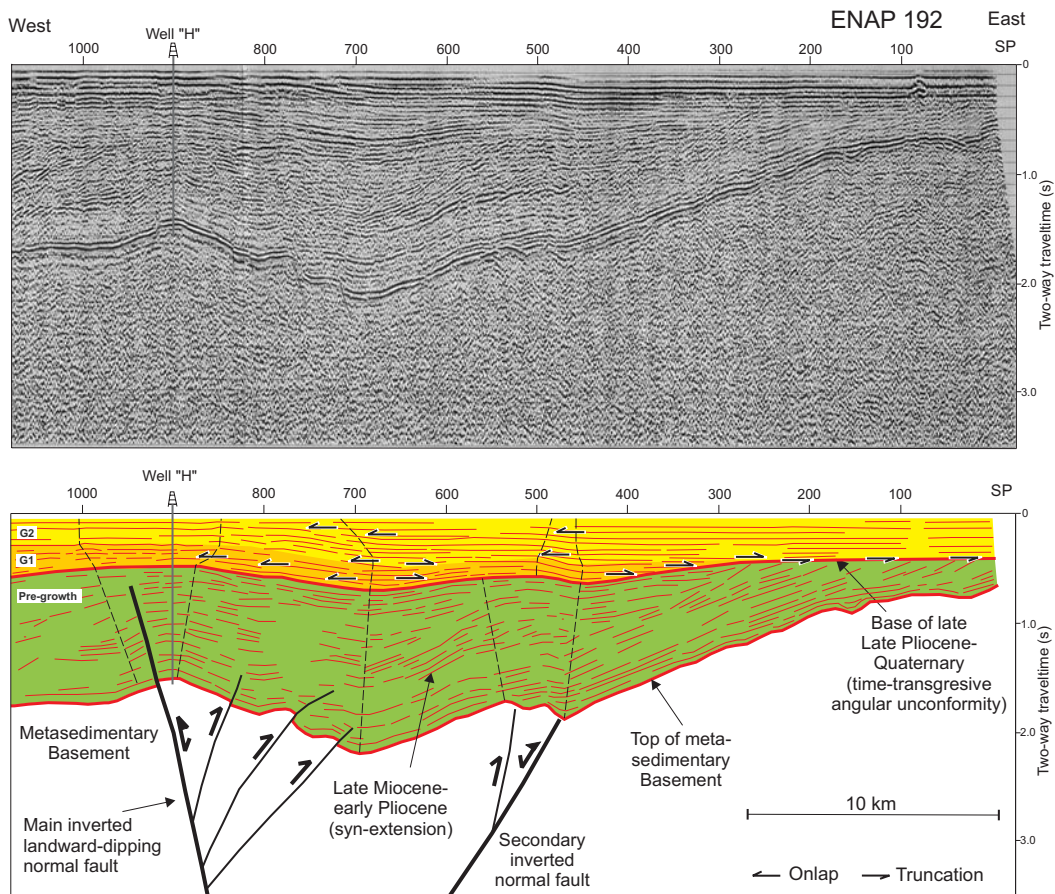


Figure A4-D: ENAP time-migrated reflection-seismic Profile 192 is east-west-oriented and located in the Valdivia Basin (see Fig. DR1 for location). This profile was originally interpreted by Mordojovich (1981, Fig. 13), but our structural understanding differs. The stratigraphy is constraint by borehole "H", which reached the Paleozoic metasedimentary basement at a depth of 1717 m below the sea floor. We interpret that a main landward-dipping normal fault, located at shotpoint (SP) 900, controlled extension and subsidence during deposition of the late Miocene-early Pliocene unit, which increases in thickness toward the center of the basin at SP 700. A secondary normal fault was probably located at SP 500. Tectonic shortening produced inversion of the normal fault at SP 900, as the reflectors at the base of the late Miocene unit are clearly offset in a reverse sense. An anticline developed in the hanging wall and three shortcutting secondary structures that offset the base of the Miocene unit as well. Two small flexures formed above the faults at SP 500. Basin inversion is recorded by the late Pliocene-Quaternary unit, which exhibits onlaps, thickness increase, and upward decreasing dip angles, interpreted as syntectonic deposition coeval to shortening. We differentiated two growth sequences, G1 and G2. The first is related to slip along the main fault at SP 900 and growth of the above-lying anticline. The base of this sequence onlaps against the late Miocene unit between SP 400 and 250. Sequence G2 is related to activity of both the main fault at SP 900 and the secondary fault at SP 500. The base of this sequence truncates the Miocene unit east of SP 200 forming a time-transgressive angular unconformity (Suppe et al., 1992), which we relate to syndeformation erosion prior to the onset of late Pliocene deposition. The inflection of kink bands denote the onset of shortening.

Appendix B

B1. Facies and sedimentology of the Santa Maria Formation

Lower marine unit

This unit is dominated by black sandstones with minor interbedded layers of clay, peat, paleosol, and locally fine conglomerate. The black sandstones are medium to coarse, occasionally showing grading to fine conglomerate. They consist mainly of volcanic lithic components (85 to 90%), minor quartz (3%), feldspars and other minerals (7 to 12%), occasionally retransported volcanic tuffs and small shell fragments (Figure B2). Within these deposits there are zones of intense vertical bioturbation and highly contorted limonitic layers. The sandstone beds are not laterally continuous and thin-out rapidly (Figure B3). The main sedimentary structures found in the black sandstone are coarse cross bedding in individual beds that can reach a thickness of 10 m, wavy flaser bedding, and fine inclined and parallel lamination. Locally, individual successive rhythmic upward-coarsening sequences of medium to pebbly sand and fine conglomerate characterize this unit. Grain-size distribution curves from this unit resemble curves obtained from present-day shore depositional environments of the island (Figure B1).

The interbedded layers consist of: (1) grey clay with 10 to 30 cm mean thickness (but locally up to 1.5 m) that typically contains charcoal and occasionally wood; (2) dark-brown clay-rich paleosols, ranging from 10 cm to ~1 m in thickness and that also contain charcoal; (3) black peat, about 1-m thick containing wood; and (4) very rounded conglomerates with metamorphic and occasional volcanic clasts, 2 to 3 cm in diameter but that can reach 30 cm. These beds usually form lenses reaching a lateral continuity of 50 m.

The volcanic-rich black sands derive from basaltic lavas of the Antuco volcano in the Main Cordillera (Figure 5.1B). During Pleistocene time, opening of Lake Laja, adjacent to the volcano, caused a catastrophic megaflood that formed fans in the Central Depression composed of volcanic-derived material (Vergara and Katsui, 1969), which have been since transported to the coast by the Laja, Itata, and Bío-Bío rivers (Figure 5.1B). These black sands are unique and thus found in the vicinity of these rivers, suggesting that the volcanic-rich sandstone and associated metamorphic and volcanic gravels were transported to the continental shelf by the Bío-Bío river when sea level was lower, and subsequently reworked in a near-shore marine environment.

Upper eolian unit

This unit consists of homogeneous very well sorted brownish sandstone. The medium size sandstone are composed of volcanic lithic components (50 to 65%), feldspars (20 to 25%), quartz (13 to 15%), and minor metamorphic lithic components and other minerals (~2 %). The main sedimentary structure is fine horizontal and inclined parallel lamination (Figures B2 and B4). Grain-size distribution curves from this unit are similar to the active dunes in the lowland, and differ from the present-day marine and Pleistocene curves (Figure B1).

A well-exposed section of these deposits exists at Punta Cochinos, the southern point of the island (section on Figure B2; aerial view on Figure 4B). This section consists of a 0.5-m-thick dark-brown paleosol at the base, directly above the Tertiary rocks, which has a radiocarbon age of 31.5 ± 1.8 cka. It is overlain by four 1- to 4-m-thick beds of very well sorted brown sandstones with a rhythmic succession of horizontal and laminations dipping 30°E, interbedded with an undated, 0.5-m-thick paleosol in the upper part of the section.

Bioturbation is common in these sandstones. At Cadenas Peninsula we found well-preserved in situ trace fossils, which are exposed along a distinct horizontal depositional surface. The traces are cavities, composed of a 15-cm-long horizontal cylindrical part that bends upward into a 3-cm-high vertical section with a small circular opening (Figure B4). These features appear to be insect burrows. Kaizuka et al. (1973) described similar features in fixed Pleistocene dunes on Arauco Peninsula. These authors reported identical cavities filled with remnants of insects that belong to the family of tiger beetles (Cicindelidae), which are restricted to dry sandy environments (Pearson, 1988).

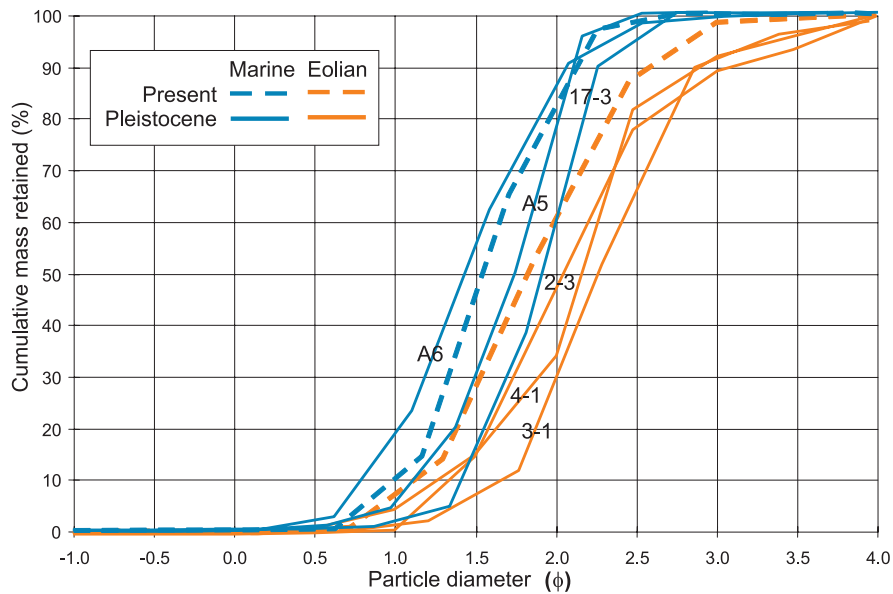


Figure B1: Grain-size distribution curves comparing present and Pleistocene marine and eolian sands. The present marine samples is from the wash zone in the beach east of Puerto Sur. The present-day eolian sample is from the windward side of active dunes in the lowlands east of Puerto Norte. The Pleistocene marine samples are from the southern domain (A6 and A5) and from the northern domain (17-3). The Pleistocene eolian samples are from the northern (4-1 and 3-1) and southern (2-3) domains. Detail descriptions and extended data set in Jara (2006).



Figure B3: View of shore facies of the marine unit north of Cadenas Peninsula. See Figure 5.3A for location. Note the rhythmic interbedding between black sandstones, dark-brown paleosols (indicated with radiocarbon ages), and white to grayish layers of clay.

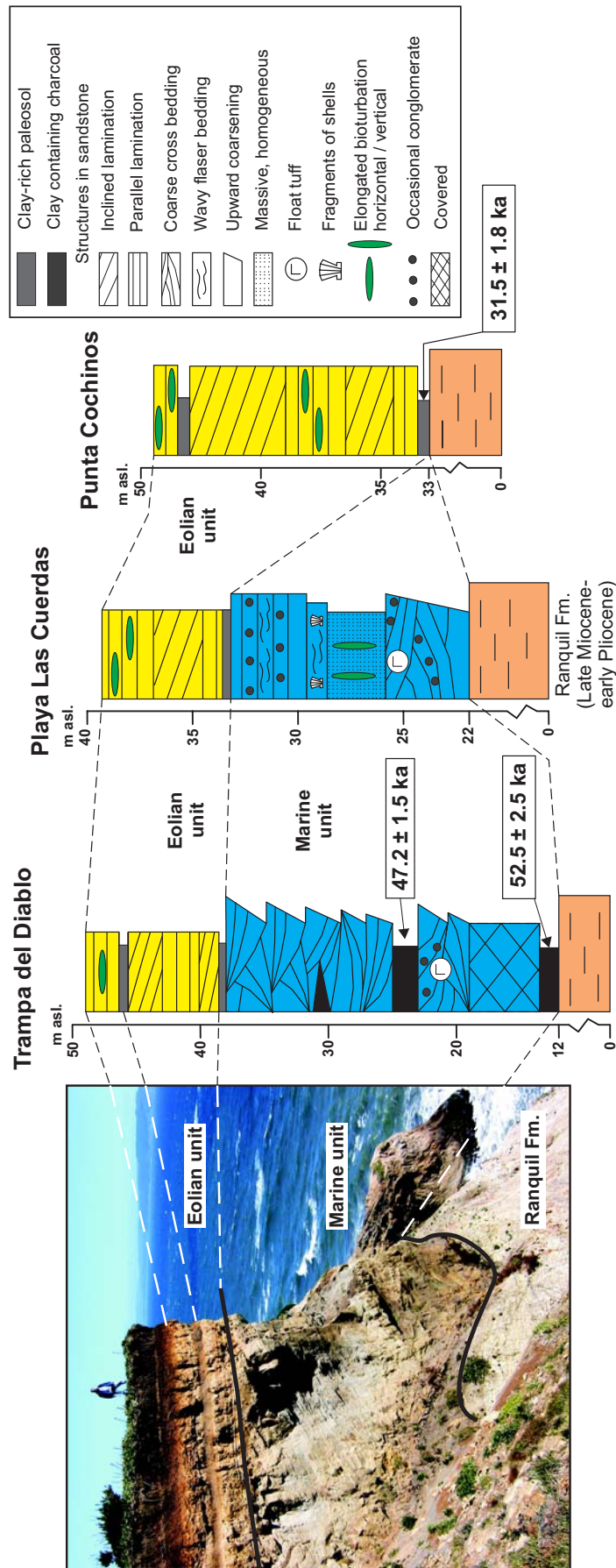


Figure B2: Field view and stratigraphic sections of the Santa María Formation. See Fig. 3B and aerial views on Figs. 4 and 5 for location.



Figure B4: View of the eolian unit at Cadenas Peninsula. Note the rhythmic succession of sandstone with inclined and horizontal lamination. Detailed view of trace fossils above the surface of the eolianite. These cavities are interpreted as insect burrows produced by tiger beetles, which presently live in dry sandy environments.

B2. Facies in incised channels surrounding Cadenas Peninsula

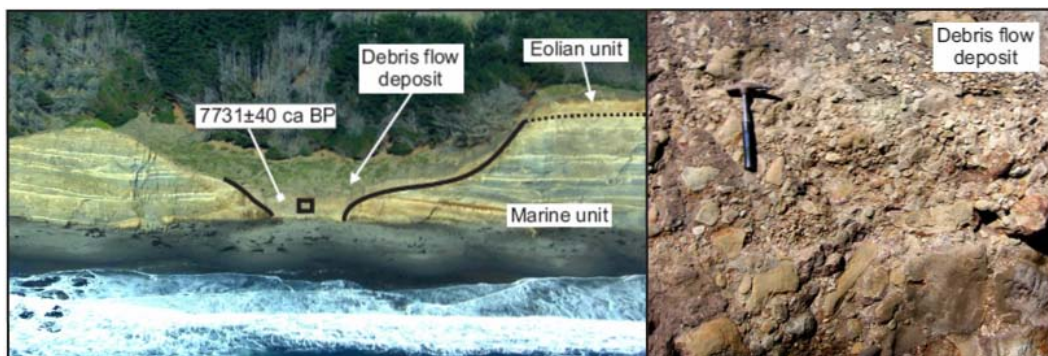


Figure B5: Aerial view of an erosive channel incised in the Santa Maria Formation immediately north of the Cadenas Peninsula. See Figure 3A for location. The stream was subsequently filled by a massive debris flow deposit. Radiocarbon age indicated in the deposit. The square shows location of detailed view on the right. The debris flow deposit is monomict, formed by angular brownish clasts from the Pleistocene eolian unit. The matrix is sandy with occasional lenses of fine material containing charcoal. Similar deposits crop out south of Cadenas Peninsula (see photo in Figure DR7-A; map on Figure 5.3A).

B3. Normal faulting and marine growth strata

Northern Fault

The northern fault is well expressed at the western coast (Figure B6). The main fault dips 80°N and offsets the Tertiary/Pleistocene unconformity by 2.6 m; at 15 m distance from this structure, an antithetic normal fault dips 75°S and offsets the unconformity by 1.4 m. Both faults delimit a southward-tilted block of the Pleistocene sequence. The dip of the Pleistocene beds in the hanging wall decreases progressively upward indicating syntectonic sedimentation caused by slip on the north dipping growth fault (Figure B6). The tilted block is offset by a recent 0.4-m-slip rupture, which may have occurred during one of the past great earthquakes (Figure B6). The fault trace is very well preserved, and only limited material from the rupture zone has been removed by erosion. Farther west, this fault controls the only deep valley in the northern sector of the island

(Figure 5.3A). The southern flank of this valley has steep slopes and the Tertiary/Pleistocene unconformity crops out continuously at ~10 m elevation. The northern flank has lower slopes formed by gently-dipping Pleistocene beds in the backlimb of the tilted block, and the Tertiary/Pleistocene unconformity crops out at 5 m elevation.

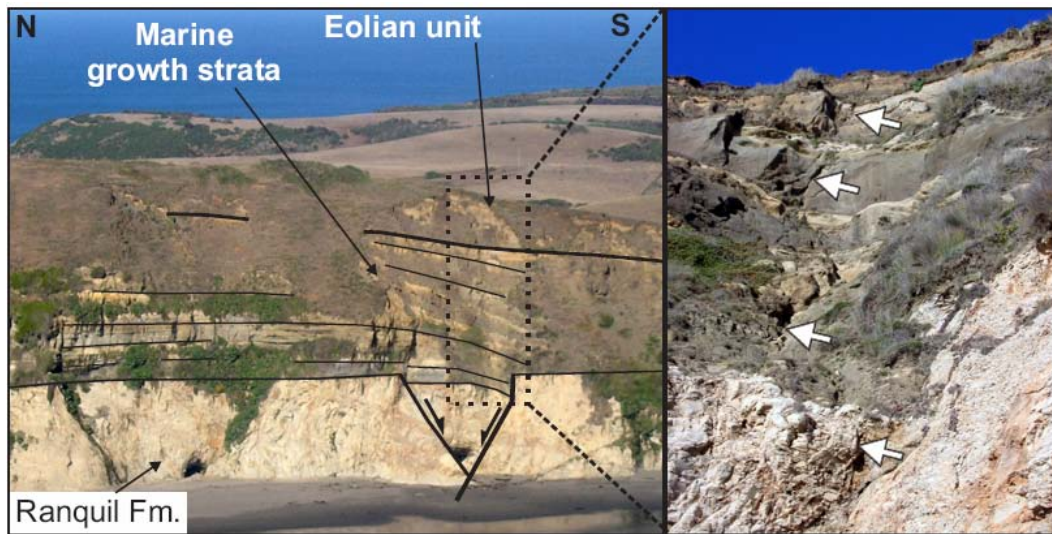


Figure B6: Oblique air photo to the east showing the northern normal fault. Note progressive upward decrease in dip of the marine unit in the hanging wall of the north dipping fault. Detail field view of a recent rupture that produced a normal offset of 0.4 m.

Central Fault System

The depression and promontory in the center of the island are controlled by several faults that form a half-graben. This fault system divides the island into the two distinct tilt domains (Figure B7). This system includes: (1) a northwest dipping master fault south of the depression (Figure B7-B); (2) normal faults that form a horst-and-graben structure (Figure B7-A); (3) zones of intense fracturing and syndimentary faulting of the Pleistocene marine sandstone; and (4) an intra-Pleistocene onlap surface (Figure B7-C). The profile shown in Figure B7-D illustrates the geometry of the central half-graben. The main fault has a 30-cm-wide cataclastic zone and juxtaposes Tertiary siltstone and the Pleistocene Santa María Formation, with intense antithetic faulting in the hanging wall (Figure B7-B). This fault does not cut the upper unit. At Cadenas Peninsula, the marine unit is formed by two lithologically identical parts separated by an onlap surface; the horizontal upper beds onlap against similar underlying layers, which dip 30°SE (Figure B7-C). We relate the tilting of the lower beds to slip on the master growth fault and the onlap surface to progressive syntectonic sedimentation.

Southern Fault

The southern fault strikes east-northeast and dips north; it is located at the southernmost point of the island and juxtaposes Tertiary rocks with the Pleistocene marine unit, which is absent in the footwall (Figure B8). The coastal marine sandstone in the hanging wall contain flame structures, injection veins, and are highly contorted, which we interpret as fault-related liquefaction features. Their distribution, as well as the intense vertical fracturation of the sandstone decreases steadily northward, away from the fault. The Tertiary rocks in the footwall are back-tilted 10°S and crop out 160 m north of the fault dipping 30°S (Figure B8). A 1.2-m-thick paleosol dips 30°S also above the Tertiary siltstone of the Ranquil Formation and the inclination of the overlying marine sequence decreases continuously upward. We thus interpret the southern fault as a growth structure that controlled the syntectonic deposition of the Pleistocene marine sediments in the hanging wall.

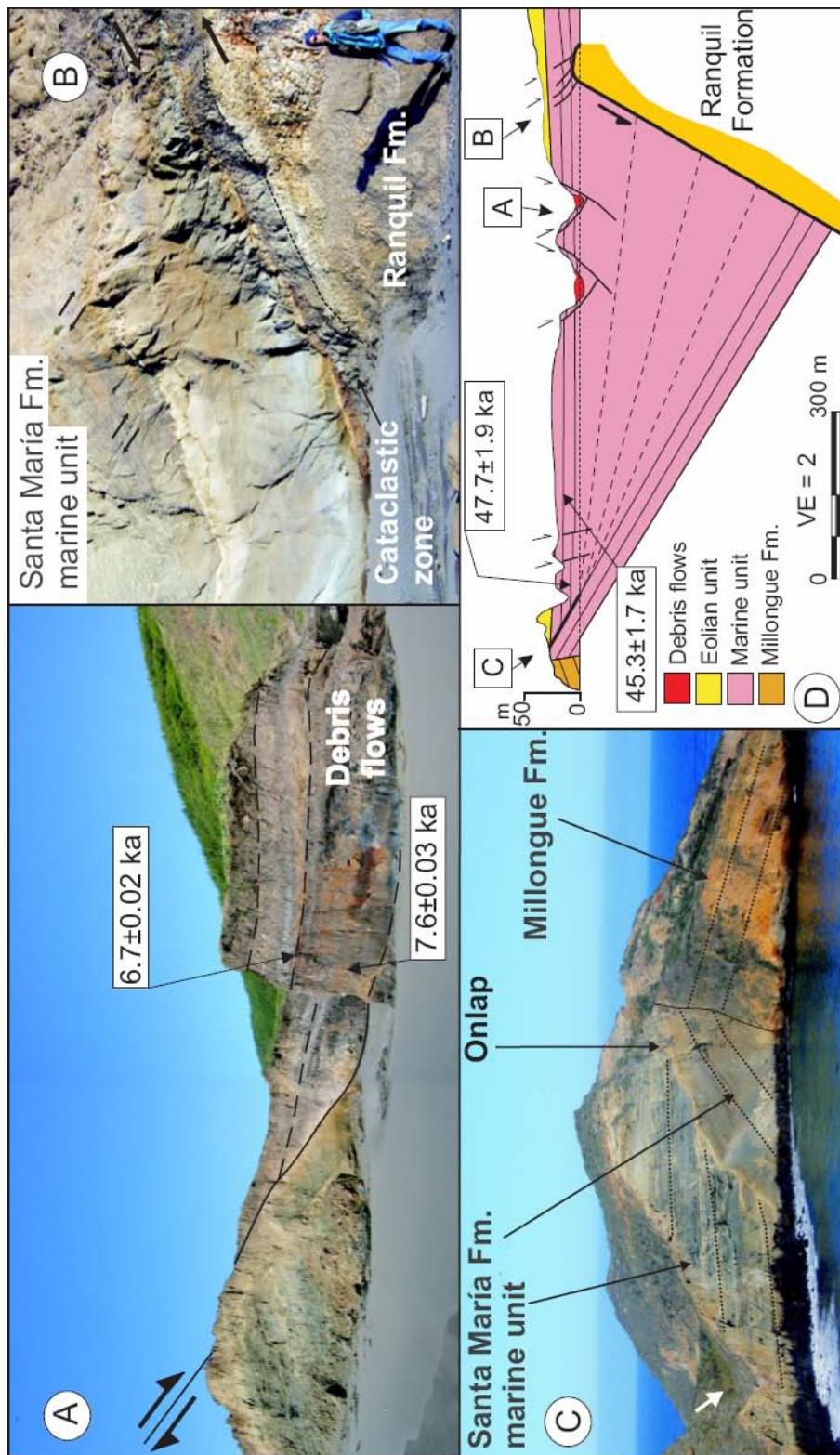


Figure B7: Structures in the central part of the island. A: View of a normal fault and debris flow deposits with peaty matrix in the hanging wall with location of ¹⁴C calibrated ages. B: View of the growth fault that juxtaposes Tertiary siltstone with Pleistocene marine sandstone. C: View toward the southwest of the Cadenas Peninsula showing the onlap surface within the marine unit of the Santa María Formation. D: Cross-section of the half-graben, location of calibrated ¹⁴C ages, and interpretation of marine growth strata. Letters in squares show location of the photos.

B4. Tilting Rates Calculation Procedure

We used three reference surfaces to calculate the tilting rates of Isla Santa María: (1) the Tertiary/Pleistocene unconformity that is equal to the base of the marine unit and for which we assume a 51.6 ± 2.9 ka age (average of three ages); (2) the base of the eolian unit for which we assume a 31.5 ± 1.8 ka age; and (3) the present surface of the island for which we infer an age of 27 ± 2 ka based on sea-level data (see text). We believe that these erosional/depositional surfaces were subhorizontal at the time of their abandonment and that the subsequent tilting is only due to tectonic deformation. The well-preserved trace fossils found on the top of the eolian unit imply that erosion of this depositional surface is limited to the fluvial system.

In order to calculate realistic tilting angles, we measured the elevation of the three reference surfaces across eight profiles perpendicular to the tilt axis of the northern and southern domains (Figure B9). We judge our ability in measuring the elevations of the reference surfaces to be within ± 0.5 m. We derived four profiles for each tilt domain. The strike of the tilt axes was determined from the isobase contours of the Tertiary/Pleistocene unconformity, thickness variations of both units of the Santa María Formation, and the present topography analyzed from the high-resolution DEM (Figure B9). The elevation data, tilt angles and rates, and propagated errors of the three surface along the eight profiles are presented in Table B1. The average values for each reference surface of both domains, together with their standard deviation and sum of errors is given in Table B2.

Profile	Northern Domain				Southern Domain			
	1	2	3	4	5	6	7	8
Base marine unit								
Elevation West (m)	23.1	20.8	26.5	28.1	48.1	53.0	42.0	20.0
Elevation East (m)	10.1	16.8	3.2	4.0	<0	<0	9.8	4.2
Profile length (m)	250	266	1577	1476	2465	2451	1751	890
Tilt angle (degrees)	2.977	0.862	0.846	0.935	1.118	1.239	1.054	1.017
Tilting rate (°/k.y.)	0.058	0.017	0.016	0.018	>0.022	>0.024	0.020	0.020
Tilting rate error	0.008	0.005	0.002	0.002	>0.002	>0.002	0.002	0.003
Base eolian unit								
Elevation West (m)	25.9	40.0	31.0	32.0	57.0	53.0	45.0	35.0
Elevation East (m)	17.0	30.5	8.5	9.2	21.5	22.7	14.2	22.2
Profile length (m)	216	232	1546	1439	2432	2340	1690	829
Tilt angle (degrees)	2.359	2.345	0.834	0.908	0.836	0.742	1.044	0.885
Tilting rate (°/k.y.)	0.075	0.074	0.026	0.029	0.027	0.024	0.033	0.028
Tilting rate error	0.013	0.013	0.003	0.003	0.002	0.002	0.003	0.004
Present surface								
Elevation West (m)	57.0	57.0	57.0	60.0	68.0	55.0	52.0	36.0
Elevation East (m)	55.0	51.0	47.0	45.0	29.0	28.0	28.0	30.0
Profile length (m)	136	190	1419	1329	2357	2246	1515	796
Tilt angle (degrees)	0.843	1.809	0.404	0.647	0.948	0.689	0.908	0.432
Tilting rate (°/k.y.)	0.031	0.067	0.015	0.024	0.035	0.026	0.034	0.016
Tilting rate error	0.019	0.017	0.003	0.004	0.004	0.003	0.004	0.004

Table B1: Field data and tilt rates calculated for three reference surfaces along eight profiles, four in each tilt domain (Figure DR9). For the calculation we assumed ages of 51.6 ± 2.9 , 31.5 ± 1.8 , and 27 ± 2 ka BP for the base of the marine unit, base of the eolian unit, and present-day surface, respectively, and ± 0.5 m error in the elevation measurements. Note that in profiles 5 and 6, the base of the marine unit is below sea level and hence we can only calculate a minimum rate.

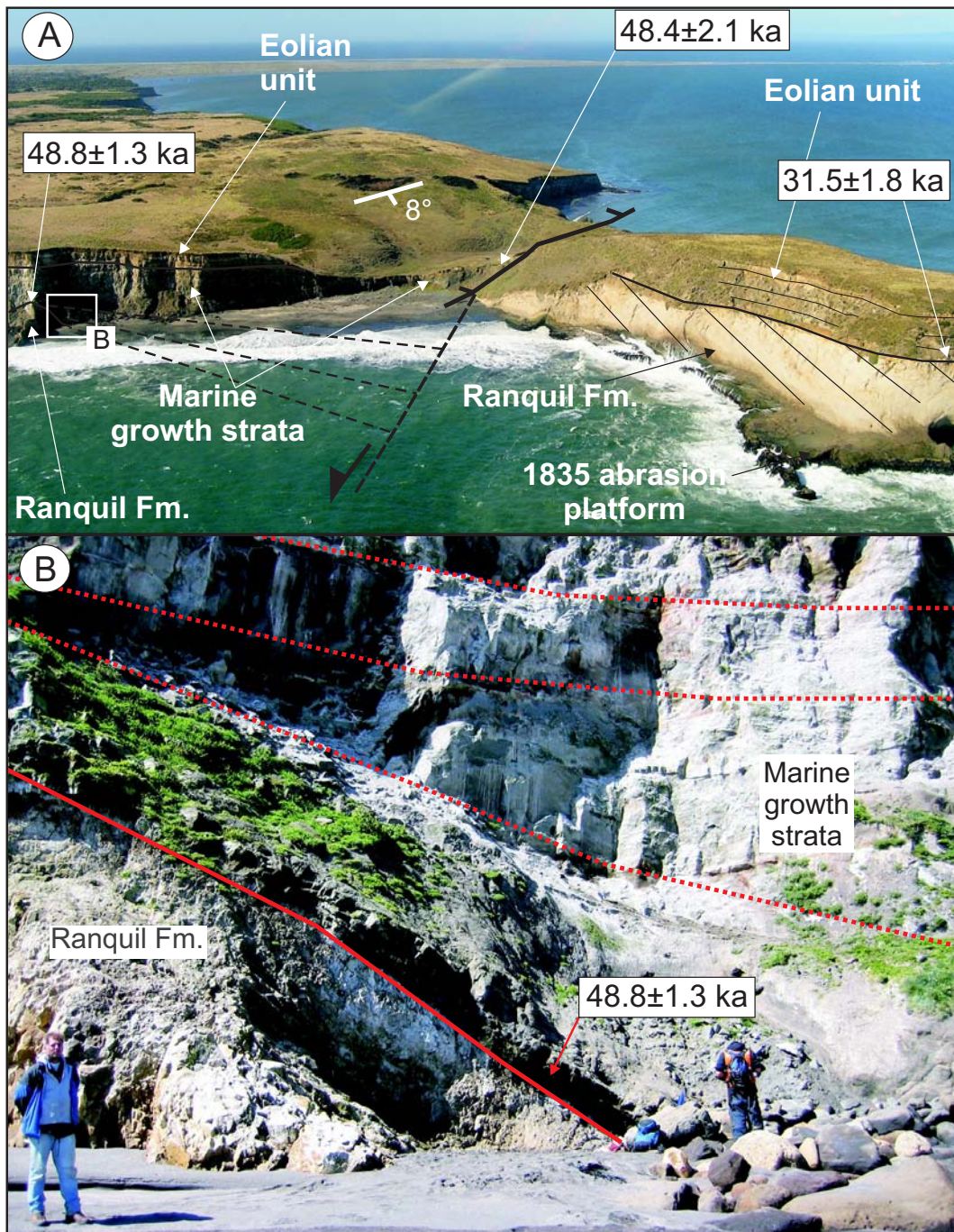


Figure B8: Oblique air photo to the east and interpretation of the growth fault at the southern point of the island indicating calibrated ^{14}C ages. Note the back-tilting of the Ranquil Fm. in the footwall and absence of the marine unit. Contortion, intense vertical fracturation and liquefaction structures in the marine unit increase continuously toward the fault. The abrasion platform emerged during the 1835 earthquake can be seen in the lower right. Right: Marine sandstone dipping 30°S above Ranquil Fm. in the hanging wall of the fault. Note the upward decrease in dip of the sandstone sequence. Paleosol with calibrated ^{14}C age at the base of the marine unit.

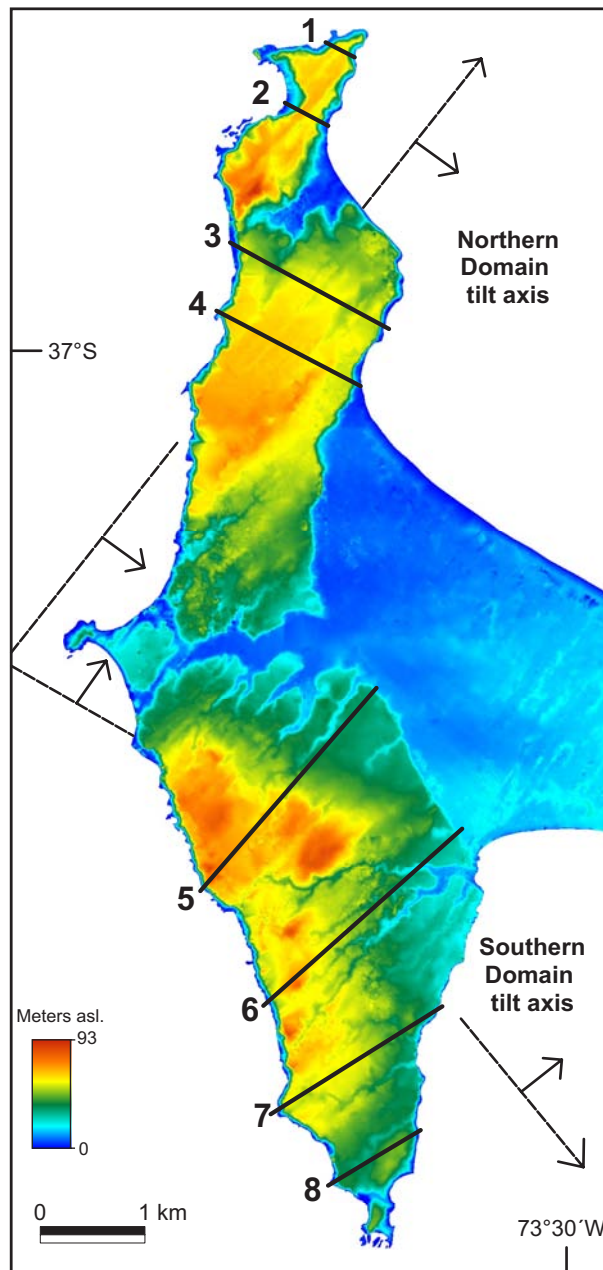


Figure B9: DEM showing location of profiles used to calculate tilting rates.

Average tilting rates (°/ka)	Base Marine			Base Eolian			Present Surface			Average	1σ SD	Σ errors
	Base Marine	1σ SD	Σ errors	Base Eolian	1σ SD	Σ errors	Present Surface	1σ SD	Σ errors			
Southern Domain	0.021	0.002	0.010	0.028	0.004	0.006	0.028	0.009	0.008	0.026	0.006	0.014
Northern Domain	0.027	0.020	0.004	0.051	0.027	0.019	0.034	0.023	0.026	0.038	0.024	0.033
Entire Island	0.024	0.014	0.011	0.039	0.022	0.020	0.031	0.016	0.028	0.032	0.018	0.036

Table B2: Average tilt rates, standard deviation, and sum of errors for the three reference surfaces of each domain and the entire island.